Energy-Efficient Trajectory Planning for Skid-Steer Rovers

Meysam Effati

A Thesis

In the Department

of

Electrical and Computer Engineering

Presented in Partial Fulfillment of the Requirements

For the Degree of

Doctor of Philosophy (Electrical and Computer Engineering) at

Concordia University

Montreal, Quebec, Canada

July 2020

CONCORDIA UNIVERSITY

SCHOOL OF GRADUATE STUDIES

This is to certify that the thesis prepared

By: Meysam Effati

Entitled: Energy-Efficient Trajectory Planning for Skid-Steer Rovers

and submitted in partial fulfillment of the requirements for the degree of

    Doctor Of Philosophy (Electrical & Computer Engineering)

complies with the regulations of the University and meets the accepted standards with respect to originality and quality.

Signed by the final examining committee:

_____ Chair
Dr. Catherine Mulligan

_____ External Examiner
Dr. James Forbes

_____ External to Program
Dr. Youmin Zhang

_____ Examiner
Dr. Luis Rodrigues

_____ Examiner
Dr. Rastko Selmic

_____ Thesis Co-Supervisor
Dr. Krzysztof Skonieczny

Approved by   _____
                     Dr. Rastko Selmic, Graduate Program Director

June 30, 2020   _____
                     Dr. Amir Asif, Dean
                     Gina Cody School of Engineering and Computer Science

Abstract

Energy-Efficient Trajectory Planning for Skid-Steer Rovers

Meysam Effati, Ph. D.

Concordia University, 2020

A skid-steer rover's power consumption is highly dependent on the turning radius of its path. For example, a point turn consumes a lot of power compared to a straight-line motion. Thus, in path planning for this kind of rover, turning radius is a factor that should be considered explicitly.

Based on the literature, there is a lack of analytical approach for finding energy-optimal paths for skid-steer rovers. This thesis addresses this problem for such rovers, specifically on obstacle-free hard ground. The *equivalency theorem* in this thesis indicates that, when using a popular power model for skid-steer rovers on hard ground, all minimum-energy solutions follow the same path irrespective of velocity constraints that may or may not be imposed. This non-intuitive result stems from the fact that with this model of the system the total energy is fully parametrized by the geometry of the path alone. It is shown that one can choose velocity constraints to enforce constant power consumption, thus transforming the *energy-optimal problem* to an *equivalent time-optimal problem*. Existing theory, built upon the basis of Pontryagin's minimum principle to find the extremals for time-optimal trajectories for a rigid body, can then be used to solve the problem. Accordingly, the *extremal paths* are obtained for the energy-efficient path planning problem. As there is a finite number of extremals, they are enumerated to find the minimum-energy path for a particular example.

Moreover, the analysis identifies that the turns in optimal paths (aside from a small number of special cases called whirls) are to be circular arcs of a particular turning radius, R', equal to half of a skid-steer rover's slip track. R' is the turning radius at which the inner wheels of a skid-steer rover are not commanded to turn, and its description and the identification of its paramount importance in energy-optimal path planning are investigated. Experiments with a Husky UGV rover validate the energy-optimality of using R' turns.

Furthermore, a *practical velocity constraint* for skid-steer rovers is proposed that maintains constant forward velocity above R' and constant angular velocity below it. Also, in separate but related work, it is shown that almost always *equal "friction requirement"* can be used to obtain optimal traction forces for a common and practical type of 4-wheel rover.

Acknowledgments

First and foremost, I would like to thank God Almighty for granting me the opportunity to perform this research study. This achievement was impossible without his blessings.

Also, my appreciation goes to Prof. Krzysztof Skonieczny that kindly and patiently supervised and supported me throughout my PhD with his invaluable experiences and knowledge. I would like to thank Prof. Devin J. Balkcom for his insightful help during the last two years of my PhD. I would also like to personally thank my friends Dr. Amir Nassiraei for his generous and valuable advice during my PhD, Jean-Sebastien Fiset with whom I collaborated for doing the experiments and we have several joint publications, and Tyson Boer who helped me to perform the experimental tests. Last but not least, I would like to express my deep gratitude to my parents and my brother. This accomplishment would not have been possible without their continuous support and encouragement.

Contents

Nomenclature

B_s Slip-track

t_0 Initial time

(X, Y) Position in rover's body coordinate system

(x, y) Position in inertial coordinate system

(x^p, y^p) Position in path-defined coordinate system

(x^p_C, y^p_C) Center of circle in path-defined coordinate system

(x_{ICRl}, y_{ICRl}) Position of vehicle's left side ICR

(x_{ICRv}, y_{ICRv}) Position of vehicle's ICR

(x_{ICRv}, y_{ICRv}) Position of vehicle's right side ICR

α_{ij} Angle of rod connecting wheel i to j

$\boldsymbol{F}$ Resultant force

$\boldsymbol{M}$ Resultant moment

ϵ_i i^{th} small positive value

λ_i i^{th} Lagrange multiplier

$\mathbb{R}$ Real Numbers

μ Friction coefficient

μ_i^f Friction requirement

μ_i Inequalty coefficients in KKT conditions

ω_z Angular velocity in Z direction

$\mathrm{L_D}$ The length of a complete straight line motion for Generic TST paths

θ^P Angle of path in path-defined coordinate system

$\theta_A, \theta_B, \theta_C$ Angle of path in inertial coordinate system at point A, B, and C respectively

θ_i i^{th} slope angle

$\tilde{\omega}_z$ Angular velocity in Z direction for the equivalent time-optimal problem

$\tilde{E}$ Energy for the equivalent time-optimal problem

$\tilde{t}_f$ Final time for the equivalent time-optimal problem

$\tilde{V}_l$	Velocity of rover's left side in the equivalent time-optimal problem
$\tilde{V}_r$	Velocity of rover's right side in the equivalent time-optimal problem
$\vec{a}_i$	Center of the ith wheel in body coordinate system
$\vec{C}_{r,l}$	Position of right/left ICR in body coordinate system
$\vec{v}$	Rover's speed
a'_1, a'_2, a'_3	First, second, and third power coefficient, respectively
E	Energy
g_j	j^{th} inequality constraint
H	Hamiltonian
h_i	i^{th} equality constraint
L	Distance between the centers of rover's wheels alongth its length
N_i	i^{th} normal force
n_w	Number of rover wheels
P	Power
P_0	Power for the turning redius of zero
P_∞	Power for the turning redius of ∞
p_i	Normal force applied to the ith wheel.
R	Turning radius
R'	Special turning radius which is half of slip-track
R'_{H_c}	The commanded turning radius for the Husky UGV that results in the inner wheels receiving a commanded velocity of 0
s	Arc length
t	Time
t_f	Final time
T_i	i^{th} traction force
V_l	Velocity of rover's left side
V_r	Velocity of rover's right side

v_x Velocity of rover in X direction

v_y Velocity of rover in Y direction

W Distance between the center of rover's wheels alongth its width

u   Vector of inputs

x   Vector of states

EST   Eastern Standard Time

ICR   Instantanous Center of Rotation

KKT   Karush-Kuhn-Tucker

SLSQP Sequential Least Squares Programming

List of Figures

List of Tables

1 Introduction

In this chapter, subsection 1.1 introduces skid-steer rovers and presents the motivation of working on energy-efficient path planning for this type of rover. Subsection 1.2 reviews different publications related to trajectory/path planning for rovers as well as equivalency between time and energy problems. Moreover, a practical control input constraint for the energy-efficient trajectory planning problem is suggested in the subsection. Next, contributions of this thesis are listed in subsection 1.3. Finally, an overview to the thesis is presented in subsection 1.4 to guide the readers through the different chapters.

1.1 Motivation

Several countries are planning missions involving an autonomous rover moving across the surface of a planet and collecting samples. Due to communication delays of up to tens of minutes the rover must be able to navigate autonomously to sites of scientific interest. To do this task, the rover must be able to plan and execute paths over natural terrains.

There are several types of rover configurations that can be used for the aforementioned missions including skid, explicit, and Ackerman steering. The rover that is chosen for our research is skid-steer. Skid-steering is a method of steering where four (or more) wheels are not themselves steered, but different velocities are commanded for the left and right wheels in order to maneuver a vehicle. Due to their mechanical simplicity, maneuverability and robustness, skid-steer rovers are widely used for excavation and loading, planetary exploration [1, 2], and other field robotics applications. It is a popular configuration, from the Clearpath Husky to the Soviet Union's 8-wheel Lunokhod rovers [1] and a series of rovers recently developed for the Canadian Space Agency (CSA) [3]. Hence, energy-optimal and time-optimal trajectories should be designed to help the rovers perform their missions efficiently[1].

A pair of skid-steer rovers, Husky UGV and Argo J5, are utilized for experiments in this work and are thus introduced here. Husky UGV (Fig. 1) is a medium sized robotic development platform.

Figure 1: Husky UGV rover

---

[1]Also, there are some interesting experimental tests for skid-steer rovers showing that based on the terrain type which kind of shortest path or energy-efficient path should be chosen [4] to obtain overall less energy consumption.

The Husky UGV's rugged construction and high-torque drivetrain make it appropriate for research in various terrains including hard ground as well as sand. In addition, it is fully supported in Robotics Operating System (ROS) with community driven Open Source code and examples.

Argo J5 (Fig. 2) is an extreme-terrain vehicle that is a commercially available version of a rover configuration developed explicitly for CSA.

Figure 2: Argo J5 rover
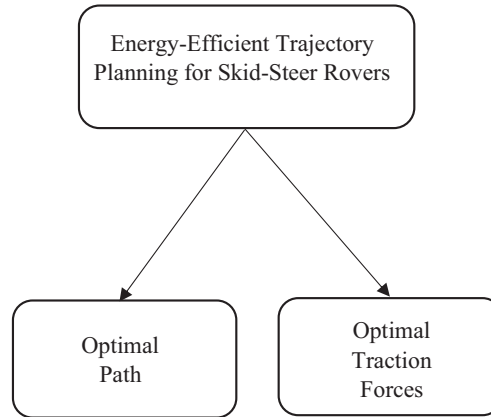
Figure 3: Two aspects of optimal trajectory planning investigated in this thesis.

Trajectory planning for this type of rover is an ongoing challenge presently. Two aspects of it, which are shown in Fig. 3, are mentioned in the following.

1. The first investigated aspect in this thesis is optimal paths (see Fig. 3). High torque is required to overcome lateral motion resistances induced during a skid-steer turn [5]. Therefore, a key challenge of skid-steer mobility for planetary rovers is the power and energy consumption of this steering configuration. **Shamah et**

al. [6] show that during a maneuver the power consumption of a skid-steer rover is inversely related to its turning radius. Accordingly, point turns (i.e. turning in place) and straight line maneuvers have the highest and lowest power consumption, respectively. For point turns, skid steering can require over twice the power of explicit steering [6]. The difference between the two steering modes drops away with increasing turning radius. Thus, the shortest distance path, which requires point turns along with straight lines, may not be the lowest-energy path. In fact, we show this to be the case. The selection of turning radii that result in the lowest overall energy consumption when traversing from a start to an end pose can be formulated as a path planning problem.

2. Based on Fig. 3, another aspect which is *optimal traction forces* is considered. In the absence of any constraints on the system (e.g. force/torque balance, maximum motor torques), the **optimal traction** solution is known to be that with equal *"friction requirements"* (ratios of tractive to normal force) for all wheels. Nevertheless, the current state-of-the-art is to routinely perform computationally expensive constrained optimization, because of the presumed importance of the constraints in a real system. Therefore, there is a worthwhile research opportunity for a thorough **investigation of the configuration space for 4-wheel rovers**, driving straight over rough terrain, in search of configurations where the unconstrained optimal answer does or does not satisfy the constraints, and thus, is or is not valid.

Since the aforementioned aspects are related to distinct subjects, separate literature reviews (presented in different subsections) are provided. Accordingly, subsection 1.2 reviews the most relevant papers to the optimal trajectory/path planning problem. Then, in subsection 7.1 the most related publications to optimal wheel traction control are presented.

1.2 Literature Review

In subsection 1.2.1, some sampling methods for obtaining paths are presented. Moreover, local and global planning methods are explained. Then, the importance of using an analytical approach in local planning methods is described by explaining the related literature. In subsection 1.2.2, the related papers to the equivalency between time-optimal and energy-optimal problems are reviewed. This part is necessary for the equivalency theorem which will be discussed in Chapter 3. Also, a suggested new practical control input constraint for skid-steer rovers is stated in subsection 1.2.3. Finally, the steps that were taken to solve the energy-efficient path planning problem are explained in 1.2.4.

1.2.1 Sample-Based and Local Planning Methods

Optimal path planning in the presence of obstacles is always challenging[2]. Generally, path planning with differential constraints are two-point boundary value problem (BVPs)

---

[2]For example, standard Piano Mover's Problem [7, 8], which is special case of motion planning under differential constraints, is NP-hard.

[9]. However, the techniques to solve BVPs cannot efficiently/entirely solve the path planning problems while considering obstacles [7]. Even for some cases without considering the differential constraints while obstacles are taken into account the optimal path planning is NP-hard, such as 3D optimal path planning for a point in an environment with polyhedral obstacles [7, 10]. Only for double integrator systems the exact paths can be found while obstacles are considered [7, 11, 12].

Hence, path planning for vehicles with differential constraints in complex environments motivates sampling-based approaches (e.g. Rapidly-exploring Random Trees (RRT)). However, there is also a need to generate feasible local paths between the nodes that sampling-based/global planning algorithms generate. Accordingly, **Local Planning Methods (LPM)** provide useful motion primitives for the global planning method [7]. It should be mentioned that in path planning problem in the presence of obstacles, each global path consists of several local paths. These local paths are generated in an obstacle-free environment, representing the space between nodes that are already chosen to avoid obstacles in a complex environment. It may be possible to explicitly optimize these simpler local paths (in terms of either length, time duration, energy consumption, etc.). There are two probable advantages of considering such optimal local paths to build overall paths [7]:

1. They can lead to more time/length/energy efficient overall paths

2. They can be more efficient in computational cost compared to executing the global algorithms with ad hoc candidate local paths

The importance of these local paths is stated by LaValle [7]:

"Although discrete-time model for path planning is the most straightforward and general, there are often many better motion primitives that can be used. For a particular system, it may be possible to design a nice family of trajectories off-line in the absence of obstacles and then use them as motion primitives in the rapidly exploring dense tree (RDT) construction. If possible, it is important to carefully analyze the system under consideration to try to exploit any special structure it may have or techniques that might have been developed for it. For motion planning of a vehicle, symmetries can be exploited to apply the primitives from different states.
Using more complicated motion primitives may increase the burden on the Local Path Model (LPM). Ideally, the LPM should behave like a good steering method, which could be obtained using methods such as Dubins path. It is important to note, though, that the RDT's ability to solve problems does not hinge on this. It will greatly improve performance if there are excellent motion primitives and a good steering method in the LPM. The main reason for this is that the difficulties of the differential constraints have essentially been overcome once this happens (except for the adverse effects of drift). Having good motion primitives can often improve performance in practice."

1.2.1.1 Sample-Based Algorithms for Global Planning Method

There are many different numerical sampling-based methods to globally search for efficient paths in complex environments (such as in the presence of obstacles), including potential fields [13], several versions of rapidly exploring random tree algorithms (such as RRT [14–16], RRT*

[17], and Theta*-RRT [18]), and several numerical methods based on heuristic (D* [19]) or meta-heuristic approaches as Genetic Algorithm (GA) [20, 21], Ant Colony Optimization (ACO) [22], and Particle Swarm Optimization (PSO) [23]. Also, there are several learning approaches in motion and path planning such as deep reinforcement learning [24, 25]. In addition, other approaches for designing optimal trajectory include using *pseudo-spectral*[3] [26, 27] and *minimum snap*[4] [28–30] optimal control. In both methods, the optimization problem is eventually solved numerically and the path types are *not* obtained analytically. It should be mentioned that there are dozens of published papers that use the mentioned algorithms in this paragraph, some of which are cited in this thesis for brevity.

For global planning methods of skid-steer rovers, there has been some work related to time-efficiency[5] and energy efficiency. In the following a method which is used for energy efficiency is explained. Sampling Based Model Predictive Optimization (SBMPO) [32] is popular for path planning with skid-steer rovers. Because SBMPO samples from the feasible space of control inputs, it can automatically satisfy any kinematic or dynamic constraints. SBMPO generates nodes on a graph where a model predicts the rover's motion after that the sampled control inputs have been applied for some specified duration. The cost at each node is the sum of the cost of getting to that node (which can be predicted by the model used) plus an "optimistic" estimate (i.e. meant to guarantee to not over-estimate) of the remaining cost to get to the goal from that node. After a node is expanded with some fixed number of new nodes and each is assigned a cost, a priority queue is re-sorted to pick the next node to expand (the one with lowest cost). Reese [33] proves that SBMPO gives the optimal path *on the graph*, but only once the priority queue is completely exhausted.

Recent attempts for global planning methods to determine energy-efficient paths for skid-steer rovers all use SBMPO. Gupta et al. [34] opt to select the first path that reaches the goal by this method (i.e. leaving nodes still available in the priority queue), resulting in a suboptimal trajectory, in order to reduce computation time. Pentzer et al. [35] assume that a point turn followed by a straight line to the goal (which, in general, may still be far away) provides an "optimistic" estimate of remaining energy cost; however, this work, using the same power model, will show that there are sometimes paths with lower cost than this option and thus it does not in fact guarantee not to over-estimate cost. Even a fully optimally implemented SBMPO provides only the optimal solution on the graph of sampled nodes. To approach a global optimum in continuous space, the sampling must thus be dense. However, it is mentioned by Gupta et al. [34] that computation time is already a limiting consideration. These challenges in practice related to suboptimality and computational cost align exactly with the points raised by LaValle [7] motivating

---

[3]The purpose of *pseudo-spectral optimal control* method is converting the optimal control problem to a nonlinear programming problem (NLP). Accordingly, the state and control variables are discretized and the control trajectory and states are approximated using Lagrange interpolating polynomials.

[4]In the *minimum snap* approach, the purpose is to minimize the integral of the square of the norms of the snap which is the second derivative of acceleration. Accordingly, the vehicle traverses through the waypoints until it reaches to the the final state in the specified time.

[5]Yamamoto et al. [31] investigate time-optimal paths for skid-steer rovers in the presence of obstacles; they find quasi-optimal solutions by using the B-spline parametrization technique.

optimal local paths.

In the following, some hybrid approaches are explained. These papers explicitly have mentioned that they use different algorithms for their global planning and obstacle-avoidance/LPM algorithms.

1.2.1.2 Hybrid Approaches

Hybrid path planning is sometimes utilized for collision avoidance in dynamic environments, while minimizing control signal for unmanned UGV, minimizing energy for differential drive robots, etc. For example, Zhong et al. [36] utilize A* for mobile robots global path planning (on a known map) and adaptive window approach for other tasks including real-time obstacle avoidance for the unpredicted obstacles. Mohamed and Ren [37] use Pontryagin's minimum principle to minimize the control signals for unmanned UGV while the obstacles are taken into account by Artificial Potential Field Method[6]. Furthermore, there are some hybrid approaches that consider the sampling methods for the *global planning method* and the analytical approach for LPM. For example, Chaudhari et al. [38] use Dubins path[7] to traverse between the waypoints of the global path obtained by A*. These turn out to be better paths, considering energy, for differential drive rovers while avoiding obstacles. Although it is known that Dubins paths are the shortest path (as a LPM) for car-like rovers, using these paths has helped Chaudhari et al. to obtain smoother energy-efficient paths compared to the path obtained by A* or even smoothed[8] A*-paths. This raises the question of what would happen if their utilized LPM was specifically designed for energy-efficiency of differential drive rovers? In this thesis, the research is *not* on differential drive rovers. However, to deal with similar situations for skid-steer rovers, we obtain energy-efficient LPM and thus provide the opportunity for more investigations on other related energy-efficient global planning methods.

1.2.1.3 LPM for Different Vehicles

There have been no optimal analytically-obtained LPM developed for skid-steer rovers that consider energy-efficiency. In related work, however, several analytical approaches to find shortest *distance* or *time* LPM paths for car-like, differential drive, omni-directional, and rigid body rovers moving on *obstacle-free* environment have been published. Dubins [39] proposes a method to obtain the shortest path for a car-like rover that can only travel forward, subject to a constraint that the average curvature everywhere is less than or equal to a given constant value. Johnson [40] obtains the Dubins paths using another method, namely Pontryagin's minimum principle. This principle, which is utilized in optimal control theory[9], helps to solve the constrained optimization problem of controlling a dynamical system to move

---

[6]In the utilized Lagrange function for Pontryagin's minimum principle, potential field's coordinates of obstacles and end point are considered.

[7]Which are obtained from analytical approach [39]

[8]The paths are smoothed by using Bezier curves.

[9] Solving for LPMs using Pontryagin's minimum principle is an application of optimal control. Another related approach is to use nonlinear model predictive control for online trajectory optimization. Performing iterative computations for finite-horizon planning, using GPOPS-II for example [41], is thus another option. Iterative approaches like this may be able to handle obstacles in many cases, providing a bridge between global methods and optimal local methods.

from one state to another. Reeds and Shepp [42] design the shortest path (a path with circular arcs and line segments) for car-like rovers that can go both forwards and backwards. In addition, Sussmann and Tang [43], Philippe Sou and Laumond [44], as well as Boissonnat et al. [45] use Pontryagin's minimum principle to develop the shortest path for the Reeds-Shepp car. Qin et al. [46] use Pontryagin's minimum principle to obtain the energy-efficient trajectory for car-like rovers. In addition, Tokekar et al. [47] work toward optimizing energy consumption for *car-like robots*; they first show how to find energy-optimal velocity profiles along a given path, and then build a discretized graph composed of individual circular arcs (or straight lines) connecting the vertices. Balkcom and Mason [48–50] design time optimal trajectories (ultimately consisting of point turns and straight lines) for differential drive vehicles in an unobstructed plane by the use of Pontryagin's minimum principle. Also, Balkcom et al. [51, 52] as well as Wang and Balkcom [53] use the Pontryagin's minimum principle to obtain time-optimal paths for omni-directional vehicles. They conclude that the optimal paths should contain circular arcs, and straight lines which are parallel to the wheel axles. In addition, Chitsaz et al. [54, 55] design the shortest path for differential drive mobile robots by using Pontryagin's minimum principle. Furthermore, Balkcom et al. [56] as well as Wang and Balkcom [57] obtain 3D time-optimal trajectories for rigid bodies. Firstly, they obtain the necessary conditions for optimality using Pontryagin's minimum principle and a geometric method. Then, they design the optimal trajectories by sufficiently dense sampling[10]. Furtuna et al. [59–62] investigate an algorithm for general parametrized model of mobile robots. They use Pontryagin's minimum principle and prove several other theorems to design the algorithm. In addition, some research on the structure of time-optimal trajectories for rigid bodies are performed in [63]. The challenge after obtaining the optimal control inputs from the Pontryagin's minimum principle is to limit the number of switches between them. Accordingly, Lyu and Balkcom [64–67] constrain the number of switches between the optimal controls to avoid the *chattering* phenomenon.

1.2.2 Literature Review for the Equivalency Theorem

Ioslovich et al. [68–70] state that by "appropriate" selection of constraints for a rigid body with the dynamic equations of motion[11], the *minimum time problem* and *minimum energy problem* are equivalent which means that they result in the same trajectory. However, their strict definition of "appropriate" ultimately renders their result trivial. The process that they have followed is as follows:

(a) The driving force, velocity, and position are considered as the state variables. Also, jerk[12] is considered as the control input. They assume that driving force, velocity, and jerk are bounded. Furthermore, they consider that the states at the starting and end pose are known.

---

[10]Also, [58] is another paper on sufficiently dense sampling for the extremal trajectories obtained by Pontryagin's minimum principle to make sure that in obstacle free environment the wheeled robot can go from any starting to end point.
[11]Equation (1) to (3) of [69]
[12]The driving force derivative

(b) Pontryagin's minimum principle is utilized to solve the *minimum time problem* for the conditions presented in part (a). Hence, $\tilde{t}_f^*$ (the optimal time for the problem) is obtained.

(c) Energy for the *energy-optimal problem* is defined as follows [68–70]:

$$\int_0^{t_f} \frac{v^2}{2} dt \qquad (1)$$

where v, t_f, and t are velocity, final time, and time, respectively.

(d) A sentence about the "appropriate" constraints for the *energy-optimal problem* is stated in each of the mentioned references:

- "*t_f is taken from the solution of the minimal time problem and all the constraints and end conditions are the same.*"[13]

- "*t_f is taken from the solution of the minimal time problem and the upper bound for v is omitted from the constraints.*"[14]

(e) Pontryagin's minimum principle is utilized to solve the *minimum energy problem* for Eq. (1) with the constraints presented in part (d).

There are some concerns about their approach:

- As mentioned in (d), t_f for the energy-efficient problem is the *optimal time* (i.e. $\tilde{t}_f^*$) taken from the solution of the *minimum time problem.* In other words, they are only searching for the most energy-efficient path from among already time-optimal paths. In the case of a unique time-optimal path (not unusual in practice), this reduces to a trivial search within a set of cardinality 1. Such an overly restrictive search can miss lower energy solutions that take some extra time.

- The definition of energy is wrong in Eq. (1). They assume that mass is 1 kg. Then, it is stated that *energy* is the integral of *kinetic energy* ($\frac{1}{2}v^2$).

There are other papers [71–77] which have cited references of [68–70]. Some of which [71–74] are written by the authors of [68–70] or Ioslovich[15] is coauthor in those papers. The rest [75–77] are written by other researchers. However, none of the follow on papers [71–77] use the idea of equivalency.

Furthermore, a thorough search is performed to find any other publications related to equivalency between time and energy optimization. There are dozens of papers in different fields that have been published on either minimum time problem or minimum energy problems. Also, there are some papers that have worked on the *time-energy* minimization such as [78–84]. They talk about time-energy optimization and they try to do a trade-off between time and energy. However, none of them work on equivalency between time and energy in their research.

---

[13]After equation (10) of [69]
[14]After equation (10) of both [68] and [70]
[15]One of the authors of [68–70]

8

1.2.3 Control Input Constraints

In general, any real rover will be subject to control input constraints due to motor saturation. In a skid-steer rover, the control inputs are the left and right wheel velocities, V_l and V_r respectively, and they have a maximum (positive) value, V_{max}, and minimum value, $V_{min} = -V_{max}$. It is typical and useful to first conduct an analysis of the case where forward velocity is held constant. This is precisely the constraint applied in state-of-the-art literature on skid-steer energy efficiency by Gupta et al. [34] and by Dogru and Marques [85]; the approach can be traced back all the way to the foundational work by Dubins [39]. *Applying constant forward velocity allows to decouple the shape of the path from the overall trajectory.*

In general, a given trajectory follows a unique path. A single path may in general, however, be followed using various trajectories (i.e. with varying velocity). A prescribed velocity constraint can ensure a unique trajectory for each path, *making the concepts of optimal **trajectory** (subject to the constraint) and optimal **path** equivalent and interchangeable.* In the context of energy efficiency, this also means power can be expressed as a univariate function of turning radius, R. It is also a common control mode in practice, where forward and angular velocities are independently set by the user (e.g. "twist" commands in ROS - Robotic Operating System).

However, as this work will show in Chapter 2, constant forward velocity does not allow us to analyze all possible shapes of skid-steer curves (a point turn, or turn in place, by definition has zero forward velocity). Therefore we present a modified constraint[16] that maintains the essence of this approach while enabling the study of all turning radii, $0 \leq R < \infty$. The experiments are conducted with this constraint, and it is considered in the optimization analysis.

The boundary between the cases where V_l and V_r are of the same or of opposite sign (i.e. when either V_l or V_r are 0) turns out to be very important. *The turning radius at this boundary is defined as R' in this thesis.* The concept is somewhat similar to R_c recently introduced by Dogru and Marques [86], but R' is more general and its importance is more fully analyzed here than any related concepts in prior literature. R_c is assumed to occur at half the rover width, not accounting for the possibility of lateral slip. Although Dogru and Marques work toward finding an optimal turning radius for skid-steer rovers in subsequent work [85], they do not explicitly link the important boundary case (i.e. R_c or, actually, R') to optimal energy consumption. A contribution of this work is thus that it provides deeper context and explanations for those earlier results in the literature.

In the next subsection, our approach to solve the energy-efficient path planning for skid-steer rovers is explained.

1.2.4 Our Approach

This research explores optimally energy-efficient local paths (LPMs) for skid-steer rovers. As mentioned in subsection 1.1, Shamah et al. [6] show the importance of turning radius in energy consumption. In addition, based on the above mentioned papers, **there is a**

---

[16]In Chapter 2, the constraint presented in Eq. (25) for the velocities

general lack of analytical work on skid-steer rovers to find paths minimizing the energy consumption.

Based on the above mentioned work, we have several contributions which are listed in the next subsection.

1.3 Contributions

This work has the following major contributions:

- The **equivalency theorem** presented in subsection 3.1 allows us to obtain the optimal path for the energy-efficient path planning problem considering any proper[17] constraint on velocity. As a result, the constant power velocity constraint is utilized to convert the *energy-optimal path planning problem for skid-steer rovers* (in subsection 2.1) to an *equivalent time-optimal* problem.

- As investigated in the literature review (subsection 1.2), there is no analytical approach to find **optimally energy-efficient paths** for skid steer rovers. Based on the work performed in chapter 3 and 4, our second contribution is finding optimally energy-efficient paths for skid-steer rovers under the practical assumptions that will be elaborated in chapter 2. The paths are obtained by solving the equivalent time-optimal problem. Hence, the extremal paths for the energy-optimal problem are the answers of the equivalent problem.

- Another key contribution of this work is a detailed exposition of **the importance of R'**, including its use in optimally energy-efficient local path planning on hard ground (see chapter 4). When considered with respect to a popular power model for skid-steer rovers [87], R' corresponds to an important transition for energy consumption: below R' energy consumption for a circular-arc maneuver is not a function of turning radius while above R' it is (see Theorem 9). It should be mentioned that all the circles of the non-whirl[18] extremal trajectories (Table 3) have the turning radius of R'. Furthermore, the importance of R' is verified by performing several experimental tests by Husky UGV on hard ground (see subsection 6.2.3.3). In addition, several experiments are done on loose soil to show the power/energy behavior of Husky UGV and Argo J5 rovers around R' (see subsection 6.3).

- In subsection 2.3, a new **practical constraint on the velocity** for skid-steer rovers is suggested, which is another contribution in this thesis. Based on the constraint, the summation of right and left wheel's absolute velocity should be constant. It is noted that the common assumption of constant forward velocity, which is considered for other type of rovers, is not feasible for skid-steer rovers. As will be discussed in subsection 2.3, considering constant forward velocity as turning radius approaches zero requires angular velocity approaches infinity which is impossible for real systems. On the other hand, the proposed constraint allows to have constant angular

---

[17]As will be explained in subsection 3.1, as long as the velocity constraint does not restrict the range of turning radii, it can be considered as a proper constraint.

[18]Non-whirl paths are described in the explanations provided after Eq. (138).

velocity below R' and constant forward velocity above R' which is obviously possible for skid-steer rovers.

- The **contributions of optimal traction** research, which is more elaborated in chapter 7, is as follows: we show, by performing a numerical simulation for a practical type of 4-wheel rovers, that almost always[19] *equal "friction requirement"* can be used to obtain optimal traction forces. Our finding results in avoiding extra optimization processes that are computationally expensive.

In the next subsection, an overview to the thesis is presented to give a brief explanation to the whole work and steps performed.

1.4   Overview to the Thesis

The subject of this research is **"Energy-Efficient Trajectory Planning for Skid-Steer Rovers"** (Fig. 4). There are several factors that can reduce the rover energy consumption during its motion: **Optimal Path**, **Optimal Traction Forces** applied to the rover wheels, etc. The major work in my research is on optimal path planning, which can be seen as a **"High Level"** problem (Fig. 4), and is elaborated in chapters 2 though 6.
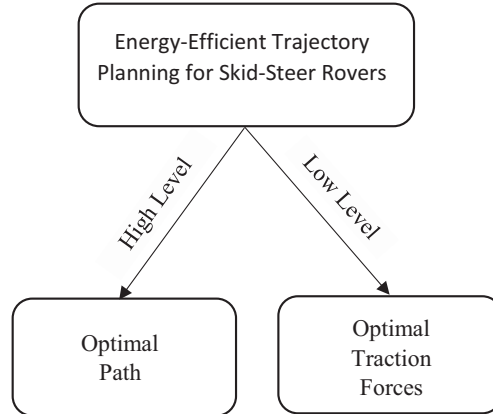
Figure 4: High level and low level aspects of the energy-efficient trajectory planning problem. Note: This figure provides more details about high and low level aspects presented in Fig. 3.

Obtaining the optimal traction forces makes up a smaller portion of the research, and is **"Low Level"** (Fig. 4) because it can be done on whatever path the higher-level planner selects; it is described, somewhat independently, in chapter 7.

Thus, the main purpose of this research is to devise energy-efficient paths for skid-steer rovers. Specifically, the situation studied is where the rover is driving on hard flat ground. The work focuses on analytical approaches to find the optimal path. The find approach is presented in chapters 3 through 5 . Chapter 6 and our existing publications

---

[19]In 99.93% of cases, solving the set of Eq. (246) through (250) converges to a valid solution.

include some work conducted before it was successfully generalized into the find approach. Before finding a general energy-efficient path, preliminary work was performed to find the optimal path within a class of predefined paths. There are several reasons why these predefined classes of paths were important for us.

- As mentioned in the Introduction (section 1), Shamah et al. [6] show the importance of skid-steer rover turning radius in power consumption. The easiest way to control turning radius in practice is to have constant-turning-radius paths by using circular arcs.

- In problems such as Dubins paths [39], it is shown that the minimum length paths for car-like rovers are always a combination of circles and straight lines. It was possible that these results would also be useful for our problem (i.e. such paths may turn out to be more energy-efficient than other ad hoc or heuristically selected paths).

- Solving simpler problems (i.e. predefined classes) before tackling the general case enabled us to learn interesting features of our overall problem during preliminary phases of the work.

The next phase of the research solved the optimal planning problem (i.e. no predefined constraints on path type) on applicable rover power models, using insights gained in the preliminary work. The mentioned phases are summarized hereunder:

1. *Predefined class of paths:* **a path including two circular arcs (CC paths):** This is the simplest case that takes into account the turning radii (Fig. 5). Therefore, it was considered as the first phase.
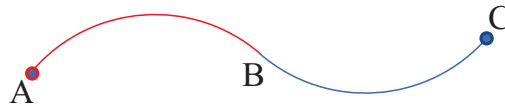
Figure 5: A path including two circular arcs

Applied approach: The Karush-Kuhn-Tucker (KKT) conditions were used to analytically obtain the stationary points. Then, the global minimum was chosen from the set of local minimums. The results are reported in subsection 6.1.2.

2. *Predefined class of paths:* **A path including two circular arcs and a line segment (CLC paths):** Since in many cases (e.g. long distance between A and C) it is not reasonable to consider long circular arcs, a combination of circular arcs and a line segment were considered (Fig. 6).
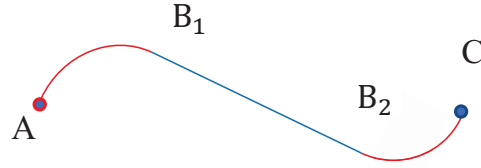
Figure 6: A path including two circular arcs and a line segment

Applied approach: The stationary points were obtained by the use of Karush-Kuhn-Tucker (KKT) conditions. Finally, the global minimum was chosen from the set of local minimums. The results are presented in subsection 6.1.2.

3. *Non-predefined class of paths:* **A general arc-based paths (Fig. 7):** To obtain this type of the paths, no further assumptions are considered beyond those described in the problem statement (chapter 2). Chapters 3, 4, and 5 are devoted to these types of paths. After obtaining all the extremal trajectories for the energy-efficient path planning problem, it became clear that the extremal paths include circular arcs with the turning radius of R'[20] , lines, or combinations thereof.
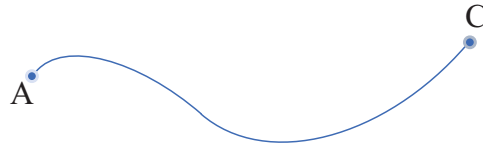
Figure 7: A general arc-based path (non-predefined class of paths)

Applied approach: As it is shown in Fig. 8, there are two options to solve the problem:

- Directly applying the Pontryagin's minimum principle.

- Using the *equivalency theorem* and obtaining an equivalent *time-optimal problem* for the main energy-optimal problem.

As will be more explained in subsection 3.1, the second approach is chosen in this thesis. Based on the *equivalency theorem* (see Theorem 2), there are several velocity constraints such as "constant power velocity constraint" which give the same optimal path for the energy-efficient path planning problem. In this thesis, the constraint is applied to convert the energy-optimal problem to an *equivalent time-optimal path planning problem*. Then, the theorems[21] developed by *A. Furtuna* [62]

---

[20]Except the whirls that will be explained in the mentioned chapters.
[21]Recall, these theorems are built upon the basis of Pontryagin's minimum principle.

for *"Minimum Time Kinematic Trajectories for Self-Propelled Rigid Bodies in the Unobstructed Plane"* are used to obtain all the extremal paths. Accordingly, the energy-optimal path planning problem is solved and all the extremals are obtained analytically.

It should be mentioned that Fig. 8 presents a concept map of the research performed in this thesis. It will be presented at the start of key chapters to link the work presented there to this overall "big picture".
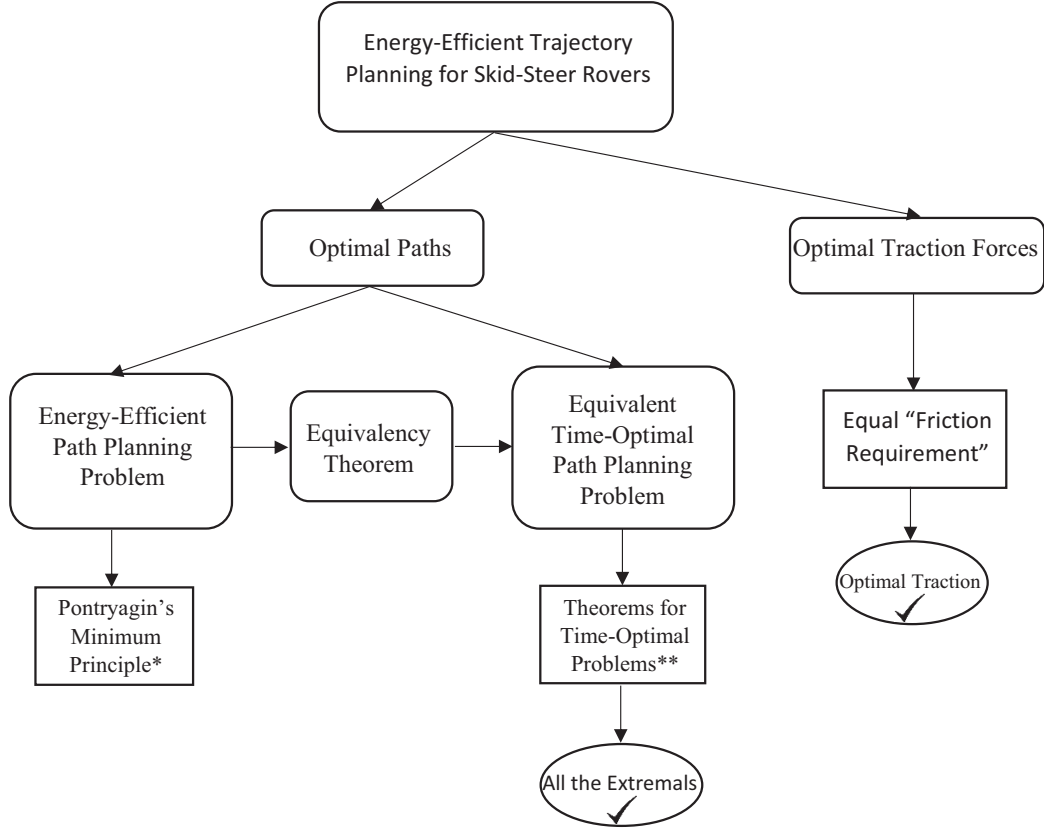
Figure 8: Concept map of the research performed in this thesis.

*In this approach, the similar process and theorems presented in A. Furtuna's PhD thesis [62] should be regenerated and revised/adjusted for the energy-optimal problem.**Several theorems are generated for skid-steer rovers; and other theorems are taken from A. Furtuna's PhD thesis. It should be mentioned that directly applying the Pontryagin's minimum principle to the energy-efficient path planning problem is another approach that could be used instead of solving the equivalent time-optimal problem.*

The research in this thesis has resulted in the following journal and conference publications:

Journals:

- **M. Effati**, J. Fiset, and K. Skonieczny, "Considering slip track for energy-efficient paths of skid-steer rovers," *Journal of intelligent and robotic systems*, 2020.

Link: https://doi.org/10.1007/s10846-020-01173-5

- **M. Effati** and K. Skonieczny, "Optimal traction forces for four-wheel rovers on rough terrain," *Canadian Journal of Electrical and Computer Engineering*, vol. 42, no. 4, pp. 215–224, 2019.

- **M. Effati** and K. Skonieczny, "Optimally energy-efficient path planning for skid-steer rovers," *In preparation*, *targeting the Journal of Autonomous Robots.*

- J. Fiset, **M. Effati**, and K. Skonieczny, "Effect of turning radius on power and energy consumption of skid-steer rovers on loose soil," *In preparation*, *targeting the Journal of Field Robotics.*

- **M. Effati**, K. Skonieczny, and D. J. Balkcom, "Energy-efficient path planning for skid-steer rovers using equivalency theorem," *In preparation*, *targeting the International Journal of Robotics Research.*

Conferences:

- J. Fiset, **M. Effati**, and K. Skonieczny, "Effects of turning radius on skid-steered wheeled robot power consumption on loose soil," *in 12th Conference on Field and Service Robotics (FSR)*. Springer, 2019.

- **M. Effati** and K. Skonieczny, "Circular arc-based optimal path planning for skid-steer rovers," *in 2018 IEEE Canadian Conference on Electrical and Computer Engineering (CCECE)*. IEEE, 2018, pp. 1–4.

Conference Posters/Presentations:

- **M. Effati**, J. Fiset, and K. Skonieczny, "Energy-efficient path planning for skid-steer rovers on flat ground," *ECE Graduate Student Research (GSR) Conference*, 2019.

- K. Skonieczny, **M. Effati**, J. Fiset, and M. Faragalli, "Energy-efficient path planning for skid-steer rovers," *19th Astronautics Conference of the Canadian Aeronautics and Space Institute (ASTRO)*, 2019.

- J. Fiset, **M. Effati**, and K. Skonieczny, "Towards a skid-steered wheeled robot power model for loose soil: 2d slip-sinkage," *ECE Graduate Student Research (GSR) Conference*, 2019.

Accordingly, in chapter 2 the *energy-efficient* path planning problem is defined and the related assumptions are presented. Then, chapter 3 introduces the *equivalency theorem*, which converts the *energy-efficient* problem to an *equivalent time-optimal* problem. Also, the *equivalent time-optimal* problem is defined in the chapter. Afterwards, all the extremal trajectories for the *equivalent time-optimal* problem are obtained in chapter 4. Moreover, a numerical scenario is solved in chapter 5 and the *minimum time path of the equivalent problem*, which is the *minimum energy path of the original problem* as well, is obtained for the scenario. In chapter 6 the focus is on the numerical/analytical/experimental works for predefined classes of paths (CC and CLC). Also, some initial investigations on revising

the existing power model are presented in this chapter. Then, the research on optimal traction forces for four-wheel rovers on rough terrain is presented in chapter 7. Finally, chapter 8 is a conclusion for all the performed research. Also, it makes suggestions for future work.

2 Problem Statement
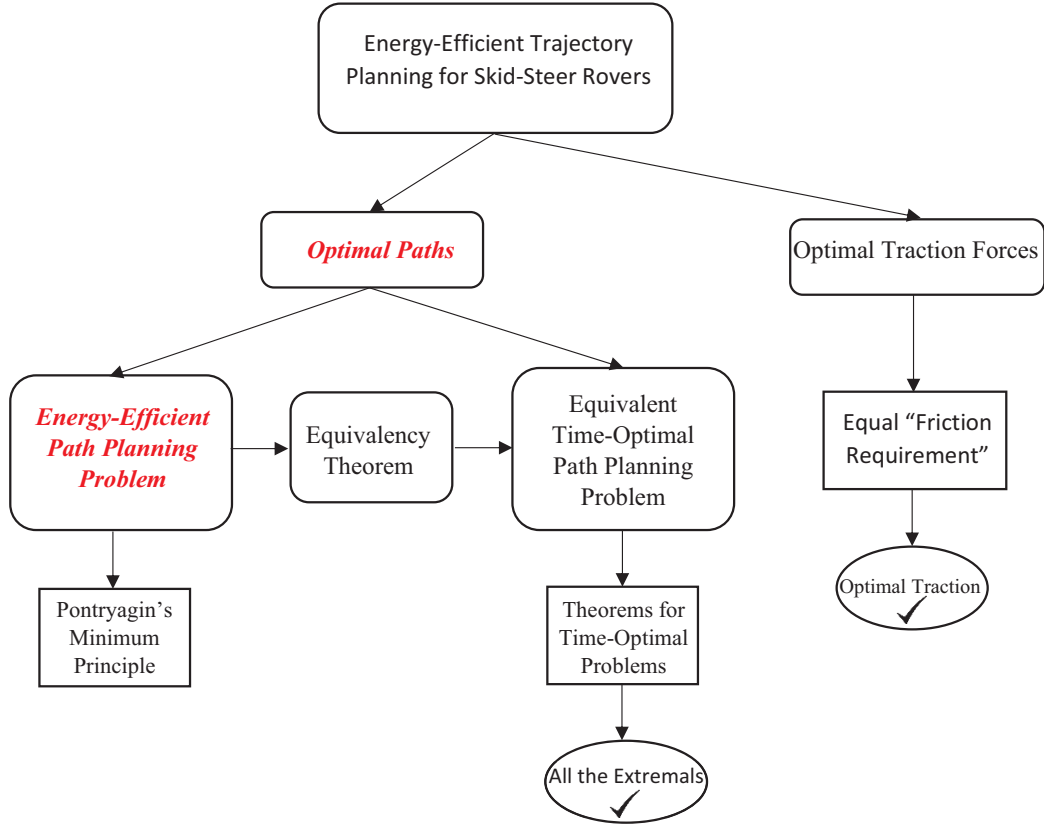
Figure 9: The task in this chapter is the problem statement of energy-efficient path planning (highlighted) for skid-steer rovers.

Firstly, the *energy-efficient* path planning problem is defined in subsection 2.1. It is important to note that the solution to this problem is sought for any and all proper velocity constraints that may, or may not, be applied. Then, 2.2 introduces and analyzes a well-known existing *power model* for skid-steer rovers. This power model is utilized for all the analysis in this thesis. Finally, in subsection 2.3 a new particular constraint on the velocity of skid-steer rovers is proposed and the behavior of these rovers under this constraint is explained.

2.1 Problem

The problem is to find an **energy-efficient**[22] trajectory (Fig. 10) between a given starting (A) and end pose (C), where the starting and end angle for the rover are θ_0 and θ_f, respectively. It should be mentioned that θ_0, θ_f as well as the position of A and C are known in

---

[22]In this thesis energy-efficient and energy-optimal are used interchangeably.

advance. In other words, if $\mathbf{x} = [x, y, \theta]^T$, then $\mathbf{x}(t = 0) = \mathbf{x}_0$ and $\mathbf{x}(t = t_f) = \mathbf{x}_f$. Where (x, y) and θ are the position and heading angle of the rover in the global coordinate system, respectively. In addition, V_l and V_r are the left and right wheel velocities, respectively. It is noted that V_l and V_r are the control inputs. Also, t is time. Moreover, t_f is the final time which is free. Therefore, the optimization problem is:

$$
\begin{aligned}
\underset{V_r,\ V_l,\ t_f}{\text{minimize}} \quad & \int_0^{t_f} P\, dt \\
\text{subject to} \quad & \dot{x} = \frac{V_r + V_l}{2} \cos\theta \\
& \dot{y} = \frac{V_r + V_l}{2} \sin\theta \\
& \dot{\theta} = \frac{V_r - V_l}{B_s} \\
& x(0) = x_0,\ y(0) = y_0,\ \theta(0) = \theta_0 \\
& x(t_f) = x_f,\ y(t_f) = y_f,\ \theta(t_f) = \theta_f
\end{aligned}
\tag{2}
$$

where P is the power which will be developed in Eq. (20). Also, B_s is slip track that will be explained in the next subsection (Eq. (10)).
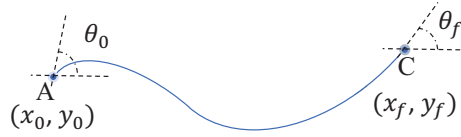
Figure 10: The general arc-based path (non-predefined class of paths) with the specified start and end pose.

The assumptions for the problems are listed in the following:
Assumptions:

- The rover is skid-steer

- The rover can do point turns or go forward or backward with any turning radius

- The rover moves on hard flat ground

- There are no obstacles

- The rover center of mass is located at its centroid

- The trajectory is piecewise C^2 differentiable

- Recall that no specific velocity constraints are required. Practical constraints to consider include motor saturation ($|V_r| < v_{max}$, $|V_l| < v_{max}$), constant v_c (see 2.3), and velocities that maintain constant power (see chapter 3).

The power model utilized for P (Eq. (20)) and the way to obtain its parameters are explained in the following subsection.

2.2 Power Modeling

Firstly, the kinematics for skid-steer rovers are stated in subsection 2.2.1. Then, the kinematics are incorporated into a popular existing power model in subsection 2.2.2.

2.2.1 Skid-Steer Rovers Kinematics

Rover kinematics can be defined based on the concept of Instantaneous Centers of Rotation (ICR) [88]. The parameters (x_{ICRv}, y_{ICRv}), (x_{ICRr}, y_{ICRr}), and (x_{ICRl}, y_{ICRl}) are the vehicle, right hand-side, and left hand-side ICR positions, respectively. These parameters are shown in Fig. 11 and are as follows:

$$x_{ICRv} = -\frac{v_y}{\omega_z} \tag{3}$$

$$x_{ICRl} = \frac{V_l - v_y}{\omega_z} \tag{4}$$

$$x_{ICRr} = \frac{V_r - v_y}{\omega_z} \tag{5}$$

$$y_{ICRv} = y_{ICRl} = y_{ICRr} = \frac{v_x}{\omega_z} \tag{6}$$

$$v_y = \frac{V_r x_{ICRl} - V_l x_{ICRr}}{x_{ICRl} - x_{ICRr}} \tag{7}$$

$$v_x = \frac{(V_l - V_r) y_{ICRv}}{x_{ICRl} - x_{ICRr}} \tag{8}$$

$$\omega_z = \frac{V_l - V_r}{x_{ICRl} - x_{ICRr}} \tag{9}$$

Moreover, v_x, v_y, and ω_z are the velocity in X, velocity in Y, and angular velocity around Z axes of the rover's body frame, respectively. Recall that V_r and V_l are the right and left wheel velocities (i.e. wheel angular velocities multiplied by wheel radius), respectively, and are control inputs. Martinez et al. [89] show that the positions of ICRs can be assumed to be approximately constant for a particular terrain type. They can be estimated by taking experimental measurements (as is done in this work, see subsection 6.2.3.2) or via dynamics simulations, for a particular soil type and narrow range of speeds.

Moreover, W and L are the distance between the center of left and right wheels in the X direction and the distance between the center of front and rear wheels in the Y direction, respectively. Also, the slip track (B_s) is defined as follows:

$$B_s = x_{ICRr} - x_{ICRl} \tag{10}$$
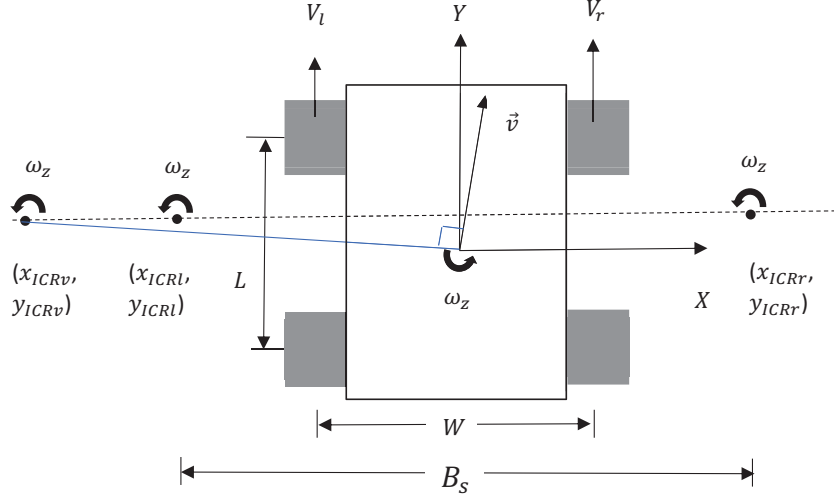
Figure 11: A schematic figure of a skid-steer rover and its associated instantaneous centers of rotation (ICRs).

and can also be seen in Fig. 11. It should be mentioned that B_s is constant for a specific terrain type and skid-steer rover. For example, B_s for Husky UGV on hard ground is estimated to be 1.3 m. The method to calculate it is explained in subsection 6.2.3.2.

Based on the assumptions listed before, the rover center of mass is located at its centroid. Accordingly, the following equations are derived:

$$x_{ICRr} = -x_{ICRl} \tag{11}$$

$$y_{ICRv} = y_{ICRl} = y_{ICRr} = 0 \tag{12}$$

Hence, from Eq. (7) through Eq. (12) it can be concluded that

$$v_x = 0 \tag{13}$$

$$v = v_y = \frac{V_r + V_l}{2} \tag{14}$$

$$\omega_z = \frac{V_r - V_l}{B_s} \tag{15}$$

$$x_{ICRr} = \frac{B_s}{2} \tag{16}$$

$$x_{ICRl} = -\frac{B_s}{2} \tag{17}$$

From the fact that $|v| = R|\omega_z|$ as well as equations (14) and (15), the turning radius can be expressed as:

$$R = \frac{B_s}{2} \left| \frac{V_r + V_l}{V_r - V_l} \right|, V_r \neq V_l \tag{18}$$

Lemma 1 *$R = R'$ is the boundary between the separate cases where V_r and V_l are either of equal or opposite sign.*

Proof: As mentioned before, R' is the turning radius at which a skid-steer rover's inner wheels are not commanded to turn. Without loss of generality consider the right wheel as the inner wheel. Therefore, at R' the right velocity should be zero ($V_r=0$). It should be mentioned that $V_r = 0$ is the boundary between when V_r is positive and negative. Hence, by using Eq. (18) the following relation for R' is obtained:

$$R' = \frac{B_s}{2}\left|\frac{V_l}{-V_l}\right| = \frac{B_s}{2} \tag{19}$$

$\blacksquare$

Definition 1 *R' is half of the slip-track ($R' = \dfrac{B_s}{2}$).*

Note: Because of the importance of R', Definition 1 is written. This definition is verified by the results of Lemma 1. Moreover, based on Martinez et al. [89], the positions of left and right ICRs are bounded and may be assumed constant for a specific terrain. Hence, B_s (Eq. (10)) and thus R' are constant.

In the next subsection, an existing power model is explained. Also, the presented kinematics will be incorporated into the power model.

2.2.2 Power Model

This part adapts a popular existing skid-steer power model for usage according to the problem definition and assumptions given in subsection 2.1. This model is based on a frictional wheel-terrain contact assumption. This power model, developed by Morales et al. [87, 90] and used by Pentzer et al. [35, 91], is as follows:

$$P = \mu|\omega_z| \sum_{n=1}^{N} \left(p_n \|\vec{a}_n - \vec{C}_{r,l}\|\right) + G(|V_r| + |V_l|) \tag{20}$$

where P is power consumed, μ is the friction coefficient, ω_z is the angular velocity, p_n is the normal force on each wheel, V_r and V_l are right and left wheel velocities, $\|\vec{a}_n - \vec{C}_{r,l}\|$ (Fig. 12) is the distance from the right or left ICR to a wheel, G is the internal and rolling resistance coefficient, and N is the number of wheels. Also, V_r and V_l are the control inputs for the power model. This power model, using Fig. 12, along with the center-of-mass at centroid assumption, is expanded as follows:

$$P = \mu|\omega_z|p\left(\sqrt{(\frac{L}{2} + y_{ICRr})^2 + (\frac{W}{2} - x_{ICRr})^2}\right.$$

$$+\sqrt{(\frac{L}{2} - y_{ICRr})^2 + (\frac{W}{2} - x_{ICRr})^2}$$

$$+\sqrt{(\frac{L}{2} + y_{ICRl})^2 + (\frac{W}{2} + x_{ICRl})^2}$$

$$\left.+\sqrt{(\frac{L}{2} - y_{ICRl})^2 + (\frac{W}{2} + x_{ICRl})^2}\right) \tag{21}$$

$$+G(|V_r| + |V_l|)$$

where p is the equal normal force applied to each wheel. The other parameters are as defined before. Using Eq. (12), (16) and (17), the power model can be simplified as follows:

$$P = 2\mu|\omega_z|p\sqrt{L^2 + (W - B_s)^2} + G(|V_r| + |V_l|) \tag{22}$$

or,

$$P = k|\omega_z| + G(|V_r| + |V_l|) \tag{23}$$

where k is

$$k = 2\mu p\sqrt{L^2 + (W - B_s)^2} \tag{24}$$
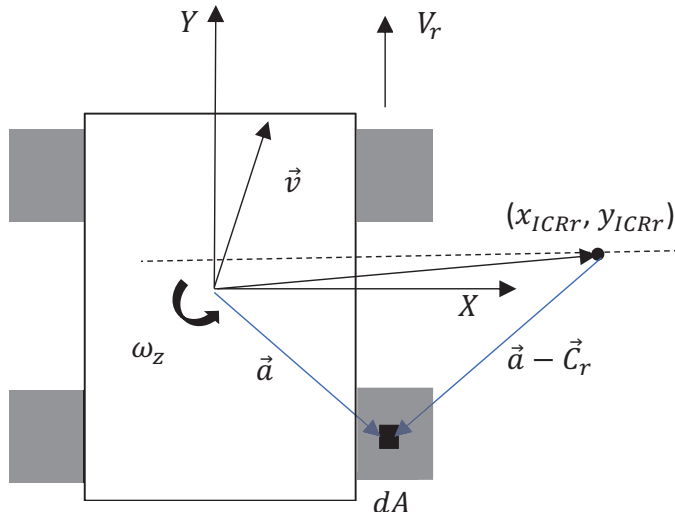
Figure 12: Distance of a wheel from ICR. To calculate $\|\vec{a}_n - \vec{C}_{r,l}\|$ for each wheel, the ICR on the same side as the wheel is always considered (i.e. for the wheels in the right hand side of the rover, $\vec{C}_r$ should be considered.)

In the next subsection, a practical constraint on V_l and V_r for skid-steer rovers is explained. This constraint enables the skid-steer rover to have constant angular velocity for $0 \le R < R'$ and constant forward velocity for $R \ge 0$.

2.3 Proposing a Practical Velocity Constraint, Constant v_c, for Skid-Steer Rovers

As mentioned in the literature review (see subsection 1.2.3) considering constant forward velocity constraint is not practical for skid-steer rovers. As turning radius approaches zero, constant forward velocity requires angular velocity, and V_l and V_r, to approach infinity, which is impossible for real systems.

In order to allow all the turning radii that skid-steer rovers make possible, including point turns, a novel variation on the common constant velocity constraint is introduced here. Namely:

$$\frac{|V_l| + |V_r|}{2} = v_c \text{ (Constant)} \tag{25}$$

When V_l and V_r are both positive, this is obviously the same as the constant forward velocity constraint. However, in tight turns, where the wheels rotate in opposite directions, the control inputs remain bounded and point turns (where $V_l = -V_r$) are also admissible. It will be shown below that when V_l and V_r are of opposite sign this constraint is equivalent to constant *angular* velocity. The control space for the constraint is shown in Fig. 13.
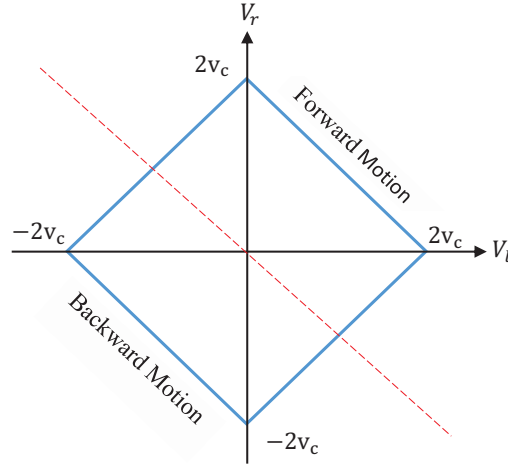
Figure 13: The control space obtained from $|V_r| + |V_l| = 2v_c$ constraint.

Under the constraint of $|V_r| + |V_l| = 2v_c$, Theorem 1 is concluded. Accordingly, the more realistic constant v_c constraint is equivalent to constant forward velocity when both wheels are turning forward, but at small turning radii where one of the wheels is in rotating backward, the sign switch makes it instead correspond to a constant angular velocity constraint.

Theorem 1 *For a skid-steer rover moving on flat ground with slip track of B_s under the constraint of $|V_r| + |V_l| = 2v_c$ (Eq. (25)): (1) The forward velocity (v) is constant for $R \geq R'$. (2) The angular velocity (ω_z) is constant for $0 \leq R < R'$.*

Proof:

The control space related to $|V_r| + |V_l| = 2v_c$ is shown in Fig. 13. Based on the figure, $R \geq R'$ happens in the first and third quadrant. Also, $0 \leq R < R'$ is related to the second and fourth quadrant. Accordingly, each quadrant is elaborated separately in the following:

First quadrant of Fig. *13* ($V_r > 0$ & $V_l \geq 0$):

$$|V_r| + |V_l| = 2v_c \Rightarrow V_r + V_l = 2v_c \tag{26}$$

$$v = \frac{V_r + V_l}{2} \Rightarrow \boxed{v = v_c} \tag{27}$$

Therefore, v is constant. It is known that for $V_r = V_l$ (straight line motion), R is $+\infty$. Also, for $V_r \neq V_l$, R is Eq. (18). Therefore,

$$R = \frac{B_s v_c}{|V_r - V_l|}, \quad V_r \neq V_l \tag{28}$$

It is clear that in the first quadrant of Fig. 13:

$$|V_r - V_l| \leq |V_r + V_l| \Rightarrow |V_r - V_l| \leq 2v_c \tag{29}$$

Hence,

$$R \geq \frac{B_s}{2} \Rightarrow \boxed{R \geq R'} \tag{30}$$

Third quadrant of Fig. *13* ($V_r \leq 0$ & $V_l < 0$):

$$|V_r| + |V_l| = 2v_c \Rightarrow V_r + V_l = -2v_c \tag{31}$$

$$v = \frac{V_r + V_l}{2} \Rightarrow \boxed{v = -v_c} \tag{32}$$

Therefore, v is constant. By the same method explained for the first quadrant, the following relation for the third quadrant is obtained:

$$\boxed{R \geq R'} \tag{33}$$

Second quadrant of Fig. *13* ($V_r > 0$ & $V_l < 0$):

$$|V_r| + |V_l| = 2v_c \Rightarrow V_r - V_l = 2v_c \tag{34}$$

$$\omega_z = \frac{V_r - V_l}{B_s} \Rightarrow \omega_z = \frac{2v_c}{B_s} \Rightarrow \boxed{\omega_z = \frac{v_c}{R'}} \tag{35}$$

Therefore, ω_z is constant.

Note: The reasons that B_s is constant are presented in the explanations for Eq. (10).

It is clear that in the second quadrant of Fig. 13:

$$|V_r + V_l| < |V_r - V_l| \Rightarrow |V_r + V_l| < 2v_c \tag{36}$$

Also, from Eq. (18) it is clear that in the second quadrant $R \geq 0$. Hence, by using Eq. (18):

$$R = \frac{B_s |V_r + V_l|}{4v_c} \tag{37}$$

24

Therefore,

$$0 \le R < \frac{B_s}{2} \Rightarrow \boxed{0 \le R < R'} \tag{38}$$

Fourth quadrant of Fig. *13* $(V_r < 0 \ \& \ V_l > 0)$:

$$|V_r| + |V_l| = 2v_c \Rightarrow -V_r + V_l = 2v_c \tag{39}$$

$$\omega_z = \frac{V_r - V_l}{B_s} \Rightarrow \omega_z = \frac{-2v_c}{B_s} \Rightarrow \boxed{\omega_z = \frac{-v_c}{R'}} \tag{40}$$

Therefore, ω_z is constant. Utilizing the same analysis explained for the second quadrant, the following result is obtained for the fourth quadrant:

$$0 \le R < \frac{B_s}{2} \Rightarrow \boxed{0 \le R < R'} \tag{41}$$

∎

Note that the absolute value functions presented in Eq. (23), in conjunction with the definition of ω_z and R (Eq. (15) and Eq. (18)), as well as Definition 1 motivate looking at the boundary between these separate cases (i.e. when either $V_r = 0$ or $V_l = 0$) corresponding to $R = R'$. Lemma 2 thus splits the consideration of turning radii between those below or above R'.

Lemma 2 *Using the power model of $P = k|\omega_z| + G(|V_r| + |V_l|)$ (Eq. (23)) and the constraint of $|V_l| + |V_r| = 2v_c$ (Eq. (25)), the power becomes as follows:*

$$P = \begin{cases} P_0 & \text{if } 0 \le R < R' \\ \dfrac{R'}{R}(P_0 - P_\infty) + P_\infty & \text{if } R \ge R' \end{cases} \tag{42}$$

where, P_0 and P_∞ are constant:

$$P_\infty = 2Gv_c \tag{43}$$

$$P_0 = \frac{kv_c}{R'} + 2Gv_c \tag{44}$$

Proof: As proved in Theorem 1, under the constraint of $|V_l| + |V_r| = 2v_c$:

- $|\omega_z| = \dfrac{v_c}{R'}$ (Eq. (35) and Eq. (40)) is constant for $0 \le R < R'$.

  Therefore, by considering Definition 1, it can be easily verified that P is constant and

$$P_0 = \frac{kv_c}{R'} + 2Gv_c \tag{45}$$

- $|v| = v_c$ (Eq. (27) and Eq. (32)) is constant for $R \ge R'$.

  It is known that $\omega_z = \dfrac{v}{R}$. Hence,

$$\lim_{R \to \infty} |\omega_z| = \lim_{R \to \infty} \frac{v_c}{R} = 0 \tag{46}$$

25

As a result, it is proved that

$$\lim_{R \to \infty} P = P_\infty = 2Gv_c \tag{47}$$

By substituting the obtained relations for P_0 and P_∞, as well as using $|\omega_z| = \dfrac{v_c}{R}$ and Definition 1, the following equality is proved:

$$\frac{B_s}{2R}(P_0 - P_\infty) + P_\infty = k|\omega_z| + G(|V_r| + |V_l|) \tag{48}$$

Using Eq. (42) for power, Fig. 14 is sketched:
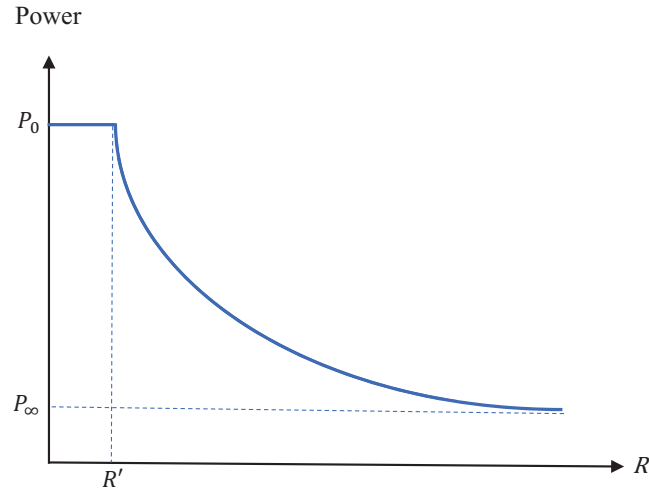
Figure 14: The power changes according to the turning radius.

■

3 Equivalency Theorem
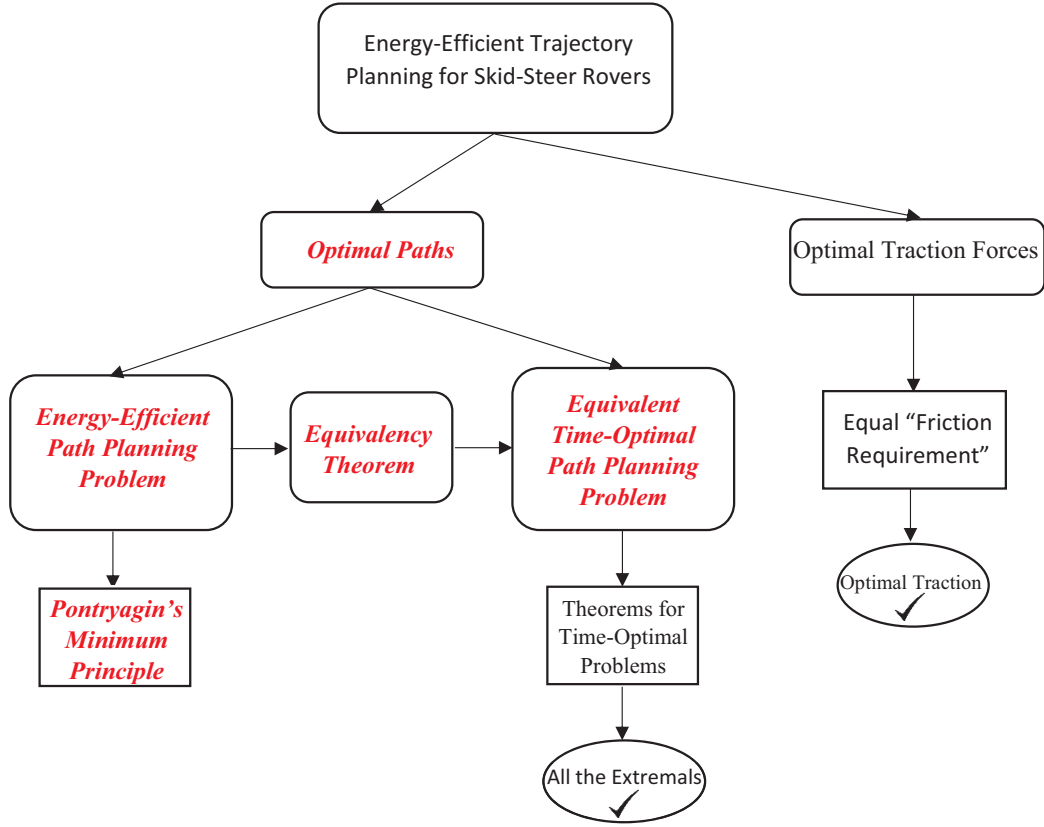
Figure 15: The tasks performed in this chapter are highlighted.

Firstly, the *equivalency theorem* is proved in subsection 3.1. This theorem shows that all minimum-energy trajectories follow the same path irrespective of velocity constraints that may or may not be imposed. This non-intuitive result stems from the fact that for the defined power model, the total energy is fully parametrized by the geometry of the path alone, as will be shown in Lemma 3. In this thesis, the theorem is utilized to obtain an *equivalent time-optimal* problem. The equivalent problem will be solved to obtain the optimal path, which is the general answer to the energy-efficient path planning problem as well. Moreover, a practical example for the *equivalency theorem* is provided in subsection 3.2.

3.1 Equivalency Theorem

Definition 2 *A general path is a sequential set of connected point turns, straight lines, and/or curves parametrized by $R(s)$.*

It is known that energy (E) can be obtained by the following equation.

$$E = \int_0^{t_f} P dt \tag{49}$$

where t is time. In addition, along a general path (Fig. 17), the related time can be obtained from the following relations:

$$t = \int_{\theta_0}^{\theta_f} \left| \frac{d\theta}{\omega_z} \right| \tag{50}$$

$$t = \int_0^{L_P} \left| \frac{ds}{v} \right| \tag{51}$$

where $d\theta$ and ds are the differential of angle and displacement of the rover, respectively. Also, L_P is the length of a path with $R(s) > 0$ for all s. Note that Eq. (50) is particularly useful for $R = 0$, while (51) is valid for all other R.

The mentioned relations are used in the following lemma to show that the energy for skid-steer rovers going along a general path can be written as a function of geometric path parameters of $\Delta\theta$, Δs, and $R(s)$.

Lemma 3 *The energy for the skid-steer rover when going along a general path (Fig. 17) while using the power model of Eq. (23) is equal to:*

$$E = \begin{cases} (k + GB_s)|\Delta\theta|, & \text{if } R = 0 \\ (k + 2GR') \int_0^{L_P} \dfrac{1}{R(s)} ds, & \text{if } 0 < R(s) < R' \\ \int_0^{L_P} \left(\dfrac{k}{R(s)} + 2G \right) ds, & \text{if } R(s) \geq R' \\ 2G\Delta s & \text{if straight line} \end{cases} \tag{52}$$

Proof: The energy for each interval of R is proved separately.

(I) $R = 0$:

Starting with the power model, Eq. (23), and the general equations (49) and (50), gives:

$$E = \int_{\theta_0}^{\theta_f} (k|\omega_z| + G(|V_r| + |V_l|)) \left| \frac{d\theta}{\omega_z} \right|$$
$$= \int_{\theta_0}^{\theta_f} \left(k + G \frac{|V_r| + |V_l|}{|\omega_z|} \right) |d\theta| \tag{53}$$

Using (15), this becomes:

$$E = \int_{\theta_0}^{\theta_f} \left(k + GB_s \frac{|V_r| + |V_l|}{|V_r - V_l|} \right) |d\theta| \tag{54}$$

28

The definition of R' ensures that for $R = 0$, V_r and V_l are of opposite sign. Therefore, the following relation can be verified:

$$|V_r - V_l| = |V_r| + |V_l| \tag{55}$$

So,

$$\frac{|V_r| + |V_l|}{|V_r - V_l|} = 1 \tag{56}$$

Hence, the energy is:

$$
\begin{aligned}
E &= \int_{\theta_0}^{\theta_f} (k + GB_s) |d\theta| \\
&= (k + GB_s) \int_{\theta_0}^{\theta_f} |d\theta| \\
&= (k + GB_s) |\Delta\theta|, \quad \text{for} \quad R = 0
\end{aligned}
\tag{57}
$$

Therefore the energy for any turn with $R = 0$ is a constant times $|\Delta\theta|$.

(II) $0 < R(s) < R'$: Starting with the power model, (23), and the general equations (49) and (51), gives:

$$
\begin{aligned}
E &= \int_0^{L_P} (k|\omega_z| + G\ (|V_r| + |V_l|)) |\frac{ds}{v}| \\
&= \int_0^{L_P} \left(k|\frac{\omega_z}{v}| + G\ \frac{|V_r| + |V_l|}{|v|} \right) ds
\end{aligned}
\tag{58}
$$

Using Eq. (14), this becomes:

$$E = \int_0^{L_P} \left(k|\frac{\omega_z}{v}| + 2G\frac{|V_r| + |V_l|}{|V_r + V_l|} \right) ds \tag{59}$$

Since V_r and V_l have the opposite sign in $0 < R(s) < R'$, the following relation can again be verified:

$$|V_r - V_l| = |V_r| + |V_l| \tag{60}$$

Therefore, using Eq. (18), the following relations are obtained:

$$R = R' \left| \frac{V_r + V_l}{V_r - V_l} \right| = R' \frac{|V_r + V_l|}{|V_r| + |V_l|}, V_r \neq V_l \tag{61}$$

So,

$$\frac{|V_r| + |V_l|}{|V_r + V_l|} = \frac{R'}{R} \tag{62}$$

Also, it is known that $|v| = R|\omega_z|$. Therefore,

$$E = \int_0^{L_P} \left(\frac{k}{R(s)} + 2G\frac{R'}{R(s)} \right) ds \tag{63}$$

29

Hence,

$$E = \int_0^{L_P} \frac{1}{R(s)} (k + 2GR') \, ds \tag{64}$$

Since $k + 2GR'$ is constant,

$$E = (k + 2GR') \int_0^{L_P} \frac{1}{R(s)} ds \tag{65}$$

(III) $R(s) \geq R'$:

Since V_r and V_l have the same sign, the following relation can be easily verified:

$$|V_r + V_l| = |V_r| + |V_l| \tag{66}$$

So, the following relation is true:

$$\frac{|V_r| + |V_l|}{|V_r + V_l|} = 1 \tag{67}$$

Also, it is known that $|v| = R|\omega_z|$. Therefore, using Eq. (59):

$$E = \int_0^{L_P} \left(\frac{k}{R(s)} + 2G \right) ds \tag{68}$$

(IV) Straight line:

In the specific case of a straight line $V_r = V_l$, $\omega_z = 0$ and thus $E = \int_0^{L_P} 2G \, ds = 2G\Delta s$ with $\Delta s = L_P$.

∎

The lemma will be used to prove the equivalency theorem (see Theorem 2).

Definition 3 *A proper constraint is one that does not place a limit on a skid-steer rover's turning radii; i.e. one that allows point turns, straight lines, and $0 < R < \infty$. Note that this includes the case of unconstrained velocities. Some velocity constraints that will be shown to be proper include:*

- Constant v_c ($|V_l| + |V_r| = 2v_c$, where v_c is constant)

- $|V_i| < |v_{max}|$, $i = \{r, l\}$ and v_{max} is constant

- Unconstrained velocity

- Constant power velocity constraint (see Fig. 16)

Definition 4 *Optimal controls are a solution $\{V_r^*, V_l^*\}$ to the energy optimization problem stated in chapter 2 (Eq. (2)).*

Definition 5 *An optimal path is the general path produced by applying optimal controls $\{V_r^*, V_l^*\}$.*

Theorem 2 *Equivalency Theorem: **An optimal path found for energy optimization with a proper velocity constraint is also an optimal path for energy optimization with **any other** proper velocity constraint.**

Proof: As can be seen in Lemma 3, the energy consumption along a general path can be fully parameterized by geometric path parameters $(\Delta\theta, \Delta s, R(s))$ and is not directly dependent on V_r, V_l.

Also, any general path can be achieved by a skid-steer rover with a proper velocity constraint. This follows directly from the definitions of a general path and a proper velocity constraint, respectively.

Moreover, there are no general paths that can result in lower energy consumption than an optimal path. Furthermore, a proper velocity constraint ensures that controls generating any such hypothetically lower-energy general path would have been included in the search space.

An energy-optimal path is thus energy-optimal regardless of velocity constraints, as long as the velocity constraints are proper. Only the particular optimal controls used to follow such an optimal path vary between problems with different proper velocity constraints. ∎

In the following more explanations are provided to clarify Theorem 2. Based on Eq. (18) it is known that the turning radius is a function of the control inputs. Therefore,

$$R(s) = R' \left| \frac{V_r(s) + V_l(s)}{V_r(s) - V_l(s)} \right|, \; V_r(s) \neq V_l(s) \tag{69}$$

Also, from the above-mentioned equation for $R(s)$ it is seen that in the case of unconstrained velocities there are infinite $\{V_l(s); V_r(s)\}$ that can produce a $R(s)$, i.e. all the $\{aV_l(s); aV_r(s)\}$ for the real number $a \neq 0$ produce the same $R(s)$.

The next step is showing that the above-mentioned velocity constraints do not limit the $R(s)$ values and are thus proper. Each constraint is evaluated separately in the following:

1. Constant v_c: Using the related figure (see Fig. 13) and the equation for the turning radius (Eq. (18)) it is evident that for $(V_l, V_r) \in \{(-v_c, v_c), (v_c, -v_c)\}$, the turning radius is zero ($R(s) = 0$). In addition, when (V_l, V_r) is infinitesimally close to the middle of line segments in the first or third quadrant of the figure (i.e. $(V_l, V_r) \approx (v_c, v_c)$ or $(-v_c, -v_c)$), the turning radius approaches to infinity ($R(s) \to \infty$). It is apparent that for other values of V_l and V_r, the range of $(0, +\infty)$ will be obtained for $R(s)$.

2. $|V_i| < |v_{\text{max}}|$, $i = r, l$: Using Eq. (18), when $V_l = -V_r$, the turning radius is zero ($R(s) = 0$). Also, when V_r and V_l are almost equal, the turning radius approaches infinity ($R(s) \to \infty$).

3. Unconstrained velocity: The similar explanation in part 2 is applicable for unconstrained velocity.

31

4. Constant power: It is proved in Appendix A that to have constant power ($P = P_c$ where P_c is a constant), the V_r and V_l should have the symmetric control space shown in Fig. 16. By considering Fig. 16 and Eq. (18), when (V_l, V_r) is the middle point of line segments in second or fourth quadrant of the figure[23], the turning radius becomes zero ($R(s) = 0$). In addition, when (V_l, V_r) is infinitesimally close to the middle of line segments in the first or third quadrant of the figure (i.e. (V_l, V_r) $\approx (\frac{P_c}{2G}, \frac{P_c}{2G})$ or $(-\frac{P_c}{2G}, -\frac{P_c}{2G})$)), the $R(s) \to \infty$. Apparently, the range of $(0, +\infty)$ will be obtained for $R(s)$ by taking other values of V_l and V_r.

This means the same path that is optimal for constant v_c, is optimal for $|V_i| < |v_{max}|$ ($i = r,\ l$), is optimal for UNCONSTRAINED velocity and is optimal for constant power's velocity constraints.
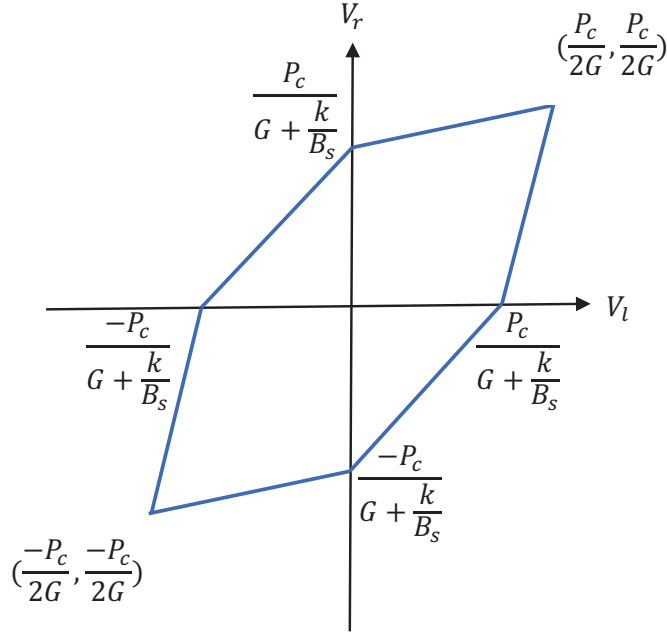
Figure 16: Control Space for Constant Power of P_c

Accordingly, to solve the *energy efficient path planning problem* (see Eq. (2)) there are two approaches:

1. *To directly apply Pontryagin's minimum principle and then prove several theorems specified for skid-steer rovers to obtain all the extremal paths for the energy-efficient path planning problem*: In this approach theorems and processes analogous to those per-

---

[23] $(V_l, V_r) \in \left\{ \left(-\dfrac{P_c}{2\left(G + \dfrac{k}{B_s}\right)}, \dfrac{P_c}{2\left(G + \dfrac{k}{B_s}\right)} \right), \left(\dfrac{P_c}{2\left(G + \dfrac{k}{B_s}\right)}, -\dfrac{P_c}{2\left(G + \dfrac{k}{B_s}\right)} \right) \right\}$

formed by A. Furtuna [24] [62] should be regenerated and then be revised/adjusted for our problem (Eq. (2)). As an example, applying *Pontryagin's minimum principle* to the "constant v_c" energy-efficient path planning problem is explained in Appendix B.2. Then, the difficulties for solving the problem are explained in Appendix B.3.

2. *To use the "constant power" constraint and find an equivalent time-optimal problem for the energy-efficient problem* (Eq. (2)): Based on the *equivalency theorem*, "constant power" is one of the several proper constraints that could be considered to obtain the *optimal path* for the *energy efficient path planning problem*. Accordingly, the constraint can be used to convert the energy-efficiency to an equivalent time-efficiency problem.[25] Hence, the theorems that are proved by A. Furtuna [62] can be used directly for solving the *equivalent time-optimal* problem. Therefore, the optimal paths for the energy-efficient path planning problem will be obtained.

In this thesis, the second approach, which is considering "constant power" and its related velocity constraints, is utilized to solve the *energy efficient path planning problem* (see Eq. (2)).

As explained in subsection 2.3, "constant v_c" is an important practical constraint. Moreover, based on the *equivalency theorem* (Theorem 2), both "constant v_c" and "constant power" constraints give the same optimal path. Accordingly, next subsection (see Theorem 3) is explaining an example, about equivalency of "constant v_c" and "constant power" energy-efficient path planning problem, to provide more insight to the "equivalency theorem". By choosing proper parameters for the constraints (see Fig. 19) it is shown that the costs of two problems are the same. Therefore, they can be used interchangeably to obtain the optimal path with the same cost.

3.2 A Practical Example for the Equivalency Theorem

Firstly, Theorem 3 is proved. This theorem provides a practical example for the *equivalency theorem* (Theorem 2) explained in the previous subsection. Furthermore, Theorem 3 shows that there is an *equivalent time-optimal* for the constant v_c *energy-efficient* problem (see Eq. (70)) with the same cost. It should be mentioned that based on the *equivalency theorem*, there is a single optimal path for the Energy-Efficient Problem (see Eq. (2)) considering:

- Constant v_c ($|V_l| + |V_r| = 2v_c$, where v_c is constant),

- Constant power velocity constraint resulting in *equivalent time-optimal problem* (see Eq. (71))

---

[24]In his PhD dissertation, several theorems are proved for time-optimal path planning of a rigid body. These theorems are for obtaining the extremal control inputs, categorizing different type of paths, limiting the number of extremals, determining the switch points of the extremals, and defining length/periodicity of the correspondent extremal paths.

[25] From Eq. (49) it is known that $E = \int_0^{t_f} P dt$. For the "constant power" constraint, since P is constant, the relation can be written as $E = Pt_f$. Therefore, E is proportional to the total time (t_f) of the problem. Hence, if the total time (t_f) is minimized, the cost (E) will be minimized.

Afterwards, Lemma 4 converts the axes of the *equivalent time-optimal problem's* control space from $(\tilde{V}_l, \tilde{V}_r)$ axis (see Fig. 19) to $(\tilde{v}, \tilde{\omega})$ axis (see Fig. 20). It should be noted that the converted control space (Fig. 20) is required to use Theorem 5 in the next chapter to obtain the extremal trajectories.

Note: In all of the following equations, $V_r = V_r(t)$, $V_l = V_l(t)$, and $R = R(t)$ are implied.

Theorem 3 *A Practical Example for the Equivalency Theorem*: *The following optimization problems for a general path going from the same starting pose to the end pose (Fig. 17) are equivalent.*

Constant v_c Energy-Efficient Problem:

$$\operatorname*{minimize}_{V_r,\,V_l,\,t_f} \quad E = \int_0^{t_f} P dt, \quad \text{where } P = k|\omega_z| + G(|V_r| + |V_l|)$$

$$\text{subject to} \quad |V_l| + |V_r| = 2v_c \ (\text{see Fig.18})$$

$$\dot{x} = \frac{V_r + V_l}{2} \cos\theta$$

$$\dot{y} = \frac{V_r + V_l}{2} \sin\theta \tag{70}$$

$$\dot{\theta} = \frac{V_r - V_l}{B_s}$$

$$x(0) = x_0, \ y(0) = y_0, \ \theta(0) = \theta_0$$

$$x(t_f) = x_f, \ y(t_f) = y_f, \ \theta(t_f) = \theta_f$$

Equivalent Time-Optimal Problem:

$$\operatorname*{minimize}_{\tilde{V}_r,\,\tilde{V}_l,\,\tilde{t}_f} \quad \tilde{E} = \int_0^{\tilde{t}_f} P_0 dt, \ P_0 \text{ is a positive constant(see Lemma2)}$$

$$\text{subject to} \quad \tilde{V}_r(s) = f_c(\tilde{V}_l(s)) \ (\text{see Eq.(72)})$$

$$\dot{\tilde{x}} = \frac{\tilde{V}_r + \tilde{V}_l}{2} \cos\tilde{\theta}$$

$$\dot{\tilde{y}} = \frac{\tilde{V}_r + \tilde{V}_l}{2} \sin\tilde{\theta} \tag{71}$$

$$\dot{\tilde{\theta}} = \frac{\tilde{V}_r - \tilde{V}_l}{B_s}$$

$$\tilde{x}(0) = x_0, \ \tilde{y}(0) = y_0, \ \tilde{\theta}(0) = \theta_0$$

$$\tilde{x}(\tilde{t}_f) = x_f, \ y(\tilde{t}_f) = y_f, \ \tilde{\theta}(\tilde{t}_f) = \theta_f$$

$$f_c(\tilde{V}_l(s)) = \begin{cases} \dfrac{P_0}{P_0 - 2P_\infty}\left(\tilde{V}_l(s) - 2v_c\right), & 2v_c \leq \tilde{V}_l(s) < \dfrac{P_0 v_c}{P_\infty} \\[2ex] \tilde{V}_l(s)\left(1 - \dfrac{2P_\infty}{P_0}\right) + 2v_c, & 0 \leq \tilde{V}_l(s) < \dfrac{P_0 v_c}{P_\infty} \\[2ex] \tilde{V}_l(s) + 2v_c, & -2v_c \leq \tilde{V}_l(s) < 0 \\[2ex] \dfrac{P_0}{P_0 - 2P_\infty}\left(\tilde{V}_l(s) + 2v_c\right), & -\dfrac{P_0 v_c}{P_\infty} \leq \tilde{V}_l(s) < -2v_c \\[2ex] \tilde{V}_l(s)\left(1 - \dfrac{2P_\infty}{P_0}\right) - 2v_c, & -\dfrac{P_0 v_c}{P_\infty} \leq \tilde{V}_l(s) < 0 \\[2ex] \tilde{V}_l(s) - 2v_c, & 0 \leq \tilde{V}_l(s) < 2v_c \end{cases} \tag{72}$$

Note: Eq. (72) is the piecewise function of the control space shown in Fig. 19.
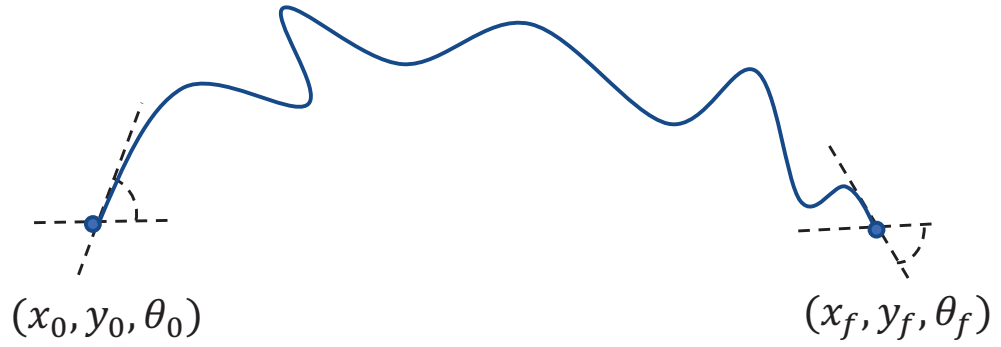
Figure 17: A general path going from a starting (x_0, y_0, θ_0) to an end pose (x_f, y_f, θ_f). The length of path is L_P.
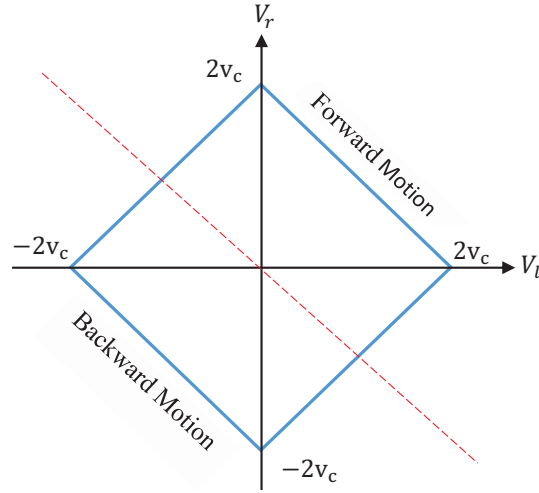
Figure 18: The control space obtained from $|V_r| + |V_l| = 2v_c$ constraint. Note that this figure is the same as Fig. 13 and just for simplicity in following the process is repeated in this section.
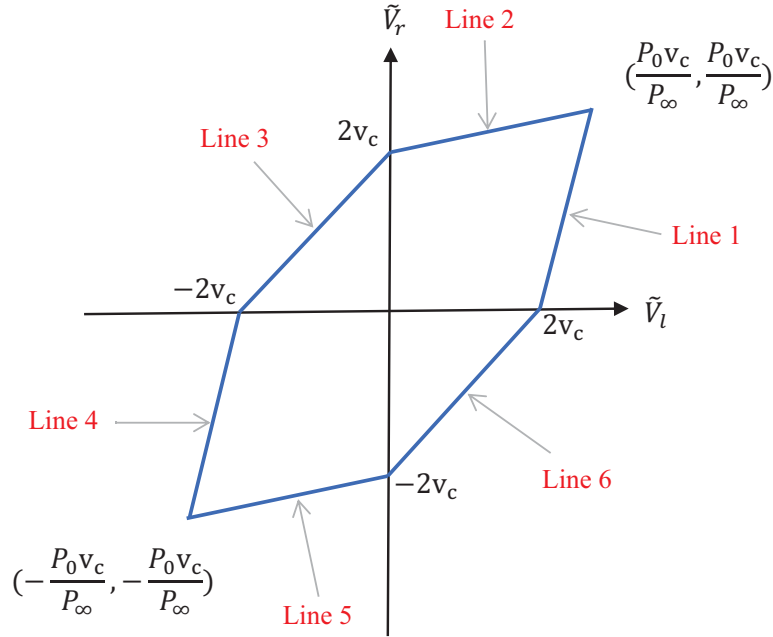
Figure 19: The control space of the *equivalent time-optimal* problem.

Proof: The proof steps are as follows:

Step 1: It will be proved that for the non-predefined path (Fig. 17), the costs of the optimization problems (Eq. (70) and Eq. (71)) under the constraint of their correspondent control spaces are equal:

$$\begin{array}{cc} E & \tilde{E} \\ = & \\ \text{s.t.} \quad |V_l| + |V_r| = 2v_c & \text{s.t.} \quad \tilde{V}_r(s) = f_c(\tilde{V}_l(s)) \end{array} \tag{73}$$

Step 2: It will be explained that for the non-predefined path (Fig. 17), how the differential relations in Eq. (70) and Eq. (71) are related together.

- In the following, *Step 1* is performed.

  Firstly, E in Eq. (70) will be expanded. Then, it will be proved that $E = \tilde{E}$.

$$E = \int_0^{t_f} P dt \tag{74}$$

In Lemma 2 (also see Fig. 14), it is proved that:

$$P = \begin{cases} P_0 & \text{if } 0 \le R < R' \\ \dfrac{kv_c}{R} + 2Gv_c & \text{if } R \ge R' \end{cases} \tag{75}$$

Therefore,

$$E = \begin{cases} \int_{\theta_0}^{\theta_f} P_0 \dfrac{d\theta}{\omega_z}, & \text{if } R(s) = 0 \\ \int_0^{L_P} P_0 \dfrac{ds}{|v|}, & \text{if } 0 < R(s) < R', \text{ where } R(s) = R' \dfrac{|V_r(s) + V_l(s)|}{|V_r(s) - V_l(s)|} \\ \int_0^{L_P} \left(\dfrac{kv_c}{R(s)} + 2Gv_c \right) \dfrac{ds}{|v|}, & \text{if } R(s) \ge R' \end{cases} \tag{76}$$

where L_P is the length of the path in Fig. 17. In addition, in Theorem 1 (Eq. (35) and Eq. (40)) it is proved that for $0 \le R(s) < R'$:

$$\omega_z = \begin{cases} \dfrac{v_c}{R'} & \text{in the second quadrant of Fig. 18} \\ -\dfrac{v_c}{R'} & \text{in the fourth quadrant of Fig.18} \end{cases} \tag{77}$$

and for $R(s) \ge R'$ (see Eq. (27) and Eq. (32)):

$$|v| = v_c \tag{78}$$

Also, for $0 < R(s) < R'$ (see Eq. (14)):

$$|v| = \frac{|V_r(s) + V_l(s)|}{2} \tag{79}$$

Therefore,

37

$$E = \begin{cases} \dfrac{(\theta_f - \theta_0)P_0}{\omega_z}, & \text{if } R(s) = 0, \text{where } \omega_z \text{ is Eq.(77)} \\[2ex] \int_0^{L_P} \dfrac{2P_0}{|V_r(s) + V_l(s)|} ds, & \text{if } 0 < R(s) < R' \\[2ex] \int_0^{L_P} \left(\dfrac{k}{R(s)} + 2G \right) ds, & \text{if } R(s) \geq R', \text{where } R(s) = R' \dfrac{|V_r(s) + V_l(s)|}{|V_r(s) - V_l(s)|} \end{cases} \tag{80}$$

Also, using the fact that $|V_r - V_l| = 2v_c$ for $0 \leq R < R'$ (Eq. (34) and Eq. (39)) and utilizing the relation for R (Eq. (18)), E is obtained as follows:

$$E = \begin{cases} \dfrac{(\theta_f - \theta_0)P_0}{\omega_z}, & \text{if } R(s) = 0, \text{where } \omega_z \text{ is Eq.(77)} \\[2ex] \int_0^{L_P} \dfrac{R'P_0}{R(s)v_c} ds, & \text{if } 0 < R(s) < R' \\[2ex] \int_0^{L_P} \left(\dfrac{k}{R(s)} + 2G \right) ds, & \text{if } R(s) \geq R', \text{where } R(s) = R' \dfrac{|V_r(s) + V_l(s)|}{|V_r(s) - V_l(s)|} \end{cases} \tag{81}$$

Therefore, Eq. (81) is the expanded E in Eq. (74). In the following it will be proved that $E = \tilde{E}$ for $R(s) = 0$, $0 < R(s) < R'$, and $R(s) \geq R'$.

(I) **For $R(s) = 0$:**

When $R(s) = 0$, a skid-steer rover does a point turn which means $V_r(s) = -V_l(s)$ and $\tilde{V}_r(s) = -\tilde{V}_l(s)$. Therefore, the middle point of the lines in the *second* and *fourth* quadrant of Fig. 18 and Fig.19 should be taken into account. Firstly, the *second* quadrant is considered. Then, the process for the *fourth* quadrant is explained.

Second Quadrant of Fig. 19: In the middle point of *Line 3*, $\tilde{V}_l(s) = -v_c$ and $\tilde{V}_r(s) = v_c$. The mentioned point corresponds to the middle point of the line in 2nd quadrant of Fig. 18. Hence, by using Eq. (15) the following relation is obtained:

$$\tilde{\omega}_z = \frac{2v_c}{B_s} = \frac{v_c}{R'} \tag{82}$$

Also, from Eq. (71) it is known that:

$$\tilde{E} = \int_0^{\tilde{t}_f} P_0 dt \tag{83}$$

Therefore,

$$\tilde{E} = \int_{\theta_0}^{\theta_f} P_0 \frac{d\theta}{\tilde{\omega}_z} \tag{84}$$

which means:

$$\tilde{E} = \frac{(\theta_f - \theta_0)P_0 R'}{v_c} \tag{85}$$

38

From Eq. (77) and Eq. (81) it is obtained that for $R(s) = 0$,

$$E = \frac{(\theta_f - \theta_0)P_0 R'}{v_c} \tag{86}$$

Therefore, comparing Eq. (85) and Eq. (86),

$$\boxed{\tilde{E} = E} \tag{87}$$

The similar process can be performed for the *fourth quadrant*.

(II) **For $0 < R(s) < R'$:**

In this range for R, right and left wheel velocities have different signs. Hence, the lines in 2nd and 4th quadrants (except their middle points which is investigated in part (I)) of Fig. 18 and 19 are related to this range.

Firstly, *Line 3* of Fig. 19 is considered which corresponds to the line in the 2nd quadrant of Fig. 18.

It is known that

$$\tilde{v}(s) = R(s)\tilde{\omega}(s) \tag{88}$$

Also, Eq. (15) gives:

$$|\tilde{\omega}| = \frac{|\tilde{V}_r - \tilde{V}_l|}{2R'} \tag{89}$$

In addition, the equation of *Line 3* in Fig. 19 gives:

$$|\tilde{V}_r - \tilde{V}_l| = 2v_c \tag{90}$$

Hence, from Eq. (88) to Eq. (90) it is obtained that

$$\tilde{v}(s) = R(s)\frac{v_c}{R'} \tag{91}$$

Moreover, from Eq. (71) the following relation is calculated:

$$\tilde{E} = \int_0^{L_P} P_0 \frac{ds}{|\tilde{v}(s)|} \tag{92}$$

Hence, using Eq. (91) and Eq. (92) it is obtained that

$$\tilde{E} = \int_0^{L_P} \frac{R' P_0}{R(s) v_c} ds \tag{93}$$

As a result, comparing Eq. (93) to Eq. (81) it is concluded that

$$\boxed{\tilde{E} = E} \tag{94}$$

Note that for $0 < R(s) < R'$, P is constant (Eq. (75)). So, it is not surprising that the *equivalent time-optimal* (Eq. (71)) problem is the same as *energy-efficient* (Eq. (70)) problem with no modifications required to the control space.

The similar process can be performed for *Line 6*.

(III) **For $R(s) \geq R'$**

Line 1:

The equation of *Line 1* and the equation for the turning radius (Eq. (18)) are presented hereunder:

$$\tilde{V}_l(s) - \tilde{V}_r(s) = -\frac{2P_\infty}{P_0}\tilde{V}_r(s) + 2v_c \tag{95}$$

$$R(s) = R'\frac{\tilde{V}_r(s) + \tilde{V}_l(s)}{\tilde{V}_l(s) - \tilde{V}_r(s)}, \qquad \tilde{V}_r(s) \neq \tilde{V}_l(s) \tag{96}$$

$$R(s) \to +\infty, \qquad \tilde{V}_r(s) = \tilde{V}_l(s) \tag{97}$$

Solving Eq. (95) and Eq. (96) for $\tilde{V}_r(s)$ and $\tilde{V}_l(s)$, gives the following relations:

$$\tilde{V}_l(s) = \frac{P_0 v_c (R(s) + R')}{P_\infty R(s) + P_0 R' - P_\infty R'} \tag{98}$$

$$\tilde{V}_r(s) = \frac{P_0 v_c (R(s) - R')}{P_\infty R(s) + P_0 R' - P_\infty R'} \tag{99}$$

Substituting Eq. (98) and Eq. (99) in the following relation (which is obtained from Eq. (14) and Eq. (92)),

$$\tilde{E} = \int_0^{L_P} 2P_0 \frac{ds}{\tilde{V}_l(s) + \tilde{V}_r(s)} \tag{100}$$

gives

$$\tilde{E} = \int_0^{L_P} \frac{P_\infty R(s) + P_0 R' - P_\infty R'}{R(s)v_c} ds \tag{101}$$

Finally, by substituting P_0 and P_∞ (see lemma 2) in Eq. (101), the following relation is obtained:

$$\tilde{E} = \int_0^{L_P} \left(\frac{k}{R(s)} + 2G\right) ds \tag{102}$$

Therefore, comparing Eq. (102) to Eq. (81) it is concluded that

$$\boxed{\tilde{E} = E} \tag{103}$$

Now, $R(s) \to +\infty$ is investigated. Using Eq. (97) and Fig. 19 it is obtained that $\tilde{V}_r = \tilde{V}_l = \frac{P_0 v_c}{P_\infty}$. Therefore, by utilizing Eq. (100) and the relation of $P_\infty = 2Gv_c$ (see Lemma 2) it is obtained:

$$\tilde{E} = \int_0^{L_P} 2G ds = 2GL_P \tag{104}$$

Also, from Eq. (81) it can be easily verified that for $R(s) \to +\infty$:

$$E = 2GL_P \tag{105}$$

Therefore,

$$\boxed{\tilde{E} = E} \tag{106}$$

Line 2:

The equation of *Line 2* and the equation for turning radius (Eq. (18)) are as follows:

$$\tilde{V}_r(s) - \tilde{V}_l(s) = -\frac{2P_\infty}{P_0}\tilde{V}_l(s) + 2v_c \tag{107}$$

$$R(s) = R'\frac{\tilde{V}_r(s) + \tilde{V}_l(s)}{\tilde{V}_r(s) - \tilde{V}_l(s)}, \quad \tilde{V}_r(s) \neq \tilde{V}_l(s) \tag{108}$$

$$R(s) \to +\infty, \quad \tilde{V}_r(s) = \tilde{V}_l(s) \tag{109}$$

Solving Eq. (107) and Eq. (108) for $\tilde{V}_r(s)$ and $\tilde{V}_l(s)$, using the results for P_0 and P_∞ in lemma 2, and substituting them in the following equation,

$$\tilde{E} = \int_0^{L_P} 2P_0 \frac{ds}{\tilde{V}_l(s) + \tilde{V}_r(s)} \tag{110}$$

the following relation is again obtained:

$$\tilde{E} = \int_0^{L_P} \left(\frac{k}{R(s)} + 2G\right) ds \tag{111}$$

Also, for $\tilde{V}_r = \tilde{V}_l$ (see Eq. (109))

$$\tilde{E} = 2GL_p \tag{112}$$

Therefore,

$$\boxed{\tilde{E} = E} \tag{113}$$

Accordingly, the similar process can be performed for *Line 4* and *Line 5* to obtain the same result for $\tilde{E}$.

• In the following, *Step 2* is explained.

Since the path of both optimization problems (Eq. (70) and Eq. (71)) is the non-predefined path (Fig. 17), $R(s)$ is the same for both problems. Hence, using Eq. (18), the following relations are obtained:

$$R(s) = \frac{B_s}{2}\left|\frac{V_r(s) + V_l(s)}{V_r(s) - V_l(s)}\right|, V_r(s) \neq V_l(s) \tag{114}$$

$$R(s) = \frac{B_s}{2}\left|\frac{\tilde{V}_r(s) + \tilde{V}_l(s)}{\tilde{V}_r(s) - \tilde{V}_l(s)}\right|, \tilde{V}_r(s) \neq \tilde{V}_l(s) \tag{115}$$

41

It is known that for both $\tilde{V}_r(s) = \tilde{V}_l(s)$ and $V_r(s) = V_l(s)$ cases:

$$R(s) \to +\infty \tag{116}$$

Therefore, considering any pair of $(V_r(s), V_l(s))$ in Fig. 18 , the correspondent $R(s)$ can be obtained from Eq. (114) or Eq. (116). Using the $R(s)$, Eq. (115) or Eq. (116), and the equations of the line segments in Fig. 19, the correspondent $(\tilde{V}_r(s), \tilde{V}_l(s))$ will be obtained. In conclusion, considering the optimization problems, for any pair of $(V_r(s), V_l(s))$ there is a correspondent $(\tilde{V}_r(s), \tilde{V}_l(s))$. Hence, for the differential equations of Eq. (117) there is the correspondent differential equation of Eq. (118).

$$\dot{x} = \frac{V_r + V_l}{2}\cos\theta$$
$$\dot{y} = \frac{V_r + V_l}{2}\sin\theta \tag{117}$$
$$\dot{\theta} = \frac{V_r - V_l}{B_s}$$

$$\dot{\tilde{x}} = \frac{\tilde{V}_r + \tilde{V}_l}{2}\cos\tilde{\theta}$$
$$\dot{\tilde{y}} = \frac{\tilde{V}_r + \tilde{V}_l}{2}\sin\tilde{\theta} \tag{118}$$
$$\dot{\tilde{\theta}} = \frac{\tilde{V}_r - \tilde{V}_l}{B_s}$$

∎

In the following lemma, it is shown that Fig. 20 with the axes of $\tilde{v}$ and $\tilde{\omega}$ is obtained from Fig. 19 with the axes of $\tilde{V}_l$ and $\tilde{V}_r$. Therefore, the figures can be used interchangeably.

Lemma 4 *By using Eq.* (14) *and Eq.* (15), *Fig. 20 is obtained from Fig. 19.*

where

$$\tilde{v}_{R'} = v_c \tag{119}$$

$$\tilde{v}_{max} = \frac{P_0 v_c}{P_\infty} \tag{120}$$

$$\tilde{\omega}_{max} = \frac{2v_c}{B_s} \tag{121}$$
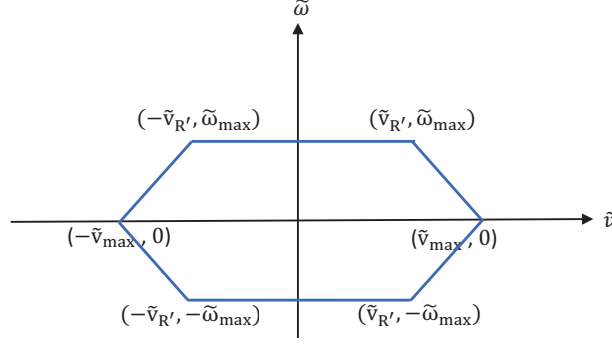
Figure 20: Control space of a skid-steer rover for the equivalent time-optimal problem.

Proof: Since Fig. 19 is symmetric, the following corners from the figure are considered:

- $(\frac{P_0 v_c}{P_\infty}, \frac{P_0 v_c}{P_\infty})$ in Fig. 19 which is correspondent to $(\tilde{v}_{max}, 0)$ in Fig. 20

- $(0, 2v_c)$ which is correspondent to $(\tilde{v}_{R'}, \tilde{\omega}_{max})$ in Fig. 20

Hence, by considering Eq. (14) and Eq. (15), the following relations are written:

$$\tilde{v}_{max} = \frac{\dfrac{P_0 v_c}{P_\infty} + \dfrac{P_0 v_c}{P_\infty}}{2} = \frac{P_0 v_c}{P_\infty} \tag{122}$$

$$\tilde{v}_{R'} = \frac{2v_c + 0}{2} = v_c \tag{123}$$

$$\tilde{\omega}_{max} = \frac{2v_c - 0}{B_s} = \frac{2v_c}{B_s} \tag{124}$$

∎

In the following chapter, by using Theorem 2 and several theorems presented in Furtuna's thesis [62], the extremal trajectories for the defined *equivalent time-optimal* problem will be obtained.

4   Extremal Trajectories for the Equivalent Time-Optimal Problem
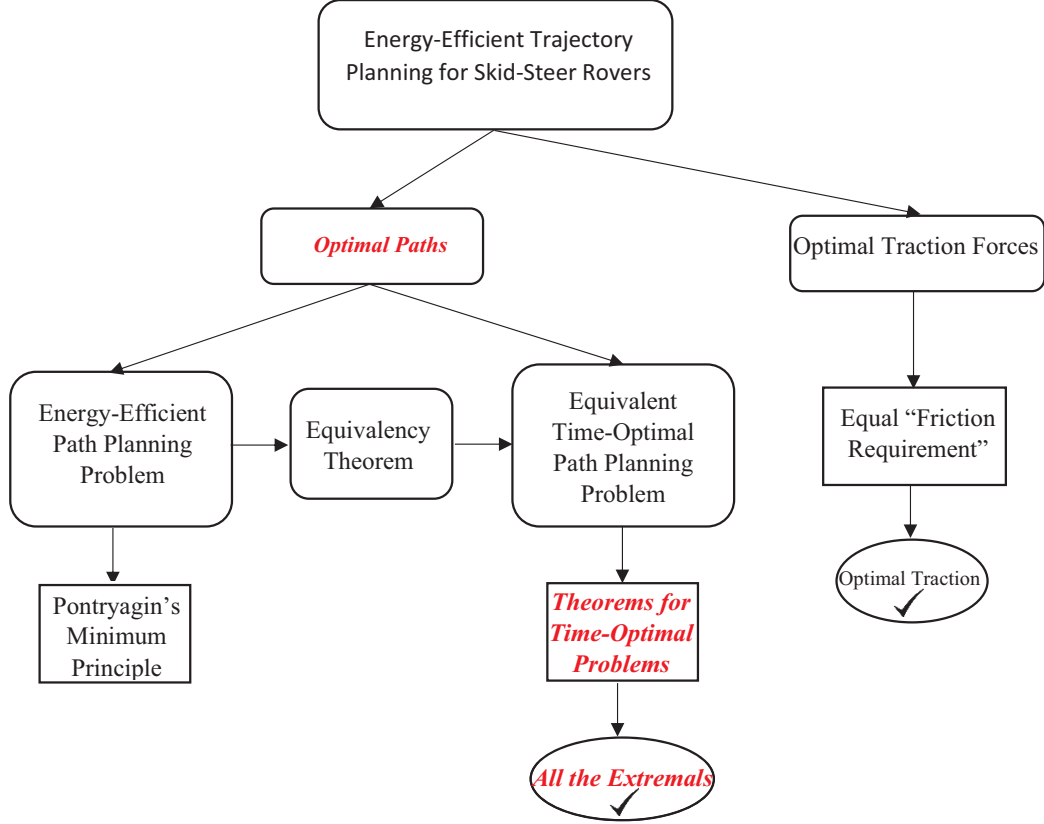
Figure 21: The tasks performed in this chapter are highlighted.

Firstly, *Pontryagin's Minimum Principle* for time-optimal problems is presented in subsection 4.1. This theorem is required to obtain Hamiltonian level sets. Then, the *optimal control inputs* are calculated in subsection 4.2 by the use of a theorem taken from Ref. [62]. Afterwards, subsection 4.3 is specified to plot the Hamiltonian level sets which give the visual notion to categorize the extremal paths. Finally, subsection 4.4 and subsection 4.5 are related to restricting the number of periods and giving the complete table of the extremal paths, respectively. These finite number of extremal paths are enumerated and compared to find the optimal solution as will be shown in Chapter 5.

4.1   Pontryagin's Minimum Principle for Time-Optimal Problems

Pontryagin's Minimum Principle for time-optimal problems (Theorem 4) is taken from Ref. [92]. This theorem is required for this research to

- define the Hamiltonian using the theorem

44

- use the concept of constant maximum of negative Hamiltonian (presented in the theorem) to obtain the Hamiltonian level sets in subsection 4.3

Theorem 4 *Let* $x(t) = (x(t),...,x_m(t))$ *be a trajectory and* $u(t)$ *mapping the time interval* $t_0 \leq t \leq t_1$ *to U:*

$$u(t) = (u_1(t),...,u_n(t)) \tag{125}$$

be the correspondent admissible (i.e., piecewise continuous) control input for transferring from $x(t_0) = x_0$ *to* $x(t_1) = x_1$. *The necessary condition for* $u(t)$ *and* $x(t)$ *to be time-optimal is as follows:*

A nontrivial continuous adjoint function of $\lambda(t) = (\lambda_1(t), \lambda_2(t),...,\lambda_m(t))$ which is in $\mathbf{R}^m$ exists that satisfies the adjoint equation:

$$\dot{\lambda}_i(t) = -\frac{\partial H}{\partial x_i}, \quad i = 1..m \tag{126}$$

where $H : \mathbf{R}^m \times SE^2 \times U \to \mathbf{R}$ is the Hamiltonian:

$$H(\mathbf{x}(t),\mathbf{u}(t),\lambda(t)) = \langle \lambda(t), \dot{\mathbf{x}}(\mathbf{x}(t),\mathbf{u}(t)) \rangle \tag{127}$$

$$\dot{\mathbf{x}} = \frac{\partial H}{\partial \lambda} \tag{128}$$

Conditions for optimality:

(I) For all t, $t_0 \leq t \leq t_1$, the maximum of $-H(\mathbf{x}(t),\mathbf{u}(t),\lambda(t))$, which is the function of the variable $\mathbf{u} \in U$, is at the point $\mathbf{u} = \mathbf{u}(t)$:

$$\max(-H(\mathbf{x}(t),\mathbf{u}(t),\lambda(t))) = M(\lambda(t),\mathbf{x}(t)) \tag{129}$$

(II) $M(\lambda(t),\mathbf{x}(t)) = \lambda_0$ is constant if $\lambda(t)$, $\mathbf{x}(t)$, and $\mathbf{u}(t)$ satisfy Eq. (126), Eq. (128), and condition (I). Thus, λ_0 satisfies the following condition for $t_0 \leq t \leq t_1$:

$$\lambda_0 \geq 0 \tag{130}$$

Proof: The proof of the theorem is presented in Ref. [92]. ∎

The following relations for the first derivatives of the states are known:

$$\dot{x}(t) = v(t)\cos(\theta(t)) \tag{131}$$

$$\dot{\theta}(t) = \omega_z(t) \tag{132}$$

$$\dot{y}(t) = v(t)\sin(\theta(t)) \tag{133}$$

Note: *All the following relations and variables in this subsection are the function of time (t) that for simplicity the time variable is not written.*

Using Eq. (127) and Eq. (131) through Eq. (133) gives the following relation for Hamiltonian:

$$H = \lambda_1 v \cos(\theta) + \lambda_2 v \sin(\theta) + \lambda_3 \omega_z \tag{134}$$

Also, using Eq. (126) gives:

$$\dot{\lambda} = (0, 0, \lambda_1 \dot{y} - \lambda_2 \dot{x}) \tag{135}$$

After integrating to solve for λ:

$$\lambda = (c_1, c_2, \eta(x, y)) \tag{136}$$

where c_i ($i = 1, 2, 3$) are the constants obtained by integration and they are not zero simultaneously. Also, η is as follows:

$$\eta(x, y) = c_1 y - c_2 x + c_3 \tag{137}$$

Substituting Eq. (136) into Hamiltonian results in the following relation:

$$H = v(c_1 \cos \theta + c_2 \sin \theta) + \omega_z(c_1 y - c_2 x + c_3) \tag{138}$$

Based on the Pontryagin's minimum principle, the *adjoint equation* (Eq. (126)) cannot be identically zero. In other words, c_1, c_2, and c_3 are not all zero. Hence, the following two cases are considered:

1. $c_1 = c_2 = 0$

2. One of c_1 or c_2 is not zero. Therefore, for simplicity and without loss of generality it is assumed[26] that $c_1^2 + c_2^2 = 1$. It should be mentioned that this assumption is considered by A. Furtuna [62] as well.

The paths that are obtained for the case when c_1 and c_2 are both zero, are called *whirls* by A. Furtuna [62]. Hence, the rest of paths are *non-whirls*[27]. *Whirls* for a skid-steer rover have maximum value of angular velocity ($|\omega_z| = 2v_c/B_s$) while their speed ($|v|$) is in $[0, v_c]$. This is equivalent to paths with maximum $|\omega_z|$ when $R \in [0, R']$. It should be mentioned that the structure of *whirls* consists of *rolls* and a *catch* [62]. The *rolls* are circular arcs by $R = R'$. The *catch* part is a circular arc by $R \in [0, R')$ that put the rover in the final pose.

In the following the second case is investigated when the following condition is held:

$$c_1^2 + c_2^2 = 1 \tag{139}$$

Lemma 5 *For a line in the plane given by the equation $ax + by + c = 0$, where a, b, and c are real constants with a and b not both zero, the perpendicular distance of a point (x_0, y_0) from the line is as follows [93]:*

---

[26]As it is known for Pontryagin's minimum principle and it is mentioned by A. Furtuna [62], the conditions of the principle are invariant to the scaling of the adjoint with a positive number.

[27]In A. Furtuna's thesis, *non-whirls* are called *control line trajectories*.

$$\text{distance} = \frac{|ax_0 + by_0 + c|}{\sqrt{a^2 + b^2}} \tag{140}$$

Considering Eq. (137) for $\eta(x,y)$, assuming Eq. (139), and using Lemma 5 it is concluded that $\eta(x,y)$ is the signed distance of the robot's centroid from a line which is named η-line [28]. For simplicity it is assumed that the center of mass and centroid of the robot are the same. The η-line (see Fig. 22) is a hypothetical control line in 2D and distance to it determines the path type; there is more discussion about it in Ref. [50] and subsection 4.4 of this thesis.
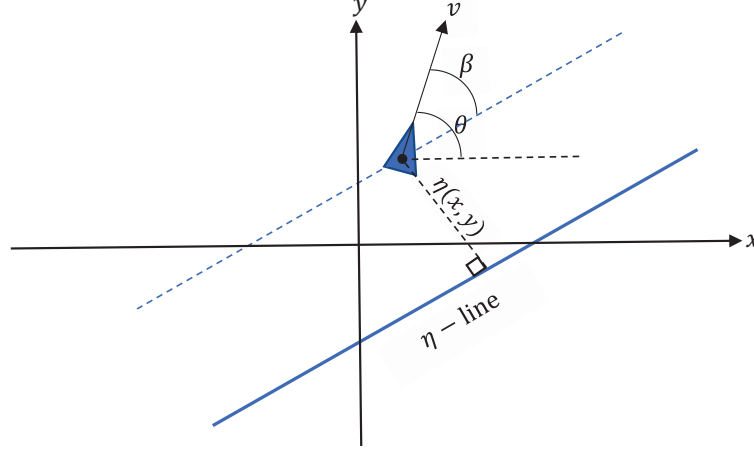
Figure 22: Schematic figure to show the η-line and the related parameters. β is the orientation of rover with respect to the η-line.

Lemma 6 *If β (see Fig. 22) is defined as Eq. (141), the Hamiltonian (Eq. (138)) will be converted to Eq. (142), while Eq. (137) and Eq. (139) are considered.*

$$\beta = \begin{cases} \theta - \arctan2(-c_2, -c_1) & \text{if } c_1 \neq 0 \\ \theta - \arctan2(-c_2, -c_1) & \text{if } c_1 = 0 \text{ and } c_2 < 0 \\ \theta - \arctan2(c_2, c_1) & \text{if } c_1 = 0 \text{ and } c_2 > 0 \end{cases} \tag{141}$$

$$-H = \begin{cases} v \cos\beta - \omega_z \eta & \text{if } c_1 \neq 0 \\ v \cos\beta - \omega_z \eta & \text{if } c_1 = 0 \text{ and } c_2 < 0 \\ -v \cos\beta - \omega_z \eta & \text{if } c_1 = 0 \text{ and } c_2 > 0 \end{cases} \tag{142}$$

Proof: The proof for $c_1 \neq 0$ as well as $c_1 = 0$ & $c_2 < 0$ exist in [50]. It should be mentioned that there is a typo in Eq. (79) of [50]. It should be written in the format of $\beta = \theta - \arctan2(-c_2, -c_1)$. Then, the results presented in the paper for the mentioned conditions of c_1 and c_2 are valid. The only remained part is $c_1 = 0$ & $c_2 > 0$ which is elaborated hereunder:

---

[28]The naming convention of η-line is taken from Ref. [50]. Also, the η-line is named *control line* in [62].

It is known that for two variables of x and y the definition of $\arctan2(y,x)$ [94, 95] is as follows:

$$\arctan2(y,x) = \begin{cases} \arctan\left(\dfrac{y}{x}\right) & \text{if } x > 0 \\ \arctan\left(\dfrac{y}{x}\right) + \pi & \text{if } x < 0 \text{ and } y \geq 0 \\ \arctan\left(\dfrac{y}{x}\right) - \pi & \text{if } x < 0 \text{ and } y < 0 \\ +\pi/2 & \text{if } x = 0 \text{ and } y > 0 \\ -\pi/2 & \text{if } x = 0 \text{ and } y < 0 \\ \text{undefined} & \text{if } x = 0 \text{ and } y = 0 \end{cases} \tag{143}$$

Therefore, the following relation is concluded for the condition of $c_1 = 0$ & $c_2 > 0$:

$$\arctan2(c_2, c_1) = +\frac{\pi}{2} \tag{144}$$

$$\text{Eq. (141)} \Rightarrow \cos\beta = \cos\left(\theta - \frac{\pi}{2}\right) = \sin(\theta) \tag{145}$$

$$\text{Eq. (142)} \Rightarrow -H = -v\sin\theta - \omega_z\eta \tag{146}$$

Also, for $c_1 = 0$ & $c_2 > 0$ and considering $c_1^2 + c_2^2 = 1$ (Eq. (139)), it is obtained that $c_2 = 1$. As a result, Eq. (138) is converted to:

$$H = v\sin\theta + \omega_z\eta \tag{147}$$

As it is seen, Eq. (146) and Eq. (147) are the same. ∎

Eq. (142) and the optimal control inputs that will be obtained in subsection 4.2, will be utilized to graph the Hamiltonian level sets in subsection 4.3.

4.2 Time-Optimal Control Inputs

The following theorem is *Theorem 2* (page 29) of Andrei Furtuna's thesis [62]. This theorem is utilized to obtain the optimal control inputs $(\tilde{v}^*, \tilde{\omega}^*)$ for the *equivalent time-optimal* problem.

Theorem 5 *The problem is time-optimal control of an autonomous rigid body and the assumptions are:*

- *moving in the Euclidean plane without obstacles;*

- *the state vector of $\boldsymbol{x} = (x, y, \theta)$ gives the configuration of the rigid body in the plane. Where (x, y) is the position of the rigid body and θ is its orientation with respect to the x axis;*

- *the model is fully kinematic, assuming that acceleration happens so fast that its time can be neglected[29];*

- *it is assumed that the control set U is a convex polyhedron in $\mathbb{R}^3$;*

---

[29]Note: this is a common assumption for rovers of low speeds

48

- *U fully specifies the vehicle's capabilities.*

For the control set U, there is canonical finite subset U_c that includes the vertices of U and at most one point on each face or edge U that intersects the $\dot{\theta} = 0$ plane, such that any mentioned optimal control problem has a solution that is a control policy which

1. *is piecewise continuous*

2. *only takes values in U_c*

A comparison between the assumptions which are stated in chapter 2 and Theorem 5 shows that the theorem is applicable for the *equivalent time-optimal* problem if it is proved that the control space in Fig. 13, thus Fig. 20, is a convex polyhedron in $\mathbb{R}^3$.

It can be considered that $|V_r| + |V_l| \leq 2v_c$ without causing any problem for the theorems proved in the previous chapter. In other words, here we allow more admissible controls, $|V_r| + |V_l| \leq 2v_c$, for the purpose of this thorem. However, once we find the optimal controls we confirm that they in fact satisfy the original constraint $|V_r| + |V_l| = 2v_c$. As a result, Fig. 13 and thus Fig. 20 becomes a convex polyhedron in $\mathbb{R}^3$. Hence, Theorem 5 will be utilized for the *equivalent time-optimal* problem. Therefore, by using Fig. 20 and Theorem 5 the canonical finite subset for the *equivalent time-optimal* problem is:

$$U_c = \{(\tilde{v}_{max}, 0), (-\tilde{v}_{max}, 0), (\tilde{v}_{R'}, \tilde{\omega}_{max}), (-\tilde{v}_{R'}, \tilde{\omega}_{max}), (\tilde{v}_{R'}, -\tilde{\omega}_{max}), (-\tilde{v}_{R'}, -\tilde{\omega}_{max})\} \quad (148)$$

In the following subsection, U_c (Eq. (148)) will be used to obtain the Hamiltonian level sets for the *equivalent time-optimal* problem.

4.3   Hamiltonian Level Sets

Firstly the Hamiltonian level sets for the following conditions

- $c_1 \neq 0$

- $c_1 = 0$ & $c_2 < 0$

are obtained in subsection 4.3.1. Then, the Hamiltonian level sets for $c_1 = 0$ & $c_2 > 0$ are explained in subsection 4.3.2. Hence, the Hamiltonian level sets for the *equivalent time-optimal* problem (Eq. (71) of Theorem 2) are obtained. These level sets will be used in obtaining the extremal paths in subsection. 4.5.

4.3.1   Hamiltonian Level Sets for $c_1 \neq 0$ or $c_1 = 0$ & $c_2 < 0$

λ_0 is defined as the maximum of Eq. (142). Therefore,

$$\lambda_0 = \max(-H(t)) \quad (149)$$

It is mentioned in Theorem 4 that λ_0 is constant. Also, Eq. (149) is a dot product of the following vectors:

$$V_u = (\tilde{v}^*, \tilde{\omega}^*) \quad (150)$$

and,

$$V_\eta = (\cos\beta, -\eta) \tag{151}$$

where $\tilde{v}^*$ and $\tilde{\omega}^*$ are the time-optimal control inputs. Also, V_u is the control vector, and V_η is called *characteristic vector* (the naming convention is taken from Balckom Masom paper [50]).

$$\begin{aligned}\lambda_0 &= \langle V_u, V_\eta \rangle \\ &= \tilde{v}^* \cos\beta - \tilde{\omega}^* \eta \end{aligned} \tag{152}$$

As mentioned before, λ_0 is constant for the *equivalent time-optimal* problem. Also, $(\tilde{v}^*, \tilde{\omega}^*)$ are the time-optimal control inputs that should be chosen from U_c (Eq. (148)). Moreover, it is known that the optimal control inputs are the vertices of the control space shown in Fig. 20. For example, if $(\tilde{v}^*, \tilde{\omega}^*) = (\tilde{v}_{\max}, 0)$ is considered, the λ_0 becomes:

$$\lambda_0 = \tilde{v}_{\max} \cos\beta \tag{153}$$

Since λ_0 is constant, $\cos\beta$ becomes constant; which means constant angle with respect to the η-line. So, for $\lambda_0 \le \tilde{v}_{\max}$ a straight forward motion is the maneuver that should be considered[30]. By using the same process all the Hamiltonian level sets can be obtained utilizing Eq. (152), which is explained in the following. Firstly, single maneuvers taken from U_c (Eq. (148)) and their related symbols are introduced in Table 1.

Table 1: Symbols and the related maneuvers. CCW and CW stand for Counter Clockwise and Clockwise, respectively.

Index	Symbol	Maneuver
1	⇑	Straight forward with $(\tilde{v}^*, \tilde{\omega}^*) = (\tilde{v}_{\max}, 0)$
2	⇓	Straight backward with $(\tilde{v}^*, \tilde{\omega}^*) = (-\tilde{v}_{\max}, 0)$
3	↰	CCW forward turn with $(\tilde{v}^*, \tilde{\omega}^*) = (\tilde{v}_{R'}, \tilde{\omega}_{\max})$
4	↱	CW forward turn with $(\tilde{v}^*, \tilde{\omega}^*) = (\tilde{v}_{R'}, -\tilde{\omega}_{\max})$
5	↰ᵇ	CCW backward turn with $(\tilde{v}^*, \tilde{\omega}^*) = (-\tilde{v}_{R'}, \tilde{\omega}_{\max})$
6	↱ᵇ	CW backward turn with $(\tilde{v}^*, \tilde{\omega}^*) = (-\tilde{v}_{R'}, -\tilde{\omega}_{\max})$

It should be mentioned that all the turns (Index 3 through 6) in Table 1 have the turning radius of R'.[31] Then, using Eq. (148) and Eq. (152) the following results are obtained for the level sets:

1. $(\tilde{v}^*, \tilde{\omega}^*) = (\tilde{v}_{\max}, 0)$

$$\lambda_0 = \tilde{v}_{\max} \cos\beta \Rightarrow \cos\beta = \frac{\lambda_0}{\tilde{v}_{\max}} \tag{154}$$

---

[30]In both Fig. 25 and Fig. 26, which will be more explained in the next pages, the level set related to straight forward maneuver ⇑ falls to the side of $(\tilde{v}_{\max}, 0)$ point of control space.

[31]Compare Fig. 19 and Fig. 20 while considering the fact that in R' just one of $\tilde{V}_r$ or $\tilde{V}_l$ should be zero.

2. $(\tilde{v}^*, \tilde{\omega}^*) = (-\tilde{v}_{\max}, 0)$

$$\lambda_0 = -\tilde{v}_{\max} \cos\beta \Rightarrow \cos\beta = \frac{-\lambda_0}{\tilde{v}_{\max}} \tag{155}$$

3. $(\tilde{v}^*, \tilde{\omega}^*) = (\tilde{v}_{R'}, \tilde{\omega}_{\max})$

$$\lambda_0 = \tilde{v}_{R'} \cos\beta - \tilde{\omega}_{\max}\eta \Rightarrow -\eta = \frac{\lambda_0 - \tilde{v}_{R'} \cos\beta}{\tilde{\omega}_{\max}} \tag{156}$$

4. $(\tilde{v}^*, \tilde{\omega}^*) = (\tilde{v}_{R'}, -\tilde{\omega}_{\max})$

$$\lambda_0 = \tilde{v}_{R'} \cos\beta + \tilde{\omega}_{\max}\eta \Rightarrow -\eta = \frac{\tilde{v}_{R'} \cos\beta - \lambda_0}{\tilde{\omega}_{\max}} \tag{157}$$

5. $(\tilde{v}^*, \tilde{\omega}^*) = (-\tilde{v}_{R'}, \tilde{\omega}_{\max})$

$$\lambda_0 = -\tilde{v}_{R'} \cos\beta - \tilde{\omega}_{\max}\eta \Rightarrow -\eta = \frac{\lambda_0 + \tilde{v}_{R'} \cos\beta}{\tilde{\omega}_{\max}} \tag{158}$$

6. $(\tilde{v}^*, \tilde{\omega}^*) = (-\tilde{v}_{R'}, -\tilde{\omega}_{\max})$

$$\lambda_0 = -\tilde{v}_{R'} \cos\beta + \tilde{\omega}_{\max}\eta \Rightarrow -\eta = \frac{-\tilde{v}_{R'} \cos\beta - \lambda_0}{\tilde{\omega}_{\max}} \tag{159}$$

It is known that $\cos\beta \in [-1, 1]$. Therefore, from Eq. (154) and Eq. (155) it is concluded that if $\lambda_0 > \tilde{v}_{\max}$, there are no $\Uparrow$ and $\Downarrow$ maneuvers. However, for $\lambda_0 \leq \tilde{v}_{\max}$ all the reported maneuvers in Table 1 are possible. In addition, it is known that $\lambda_0 > 0$ (Theorem 4).[32] Therefore, the following categories for λ_0 are considered:

(i) $\lambda_0 > \tilde{v}_{\max}$

   Feasible Maneuvers: $\curvearrowleft$, $\curvearrowright$, $\overset{b}{\curvearrowleft}$, and $\overset{b}{\curvearrowright}$

(ii) $\lambda_0 = \tilde{v}_{\max}$

   Feasible Maneuvers: $\Uparrow$, $\Downarrow$, $\curvearrowleft$, $\curvearrowright$, $\overset{b}{\curvearrowleft}$, and $\overset{b}{\curvearrowright}$

(iii) $0 < \lambda_0 < \tilde{v}_{\max}$

   Feasible Maneuvers: $\Uparrow$, $\Downarrow$, $\curvearrowleft$, $\curvearrowright$, $\overset{b}{\curvearrowleft}$, and $\overset{b}{\curvearrowright}$

The feasible equations, considering the above categories for λ_0, from amongst Eq. (154) through Eq. (159) are considered. Hence, the following conclusions are obtained for Hamiltonian level sets:

---

[32] If $\lambda_0 = 0$, the Hamiltonian level set becomes a point at the origin (see Fig. 26). Therefore, no path will be produced. This point is more discussed in Lemma 8 which will be proved in the next chapter.

- The Hamiltonian level set for $\lambda_0 > \tilde{v}_{max}$ is shown in Fig. 24

- The Hamiltonian level set for $\lambda_0 = \tilde{v}_{max}$ is shown in Fig. 25

- The Hamiltonian level set for $0 < \lambda_0 < \tilde{v}_{max}$ is shown in Fig. 26

It should be noted that for the figures (Fig. 24 through 26), the line segments of Hamiltonian level set closest to the origin are kept. Because $\lambda_0 = \max(-H(t))$ (see Eq. (149)), for the farther part of a level set's line, always there is another line with higher λ_0. For example, consider the dashed line which is extension of P_1P_2 (level set's line) in Fig. 23. There are other level set's lines, which are parallel to P_2P_3, with higher λ_0, i.e. the line segment that crosses the dashed line at P_{Cross}. Therefore, the dashed line shouldn't be sketched/considered. Hence, by the similar explanation, the other line segments for the Hamiltonian level sets in Fig. 24 through Fig. 26 are obtained.
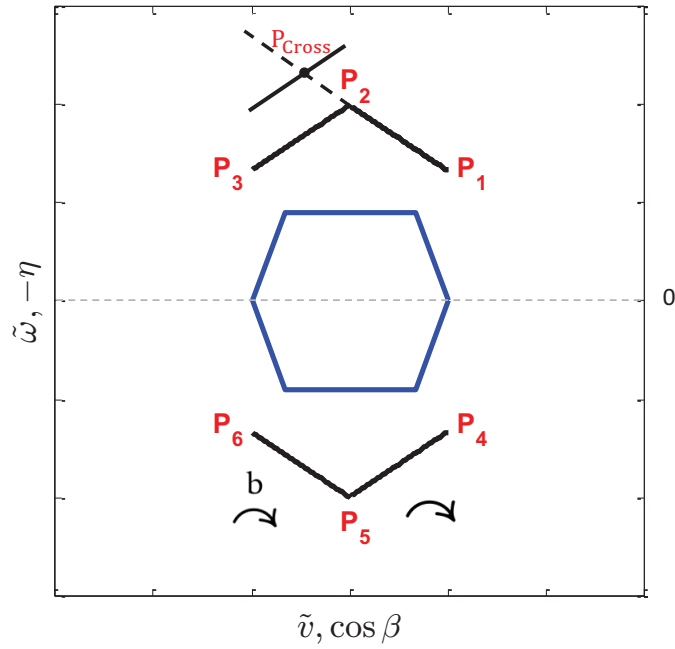
Figure 23: An example to show why the level set's lines shouldn't be extended in Fig. 24.

P_i, $i = 1..6$ (Table 2) are the vertices of the Hamiltonian level sets (see Fig. 24 through Fig. 26). Depending on the value of λ_0 these points move on the plane.

Table 2: The vertices of Hamiltonian level set in Fig. 24 through Fig. 26.

Point	$(\cos\beta, -\eta)$ for Fig. 24 and 25	$(\cos\beta, -\eta)$ for Fig. 26
P_1	$\left(1, \dfrac{\lambda_0 - \tilde{v}_{R'}}{\tilde{\omega}_{\max}}\right)$	$\left(\dfrac{\lambda_0}{\tilde{v}_{\max}}, \dfrac{\lambda_0 - \tilde{v}_{R'}\cos\beta}{\tilde{\omega}_{\max}}\right)$
P_2	$\left(0, \dfrac{\lambda_0}{\tilde{\omega}_{\max}}\right)$	$\left(0, \dfrac{\lambda_0}{\tilde{\omega}_{\max}}\right)$
P_3	$\left(-1, \dfrac{\lambda_0 - \tilde{v}_{R'}}{\tilde{\omega}_{\max}}\right)$	$\left(-\dfrac{\lambda_0}{\tilde{v}_{\max}}, \dfrac{\lambda_0 - \tilde{v}_{R'}\cos\beta}{\tilde{\omega}_{\max}}\right)$
P_4	$\left(1, \dfrac{\tilde{v}_{R'} - \lambda_0}{\tilde{\omega}_{\max}}\right)$	$\left(\dfrac{\lambda_0}{\tilde{v}_{\max}}, \dfrac{\tilde{v}_{R'}\cos\beta - \lambda_0}{\tilde{\omega}_{\max}}\right)$
P_5	$\left(0, \dfrac{-\lambda_0}{\tilde{\omega}_{\max}}\right)$	$\left(0, \dfrac{-\lambda_0}{\tilde{\omega}_{\max}}\right)$
P_6	$\left(-1, \dfrac{\tilde{v}_{R'} - \lambda_0}{\tilde{\omega}_{\max}}\right)$	$\left(-\dfrac{\lambda_0}{\tilde{v}_{\max}}, \dfrac{\tilde{v}_{R'}\cos\beta - \lambda_0}{\tilde{\omega}_{\max}}\right)$
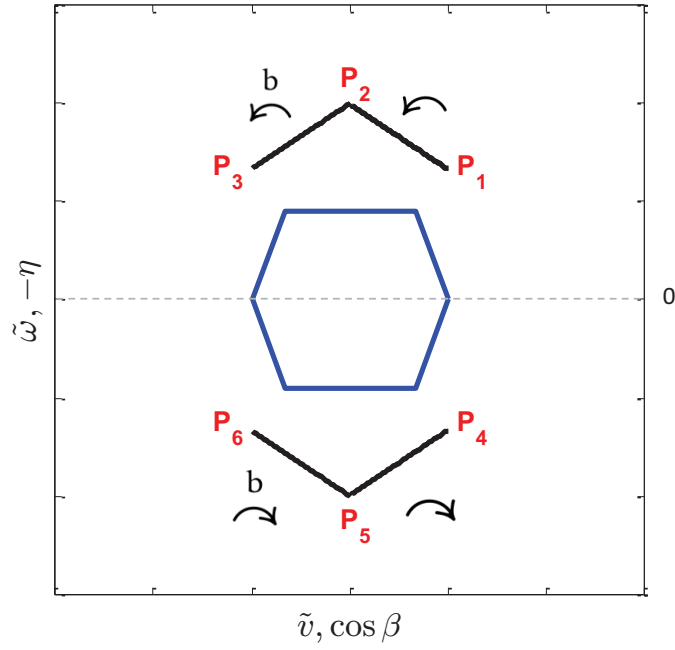
Figure 24: The level set (*black lines*) for $\lambda_0 > \tilde{v}_{\max}$. The *blue hexagon* is the control space shown in Fig. 20.
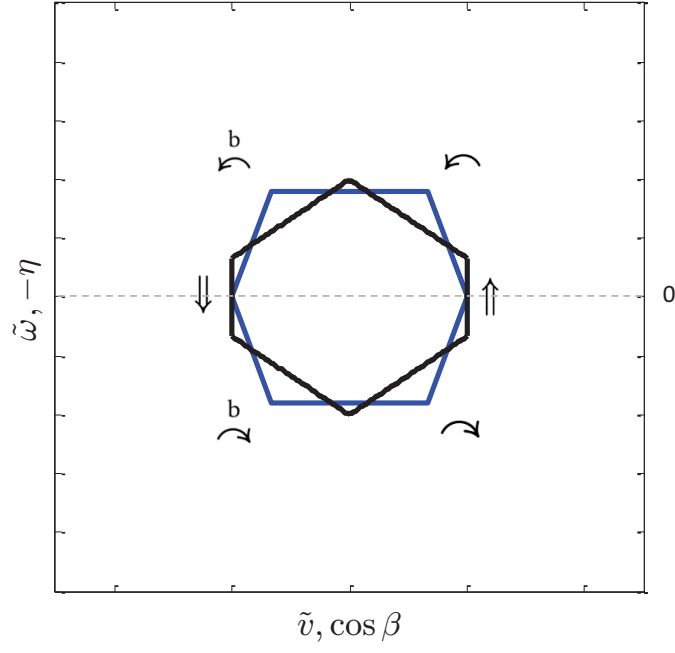
Figure 25: The level set (*black hexagon*) for $\lambda_0 = \tilde{v}_{max}$. The *blue hexagon* is the control space shown in Fig. 20.
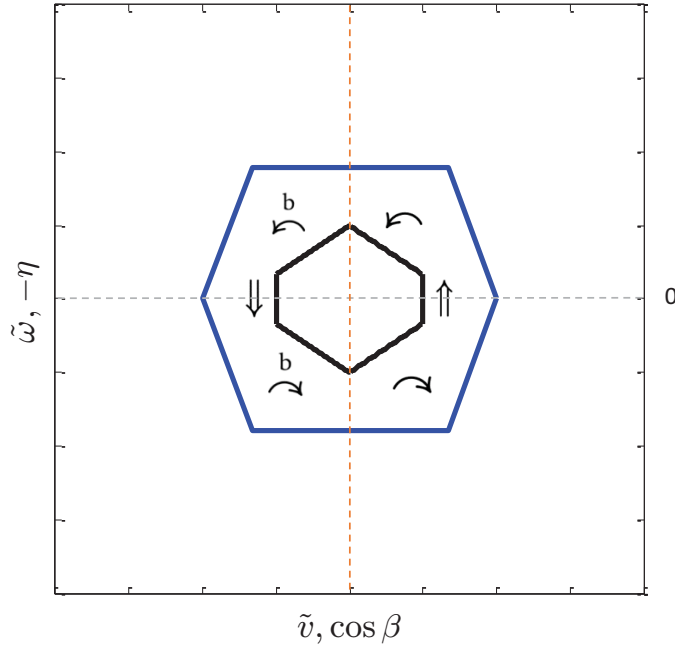
Figure 26: The level set (*black hexagon*) for $0 < \lambda_0 < \tilde{v}_{max}$. The *blue hexagon* is the control space shown in Fig. 20.

4.3.2 Hamiltonian Level Sets for $c_1 = 0$ & $c_2 > 0$

If the same process that was explained in subsection 4.3.1 is followed for the Hamiltonian level sets, Fig. 24 to Fig. 26 will be mirrored with respect to the $\cos\beta = 0$ line. The reason for being mirrored is the negative sign which is multiplied to $\cos\beta$ (see $-H$ equation for the condition of $c_1 = 0$ & $c_2 > 0$ in Eq. (142)). For example in Fig. 26, the hexagonal shape level set is mirrored with respect to the vertical orange line. Therefore, Fig. 27 is obtained.
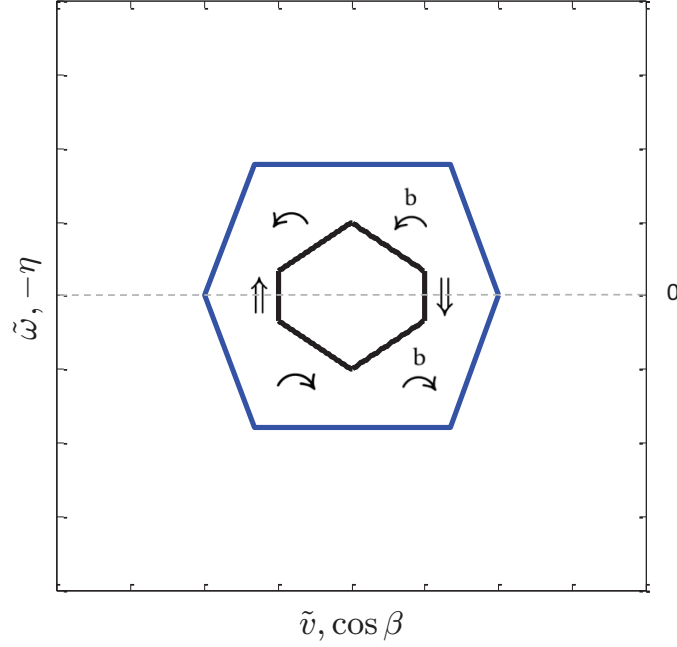
Figure 27: The level set (*black hexagon*) for $0 < \lambda_0 < \tilde{v}_{max}$ and the condition of $c_1 = 0$ & $c_2 > 0$. The *blue hexagon* is the control space shown in Fig. 20.

The Hamiltonian level sets will be used to obtain the shape of the extremal paths in subsection 4.4 and 4.5. Also, some constraints on the period of the paths should be considered which are explained in subsection 4.4.

4.4 Restricting the Number of Periods for the Obtained Paths

Using the obtained Hamiltonian level sets and the geometrical interpretation presented in Ref. [50], the extremal paths can be obtained. Actually, the distance of the rover's centroid to the η-line determines the control policy [50]. Therefore, different paths that are shown in Fig. 28 are obtained from the level sets that were shown in Fig. 24, Fig. 25, and Fig. 26. As it is shown in Fig. 28, there are 3 types of paths:

- *Generic Turns* which consist of only turns

- *Singular* paths

- *Generic TST* which stands for generic paths with sequences of Turns, Straight lines, and Turns

It should be noted that the naming convention of Generic and Singular paths are taken from Ref. [50] and [62].

Generic Turns

$\lambda_0 > \tilde{v}_{max}$

$\eta - \text{line}$

Singular

$\lambda_0 = \tilde{v}_{max}$

$\eta - \text{line}$

○ Singular Point

Generic TST

$\lambda_0 < \tilde{v}_{max}$
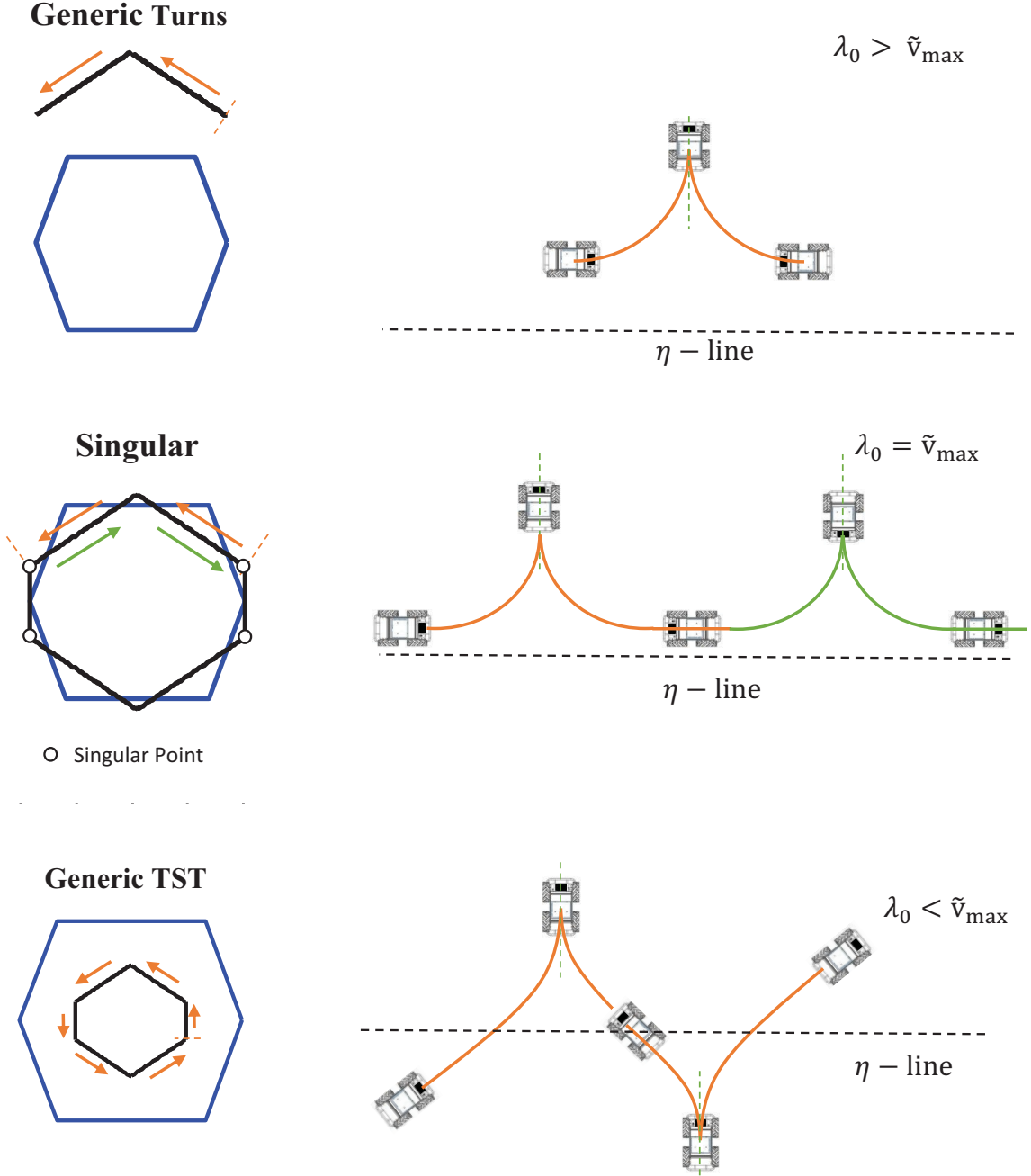
$\eta - \text{line}$

Figure 28: Different path types based on the λ_0 categories.

Also, the difference between the above-mentioned paths is explained in the following:

For *Generics* (Generic Turns and Generic TST) the position of the η–line uniquely determines the optimal control inputs. Therefore, the paths will be unique.

However, *Singulars* are the paths that may include singularities. As it can be seen in Fig. 28, since in the singular points the angle of the robot with respect to the η–line is 0 or 180°, the robot can maintain its straight line motions or can switch to turns at any particular point in time. Specifically, *Singulars* are the paths that their straight line motions ($\Uparrow$, $\Downarrow$) are parallel to the η–line.

Now, by using Fig. 28 all the paths will be obtained. However, the period of paths should be restricted. Accordingly, the following theorems are proved/presented.

Theorem 6 *The generic (non-singular) paths contain no more than one period if the following conditions are held:*

1. *The image of $\theta(t)$ is not S^1*

2. *$\dot{\theta}(0) \neq 0$*

Proof: It is proved in page 46 (*Lemma 16*) of Furtuna's thesis [62]. ∎

All the *generic TST* paths which will be reported in Table 3, except those extremal trajectories that start with a straight line motions (i.e. $\Uparrow \curvearrowright_{\frac{\pi}{2}} \overset{b}{\curvearrowright}_{\pi} \Downarrow \overset{b}{\curvearrowright}_{\frac{\pi}{2}} \curvearrowright_{\frac{\pi}{2}}$), are satisfying the conditions in Theorem 6. Moreover, based on Theorem 5 of [60], it is concluded that the *generic TST* paths starting with a straight line motion should be less than one period, as well. [33]

Theorem 7 *The total turning angle of singular paths is less than 3π.*

Proof: As it is shown in Fig. 28 for singular paths there are three types of singular paths, based on the starting maneuver:

(I) CCLCCLCC..., i.e. $\curvearrowright \overset{b}{\curvearrowright}_{\frac{\pi}{2}} \Downarrow \overset{b}{\curvearrowright}_{\frac{\pi}{2}} \curvearrowright_{\frac{\pi}{2}} \Uparrow \curvearrowright_{\frac{\pi}{2}} \overset{b}{\curvearrowright}$

(II) CLCCLCCL..., i.e. $\overset{b}{\curvearrowright} \Downarrow \overset{b}{\curvearrowright}_{\frac{\pi}{2}} \curvearrowright_{\frac{\pi}{2}} \Uparrow \curvearrowright_{\frac{\pi}{2}} \overset{b}{\curvearrowright}$

(III) LCCLCCLC..., i.e. $\Uparrow \curvearrowright_{\frac{\pi}{2}} \overset{b}{\curvearrowright}_{\frac{\pi}{2}} \Downarrow \overset{b}{\curvearrowright}_{\frac{\pi}{2}} \curvearrowright_{\frac{\pi}{2}}$

In the following each type is elaborated separately.

(I) CCLCCLCC...

- *If the turning of starting 'C' is less than $\dfrac{\pi}{2}$, the maximum length optimal Type(I) path is CCLCCLCC which the turning of the last 'C' is less then $\dfrac{\pi}{2}$:*

---

[33]It can be easily verified that if the path is extended to $\Uparrow \curvearrowright_{\frac{\pi}{2}} \overset{b}{\curvearrowright}_{\pi} \Downarrow \overset{b}{\curvearrowright}_{\frac{\pi}{2}} \curvearrowright_{\frac{\pi}{2}} \Uparrow$, it can be replaced by $\Uparrow \curvearrowright_{\frac{\pi}{2}} \overset{b}{\curvearrowright}_{\pi} \Downarrow \overset{b}{\curvearrowright}_{\frac{\pi}{2}} \curvearrowright_{\frac{\pi}{2}}$.

Without loss of generality, let's consider $\curvearrowright\overset{b}{\curvearrowright}_{\frac{\pi}{2}}\Downarrow\overset{b}{\curvearrowright}_{\frac{\pi}{2}}\curvearrowright_{\frac{\pi}{2}}\Uparrow\curvearrowright_{\frac{\pi}{2}}\overset{b}{\curvearrowright}$ where the turning of each $\curvearrowright$ and $\overset{b}{\curvearrowright}$ is less than $\frac{\pi}{2}$. If the path is extended to $\curvearrowright\overset{b}{\curvearrowright}_{\frac{\pi}{2}}\Downarrow\overset{b}{\curvearrowright}_{\frac{\pi}{2}}\curvearrowright_{\frac{\pi}{2}}\Uparrow\curvearrowright_{\frac{\pi}{2}}\overset{b}{\curvearrowright}_{\frac{\pi}{2}}$, it can be replaced by $\curvearrowright\overset{b}{\curvearrowright}_{\frac{\pi}{2}}\Downarrow$. As straight lines are commanded at $\tilde{v}_{\max}$ and are by definition the shortest path between two points, a $\Uparrow$ is always more time optimal than a path that includes turns. It should be noted that in singular paths the length of straight line motions ($\Uparrow, \Downarrow$) is in $[0, +\infty)$. By the similar explanation, it can be verified that always there is a subset of $\curvearrowright\overset{b}{\curvearrowright}_{\frac{\pi}{2}}\Downarrow\overset{b}{\curvearrowright}_{\frac{\pi}{2}}\curvearrowright_{\frac{\pi}{2}}\Uparrow\curvearrowright_{\frac{\pi}{2}}\overset{b}{\curvearrowright}$ which can be replaced by any extension of it ($\curvearrowright\overset{b}{\curvearrowright}_{\frac{\pi}{2}}\Downarrow\overset{b}{\curvearrowright}_{\frac{\pi}{2}}\curvearrowright_{\frac{\pi}{2}}\Uparrow\curvearrowright_{\frac{\pi}{2}}\overset{b}{\curvearrowright}$).

- *If the turning of starting 'C' is equal to $\frac{\pi}{2}$, the maximum length optimal Type(I) path is CCLCC which the turning of the last 'C' is less then $\frac{\pi}{2}$:* Without loss of generality let's consider $\curvearrowright_{\frac{\pi}{2}}\overset{b}{\curvearrowright}_{\frac{\pi}{2}}\Downarrow\overset{b}{\curvearrowright}_{\frac{\pi}{2}}\curvearrowright$. If the path is extended to $\curvearrowright_{\frac{\pi}{2}}\overset{b}{\curvearrowright}_{\frac{\pi}{2}}\Downarrow\overset{b}{\curvearrowright}_{\frac{\pi}{2}}\curvearrowright_{\frac{\pi}{2}}$. The extended path easily can be replaced by $\Uparrow$. Utilizing the similar approach, any extension can be replaced with a shortest path.

(II) CLCCLCCL...

The maximum length optimal Type(II) path is CLCCLCC which the turning of last 'C' is less than $\frac{\pi}{2}$. It should be mentioned that the turning of the starting 'C' can be less or equal than $\frac{\pi}{2}$:

Without loss of generality let's consider $\overset{b}{\curvearrowright}\Downarrow\overset{b}{\curvearrowright}_{\frac{\pi}{2}}\curvearrowright_{\frac{\pi}{2}}\Uparrow\curvearrowright_{\frac{\pi}{2}}\overset{b}{\curvearrowright}$. The extended path is $\overset{b}{\curvearrowright}\Downarrow\overset{b}{\curvearrowright}_{\frac{\pi}{2}}\curvearrowright_{\frac{\pi}{2}}\Uparrow\curvearrowright_{\frac{\pi}{2}}\overset{b}{\curvearrowright}_{\frac{\pi}{2}}$ which can be replaced by $\overset{b}{\curvearrowright}\Downarrow$. Utilizing the similar approach, any extension can be replaced by a subset of the path.

(III) LCCLCCLC...

The maximum length optimal Type(III) path is LCCLCC which the turning of last 'C' is less than $\frac{\pi}{2}$: Without loss of generality let's consider $\Uparrow\curvearrowright_{\frac{\pi}{2}}\overset{b}{\curvearrowright}_{\frac{\pi}{2}}\Downarrow\overset{b}{\curvearrowright}_{\frac{\pi}{2}}\curvearrowright$. If the path is extended to $\Uparrow\curvearrowright_{\frac{\pi}{2}}\overset{b}{\curvearrowright}_{\frac{\pi}{2}}\Downarrow\overset{b}{\curvearrowright}_{\frac{\pi}{2}}\curvearrowright_{\frac{\pi}{2}}$, it can be replaced by $\Uparrow$. Utilizing the similar approach, any extension can be replaced by a subset of the path.

∎

Theorem 8 *The total turning of Generic Turns should be less than 3π.*

Proof: Considering Fig. 28, it could be concluded that *Generic Turns* are *Singularities* without considering the straight line motions ($\Uparrow$, $\Downarrow$). Accordingly, the total turning of *Generic Turns* should be less than 3π (see Theorem 7).

∎

4.5 Extremal Paths Table

From Theorem 5, the set of the optimal control inputs (U_c) is obtained. The control inputs are utilized to obtain and draw Hamiltonian level sets (Fig. 24 through Fig. 26). A sample for the related path to each level set is shown in Fig. 28. Then, Theorem 6 through Theorem 8 are utilized to constrain the number of periods for the Generics and Singulars. Hence, the following table for the extremal paths is obtained:

Table 3: Extremal paths for the *equivalent time-optimal* problem.

Path Type	Paths		
Generic Turns	⌢⌢π⌢π⌢ ⌢⌢π⌢π⌢	⌢⌢π⌢π⌢	⌢⌢π⌢π⌢
Singular	(paths with $\frac{\pi}{2}$ segments)	(paths with $\frac{\pi}{2}$ segments)	(paths with $\frac{\pi}{2}$ segments)
Generic TST	(TST paths)	(TST paths)	(TST paths)

All the shown paths and their subpaths should be evaluated to obtain the *optimal* path for a given start and end pose. In the following chapter, a numerical scenario is solved for the above-mentioned table. In addition, some of the paths in the table are visualized.

5   Numerical Scenario
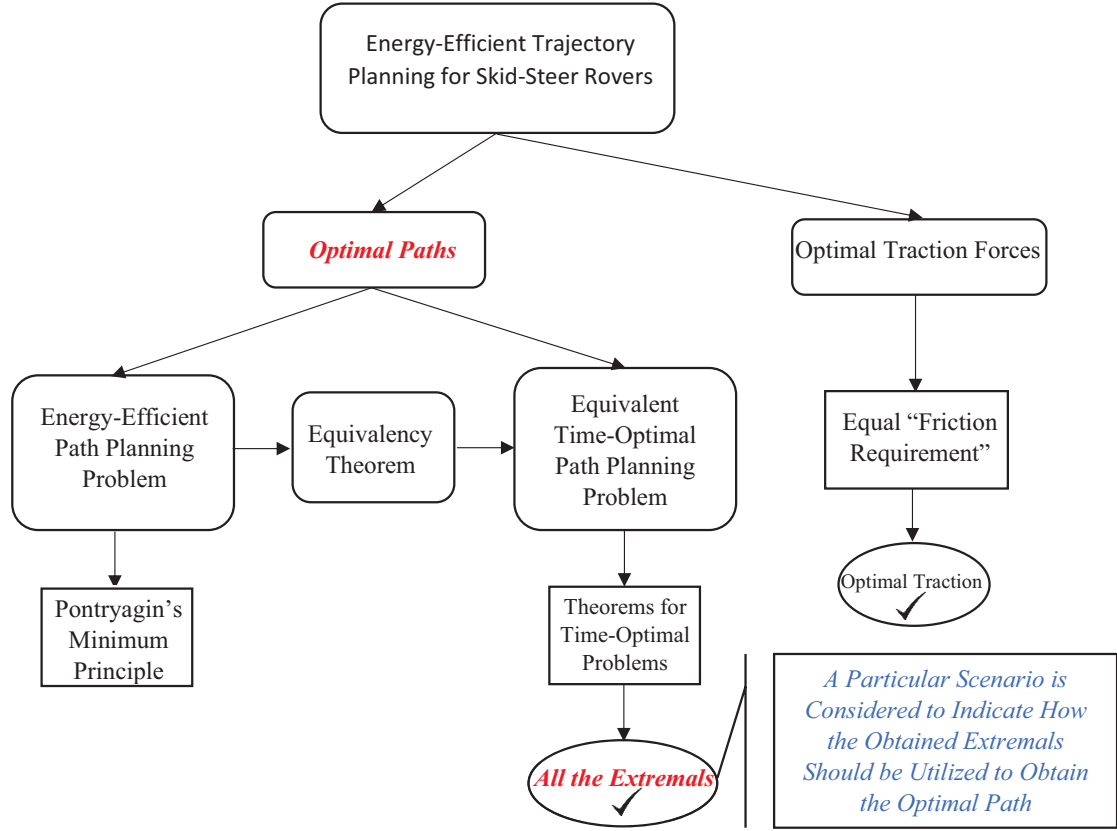
Figure 29: The tasks performed in this chapter are Highlighted.

The goal of this chapter is solving a numerical example to show how Table 3 should be used for a particular scenario. Firstly, in subsection 5.1, two lemmas are presented which will be used to calculate the length of straight lines for *generic TST* paths. Then, the scenario for the numerical example is explained in 5.2. Afterwards, the *algorithms* to obtain the feasibility region for the extremal paths are explained in subsection 5.3. These regions show the feasible starting points of the extremal paths for the considered scenario. Finally, the goal of 5.4 is to draw a map (see Fig. 41) for the particular scenario (Table 4) that shows which extremal path is optimal at each starting point in the 2D plane. The costs of the finite number of extremal paths are enumerated and compared to draw the map.

5.1   Length of Straight Lines in Generic TST Paths

Firstly, a *complete maneuver* is explained in Definition 6. Then, the length of complete ⇑ or ⇓ for *generic TST* paths (see Fig. 28) is mathematically obtained in Lemma 7.

Definition 6 *For the maneuvers shown in Table 1, a **complete maneuver** for a particular λ_0 includes all the possible η and $\cos\beta$ for its related line segment of the level set (i.e. from one switching point to the other).*

*   **For example**, $\Uparrow$ in Fig. 30 is a complete maneuver if its related level set's line segment includes all the points between A and B inclusive. It should be noted that point A is the switching point between $\curvearrowright$ and $\Uparrow$. Also, B is the switching point between $\Uparrow$ and $\curvearrowleft$.*
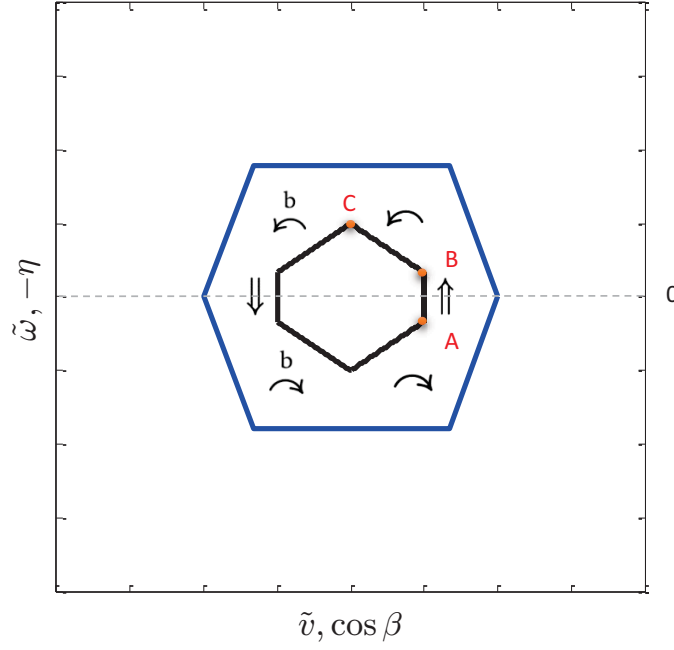
Figure 30: The level set for explaining a complete maneuver.

Lemma 7 *The length of a complete $\Uparrow$ or $\Downarrow$ maneuver for Generic TST paths is*

$$L_D = \frac{2\eta_c}{\sin\beta_c}, \quad \beta_c \neq 0 \tag{160}$$

where, η_c is the maximum distance of the maneuver from the $\eta-$line. Also, β_c is the acute angle between the maneuver and $\eta-$line. Note that for generic TST paths, $\cos\beta < 1$.[34] The parameters are shown in Fig. 31 and are obtained from the following relations:

$$\beta_c = \cos^{-1}\left(\frac{\lambda_0}{\tilde{v}_{max}}\right) \tag{161}$$

$$\eta_c = \frac{\lambda_0}{\tilde{\omega}_{max}}\left(1 - \frac{\tilde{v}_{R'}}{\tilde{v}_{max}}\right) \tag{162}$$

$\tilde{v}_{max}, \tilde{v}_{R'},$ and $\tilde{\omega}_{max}$ were indicated in Fig. 20.
    Proof:

---

[34]See Fig. 26 and Fig. 28

61

In the following, the analysis is done for complete ⇑ maneuver that the similar evaluation can be performed for complete ⇓ maneuver.
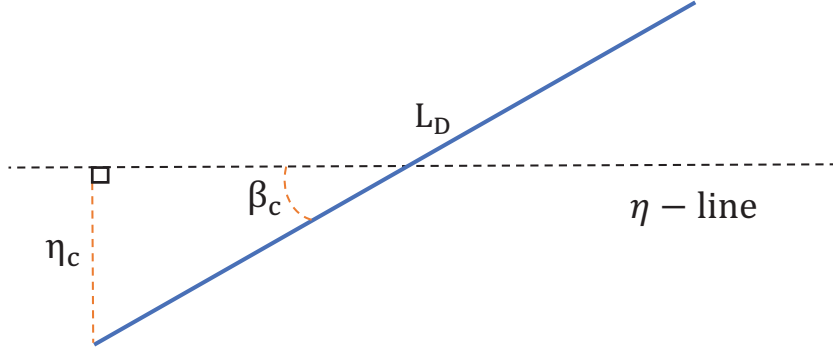
Figure 31: Complete ⇑ maneuver for a generic TST path in Fig. 28.

From the symmetry of the level sets (Fig. 28) it is known that the η–line crosses the middle of a complete ⇑. Hence, by considering Fig. 31 the following relation is obtained:

$$\sin \beta_c = \frac{2\eta_c}{L_D} \tag{163}$$

Therefore,

$$L_D = \frac{2\eta_c}{\sin \beta_c}, \ \beta_c \neq 0 \tag{164}$$

Since ⇑ is a *complete maneuver*, η_c occurs at the *switching point* of ⤳⇑ or ⇑⤾ path. In the following each one is analyzed separately:

- Switching point of ⤳⇑

  Eq. (154) and Eq. (157) give the following relations at the switching point:

$$\lambda_0 = \tilde{v}_{\max} \cos \beta_{s_1} \tag{165}$$

$$\lambda_0 = \tilde{v}_{R'} \cos \beta_{s_1} + \tilde{\omega}_{\max} \eta_{s_1} \tag{166}$$

  where η_{s_1} and β_{s_1} are the η and β at the switching point of ⤳⇑, respectively. By solving the above two equations, the following results are obtained for η_{s_1} and β_{s_1}:

$$\eta_{s_1} = \frac{\lambda_0}{\tilde{\omega}_{\max}} \left(1 - \frac{\tilde{v}_{R'}}{\tilde{v}_{\max}}\right) \tag{167}$$

$$\beta_{s_1} = \cos^{-1}\left(\frac{\lambda_0}{\tilde{v}_{max}}\right) \tag{168}$$

  Therefore, η_c is the absolute value of η_{s_1}. Also, it is known that $\tilde{v}_{R'} < \tilde{v}_{\max}$ (see Fig. 20). Hence,

$$\eta_c = |\eta_{s_1}| = \frac{\lambda_0}{\tilde{\omega}_{\max}} \left(1 - \frac{\tilde{v}_{R'}}{\tilde{v}_{\max}}\right) \tag{169}$$

62

For *generic TST* paths, it is known that $0 < \lambda_0 < \tilde{v}_{max}$ (see Fig. 26. Thus, $0 < \beta_{s_1} < \dfrac{\pi}{2}$ (β_{s_1} is acute). So,

$$\beta_c = |\beta_{s_1}| = \cos^{-1}\left(\frac{\lambda_0}{\tilde{v}_{max}}\right) \tag{170}$$

- Switching point of ⇑ ↶

  Eq. (154) and Eq. (156) give the following relations at the switching point:

$$\lambda_0 = \tilde{v}_{max} \cos\beta_{s_2} \tag{171}$$

$$\lambda_0 = \tilde{v}_{R'} \cos\beta_{s_2} - \tilde{\omega}_{max}\eta_{s_2} \tag{172}$$

where η_{s_2} and β_{s_2} are the η and β at the switching point of ⇑ ↶, respectively. By solving the above two equations, the following results are obtained for η_{s_2} and β_{s_2}:

$$\eta_{s_2} = \frac{\lambda_0}{\tilde{\omega}_{max}}\left(\frac{\tilde{v}_{R'}}{\tilde{v}_{max}} - 1\right) \tag{173}$$

$$\beta_{s_2} = \cos^{-1}\left(\frac{\lambda_0}{\tilde{v}_{max}}\right) \tag{174}$$

Hence, η_c and is the absolute value of η_{s_2}. Accordingly,

$$\eta_c = |\eta_{s_2}| = \frac{\lambda_0}{\tilde{\omega}_{max}}\left(1 - \frac{\tilde{v}_{R'}}{\tilde{v}_{max}}\right) \tag{175}$$

Also,

$$\beta_{s_1} = \beta_{s_2} = \beta_c \tag{176}$$

∎

Lemma 8 *For Generic TST paths:*

$$\lambda_0 \neq 0 \tag{177}$$

Proof: Consider Eq. (160) through Eq. (162). If $\lambda_0 = 0$, it will result in $\beta_c = \dfrac{\pi}{2}$ and $\eta_c = 0$. Hence, $L_D = 0$. Therefore, the Hamiltonian level set becomes a point at the origin of Fig 26 (or see Fig. 28 for generic TST paths). As a result, no *Generic TST* path will be produced. Therefore, λ_0 should not be zero. ∎

The proved lemmas will be used in Algorithm 1 to create a table. Before that step, the scenario will be defined in the following subsection.

5.2 Particular Scenario and Steps to Find the Optimal Paths

Scenario: To go from start poses anywhere in the $x-y$ plane (at the start orientation of $\pi/4$) to the origin (see Table 4) in minimum time while constrained to the control space in Fig. 32. Also, the considered B_s is 1.32 m which is the measured B_s for Husky UGV on hard ground. Therefore,

$$R' = \frac{B_s}{2} = 0.66 \ m \tag{178}$$

Table 4: The start (S) and end (E) pose of the considered scenario. This type of particular scenario is useful for illustrating the kind of paths that are optimal depending on where the rover starts relative to a desired goal.

Point	Coordination
(x_S, y_S, θ_S)	$\left(x, y, \dfrac{\pi}{4}\right)$
(x_E, y_E, θ_E)	$(0,0,0)$

Inspecting Fig. 20 and Fig. 32 reveals that:

$$\tilde{v}_{max} = 1$$
$$\tilde{v}_{R'} = \frac{2}{3} \tag{179}$$
$$\tilde{\omega}_{max} = 1$$
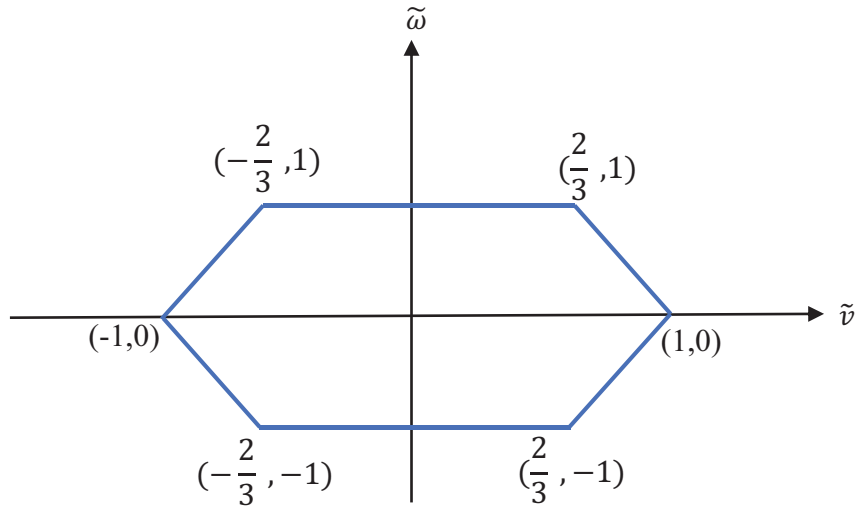
Figure 32: The example control space considered for the numerical scenario

There are *three main steps* for producing the optimal map shown in Fig. 41:

I Generating all the extremal paths reported in Table 3 and their subpaths by using *turtle library* in Python.

II Finding the feasibility region for each of the paths for the considered scenario. Also, calculating the cost of the paths.

III Comparing the cost of the paths and drawing the optimal map.

Step I and *step II* are explained in subsection 5.3. Also, *Step III* is performed in subsection 5.4.

5.3 Generating Extremals and Finding the Feasibility Regions

An example for a subpath of each *generic Turns*, *singular*, and *generic TST* paths are plotted in Fig. 33, Fig. 34, and Fig. 35, respectively. Also, a sample of a CLC path which is a subpath of *generic TST paths* is shown in Fig. 36. All of these paths are generated by using *turtle* library in Python.
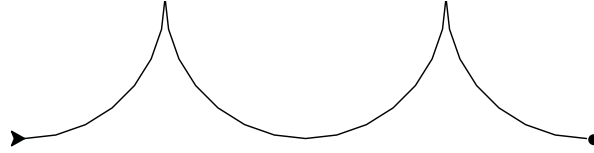
Figure 33: $\curvearrowright_{\frac{\pi}{2}} \overset{b}{\curvearrowright}_{\pi} \curvearrowright_{\frac{\pi}{2}}$ path. It is going from (x,y,0) to (0,0,0) which is denoted by ●.

Figure 34: $\Downarrow \overset{b}{\curvearrowright}_{\frac{\pi}{2}} \curvearrowright_{\frac{\pi}{2}} \Uparrow \curvearrowright_{\frac{\pi}{2}} \overset{b}{\curvearrowright}_{\frac{\pi}{2}}$ path. It is going from (x,y,0) to (0,0,0) which is denoted by ●.
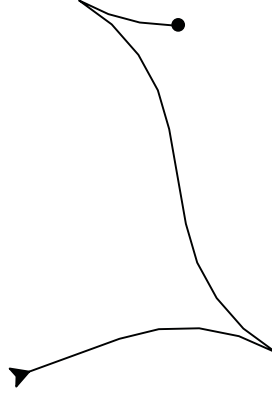
Figure 35: $\Uparrow\leftusr\overset{b}{\leftusr} \Downarrow\overset{b}{\leftusr}\leftusr$ path. It is going from (x, y, θ) to (0,0,0) which is denoted by ●.
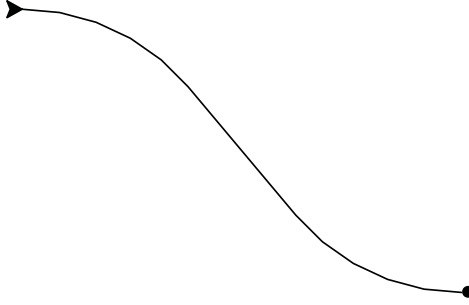
Figure 36: $\leftusr\Uparrow\leftusr$ path. It is going from (x, y, θ) to (0,0,0) which is denoted by ●.

Feasibility Regions: To obtain the feasibility region the end pose of the paths are forced to be at $(x_E, y_E, \theta_E) = (0, 0, 0)$. Then, the turns and straight line maneuvers are allowed to vary in their acceptable range for the considered path. Afterwards, θ_S is checked. If θ_S is $\pi/4$ with an small error (ϵ_{th} = 0.1 degree which is ϵ_{th} = 0.0006π radian), (x_S, y_S) is saved. Therefore, the *feasibility regions/lines* for each of the *generic Turns*, *singular*, and *generic TST* paths or their subpaths are obtained.

In the following the *algorithms* utilized to obtain the feasibility regions/lines for the paths (and their subpaths) shown in Fig. 33, Fig. 34, and Fig. 35 are explained. The algorithms of all remaining paths and their subpaths are obtained with the same methodology.

Algorithm 1 uses Lemma 7 to generate a table including L_D and the related β_c. The table produced by this algorithm is used in Algorithm 4 which calculates the feasibility regions for subpaths of Fig. 35 (an example of *generic TST* paths). In addition, Algorithm 2 and Algorithm 3 are utilized to obtain the feasibility region/line for subpaths of Fig. 33 (an example of *generic Turns*) and subpaths of Fig. 34 (an example of *singular*) paths, respectively. In all these cases, subpaths are defined such that the first and last maneuvers

66

need not be complete (by Definition 6).

Algorithm 1: Algorithm to create the L_D table

Result: A table that includes the angles with respect to the η−line and their related straight line lenght, for complete manuevers of various λ_0.

for λ_0 *in* $(0,1)$ **do**

    β_c= Eq. (161) for the given λ_0;

    η_c= Eq. (162) for the given λ_0;

    L_D= Eq. (160) for the caluclated β_c and η_c;

    Save $[\beta_c, L_D]$

end

Algorithm 2: Algorithm to obtain the feasibility line shown in Fig. 37

Result: Feasibility line and the related costs for $\curvearrowright\overset{b}{\curvearrowleft}_\pi\curvearrowright$ path (subpaths of Fig. 33)

Note: $\Delta\theta_1$, $\Delta\theta_2$, and $\Delta\theta_3$ are the turns for $\curvearrowright$, $\overset{b}{\curvearrowleft}_\pi$, and $\curvearrowright$, respectively.;

for $\Delta\theta_1$ *in* $\left[0, \dfrac{\pi}{2}\right]$ **do**

    for $\Delta\theta_3$ *in* $\left[0, \dfrac{\pi}{2}\right]$ **do**

        $\Delta\theta_2 = \pi$;

        Generate the $\curvearrowright\overset{b}{\curvearrowleft}_\pi\curvearrowright$ path by using *Python turtle* while the end point is forced to have $(x_E, y_E, \theta_E)=(0,0,0)$;

        Get $\{x_S, y_S, \theta_S\}$ of the generated path;

        if $\left|\theta_S - \dfrac{\pi}{4}\right| < \epsilon_{th}$ **then**

            Save the $\{x_S, y_S\}$;

            Cost[a]=$\Delta\theta_1+\Delta\theta_2+\Delta\theta_3$;

            Save the Cost;

        end

    end

end

---

[a]Recall, for all turns, $\omega_z=\tilde{\omega}_{max} = 1\dfrac{rad}{s}$.

Algorithm 3: Algorithm to obtain the feasibility line shown in Fig. 38

Result: Feasibility line and the related costs for $\Downarrow\overset{b}{\curvearrowright}_{\frac{\pi}{2}}\curvearrowleft_{\frac{\pi}{2}}\Uparrow\curvearrowleft_{\frac{\pi}{2}}\overset{b}{\curvearrowright}$ path (subpath of Fig. 34)

Note: $\Delta\theta_1$, $\Delta\theta_2$, $\Delta\theta_3$, and $\Delta\theta_4$ are the turns for $\overset{b}{\curvearrowright}_{\frac{\pi}{2}}$, $\curvearrowleft_{\frac{\pi}{2}}$, $\curvearrowleft_{\frac{\pi}{2}}$, and $\overset{b}{\curvearrowright}$, respectively. Also, ΔD_1 and ΔD_2 are the length for $\Downarrow$ and $\Uparrow$, respectively. Furthermore, in the following algorithm $+\infty$ is replaced with a sufficiently large number to avoid an infinite loop.;

for $\Delta\theta_4$ *in* $\left[0,\dfrac{\pi}{2}\right]$ **do**

    for ΔD_1 *in* $[0,+\infty)$ **do**

        for ΔD_2 *in* $[0,+\infty)$ **do**

            $\Delta\theta_1 = \Delta\theta_2 = \Delta\theta_3 = \dfrac{\pi}{2}$;

            Generate the $\Downarrow\overset{b}{\curvearrowright}_{\frac{\pi}{2}}\curvearrowleft_{\frac{\pi}{2}}\Uparrow\curvearrowleft_{\frac{\pi}{2}}\overset{b}{\curvearrowright}$ path by using *Python turtle* while the end point is forced to have $(x_E, y_E, \theta_E) = (0,0,0)$;

            Get $\{x_S, y_S, \theta_S\}$ of the generated path;

            if $\left|\theta_S - \dfrac{\pi}{4}\right| < \epsilon_{th}$ **then**

                Save the $\{x_S, y_S\}$;

                Cost* = $\Delta\theta_1 + \Delta\theta_2 + \Delta\theta_3 + \Delta\theta_4 + \Delta D_1 + \Delta D_2$;

                Save the Cost;

            end

        end

    end

end

*Recall, for $\Uparrow$ and $\Downarrow$, $v = \tilde{v}_{max} = 1\ \dfrac{m}{s}$. Also, for all turns, $\omega_z = \tilde{\omega}_{max} = 1\dfrac{rad}{s}$.

Algorithm 4: Algorithm to obtain the feasibility region shown in Fig. 39

Result: Feasibility region and the related costs for $\Uparrow \curvearrowright \overset{b}{\curvearrowright} \Downarrow \overset{b}{\curvearrowleft} \curvearrowleft$ path

Note: $\Delta\theta_1$, $\Delta\theta_2$, $\Delta\theta_3$, and $\Delta\theta_4$ are the turns for $\curvearrowright$, $\overset{b}{\curvearrowright}$, $\overset{b}{\curvearrowleft}$, and $\curvearrowleft$, respectively. Also, ΔD_1 and ΔD_2 are the length for $\Uparrow$ and $\Downarrow$, respectively. Also, $\Delta\theta_1$, $\Delta\theta_2$, $\Delta\theta_3$, and ΔD_2 are complete maneuvers. ;

for $\Delta\theta_1$ *in* $\left(0, \dfrac{\pi}{2}\right)$ **do**

    L_D is obtained by lookup table (Algorithm 1) for the $\beta_c = \dfrac{\pi}{2} - \Delta\theta_1$.*;

    $\Delta D_2 = L_D$;

    for ΔD_1 *in* $[0, \Delta D_2]$ **do**

        for $\Delta\theta_4$ *in* $[0, \Delta\theta_1]$ **do**

            $\Delta\theta_2 = \Delta\theta_3 = \Delta\theta_1$;

            Generate the $\Uparrow \curvearrowright \overset{b}{\curvearrowright} \Downarrow \overset{b}{\curvearrowleft} \curvearrowleft$ path by using *Python turtle* while the end point is forced to have $(x_E, y_E, \theta_E) = (0, 0, 0)$;

            Get $\{x_S, y_S, \theta_S\}$ of the generated path;

            if $\left|\theta_S - \dfrac{\pi}{4}\right| < \epsilon_{th}$ **then**

                Save the $\{x_S, y_S\}$;

                Cost**$= \Delta\theta_1 + \Delta\theta_2 + \Delta\theta_3 + \Delta\theta_4 + \Delta D_1 + \Delta D_2$;

                Save the Cost;

            end

        end

    end

end

*Consider the complete $\curvearrowright$ maneuver in Fig. 30. Over the course of the complete $\curvearrowright$, β changes from $\dfrac{\pi}{2}$ to β_c. Therefore, $\Delta\theta_1 = \dfrac{\pi}{2} - \beta_c$, or equivalently $\beta_c = \dfrac{\pi}{2} - \Delta\theta_1$.

**Recall, for $\Uparrow$ and $\Downarrow$, $v = \tilde{v}_{max} = 1\ \dfrac{m}{s}$. Also, for all turns, $\omega_z = \tilde{\omega}_{max} = 1\dfrac{rad}{s}$.
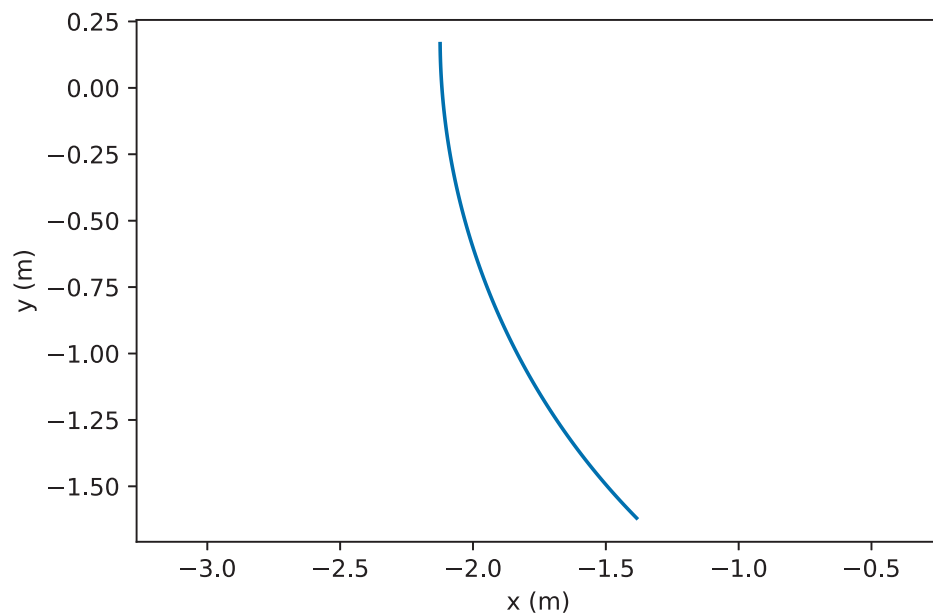
Figure 37: Resulting feasibility line for all subpaths of ⌐⌐ᵇ⌐π⌐.
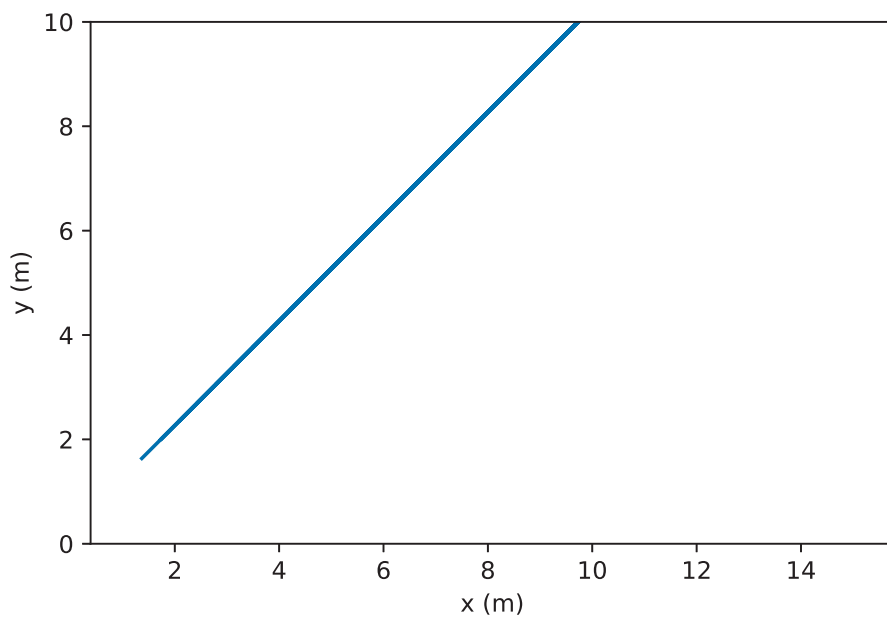
Figure 38: Resulting feasibility line for all subpaths of ⇓⌐ᵇ⌐$\frac{\pi}{2}$⌐$\frac{\pi}{2}$⇑⌐$\frac{\pi}{2}$⌐ᵇ. The plot is trimmed for y values.
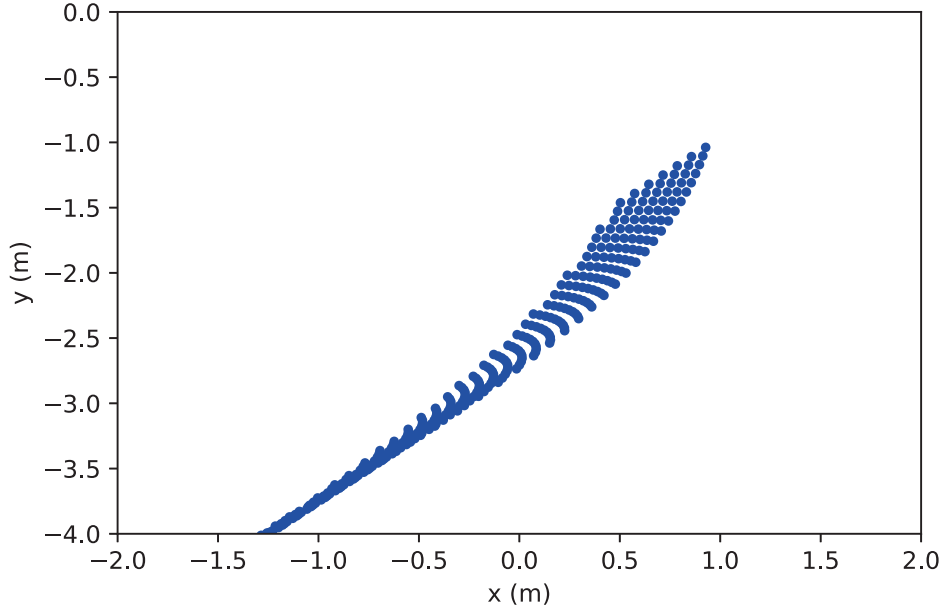
Figure 39: Resulting feasibility region for all subpaths of ⇑↝⤳ ⇓⤺↶. The plot is trimmed for y values.

Also, the feasibility region for the CLC (Fig. 36) staring points is shown in Fig. 40.
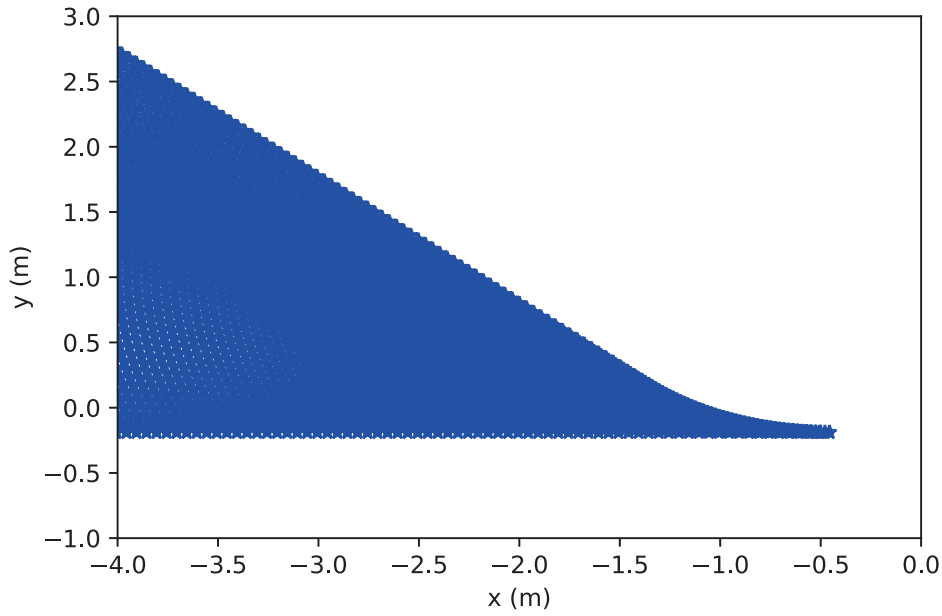
Figure 40: Resulting feasibility region for all subpaths of ↝⇑↶. The plot is trimmed for x values.

As explained in subsection 4.1, *whirls* have the structure of 'roll-and-catch'. Rolls are R'-circular arcs that finally will be followed by a catch which is a circular arc by $R \in [0, R')$. Therefore, the feasibility region for the *whirls* should be produced by varying the angles for each part (for rolls and catch) while considering their proper turning radii.

Considering the scenario, the feasibility regions for the starting points of the extremals are sketched and the related costs are calculated. In the following subsection, the costs are compared to determine the path with the minimum cost when starting in different parts of the $x - y$ plane in 2D.

5.4 Map of the Optimal Paths

The subsequent process for the considered scenario is followed to compare the costs and draw the map (Fig. 41) of the optimal paths:

- The parameters reported in Table 5 are considered for the scenario (that was introduced in subsection 5.2).

- Algorithm 5 is applied to all the feasibility regions obtained in subsection 5.3: in order to compare the costs of extremal paths, they should have the same (x, y) for the samples/grids. Therefore, this algorithm is used to create those samples/grids by using the data of the existing samples in the feasibility region of each path.

- Algorithm 6 is applied to the data produced in the previous step. Therefore, the minimum-cost path for each (x, y) is chosen and plotted in Fig. 41.

Table 5: The parameters considered for the algorithms to obtain the map (Fig 41).

Parameter	Value
x_{step}	$0.1\ m$
y_{step}	$0.1\ m$
$\{x_{\text{min}}, y_{\text{min}}\}$	$\{-5\ m, 5\ m\}$
$\{x_{\text{max}}, y_{\text{max}}\}$	$\{-5\ m, 5\ m\}$
n_{NN}	5-10

Algorithm 5: Grid producing algorithm for an extremal path.

Load the data of feasibility region for the extremal path;

for x in $[x_{step}.floor(x_{minfeas}/x_{step}), x_{maxfeas}]^*$ *with* x_{step} **do**

    for y in $[y_{step}.floor(y_{minfeas}/y_{step}), y_{maxfeas}]$ *with* y_{step} **do**

        if *(x,y) is inside of the feasibility region* **then**

            Select n_{NN} nearest neighbors and get their $\Delta\theta$s and ΔDs;

            Do a local search to obtain an extremal path that goes from $(x, y, \frac{\pi}{4})$ to $(0, 0, 0)$.**;

            Save the position and cost ($\{x, y, \text{cost}\}$) of the found extremal path;

        end

    end

end

$^*\{x_{minfeas}, y_{minfeas}\}$ and $\{x_{maxfeas}, y_{maxfeas}\}$ are the minimum and maximum $\{x, y\}$ for the feasibility region of the extremal path.;

**The errors considered to terminate the local search are 0.05 m for the distance and 0.05^o for the heading angle.;

Algorithm 6: Comparing the costs and drawing the optimal map.

Apply Algorithm 5 to all the feasibility regions obtained in subsection 5.3;

for x in $[x_{step}.floor(x_{min}/x_{step}), x_{max}]$ *with* x_{step} **do**

    for y in $[y_{step}.floor(y_{min}/y_{step}), y_{max}]$ *with* y_{step} **do**

        Find all the extremal paths that have (x, y) and make a *list* of them;

        Choose the path from the *list* with minimum cost;

        Plot the (x, y) and assign it to the selected path;

    end

end
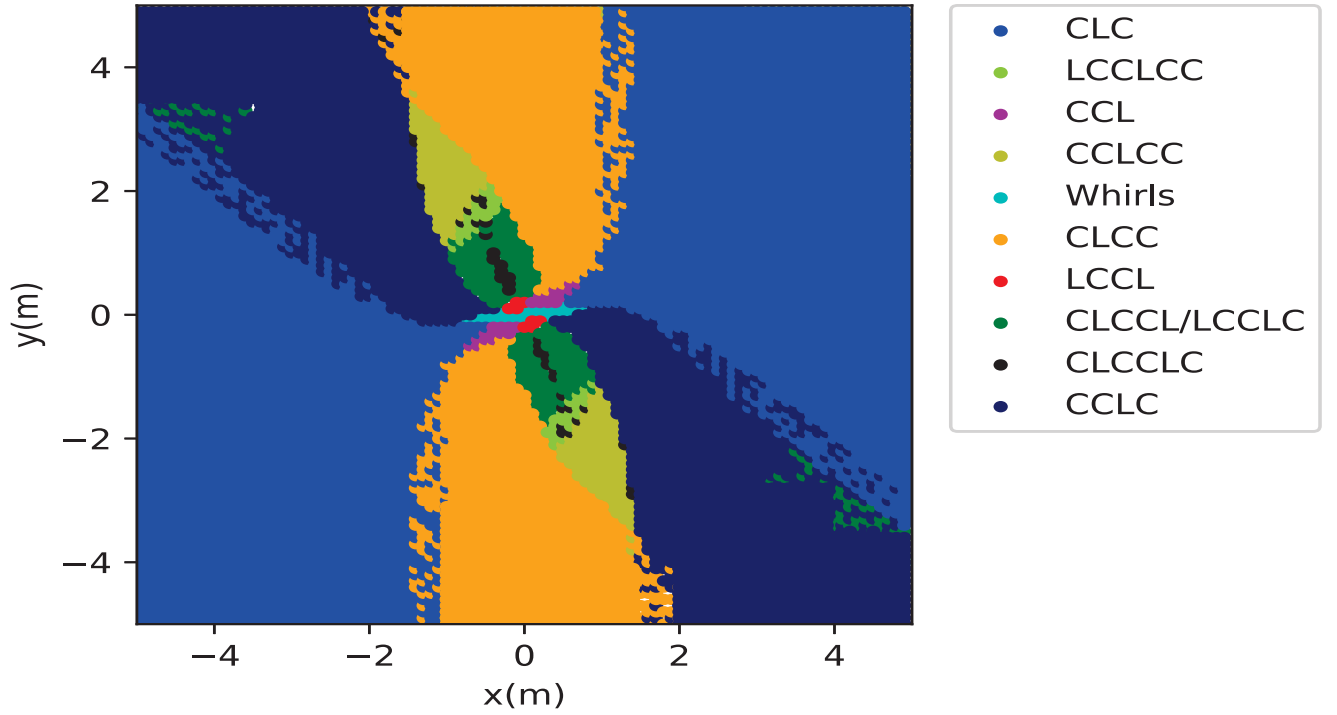
Figure 41: Map indicating the optimal paths to the origin when starting at different $(x, y, \frac{\pi}{4})$ on the $x - y$ plane.

The legends for the optimal paths shown in Fig. 41 are indicated in Table 6 by using the maneuver symbols defined in Table 1. As it can be seen from the map, there are three types of paths that cover the largest areas of the figure and extend to its boundaries. They are as follows:

- CLC

- CCLC

- CLCC

where "C" stands for R'-circular arcs and "L" stands for lines. To interpret the map, consider as an example the coordination of (4,1). Based on the map, the *optimal* path to go from $(4, 1, \pi/4)$ to $(0, 0, 0)$ is a CLC path. It should be mentioned that each of the categories for the paths that were mentioned includes several path types. For example, the CLC (true blue region) path in the map includes all the path types that are reported in Table 6 and shown in Fig. 42.
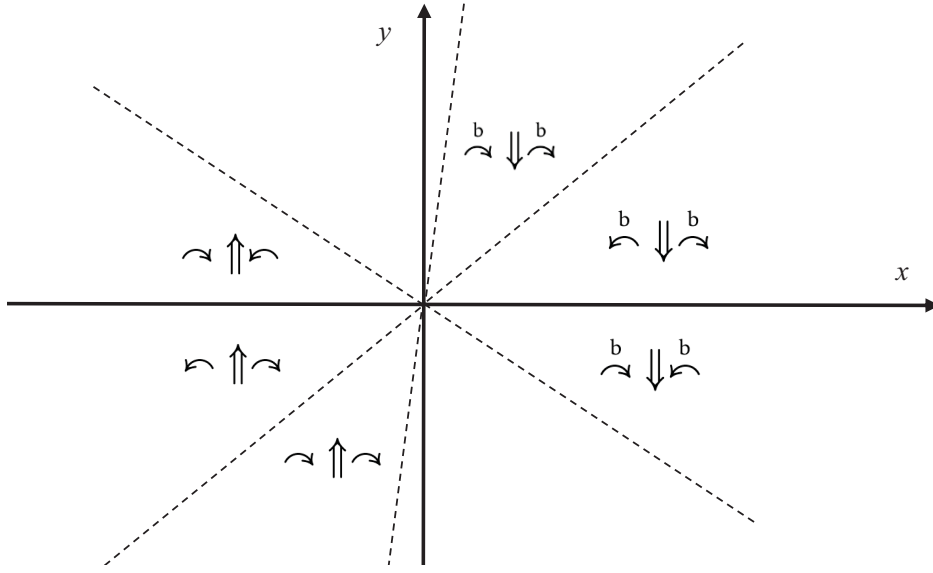
Figure 42: The paths related to the true blue region (CLC) in Fig. 41

Table 6: The correspondent maneuver symbols for the paths shown in Fig. 41.

Path	Arrows	
CLC	⤳ᵇ ⇓ ⤳ᵇ	↶ ⇑ ↷
	↶ᵇ ⇓ ⤳ᵇ	⤳ ⇑ ↶
	⤳ᵇ ⇓ ⤳ᵇ	⤳ ⇑ ⤳
CCL	⤳ᵇ ⤳ ⇑	⤳ ⤳ ⇓ᵇ
LCCL	⇓ ⤳ᵇ ⤳ ⇑	⇑ ↶ ⤳ ⇓ᵇ
CLCC	↶ᵇ ⇓ ⤳ᵇ ⤳	↶ ⇑ ⤳ ⤳ᵇ
CCLC	⤳ ⤳ ⇓ ↶ᵇ	⤳ ⤳ ⇑ ↶ᵇ
CCLCC	⤳ᵇ ⤳ ⇑ ↶ ↶ᵇ	⤳ ⤳ ⇓ᵇ ↶ ↶ᵇ
LCCLCC	⇓ ↶ᵇ ⤳ ⇑ ↶ ↶ᵇ	⇑ ↶ ⤳ᵇ ⇓ ↶ ↶ᵇ
LCCLC	⇓ ↶ᵇ ⤳ ⇑ ↶ᵇ	⇑ ↶ ⤳ᵇ ⇓ ↶ᵇ
CLCCL	↶ᵇ ⇓ ⤳ ⤳ ⇑ᵇ	↶ ⇑ ⤳ ⤳ ⇓ᵇ

Whirls and their feasibility regions are explained in subsection 4.1 and 5.3, respectively. As mentioned before, *whirls* have the structure of 'roll-and-catch'; R'-circular arcs, starting from the initial pose, eventually followed by a turning by $R \in [0, R')$ which puts the rover to the final pose. The *Cyan* color in the map (see Fig. 41) includes two types of whirls:

- Whirls that are closer to the origin just consist of catch part

75

- The other whirls which are far enough from the origin include a roll (a circular arc with R') and a catch part.

More discussion on the map: Since there are some similarities between the dynamic of differential drive rovers and skid-steer rovers, and also Balkcom Mason in [50] performed the similar scenario of Table 4 for differential drive rovers, in the following similarities and differences between the results are discussed to provide more notion to the path planning problem. Accordingly, the map (Fig. 41) and figure 12 of ref. [50] are compared. In both figures, there is a type of path which is dominant (covers the most region): PLP for differential drive and CLC for skid-steer rovers. Also, the comparison reveals that instead of R'-circular arcs ('C'), differential drive rovers do point turns ('P'). Moreover, it seems that the behavior of the paths are almost similar. For example, instead of Line-Point turn-Line (LPL) for differential drive, the skid-steer rovers perform LCCL. Also, instead of PLPL for differential drive rovers, skid-steer rovers do CLCCL.

Expectation/Prediction about other scenarios: We expect that for other scenarios, different than the scenario that was mentioned in Table 4, the CLC paths will be dominant in the correspondent optimal map. The reason is that avoiding extra turnings and instead doing straight lines will result in more efficient paths. Therefore, for those regions that CLC paths are feasible, they should be the most efficient path. It should be mentioned that the explained regions will happen when the starting pose is far enough from the goal pose.

As mentioned, CLC paths are one of the most prevalent path types in the *optimal map* (Fig. 41). Also, separate earlier phase of this research focused on predefined classes of paths (CC and CLC). Furthermore, there are several experimental tests' results for the predefined class of paths. Hence, in the following chapter, the analytical approach and experimental results for the predefined class of paths are discussed.

6 Energy-Efficient Path Planning for the Predefined Class of Paths
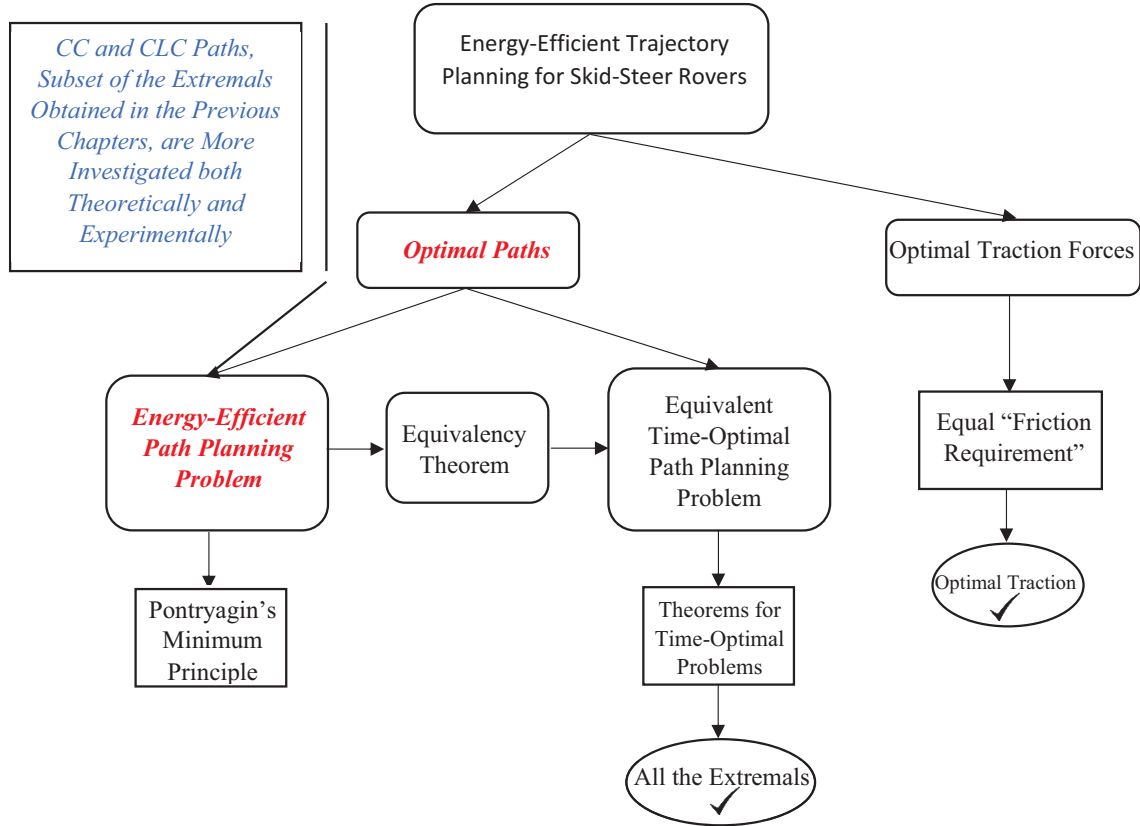
Figure 43: The tasks performed in this chapter are highlighted.

This chapter reports all the *analytical, numerical, and experimental* research on predefined classes of paths (CC and CLC).

In subsection 6.1 path planning on *hard ground without lateral slippage* is discussed. In this subsection the *analytical* approach is used to find the energy-efficient path for the predefined class of paths. Subsection 6.2 covers both *theoretical* and *experimental* results for the energy-efficient path planning problem. It should be mentioned that the *lateral slippage* is considered in the analyses and all the tests are performed on *hard ground*. Also, there are some discussions about the experimentally obtained power for skid-steer rovers on hard ground.

Since all the theoretical and analytical approaches performed in this thesis use the existing power model which is designed for hard ground, several experimental tests are performed on another terrain, loose soil, and compared to the results of the approaches to show the differences (subsection 6.3). These comparisons can be used as a proper starting point for future work for energy-efficient path planning of skid-steer rovers on loose soil.

6.1 Energy-Efficient Path Planning on Hard Ground by Using KKT Conditions without Considering the Lateral Slippage

The contributions and the work of this subsection are stated in the following:

- A thorough analytical approach using Karush-Kuhn-Tucker (KKT) [96] conditions is developed for finding energy-efficient paths for skid-steer rovers. The globally optimal answer from among a predefined class of paths can be obtained for each scenario by comparing the KKT candidates.

- It is shown by analysis that there are scenarios in which CLC paths are more energy-efficient than PLP paths.

- It is shown that when optimizing CLC paths using KKT conditions analytically (utilizing an existing power model developed by Morales et al. ([87] [90]) circular arcs of radius W/2 (where W is the distance between two wheels' centers along the rover width) make up the optimal 'C' segments. With no lateral slippage, W/2=R'.

In 6.1.1 the optimal path planning problem is defined and the assumptions are presented. In 6.1.2 this optimization problem is solved analytically. Subsection 6.1.3 presents numerical as well as experimental results comparing CLC paths to PLP paths. Finally, 6.1.4 summarizes the conclusions.

6.1.1 Problem Statement

Problem: The following optimization problem is investigated to obtain the optimally energy-efficient path.
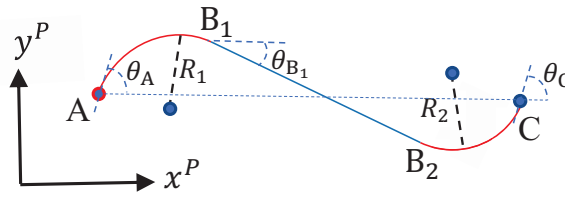
Figure 44: A CLC path including two circular arcs and a line segment

$$
\begin{aligned}
&\underset{R_1, R_2, \theta_{B_1}}{\text{minimize}} \quad E \\
&\text{subject to} \quad h_i = 0, i = 1..n \\
&\qquad\qquad\; g_j \leq 0, j = 1..m \\
&\qquad\qquad\; \text{and it is assumed that } |V_l| + |V_r| = 2v_c
\end{aligned}
\tag{180}
$$

where E, h_i, and g_j are the energy consumed during the path, and the equality constraints and inequality constraints (defined in subsequent subsections of section 6.1.2), respectively. Also, n and m are the numbers of equality and inequality constraints, respectively.

In addition, R_k ($k = 1, 2$) and θ_{B_1} are the turning radii of the circles and angle of the straight line (with respect to a path-defined coordinate system) in Fig. 44, respectively.

Assumptions: The assumptions are the same of those mentioned in subsection 2.1. Except that just forward motion is allowed for the CLC paths in the following analysis. Also, a further assumption is employed purely to simplify the analysis of the example cases studied:

- Both θ_A and θ_C are in the same quadrant

It should be mentioned again that before finding general arc-based paths (Chapter 2 to 5), the solutions were restricted to predefined classes of paths that are combinations of circular arcs and line segments (i.e. circle-line-circle, CLC, paths and circle-circle, CC, paths).

6.1.2 Analytical Approach to Find an Optimal Path for the Predefined Classes of CLC and CC Paths

In the following, first the power model is described. Then, the analytical approach to find optimally energy-efficient CLC and CC paths is presented.

6.1.2.1 Power and Energy Model for a Circular Arc
When there is no lateral slippage, B_s is equal to W. Therefore, Eq. (42) is converted to:

$$
P = \begin{cases} 4\mu\dfrac{v_c}{W}pL + 2Gv_c & \text{if } 0 \le R \le \dfrac{W}{2} \\[2mm] 2\mu\dfrac{v_c}{R}pL + 2Gv_c & \text{if } R > \dfrac{W}{2} \end{cases} \tag{181}
$$

From Theorem 1, it is known that for the skid-steer rover, when $0 \le R < W/2$, V_r and V_l have opposite signs. Therefore, ω_z and P (Eq. (181)) are constant. Also, when $R > W/2$ (i.e. forward motion) V_r and V_l have the same sign. Hence, v is constant and P is a function of R.

In addition it is known that the energy is $E = \int P \, dt$. Thus, by using Eq. (181) the energy for a circular arc (with constant turning radius) is obtained as follows:

$$
E_C = \begin{cases} \left(4\mu\dfrac{v_c}{W}pL + 2Gv_c\right)\left|\dfrac{\Delta\theta}{\omega_z}\right| & \text{if } 0 \le R \le \dfrac{W}{2} \\[3mm] \left(2\mu\dfrac{v_c}{R}pL + 2Gv_c\right)\left|\dfrac{R\Delta\theta}{v_c}\right| & \text{if } R > \dfrac{W}{2} \end{cases} \tag{182}
$$

Note: *More general definition of E_C (when considering the lateral slippage) is presented in 6.2.2.1.*

6.1.2.2 Mathematical Formulations of Circle-Line-Circle Paths
The CLC path is shown in Fig. 45. Using Eq. (181), the energy for the path including energy of circle 1 (E_{C_1}), energy of line (E_L), and energy of circle 2 (E_{C_2}) is obtained as follows:

$$
E_{CLC} = E_{C_1} + E_L + E_{C_2} \tag{183}
$$

79

with E_{C_1} and E_{C_2} computed using Eq. (182). As E_C is not differentiable at $R = W/2$ (see Eq. (182)), paths with different possible combinations of R_1 and R_2 (see Table 7) must be optimized and compared to select the globally minimum energy path.
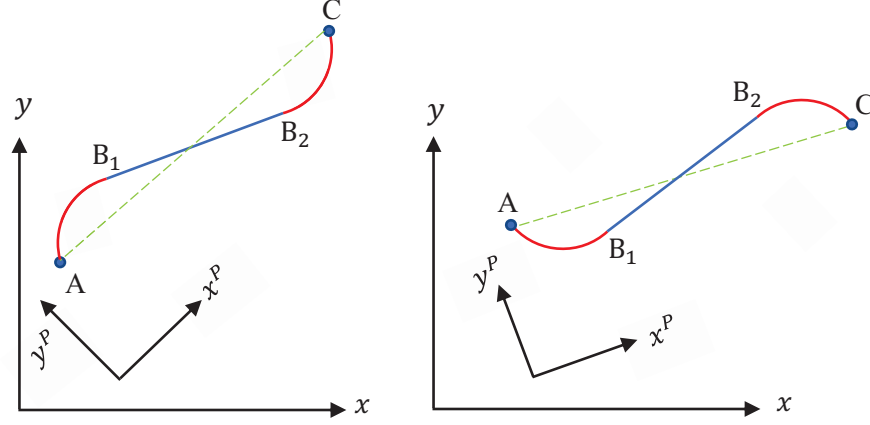
Figure 45: CLC paths between a starting and end point in the global and path-defined coordinate system. The axes x^P and y^P indicate the path-defined coordinate system. Also, axes x and y indicate the global coordinate system.

Table 7: Different intervals for the turning radii

Combination	R_1	R_2
1st	$(0, W/2]$	$(0, W/2]$
2nd	$(0, W/2]$	$(W/2, +\infty)$
3rd	$(W/2, +\infty)$	$(0, W/2]$
4th	$(W/2, +\infty)$	$(W/2, +\infty)$

To show how the mathematical calculations should be performed, the optimization problem for the 1st combination (Eq. (184)) is described in the following. Using the same method, the optimization problem for the other combinations (2nd, 3rd, and 4th) are solved.

$$\begin{aligned}
\underset{R_1, R_2, \theta_{B_1}^P}{\text{minimize}} \quad & E_{\text{CLC}} \\
\text{subject to} \quad & h_i = 0, i = 1, 2 \\
& 0 < k\theta_{B_1}^P \le \frac{\pi}{2}, 0 < R_j \le \frac{W}{2} (j = 1, 2)
\end{aligned} \tag{184}$$

80

The inequality constraints on R_1 and R_2 are considered based on the combination mentioned in Table 7. The inequality constraint on $\theta_{B_1}^P$ is based on the constraints imposed on start and end poses (Eq. (188)) and inspection of the resulting paths (Fig. 45); $\theta_{B_1}^P$ angles outside these bounds cannot smoothly connect circle 1 to circle 2, and additional loops ($|\theta_{B_1}^P| > 2\pi$) are obviously not optimal and need not be considered. In addition, E_{CLC} (which is obtained from Eq. (182) and Eq. (183) when $0 < R_j \leq W/2$) and the equality constraints (h_i) which define the path shape are as follows:

$$E_{\text{CLC}} = \left(4\mu\frac{v_c}{W}pL + 2Gv_c\right)\left|\frac{\theta_{B_1}^P - \theta_A^P}{\omega_z}\right|$$
$$+ \left(4\mu\frac{v_c}{W}pL + 2Gv_c\right)\left|\frac{\theta_{B_1}^P - \theta_C^P}{\omega_z}\right| \tag{185}$$
$$+2G\sqrt{(x_{B_1}^P - x_{B_2}^P)^2 + (y_{B_1}^P - y_{B_2}^P)^2}$$

$$h_1 = (x_{B_2}^P - x_{B_1}^P)^2$$
$$- \cos^2\theta_{B_1}^P\left((x_{B_2}^P - x_{B_1}^P)^2 + (y_{B_2}^P - y_{B_1}^P)^2\right) \tag{186}$$
$$h_2 = y_{B_2}^P - y_{B_1}^P - (x_{B_2}^P - x_{B_1}^P)\tan\theta_{B_1}^P$$

where

$$x_{B_1}^P = x_A^P + kR_1(-\sin\theta_A^P + \sin\theta_{B_1}^P)$$
$$y_{B_1}^P = y_A^P + kR_1(\cos\theta_A^P - \cos\theta_{B_1}^P)$$
$$x_{B_2}^P = x_C^P + kR_2(\sin\theta_C^P - \sin\theta_{B_1}^P) \tag{187}$$
$$y_{B_2}^P = y_C^P + kR_2(-\cos\theta_C^P + \cos\theta_{B_2}^P)$$

$$k = -\frac{\sin\theta_A^P}{|\sin\theta_A^P|}, \ \theta_A^P \neq 0 \tag{188}$$
$$\{\theta_A^P, \ \theta_C^P \in (0, \frac{\pi}{2}]\} \text{ Or } \{\theta_A^P, \ \theta_C^P \in [-\frac{\pi}{2}, 0)\}$$

which means θ_A^P and θ_C^P are either both in the first or both in the fourth quadrant of path-defined coordinate system (see Fig. 45). Karush-Kuhn-Tucker (KKT) [96] conditions are used to find the optimal value for the energy.

As KKT conditions are only necessary (but not sufficient) for optimality, all the candidate cases obtained for our problem are evaluated to identify the best candidate.

The Lagrange equation [96] is written as follows:

$$L = E_{\text{CLC}} + \lambda_1 h_1 + \lambda_2 h_2 + \mu_1(\epsilon_1 - k\theta_{B_1}) + \mu_2(k\theta_{B_1} - \frac{\pi}{2})$$
$$+ \mu_3(\epsilon_2 - R_1) + \mu_4(\epsilon_3 - R_2) + \mu_5(R_1 - \frac{W}{2}) + \tag{189}$$
$$\mu_6(R_2 - \frac{W}{2}), \ \mu_i \geq 0, \ i = 1..4$$

It should be noted that $\epsilon_j(j = 1, 2, 3)$ are infinitesimal values that in their limits approach to zero. They are considered to convert the strict to non-strict inequities. For example, ϵ_1 converts the inequality equation of $0 < k\theta_{B_1}^P$ to $\epsilon_1 \leq k\theta_{B_1}^P$ for using in KKT conditions.

Therefore, to find the stationary points the following equations should be solved together:

$$\frac{\partial L}{\partial R_1} = 0, \frac{\partial L}{\partial R_2} = 0, \frac{\partial L}{\partial \lambda_1} = 0, \frac{\partial L}{\partial \lambda_2} = 0, \frac{\partial L}{\partial \theta_{B_1}^P} = 0,$$

$$\mu_1(\epsilon_1 - k\theta_{B_1}) = 0, \mu_2(k\theta_{B_1} - \frac{\pi}{2}) = 0,$$

$$\mu_3(\epsilon_2 - R_1) = 0, \mu_4(\epsilon_3 - R_2) = 0, \mu_5(R_1 - \frac{W}{2}),$$

$$\mu_6(R_2 - \frac{W}{2}) = 0$$

$$\mu_1 \geq 0, \ \mu_2 \geq 0, \ \mu_3 \geq 0, \ \mu_4 \geq 0, \ \mu_5 \geq 0, \ \mu_6 \geq 0,$$

(190)

6.1.2.3 Logical Analysis of KKT Conditions for the CLC Paths To solve Eq. (190), a logical evaluation should be done for the inequality constraints. Nominally, 64 (2^6) cases are to be considered covering each i ($i = 1...6$) (see Eq. (190)) being either greater than or equal to zero. However, some of these cases can immediately be deemed impossible in general (R cannot simultaneously both approach 0 and W/2, θ cannot both simultaneously approach 0 and $\pi/2$). As a result, it is impossible for more than 3 μ's to be non-zero simultaneously. Similarly, there are only 8 (2^3) combinations of valid cases with exactly 3 non-zero μ's, and 12 ($2 \times 2^2 + 2 \times 2^1$) valid cases with exactly 2 non-zero μ's. All six possible cases with exactly 1 non-zero μ are generally admissible. Table 8 summarizes which candidate solutions to the optimization are potentially valid, based on this reasoning.

82

Table 8: Logical Table for the Inequality Coefficients

Case	μ_1	μ_2	μ_3	μ_4	μ_5	μ_6
1	0	0	0	0	0	0
2	0	0	0	+	0	0
3	0	0	+	0	0	0
4	0	+	0	0	0	0
5	+	0	0	0	0	0
6	0	0	+	+	0	0
7	0	+	0	+	0	0
8	+	0	0	+	0	0
9	+	0	+	0	0	0
10	0	+	+	0	0	0
11	+	0	+	+	0	0
12	0	+	+	+	0	0
13	0	0	0	0	+	0
14	0	0	0	+	+	0
15	0	+	0	0	+	0
16	+	0	0	0	+	0
17	0	+	0	+	+	0
18	+	0	0	+	+	0
19	0	0	0	0	0	+
20	0	0	+	0	0	+
21	0	+	0	0	0	+
22	+	0	0	0	0	+
23	+	0	+	0	0	+
24	0	+	+	0	0	+
25	0	0	0	0	+	+
26	0	+	0	0	+	+
27	+	0	0	0	+	+

Three of the cases (see Table 8) are explained in the following and the rest are elaborated in Appendix C.

Case 1: $\left(\mu_1 = 0, \mu_2 = 0, \mu_3 = 0, \mu_4 = 0, \mu_5 = 0, \mu_6 = 0\right)$
Eq. (190) should be solved for $\mu_1 = 0$, $\mu_2 = 0$, $\mu_3 = 0$, $\mu_4 = 0$, $\mu_5 = 0$, and $\mu_6 = 0$. Then, the answers should be checked for

$$0 < k\theta_{B_1} \leq \frac{\pi}{2}, \ 0 < R_1 \leq \frac{W}{2}, 0 < R_2 \leq \frac{W}{2} \tag{191}$$

Accordingly, R_1^*, R_2^*, and $\theta_{B_1}^{*P}$ will be obtained.
Case 2: $\left(\mu_1 = 0, \mu_2 = 0, \mu_3 = 0, \mu_4 > 0, \mu_5 = 0, \mu_6 = 0\right)$

$$\mu_4 > 0 \Rightarrow R_2^* = \epsilon_3 \tag{192}$$

Eq. (190) should be solved while $\mu_1 = 0$, $\mu_2 = 0$, $\mu_3 = 0$, $R_2 = \epsilon_3$, $\mu_5 = 0$, and $\mu_6 = 0$. Also, the following conditions should be checked.

$$0 < k\theta_{B_1} \le \frac{\pi}{2}, \ 0 < R_1 \le \frac{W}{2}, \mu_4 > 0 \tag{193}$$

Accordingly, R_1^*, R_2^*, and $\theta_{B_1}^{*P}$ will be obtained.

Case 3: $\left(\mu_1 = 0, \mu_2 = 0, \mu_3 > 0, \mu_4 = 0, \mu_5 = 0, \mu_6 = 0\right)$

$$\mu_3 > 0 \Rightarrow R_1^* = \epsilon_2 \tag{194}$$

Eq. (190) should be solved while $\mu_1 = 0$, $\mu_2 = 0$, $R_1 = \epsilon_2$, $\mu_4 = 0$, $\mu_5 = 0$, and $\mu_6 = 0$. Also, the following conditions should be checked.

$$0 < k\theta_{B_1} \le \frac{\pi}{2}, \ 0 < R_1 \le \frac{W}{2}, \mu_3 > 0 \tag{195}$$

Accordingly, R_1^*, R_2^*, and $\theta_{B_1}^{*P}$ will be obtained.

6.1.2.4 Mathematical Formulations of CC Optimal Paths

CC path is a special case of the problem stated in subsection 6.1.2.2, when there is no straight line motion. Hence, using Eq. (185), the following optimization problem is defined for the first combination (see Table 7) of CC paths.

$$\underset{R_1, R_2, \theta_{B_1}^P}{\text{minimize}} \quad E_{CC}$$

$$\text{subject to} \quad \tilde{h}_i = 0, i = 1, 2 \tag{196}$$

$$0 < k\theta_{B_1}^P \le \frac{\pi}{2}, 0 < R_j \le \frac{W}{2} \ (j = 1, 2)$$

where

$$E_{CC} = \left(4\mu\frac{v_c}{W}pL + 2Gv_c\right)\left|\frac{\theta_{B_1}^P - \theta_A^P}{\omega_z}\right|$$

$$+ \left(4\mu\frac{v_c}{W}pL + 2Gv_c\right)\left|\frac{\theta_{B_1}^P - \theta_C^P}{\omega_z}\right| \tag{197}$$

$$\tilde{h}_1 = x_C^P + kR_2(\sin\theta_C^P - \sin\theta_{B_1}^P)$$
$$- x_A^P - kR_1(-\sin\theta_A^P + \sin\theta_{B_1}^P)$$
$$\tilde{h}_2 = y_C^P + kR_2(-\cos\theta_C^P + \cos\theta_{B_1}^P) \tag{198}$$
$$- y_A^P - kR_1(\cos\theta_A^P - \cos\theta_{B_1}^P)$$

$$k = -\frac{\sin\theta_A^P}{|\sin\theta_A^P|}, \ \theta_A^P \ne 0 \tag{199}$$

$$\{\theta_A^P, \theta_C^P \in (0, \frac{\pi}{2}]\} \text{ Or } \{\theta_A^P, \theta_C^P \in [-\frac{\pi}{2}, 0)\}$$

After obtaining the Lagrange equation and its derivatives, the same process described in 6.1.2.3 should be followed to obtain the optimal path, which for brevity is not restated here.

6.1.3 Numerical Results

This part presents two solved example path-planning problems (CLC and CC) for the same start and end pose for a Clearpath Husky UGV A200 rover. Numerical results for the optimization method that was presented in subsection 6.1.2.2 (for CLC paths) and subsection 6.1.2.4 (for CC paths) are summarized. Comparison of the results will show that the energy consumption of the CLC path is less than the CC path. Then, experimental results focus on comparing CLC results to PLP.

6.1.3.1 Numerical Example for CLC Paths
The example path-planning problem to be solved is defined by the start (A) and end (C) pose, as well as rover specifications, given in Table 9. For a convenient visual summary of the results, Table 10 introduces arrow notations for various parts of the CLC and PLP paths.

Table 9: Path and Rover Parameters for the Example Problem

Parameter	A	C	θ_A^P	θ_C^P	μ	G	v_c	L	W	m	g	p
Value	[0,0]	[10,0]	$\pi/4$	$\pi/4$	1.00	64.49	0.3	0.52	0.55	63	9.81	mg/4
Unit	m	m	rad	rad	-	N	m/s	m	m	kg	m/s^2	N

The optimization process for the 1st combination of turning radii (see Table 7) gives the results reported in Table 11 (an the summary in Table 12). In the table, $C_{\frac{W}{2}}$ is a circle with turning radius of W/2, L is a straight line, and P is a point turn.

Several of the cases that may be admissible in general are not valid for this particular set of start and end poses (case 4, 7, 10, 12, 15, 17, 21, 24, 26, 27), for reasons given in the table. The solutions that are valid actually take only one of four possible forms, as summarized in Table 12. The lowest energy is found in Case 1 where both R_1^* and R_2^* are equal to W/2.

A similar process to the one described above is followed for the 2nd, 3rd, and 4th combinations of turning radii (Table 7). The final answers for each optimization process are reported in Table 13. As it is clear, all of them have converged to the same optimal answer which shows that the optimally energy-efficient CLC path is a path with $R_1^* = R_2^* = \dfrac{W}{2} = 0.275 \ m$.

Note that PLP is one of the candidate solutions identified by the KKT conditions, but the analysis predicts a higher total energy for that candidate solution.

6.1.3.2 Numerical Solution for CC Paths
Using the same process explained in 6.1.2.3, the optimization problem stated in Eq. (196) to Eq. (199) (section 6.1.2.4) and using the initial conditions stated in Table 9, the problem is solved and the answers are reported in Table 14. Based on the results the minimum energy happens for the case where both turning radii are equal to 3.535 m.

Comparing the energy-efficient results of Table 13 and Table 15 indicates that the $C_{\frac{W}{2}}LC_{\frac{W}{2}}$ path has 21% less energy consumption than the CC path.

Table 10: Arrow representations for basic maneuvers

Arrow	Maneuver
↷	Clockwise Circular-Arc
↶	Counter Clockwise Circular-Arc
↻	Clockwise Point Turn
↺	Counter Clockwise Point Turn
⇑	Straight Line

6.1.4   Conclusions of the Subsection

Energy-efficient path planning from among predefined classes of paths (CC and CLC) for skid-steer rovers are investigated in the absence of lateral slippage. As the power consumption of a skid-steer rover is highly dependent on the path's turning radius, it is considered explicitly in our calculation of consumed energy. The assumptions are that the rover moves forward on flat ground with a constraint on the right and left wheels' velocities. Karush-Kuhn-Tucker conditions are used and different candidates for the energy-efficient CLC and CC paths on hard ground (using the existing power model) are obtained. Then, a scenario is considered and the candidates are considered to analytically obtain the optimally energy-efficient CLC and CC paths. The results show that for the scenario there are just four types of path as optimal candidates for among the CLC class of paths: $C_{\frac{W}{2}}LC_{\frac{W}{2}}$, $C_{\frac{W}{2}}LP$, $PLC_{\frac{W}{2}}$, and PLP. Also, CC, CP, and PC are the optimal candidates for the circle-circle class of paths. The numerical analysis indicates that $C_{\frac{W}{2}}LC_{\frac{W}{2}}$ and CC have the lowest energy-consumption among their related candidates. Then, it is shown that for the scenario the $C_{\frac{W}{2}}LC_{\frac{W}{2}}$ has 21 % less energy consumption than CC. Note that in the absence of lateral slippage, $W/2 = R'$.

Table 11: Candidate solutions obtained for **CLC** paths according to the different cases for inequality constraints' coefficients (for example problem), when $0 < R_1 \leq (W/2)$ and $0 < R_2 \leq (W/2)$

Case	$\left(R_1^*(m), R_2^*(m), \theta_{B_1}^{*P}(rad)\right)$	Energy (J)
1	(0.275, 0.275, -0.0168)	1553.352
2	(0.275, 0.000, -0.008)	1575.759
3	(0.000 , 0.275, -0.008)	1575.759
4	$\theta_{B_1}^P$ cannot be $-\dfrac{\pi}{2}$	✗
5	(0.000, 0.000, 0.000)	1597.942
6	(0.000, 0.000, 0.000)	1597.942
7	$\theta_{B_1}^P$ cannot be $-\dfrac{\pi}{2}$	✗
8	(0.000, 0.000, 0.000)	1597.942
9	(0.000, 0.000, 0.000)	1597.942
10	$\theta_{B_1}^P$ cannot be $-\dfrac{\pi}{2}$	✗
11	(0.000, 0.000, 0.000)	1597.942
12	$\theta_{B_1}^P$ cannot be $-\dfrac{\pi}{2}$	✗
13	(0.275, 0.000, -0.008)	1575.759
14	(0.275, 0.000, -0.008)	1575.759
15	$\theta_{B_1}^P$ cannot be $-\dfrac{\pi}{2}$	✗
16	(0.275, 0.000, -0.008)	1575.759
17	$\theta_{B_1}^P$ cannot be $-\dfrac{\pi}{2}$	✗
18	(0.275, 0.000, -0.008)	1575.759
19	(0.000 , 0.275, -0.008)	1575.759
20	(0.000 , 0.275, -0.008)	1575.759
21	$\theta_{B_1}^P$ cannot be $-\dfrac{\pi}{2}$	✗
22	(0.000 , 0.275, -0.008)	1575.759
23	(0.000 , 0.275, -0.008)	1575.759
24	$\theta_{B_1}^P$ cannot be $-\dfrac{\pi}{2}$	✗
25	(0.275, 0.275, -0.0168)	1553.352
26	$\theta_{B_1}^P$ cannot be $-\dfrac{\pi}{2}$	✗
27	if $R_1 = R_2 = \dfrac{W}{2}$ $\Rightarrow \theta_{B_1}^P$ cannot be infinitesimal	✗

Table 12: Summary of Table 11.

Case	Type	Maneuver	$\left(R_1^*(m), R_2^*(m), \theta_{B_1}^{*P}(rad), E(J)\right)$
1,25	$C_{\frac{W}{2}}LC_{\frac{W}{2}}$	⤴⇑⤵	(W/2, W/2, -0.0168, 1553.352)
5, 6, 8, 9, 11	PLP	↻⇑↻	(0.000, 0.000, 0.000,1597.942)
2, 13, 14, 16, 18	$C_{\frac{W}{2}}LP$	⤴⇑↻	(W/2, 0.000, -0.008, 1575.759)
3, 19, 20, 22, 23	$PLC_{\frac{W}{2}}$	↻⇑⤵	(0.000 , W/2, -0.008, 1575.759)

Table 13: The results for the four different combinations of the turning radii for CLC paths

Com.	R_1	R_2	$\left(R_1^*(m), R_2^*(m), \theta_{B_1}^{*P}(rad), E(J)\right)$
1st	(0, W/2]	(0, W/2]	(W/2, W/2, -0.0168, 1553.352)
2nd	(0, W/2]	(W/2, +∞)	(W/2, W/2, -0.0168, 1553.352)
3rd	(W/2, +∞)	(0, W/2]	(W/2, W/2, -0.0168, 1553.352)
4th	(W/2, +∞)	(W/2, +∞)	(W/2, W/2, -0.0168, 1553.352)

Table 14: Summary of candidate solutions obtained for **CC** paths according to the different cases for inequality constraints' coefficients (for example problem), when $0 < R_1 \le (W/2)$ and $0 < R_2 \le (W/2)$

Type	$\left(R_1^*(m), R_2^*(m), \theta_{B_1}^{*P}(rad), E(J)\right)$	Maneuver
CC	$(3.535, 3.535, -\pi/4, 1937.268)$	⤴⤵
PC	$(0.00, 7.070, -\pi/4, 1992.942$	↻⤵
CP	$(7.070, 0.00, -\pi/4, 1992.942$	⤴↻

Table 15: The results for the four different combinations of the turning radii for CC paths

Com.	R_1	R_2	$\left(R_1^*(m), R_2^*(m), \theta_{B_1}^{*P}(rad), E(J)\right)$
1st	(0, W/2]	(0, W/2]	$(3.535, 3.535, -\pi/4, 1937.268)$
2nd	(0, W/2]	(W/2, +∞)	$(3.535, 3.535, -\pi/4, 1937.268)$
3rd	(W/2, +∞)	(0, W/2]	$(3.535, 3.535, -\pi/4, 1937.268)$
4th	(W/2, +∞)	(W/2, +∞)	$(3.535, 3.535, -\pi/4, 1937.268)$

6.2 Energy-Efficient Path Planning, Theoretical and Experimental, on Hard Ground while Considering the Lateral Slippage

This subsection is published in *Journal of Intelligent and Robotic Systems*. It is slightly revised to fit into the rest of this thesis.

The *contributions and organization* of this subsection are summarized in the following:

A key contribution of this subsection is a detailed exposition of the importance of R', including its use in optimally energy-efficient local path planning on hard ground. It should be noted that:

- $R' = \dfrac{B_{\mathrm{s}}}{2}$ when the lateral slippage is considered

- $R' = \dfrac{W}{2}$ when the lateral slippage is *ignored*

When considering with respect to a popular power model for skid-steer rovers [87], R' corresponds to an important transition for energy consumption: based on Eq. (42) and Fig. 14, below R' (for radii $0 \leq R < R'$) energy consumption is not a function of turning radius while above R' it is. CLC paths, with the 'C' segments consisting of circular arcs of radius R', are found to be optimally energy efficient in both simulation and experiments on hard ground.

In addition, it is explicitly shown that there are CLC paths that are more energy-efficient than point turn-line-point turn (PLP) paths on hard ground. Thus R'-CLC paths (CLC paths with $R = R'$) should be used as "optimistic" (see the 3rd paragraph of 1.2.1.1) estimates of cost to a goal, rather than PLP paths.

In subsection 6.2.1, the problem of theoretical and experimental investigation for skid-steer rovers' energy-efficient CLC paths are defined. The kinematics and power model of the problem are also introduced. Then, section 6.2.2 specifies the energy-efficient CLC path planning problem. Section 6.2.3 reports the numerical analysis and experimental tests for comparison of energy-efficient CLC with PLP paths. Finally, section 6.2.4 reports conclusions regarding the optimality of R' and the conditions in which energy-efficient CLC paths consume less energy than PLP.

6.2.1 Problem Statement and System Definition

To investigate the significance of R', the usefulness of CLC paths, and the relationship between these two contributions, the following problem is studied:

Problem: Finding energy-efficient CLC (Fig. 44) paths for skid-steer rovers while considering the *lateral slippage* both theoretically by using the existing power model and experimentally by commanding different CLC paths with a Husky UGV. The sub-problems are summarized as follows:

i Computing the optimally energy-efficient CLC path by theoretical analysis, and comparing these results to PLP (Fig. 46) paths (shortest path).

ii Experimentally measuring the energy required to perform PLP paths and CLC paths with turning radii at and around those suggested by the analysis in *Problem-i*, on hard ground.

iii Comparing the results of *Problem-i* and *Problem-ii*.

Figure 46: A PLP path consisting of two point turns and a line segment

Problem-i is further explicitly defined here: This **problem** and its **assumptions** are almost the same as subsection 6.1.1. Just the assumption of considering the lateral slippage should be added. Also, there is *no assumption* of $|V_l| + |V_r| = 2v_c$ in all the theoretical analysis in this subsection (6.2), which result in more general investigation of CLC paths as well as the importance of R' (see Theorem 9) for skid-steer rovers.

6.2.1.1 Skid-Steer Rover Kinematics and Power Model The kinematics and power model were presented in subsection 2.2.

6.2.2 Energy-Efficient CLC Paths

This subsection focuses on the mathematical formulation of *Problem-i* (see subsection 6.2.1). Accordingly, the energy consumptions of a skid-steer rover during a circular-arc path segment and a straight line motion are formulated. Then, using these equations, the optimization problem for an energy-efficient CLC path with all of its equality and inequality constraints is defined.

6.2.2.1 Energy Consumption During a Circular-arc and a Straight Line It is known that energy (E) can be obtained by the following equation.

$$E = \int_{t_0}^{t_f} P \, dt \qquad (200)$$

where t is time. In addition, along a circular arc and a straight line, the related time is respectively equal to:

$$t = \int_{\theta_0}^{\theta_f} |\frac{d\theta}{\omega_z}| \qquad (201)$$

$$t = \int_0^{L_S} |\frac{ds}{v}| \qquad (202)$$

where $d\theta$ and ds are the differential of angle and displacement of the rover, respectively. Also, L_S is the length of straight line.

Theorem 9 *The energy for the skid-steer rover when doing a circular arc maneuver (using the power model of Eq. (23)) is equal to:*

90

$$E_C = \begin{cases} (k + GB_s)|\Delta\theta|, & \text{if } 0 \le R \le R' \\ (k + 2RG)|\Delta\theta|, & \text{if } R > R' \end{cases} \tag{203}$$

Proof: Starting with the power model, (23), and the general equations (200) and (201), gives:

$$\begin{aligned} E_C &= \int_{\theta_0}^{\theta_f} (k|\omega_z| + G(|V_r| + |V_l|))\left|\frac{d\theta}{\omega_z}\right| \\ &= \int_{\theta_0}^{\theta_f} \left(k + G\frac{|V_r| + |V_l|}{|\omega_z|}\right)|d\theta| \end{aligned} \tag{204}$$

Using (15), this becomes:

$$E_C = \int_{\theta_0}^{\theta_f} \left(k + GB_s\frac{|V_r| + |V_l|}{|V_r - V_l|}\right)|d\theta| \tag{205}$$

The definition of R' ensures that in the region $0 \le R < R'$, V_r and V_l are of opposite sign. Therefore, the following relation is always true:

$$\frac{|V_r| + |V_l|}{|V_r - V_l|} = 1 \tag{206}$$

Without loss of generality, consider V_r positive. Then, $|V_r| = V_r$ and $|V_l| = -V_l$. Hence, Eq. (206) can be proved. As a result, the energy is:

$$\begin{aligned} E_C &= \int_{\theta_0}^{\theta_f} (k + GB_s)|d\theta| \\ &= (k + GB_s) \int_{\theta_0}^{\theta_f} |d\theta| \\ &= (k + GB_s)|\Delta\theta|, \text{ for } \quad 0 \le R \le R' \end{aligned} \tag{207}$$

Therefore the energy for any turn with $0 \le R < R'$ is a constant times $|\Delta\theta|$. When $R > R'$, it is known that both V_r and V_l have the same sign (both are positive or negative). Accordingly, it can be proved that equation (18) can be written in the following format:

$$R = \frac{B_s}{2}\frac{|V_r| + |V_l|}{|V_r - V_l|} \tag{208}$$

Hence, using Eq. (205), the energy for a constant radius arc is as follows:

$$\begin{aligned} E_C &= \int_{\theta_0}^{\theta_f} (k + 2RG)|d\theta| \\ &= (k + 2RG) \int_{\theta_0}^{\theta_f} |d\theta| \\ &= (k + 2RG)|\Delta\theta|, \text{ for } \quad R > R' \end{aligned} \tag{209}$$

Accordingly, using Theorem 9, the energy function for arc of a circle with turning radius of R can be written as follows:

$$E_C = (k + GB_s)|\Delta\theta|(H[R] - H[R - R']) \\ + (k + 2GR)|\Delta\theta|H[R - R'] \tag{210}$$

where the Heaviside function for real numbers, n, is as follows:

$$H[n] = \begin{cases} 0, & \text{if } n \le 0 \\ 1, & \text{if } n > 0 \end{cases} \tag{211}$$

After more simplifications, the energy equation presented by Eq. (210) becomes as follows:

$$E_C = a_1' \, |\Delta\theta| \, H[R] + (-a_2' + a_3'R) \, |\Delta\theta| \, H[R - R'] \tag{212}$$

where

$$a_1' = k + GB_s \tag{213}$$

$$a_2' = GB_s \tag{214}$$

$$a_3' = 2G \tag{215}$$

Lemma 9 *The energy for the skid-steer rover when doing a straight line maneuver (using the power model of Eq. (23)) is equal to:*

$$E_L = 2G\sqrt{(x_{B_1}^P - x_{B_2}^P)^2 + (y_{B_1}^P - y_{B_2}^P)^2} \tag{216}$$

where (x_{B_1}, y_{B_1}) and (x_{B_2}, y_{B_2}) are the start and end of straight line maneuver, respectively.
Proof: It is known that $\omega_z = 0$ for a straight line motion. Hence, starting with the power model, (23), and the general equations (200) and (202), gives:

$$E_L = \int_0^{L_S} (G \, (|V_r| + |V_l|)) |\frac{ds}{v}| \\ = \int_0^{L_S} \left(G \frac{|V_r| + |V_l|}{|v|}\right) |ds| \tag{217}$$

Using Eq. (14), this becomes:

$$E_L = \int_0^{L_S} \left(2G \frac{|V_r| + |V_l|}{|V_r + V_l|}\right) |ds| \tag{218}$$

Since V_r and V_l have the same sign at the straight line motion, the following relation is always true:

$$\frac{|V_r| + |V_l|}{|V_r + V_l|} = 1 \tag{219}$$

Therefore,

$$
\begin{aligned}
E_L &= 2G \int_0^{L_S} |ds| \\
&= 2GL_S \\
&= 2G\sqrt{(x^P_{B_1} - x^P_{B_2})^2 + (y^P_{B_1} - y^P_{B_2})^2}
\end{aligned}
\tag{220}
$$

∎

6.2.2.2 Mathematical Formulations of Optimal CLC Paths *This subsection is similar to 6.1.2.2. The only difference is that in this subsection the lateral slippage is taken into account.* This subsection sets up the optimization problem for finding energy-efficient CLC paths (Fig. 45). The notation is based on prior work optimizing Circle-Circle (CC) paths [97]; as points A and C grow farther apart, the motivation for this present work adding a straight line segment becomes clear.

By using Eq. (212), Lemma 9, and the assumptions described in section 6.2.1 the energy for the full path is obtained as follows:

$$
E = E_{AB_1} + E_{B_1 B_2} + E_{B_2 C}
\tag{221}
$$

$$
\begin{aligned}
E = &(a'_1 \, H[R_1] + (-a'_2 + a'_3 R_1)H[R_1 - R'])|\theta^P_{B_1} - \theta^P_A| \\
&+ (a'_1 \, H[R_2] + (-a'_2 + a'_3 R_2)H[R_2 - R'])|\theta^P_{B_1} - \theta^P_C| \\
&+ 2G\sqrt{(x^P_{B_1} - x^P_{B_2})^2 + (y^P_{B_1} - y^P_{B_2})^2}
\end{aligned}
\tag{222}
$$

As mentioned in the previous sections, R_1 and R_2 are the radii of the first and second circles (Fig. 45), respectively. Also, $\theta^P_{B_1}$, θ^P_A, and θ^P_C are the heading angles of the path at points B_1, A, and C in the path-defined coordinate system (see Fig. 44 also), respectively. In addition, $(x^P_{B_1}, y^P_{B_1})$ and $(x^P_{B_2}, y^P_{B_2})$ are the position of points B_1 and B_2 in the path-defined coordinate system.

The optimally energy-efficient CLC path problem defined in section 6.2.1 can be written as follows:

$$
\begin{aligned}
\underset{R_1, R_2, \theta^P_B}{\text{minimize}} \quad & E \\
\text{subject to} \quad & h_i = 0, i = 1, 2 \\
& 0 < k\theta^P_{B_1} \leq \frac{\pi}{2} \\
& R_j \geq 0, j = 1, 2
\end{aligned}
\tag{223}
$$

To avoid searching for $\theta^P_{B_1} > 2\pi$ or $\theta^P_{B_1} < -2\pi$ in the optimization process, the inequality constraints in (223) are written; it is clear when (227), written based on the simplifying assumption mentioned in the problem statement, is held then $0 < k\theta^P_{B_1} \leq \frac{\pi}{2}$ is required for minimum energy. Also, E is given by (222), and the equality constraints (h_i) which define the CLC paths are as follows:

$$
h_1 = x^P_{B_2} - x^P_{B_1} - \cos\theta^P_{B_1}\sqrt{(x^P_{B_2} - x^P_{B_1})^2 + (y^P_{B_2} - y^P_{B_1})^2}
\tag{224}
$$

93

$$h_2 = y_{B_2}^P - y_{B_1}^P - (x_{B_2}^P - x_{B_1}^P) \tan \theta_{B_1}^P \tag{225}$$

where

$$\begin{aligned}
x_{B_1}^P &= x_A^P + kR_1(-\sin\theta_A^P + \sin\theta_{B_1}^P) \\
y_{B_1}^P &= y_A^P + kR_1(\cos\theta_A^P - \cos\theta_{B_1}^P) \\
x_{B_2}^P &= x_C^P + kR_2(\sin\theta_C^P - \sin\theta_{B_1}^P) \\
y_{B_2}^P &= y_C^P + kR_2(-\cos\theta_C^P + \cos\theta_{B_1}^P) \\
k &= -\frac{\sin\theta_A^P}{|\sin\theta_A^P|}, \quad \theta_A^P \neq 0
\end{aligned} \tag{226}$$

and

$$\{\theta_A^P, \ \theta_C^P \in (0, \frac{\pi}{2}]\} \ \text{Or} \ \{\theta_A^P, \ \theta_C^P \in [-\frac{\pi}{2}, 0)\} \tag{227}$$

which means θ_A^P and θ_C^P are both in the first or both in the fourth quadrant of path-defined coordinate system (see Fig. 45). It should be mentioned that h_1 and h_2 are required to ensure that different segments of the CLC path, including two circles and a line, are connected.

6.2.3 Simulation and Experimental Results of CLC and PLP Paths

This part presents simulation and experimental results for optimizing CLC paths (i.e. *Problem-ii* in section 6.2.1). Numerical results of the optimization set up in the preceding section are presented. The CLC paths are performed experimentally on hard ground with a Husky rover, shown in Figure 47, in addition to PLP paths with the same start/end poses for comparison. Furthermore, some of the performed experimental tests are discussed in additional detail, as are the results of experiments exploring power consumption as a function of turning radius.

Figure 47: Husky UGV Rover on hard ground.

Relevant rover parameters are given in Table 16. Note that a weight (bin filled with sand) is attached to the rover such that the resulting center of mass is at the rover's geometric center; this increases the rover's total mass.

Table 16: Husky Rover Parameters on Hard Ground (HG) used in the Numerical Computations

Parameter	μ	G	$|V_l| + |V_r|$	L	W	m	g	p	B_s
Value	0.74	30.85	0.6	0.52	0.55	63	9.81	mg/4	1.29
Unit	-	Ws/m	m/s	m	m	kg	m/s^2	N	m

6.2.3.1 Test Plan This subsection provides the plan for both the numerical and experimental tests. Because of the skid-steer rovers' ability to do point turns the simplest way to traverse a distance between two points is by doing a PLP. However, we will show that CLC paths can consume less energy than PLP paths. Accordingly, different scenarios for CLC and PLP paths are considered for the Husky, in simulation and in experiments on hard ground (concrete).

The test plan is shown in Table 17. Two scenarios are studied on hard ground, one with equal start and end angle, relative to the path-defined coordinate system (whose x-axis is aligned with the line connecting points A and C), and another with different start and end angles. Because in practice the specified distances are not exactly achieved, the actually displaced Euclidian distance from start (A) to end (C) pose (measured using a laser total station that returns the 3D point location of a tracked prism in a global coordinate frame, shown in Fig. 48) in the CLC path is used to prescribe the distance for the PLP path. The final displacements from start to end poses for CLC and PLP paths are confirmed to be within 0.5% of one another, to ensure a fair comparison.
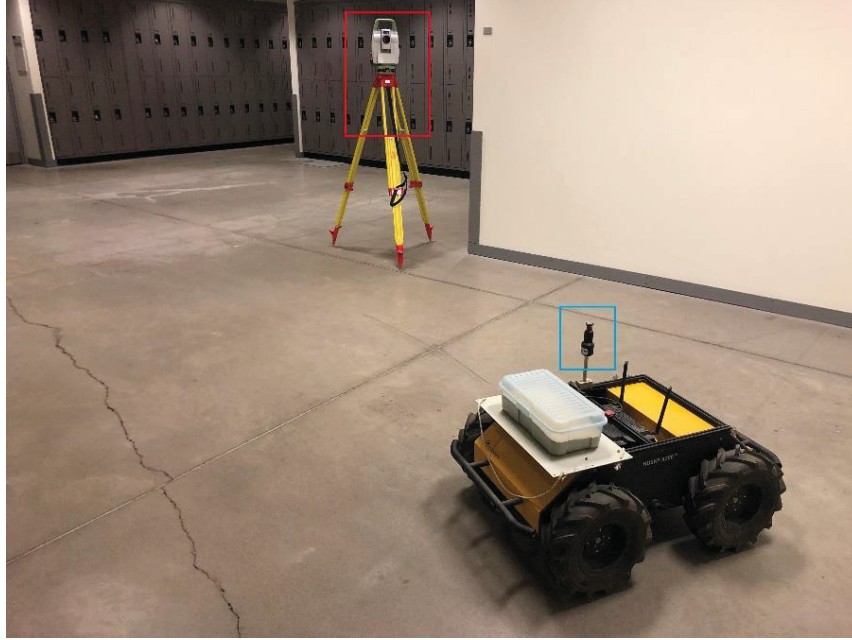
Figure 48: The laser total station (red box) and the prism on the rover (blue box) used for tracking rover motion.

Table 17: Husky Rover Test Plan on Hard Ground

Terrain	Maneuver	(θ_A^P, θ_C^P)	Commanded $\left\| \overrightarrow{AC} \right\|$ for Husky
Concrete	CLC	$(45^o, 45^o)$	10 m
		$(60^o, 30^o)$	8 m
Concrete	PLP	$(45^o, 45^o)$	Measured Dis. for CLC $(45^o, 45^o)$
		$(60^o, 30^o)$	Measured Dis. for CLC $(60^o, 30^o)$

6.2.3.2 Numerical Solutions of the Optimization Problem This subsection addresses the numerical optimization of CLC paths by utilizing the optimization problem formulated in subsection 6.2.2.2.

Parameters used to compute energy for the various scenarios listed in the test plan (Table 17) are provided in Table 16 for the Husky on hard ground. The parameters μ (friction coefficient), G (internal/rolling resistance coefficient), and B_s (slip track) are obtained experimentally, and are dependent on rover-terrain combination. B_s is calculated from the experimental data by using an Extended Kalman Filter, according to the procedure outlined by Pentzer et al. [91]. G is obtained from straight-line maneuvers given V_l,

V_r and the measured power, using (22). Then, CLC maneuvers are utilized to calculate μ by using (22) and the calculated G.

To solve the constrained optimization problem presented by (223) in 6.2.2.2, the *minimize* function from the *scipy.optimize* package in python is used. In the *minimize* function, Sequential Least Squares Programming (SLSQP) algorithm is chosen. The optimization results are presented in the rows marked 'CLC' in Table 18 for the Husky on hard ground. Comparing the optimal turning radii returned by the optimization, in Table 18 to the B_s input parameter in Table 16, it is clear that, for the tested start/end conditions, $R_1^* = R_2^* = \dfrac{B_s}{2} = R'$. The fact that R' is the optimal turning radius predicted by these numerical analyses highlights its importance.

Table 18: Numerically Computed Energy-Efficient CLC Paths for Husky Rover on Hard Ground

Path Type	(θ_A^o, θ_C^o)	Distance (m)	$(R_1(\text{m}), R_2(\text{m}), \theta_B(\text{rad}))$	Energy (J)
CLC	(45,45)	10	(0.645, 0.645, -0.0417)	965.83
PLP	(45,45)	10	(0,0,0)	1004.38
CLC	(60,30)	8	(0.645, 0.645, -0.0577)	851.21
PLP	(60,30)	8	(0,0,0)	880.98

Table 18 also provides the computed energy for PLP paths that achieve the same displacement from start to end pose. In both cases, the optimal CLC path is predicted to require less energy than the corresponding PLP path. The numerically computed CLC path energy is lower than the computed PLP path energy by no more than 3.5% in the cases studied in Table 18. It could be conceivable that uncertainties ignored by the theoretical model (i.e. Eq. (22)) could in reality obscure advantages of this magnitude. However, as will be shown in the experimental results in the next subsection, rather than identifying small theoretical differences that are obscured in reality, the simplifications of the theoretical model actually somewhat downplay the real advantages of CLC paths (particularly with R' circular arcs) relative to PLP paths.

6.2.3.3 Experimental Results on Hard Ground

This subsection studies the scenarios presented in Table 17 experimentally. For both CLC and PLP paths the constraint on the right and left wheel velocities is $|V_l| + |V_r| = 0.6 m/s$, the same constraint that is mentioned in Table 16. When driving straight, the commanded linear velocity is 0.3 m/s. When performing a point turn, each side is commanded at 0.3 m/s but in opposite directions. When performing an R' circular arc, the outer wheel is commanded at 0.6 m/s and the inner wheel is not commanded to move. The constraint enforces that the commanded angular velocity is constant, at 0.55 rad/s, for any turn with $0 \leq R \leq R'$. To command a CLC path experimentally, the total desired Euclidean distance (between points A and C), the start and end angles, and the commanded radii R_1 and R_2 are used to find the

required angle subtended by each circular arc (at the center of the corresponding circle). Each circular arc is commanded until the rover's Inertial Measurement Unit (a VectorNav VN-100R) shows the required turn angle has been achieved. The straight line segments are commanded via dead-reckoning that accounts for an empirically estimated slip ratio. Because in practice the specified distances are not exactly achieved, the actually displaced Euclidean distance from start to end pose (measured using a laser total station shown in Fig. 48) in the CLC path is used to prescribe the distance for the PLP path. The final displacements from start to end poses for CLC and PLP paths are confirmed to be within 0.5% of one another, to ensure a fair comparison.

The power consumption of the rover is measured with two Texas Instruments INA226 bidirectional current and power sensors on the Husky. These sensors measure the current and voltage of the left and right motor drivers. Accordingly, the instantaneous power is obtained by multiplying the measured current and voltage.

The following definitions are given to distinguish between the commanded and measured turning radii for the Husky UGV:

Definition 7 R'_{H_c} *is the commanded turning radius for the Husky UGV that results in the inner wheels receiving a commanded velocity of 0.* $R'_{H_c} = 0.55m$.

Definition 8 R'_H *is the actual turning radius that the Husky follows when* R'_{H_c} *is commanded to it.*

Definition 9 R_e *is the actual turning radius that a rover follows during any generic circular arc, as measured experimentally. As will be explained in this subsection, the commanded* R_1 *and* R_2 *are equal for all the experimental tests. The measured* R_1 (R_1^m) *and measured* R_2 (R_2^m) *will also be equal. So,* $R_e = R_1^m = R_2^m$.

It is worth noting that the R'_{H_c} of 0.55 m accounts for the fact that the rover will generally experience lateral slip. Clearpath Robotics have programmed a slip track, B_s, of 1.1 m into the Husky's controls for converting paired v and ω_z commands into V_r and V_l control inputs according to (14) and (15). For hypothetical operation without lateral slip, the slip track would have been exactly equal to the rover width, but this programmed slip track is twice the rover width; this highlights the important distinction between $R_c = W/2$ and $R' = B_s/2$. Clearpath's programmed slip track is presumably based on some average slip track measured from tests on reference terrain(s). In practice, the actual slip track differs from this value.

In the case where the Husky is commanded with R'_{H_c}, $R_e = R'_H$. However, other turning radii can also be, and are, explored experimentally. For each test, the actual turning radius driven was derived from laser total station and IMU measurements. Because the offset between the total station prism (attached to the rover) and the rover center is known and constant, the rover center location can be computed by a simple transformation knowing the prism location and rover heading angle. A circle is fit to the rover center data points to find an actual turning radius. Note that the associated timestamps can further be used to compute the rover's forward velocity, angular velocity, and the velocity of its left and right sides. On concrete $R'_H = 0.645$ m.

In subsection 6.2.3.2, it is shown that the minimum energy is always numerically predicted at $R_1 = R_2 = R'$ (R'_H for Husky). Therefore, several CLC maneuvers are commanded around R'_{H_c} for the Husky UGV. Specifically, tests are performed with the following commanded turning radii: $0.5R'_{H_c}, R'_{H_c}, 1.5R'_{H_c}, 2R'_{H_c}$. Each of these tests is compared to its own respective PLP test[35] for the fairest possible comparison, as described earlier. In these tests, the difference in total distance for all the CLC/PLP pairs was always kept small, with the PLP path being around 0.5% shorter than CLC.

The energy consumption of each CLC path (E_{CLC}) is compared to the energy consumption of the corresponding PLP path (E_{PLP}), quantified as a percentage difference given by the following equation:

$$\Delta E = \frac{E_{CLC} - E_{PLP}}{E_{PLP}} \times 100\% \tag{228}$$

In cases where the above metric is negative, the energy consumed by the CLC path is lower than the corresponding PLP path. Using Eq. (228), Figure 49 and Figure 50 are plotted to show the experimental results for the hard ground experiments described in the test plan, Table 17. For each example path, 3 runs were conducted at each commanded turning radius, for a total of 12 CLC paths; 12 corresponding PLP paths were also run. For both example paths studied, the lowest energy consumption on average is observed for CLC paths with turning radii R'_H, exactly as predicted by the numerical analysis (see Table 18). The experimental results for CLC paths with turning radii R'_H on average consume almost 10% less energy than corresponding PLP paths. The numerical results, on the other hand, only predicted reductions no greater than 3.5%. One of the important possible explanations for this is that internal frictional losses as well as electrical losses (e.g. consumed by the motor controller) are not modeled. At R' the inner wheels are not commanded to drive at all and thus these internal losses, present during other maneuvers, are avoided resulting in relatively more energy savings. Another possible source of difference between experimental and theoretical results is uncertainty in selecting model parameters such as μ, G, and B_s, or even other unmodeled aspects; however, there is no particular reason to believe any of these associated errors would in general bias in favor of lower experimental energy consumption.

---

[35]i.e. commanded turning radius of 0
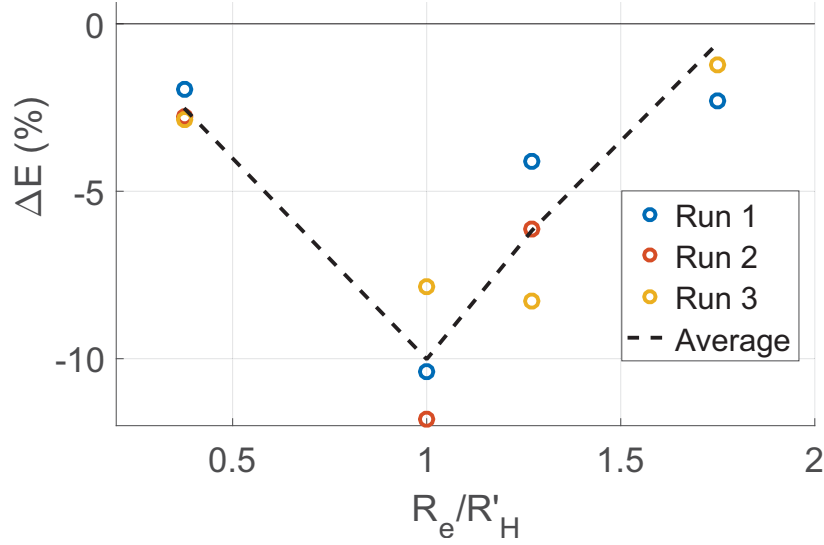
Figure 49: Comparison of experimentally measured energy consumption for CLC paths vs. PLP paths for the Husky rover on hard ground. Start and end angle 45°; distance 10 m. Lowest energy is observed for CLC paths with turning radius R'_H.
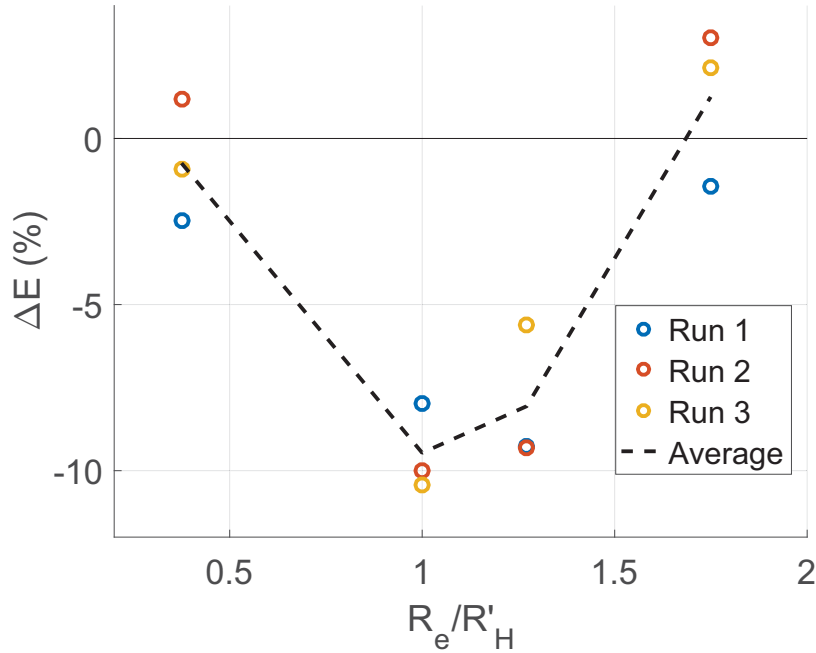
Figure 50: Comparison of experimentally measured energy consumption for CLC paths vs. PLP paths for the Husky rover on hard ground. Start angle 60°; end angle 30°; distance 8 m. Lowest energy is observed for CLC paths with turning radius R'_H.

Figure 51 compares the power consumption profiles for a PLP path versus its corresponding CLC path with $R = R'_H$. The example shown is Run 1 from Fig. 49 (at $R_e/R'_H = 1$),

i.e. with start and end angles of 45° and a displacement of 10 m. The total time required for the CLC maneuver is shorter, because the straight line segment is shorter due to the R' turn contributing to forward progress (as opposed to a point turn). The average power during the R' turns is also lower than point turns on this terrain, by about 20%, while the time required to complete each arc is less than 10% longer than it takes to complete the point turn. Taken together, the total energy is approximately 10% lower for the CLC path with $R = R'$ (which we can call the R'-CLC path) compared to the PLP path, as can be seen again in Fig. 49.
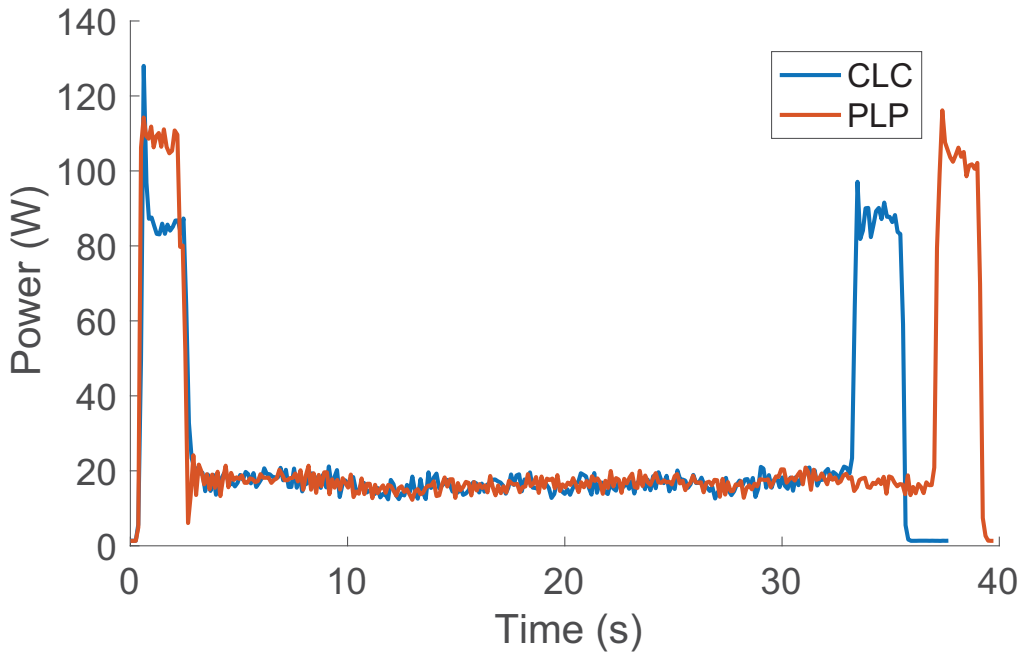
Figure 51: Comparison of experimentally measured power consumption vs. time for a CLC path (with $R = R'_H$) and PLP path for the Husky rover on hard ground.

6.2.3.4 Experimental Power for Husky UGV

This subsection presents power data measured experimentally for a skid-steer rover on hard ground, and discusses nuanced differences observed between this data and points discussed in prior literature.

A Husky UGV was commanded to execute 90 degree turns at various turning radii, subject to a constant forward velocity of $0.3m/s$, on hard ground (concrete). Power was measured for both the left and right motors using a Texas Instruments INA226 bidirectional current and power sensor, and the total power was averaged over the duration of the 90 degree turn. The turns start at the commanded R'_{H_c} and explore left and right power consumption as the turning radius is increased towards infinity.

Experimental data collected on hard ground (Figure 52) shows approximate correspondence with observations made in prior literature. It can also be seen that inner wheel power consumption becomes negative after R', as observed previously above R_c by Dogru and Marques [85, 86]. However, once the turning radius increases past a certain point (17 m on this particular terrain), inner wheel power consumption becomes positive again.

This is consistent with a reasonable expectation that power consumption changes gradually at large turning radii, rather than jumping suddenly to be negative as soon as left and right wheel velocities become unequal (i.e. the power does not remain negative for all of $R' < R < \infty$, but rather for $R' < R < R_T$, where $R_T \ll \infty$ is a threshold radius).
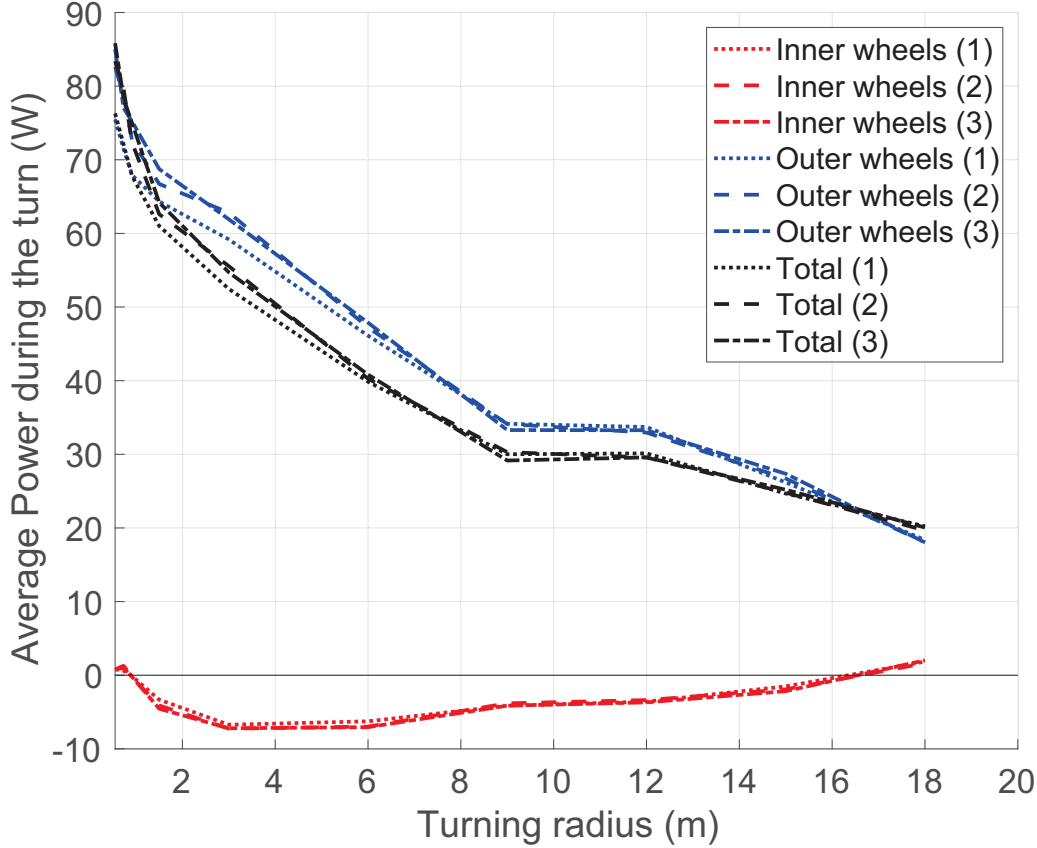
Figure 52: Husky UGV power consumption as a function of commanded turning radii bigger than R'. The tests are performed on hard ground consisting of concrete.

6.2.3.5 Interpretation and Generalization of Optimization Results

The simulated and experimental results on hard ground both show that optimal energy consumption with CLC paths occurs with turning radii of R'. It is instructive to now re-examine theory presented earlier in light of this result.

For $0 \leq R \leq R'$, Theorem (9) shows that energy consumed by a turn is a constant times $|\Delta\theta|$. In other words, the energy required to change heading is the same regardless of whether a point turn or R' turn is employed. However, when constructing a CLC path this choice affects the length of the straight line, and thus $E_{B_1 B_2}$. In general, R'-CLC paths require more $|\Delta\theta|$ than PLP paths, but as the distance between the start and end points is increased, the difference in $|\Delta\theta|$ approaches zero. On the other hand, because the R' turns also make forward progress, the line in a CLC path will be shorter than a PLP path.

This is exactly what is seen in the simulations and experiments explored in the preceding subsections.

The experimental energy consumption data generally support the observations discussed here, but with a caveat. As can be seen in Figure 53, below R' the energy consumed over the course of a 90 degree turn is roughly constant: all the points would fall within the confidence bounds based on the variance of the others, and there is no clear trend in the Run 1 or Run 3 data even though Run 2 demonstrates a slight positive slope. On the other hand, at R' there is a notable drop in energy consumption, which is not something predicted by the theoretical model. As was discussed in Section 6.2.3.3, this can be explained by additional unmodeled energy savings from avoiding internal friction and electrical losses when the inner wheel is not commanded. Above R' the energy consumption rises proportionally to R, as predicted by Theorem (9).
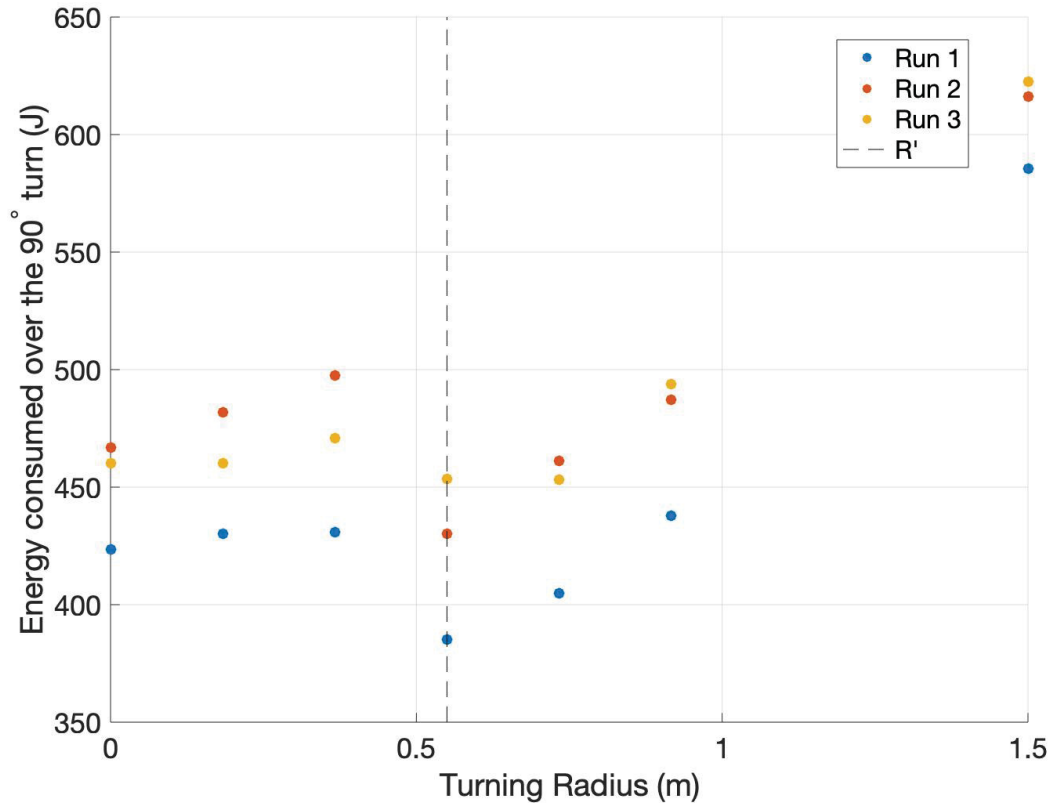
Figure 53: Comparison of experimentally measured energy consumption over a 90 degree turn as a function of turning radius.

Note that the argument introduced above does not necessarily hold for small distances between A and C, and future work will explore the threshold at which R'-CLC curves stop being the optimal choice.

6.2.4 Conclusions of the Subsection

This subsection identifies R', equal to half a skid-steer rover's slip track and also the radius at which the inner wheels are not commanded to turn, as a crucial concept in understanding the energy-efficiency of skid-steer rovers. When considered with respect to a popular power model for skid-steer rovers, R' corresponds to an important transition for energy consumption: below R' energy consumption is not a function of turning radius while above R' it is.

This research searches, both in numerical simulation and in experiments on hard ground, for the most energy-efficient path from among CLC paths, a generalization of PLP paths (PLP paths are the simplest path to execute for a skid-steer rover traversing between general start and end poses). Because energy consumption is not a function of R below R', an R' circular arc requires the same energy as a point turn through the same angle, but also accomplishes displacement that shortens the straight line portion of the path. Therefore, R'-CLC paths (or perhaps just straight lines) should be used as "optimistic" estimates of cost to a goal, rather than PLP paths.

From the evaluations and investigations reported here, the following findings are concluded:

- Numerically optimizing CLC paths for energy-efficiency shows that, for the existing power model and all cases examined, $R = R'$ gives the minimum energy consumption.

- Results obtained from experiments on hard ground (concrete) for CLC paths also show minimum energy consumption with $R = R'$, thus agreeing with the numerical predictions regarding the importance of this special turning radius.

- Experimental results indicate that in the example scenarios studied, with the end goal several rover lengths away from the start point, there is always a CLC path that can be found that is more efficient than its corresponding PLP path.

- When examining power consumption of inner and outer wheels during a skid-steer turn, inner wheel power does not remain negative for all of $R' < R < \infty$, but rather for $R' < R < R_T$, where $R_T \ll \infty$ is a threshold radius.

6.3 Experimental Results Obtained from the Tests Performed by Husky UGV and Argo Rover on Loose Soil

All the theoretical and analytical investigations performed in the previous sections and chapters are based on the assumption of moving on hard ground. In the following, experimental results obtained from the tests on loose soil are compared to the theoretical/analytical results on hard ground. This comparison will reveals the differences and it can be utilized as the starting point of future work for the energy-efficient path planning for skid-steer rovers on loose soil.

Therefore, the test plans that were designed to perform the tests are explained. Then, several plots are given to compare the different predefined paths based on their energy

consumption. In addition, numerical results of the optimization set up in the preceding subsection are presented. Moreover, CLC paths are conducted experimentally with both Husky and Argo J5 skid-steer rovers, in addition to PLP paths with the same start/end poses for comparison. Furthermore, some of the performed experimental tests are discussed in additional detail.

Figure 54: The laser total station (red box) and the prism, it travels on the rover (yellow box)

6.3.1 Test Plan

This subsection provides the plan for both of the numerical and experimental tests. Because of the skid-steer rovers' ability to do point turns the simplest way to traverse a distance between two points is by doing a PLP. However, we will show that CLC paths can consume less energy than PLP paths. Accordingly, different scenarios for CLC and PLP paths are considered for both the Husky and Argo J5 rovers, in simulation and in experiments on sandy terrain at the Canadian Space Agency (CSA).

The test plan is shown in Table 19. All tests prescribe the same start and end angle, relative to the path-defined coordinate system (whose x-axis is aligned with the line connecting points A and C), for simplicity.

Three different angles of 10°, 45°, and 90° are chosen to consider small, medium, and large angles. To command a CLC path experimentally, the total desired distace (between points A and C), the start and end angles, and the commanded radii R_1 and R_2 are used to find the required angle subtended by each circular arc (at the center of the corresponding circle). Each circular arc is commanded until the rover's Inertial Measurement Unit (a VectorNav VN-100R) shows the required turn angle has been achieved. The straight line segments are commanded via dead-reckoning that accounts for an empirically estimated slip ratio. Because in practice the specified distances are not exactly achieved, the actual traveled distance (measured using a laser total station shown in Fig. 54) in the CLC path is used to prescribe the distance for the PLP path. The CLC and PLP distances actually traveled are confirmed to be within 2% of one another, to ensure a fair comparison.

Table 19: Husky and Argo Rover Test Plan

Maneuver	(θ_A^P, θ_C^P)	Commanded $\left\|\overrightarrow{AC}\right\|$ for Husky	Commanded $\left\|\overrightarrow{AC}\right\|$ for Argo
CLC	$(10^o, 10^o)$		
	$(45^o, 45^o)$	10 m	12 m
	$(90^o, 90^o)$		
PLP	$(0^o, 0^o)$	Measured Dis. for CLC $(10^o, 10^o)$	Measured Dis. for CLC $(10^o, 10^o)$
		Measured Dis. for CLC $(45^o, 45^o)$	Measured Dis. for CLC $(45^o, 45^o)$
		Measured Dis. for CLC $(90^o, 90^o)$	Measured Dis. for CLC $(90^o, 90^o)$

6.3.2 Numerical Solution of the Optimization Problem

This subsection addresses the numerical analysis by utilizing the optimization problem formulated in subsection 6.2.2.2. Using the test plan (Table 19) and for the parameters given in Table 20 and Table 21, calculations of the total path energies for the Husky and Argo rovers are performed.

Table 20: Argo Rover Parameters used in Numerical Computations

Parameter	μ_A	G_A	v_c	L_A	W_A	m_A	g	p_A	B_{s_A}
Value	0.91	387.84	0.3	0.98	1.14	372	9.81	mg/4	1.68
Unit	-	Ws/m	m/s	m	m	kg	m/s^2	N	m

Table 21: Husky Rover Parameters used in Numerical Computations

Parameter	μ_H	G_H	v_c	L_H	W_H	m_H	g	p_H	B_{s_H}
Value	1.00	64.49	0.3	0.52	0.55	63	9.81	mg/4	0.65
Unit	-	Ws/m	m/s	m	m	kg	m/s^2	N	m

Table 22: Numerically Computed Energy-Efficient CLC Paths for Argo Rover

Path Type	(θ_A^o, θ_C^o)	Distance (m)	$(R_1(m), R_2(m), \theta_B(rad))$	Energy (J)
CLC	(10,10)	12	(0.84, 0.84, -0.0022)	9966.04
PLP	(10,10)	12	(0,0,0)	10184.14
CLC	(45,45)	12	(0.84, 0.84, -0.0466)	12510.45
PLP	(45,45)	12	(0,0,0)	13250.05
CLC	(90,90)	12	(0.84, 0.84, -0.1670)	16615.65
PLP	(90,90)	12	(0,0,0)	17191.94

Table 23: Numerically Computed Energy-Efficient CLC Paths for Husky Rover

Path Type	(θ_A^o, θ_C^o)	Distance (m)	$(R_1(m), R_2(m), \theta_B(rad))$	Energy (J)
CLC	(10,10)	10	(0.325, 0.325, -0.0017)	1347.55
PLP	(10,10)	10	(0,0,0)	1361.55
CLC	(45,45)	10	(0.325, 0.325, -0.035)	1565.10
PLP	(45,45)	10	(0,0,0)	1612.68
CLC	(90,90)	10	(0.325, 0.325, -0.1239)	1895.18
PLP	(90,90)	10	(0,0,0)	1935.56

It should be mentioned that μ and G for Husky UGV and Argo J5 rover (in Table 20 and 21) are obtained from experimental results. B_s is calculated by from the experimental data using an Extended Kalman Filter, according to the procedure outlined by Pentzer et al. [91]. Using (22), G is obtained from straight-line maneuvers given v_c and the measured power. Then, CLC maneuvers are utilized to calculate μ while using (22) and the calculated G.

For solving the constrained optimization problem presented by (223), the *minimize* function from the *scipy.optimize* package in python is used. In the *minimize* function, Sequential Least Squares Programming (SLSQP) algorithm is chosen. The optimization results are presented in the rows marked 'CLC' in Table 22 and Table 23 for the Argo and Husky rover, respectively. Comparing the optimal turning radii returned by the optimization, in Tables 22 and 23, to the B_s input parameters in Tables 20 and 21, it is clear that for both rovers and for all tested start/end conditions, $R_1^* = R_2^* = \dfrac{B_s}{2} = R'$. The fact that R' is the optimal turning radius highlights its importance.

Table 22 and Table 23 also provide the computed energy for PLP paths that achieve the same displacement from start to end pose. In all cases, the optimal CLC path requires less energy than the corresponding PLP path.

6.3.3 CLC and PLP Experimental Tests

Firstly, several important definitions are presented to distinguish between the commanded and measured R's for Husky UGV and Argo J5 rover:

Definition 10 R'_{A_c} is the commanded turning radius for the Argo J5 that results in the inner wheels receiving a commanded velocity of 0, and the outer wheel receiving a commanded velocity of $2v_c$. $R'_{A_c} = 0.57m$.

Definition 11 Using the definition of R' and Table 21, then $R'_H = \dfrac{B_{s_H}}{2} = 0.325$ m. In other words, R'_H is the actual turning radius that the Husky follows when R'_{H_c} is commanded to it.

Definition 12 Using the definition of R' and Table 20, then $R'_A = \dfrac{B_{s_A}}{2} = 0.84$ m. In other words, R'_A is the actual turning radius that the Argo J5 follows when R'_{A_c} is commanded to it.

In subsection 6.3.2, it is shown that the minimum energy always happens at $R_1 = R_2 = R'$ (R'_A for Argo J5 and R'_H for Husky). Therefore, several CLC maneuvers are commanded at and around the commanded R' (R'_{A_c} for Argo J5 and R'_{H_c} for Husky UGV). Specifically, the tests in Table 19 are performed with the following commanded turning radii:

- $0.5R'_{A_c}$ and $0.5R'_{H_c}$

- R'_{A_c} and R'_{H_c}

- $1.5R'_{A_c}$ and $1.5R'_{H_c}$

- $2R'_{A_c}$ and $2R'_{H_c}$

Figure 55: A CLC path performed by Husky rover

For the Husky UGV, 2 tests each were conducted at each commanded turning radius for $(45^o, 45^o)$ and $(90^o, 90^o)$ start /end angles. Only a single $(10^o, 10^o)$ test was performed at R'_{H_c}. Also, for each of the CLC tests, a corresponding PLP test is performed. As an example, one of the resulting CLC paths traversed by the Husky UGV is shown in Fig. 55.

For each test, the actual turning radius driven was derived from laser total station measurements. These experimentally measured turning radii are denoted R_e.

Fig. 56 shows the energy consumption of each CLC path (E_{CLC}) compared to the energy consumption of the corresponding PLP path (E_{PLP}). Energy consumption over each path is measured with the TI INA226 bidirectional current and power sensor on the Husky, and onboard motor current and voltage sensors on the Argo. This comparison is quantified as a percentage difference given by the following equation:
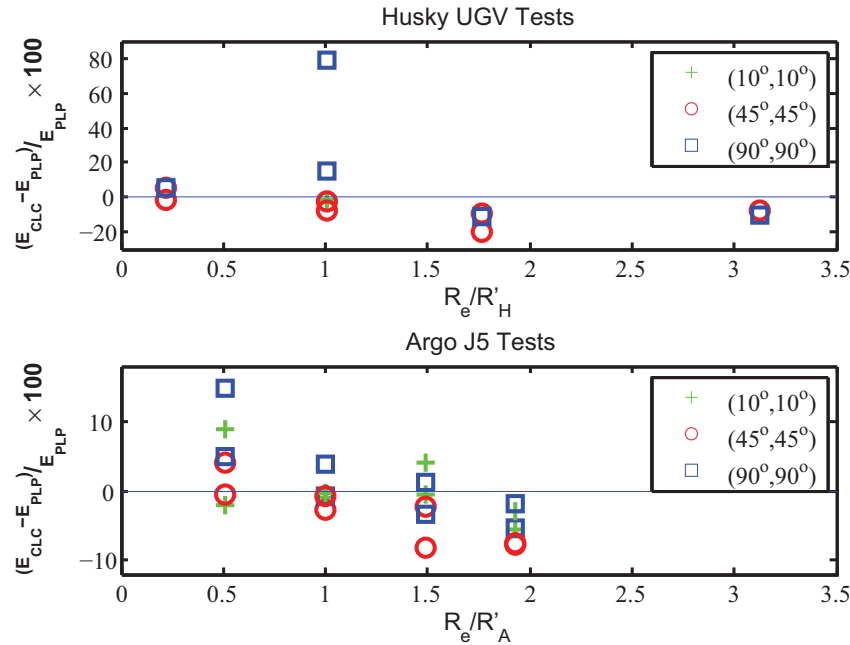
Figure 56: Comparison of Husky and Argo experimental results

$$\frac{E_{\mathrm{CLC}} - E_{\mathrm{PLP}}}{E_{\mathrm{PLP}}} \times 100 \tag{229}$$

In cases where the above metric is negative, the energy consumed by the CLC path is lower than the corresponding PLP path; these cases appear below the reference line in Fig. 56. As it can be seen in the figure, the energy consumption of CLC is less than PLP (the percentage < 0) for the following conditions:

- when (θ_A, θ_C) is $(45^o, 45^o)$, for both Husky and Argo J5 the turning radius should be $R \geq R'$.

- when (θ_A, θ_C) is $(90^o, 90^o)$, for both Husky and Argo J5 the turning radius should be $R > 1.5R'$.

- when (θ_A, θ_C) is $(10^o, 10^o)$, the performed tests show that $R > 1.5R'$ for Argo J5. No tests at $(\theta_A, \theta_C) = (10^o, 10^o)$, when $R > R'$, for Husky UGV are performed.

It is worth noting that during one test at R'_H and $(\theta_A, \theta_C) = (90^o, 90^o)$, E_{CLC} is 80% higher than E_{PLP}. A high degree of slip occurred during this test. Also, as the figure indicates, at almost $R_e = 3.2R'_H$ the energy percentage a bit increases, compared to the tests performed at $R_e = 1.8R'_H$. Therefore, it is possible that the minimum percentage happens in the $1.8R'_H < R_e < 3.2R'_H$. However, more tests should be performed to provide more precise results (future work).

Conclusion of the Subsection: CLC paths often consume less energy than PLP paths. Such cases can be found for turning radii at or above R' (R'_H and R'_A). However, CLC paths at exactly R' risk a possible significant *increase* in energy consumption. In Fig. 56 it can be seen that the best performance of CLC paths relative to PLP paths (consistent energy savings of up to 10% and 20% for the Argo and Husky, respectively) is observed just below $\left\{ \dfrac{R_e}{R'_H}, \dfrac{R_e}{R'_A} \right\} = 2$. Future work will study this region of the performance curve in greater detail, and attempt to link the results to a experimental power curve.

6.3.4 Elaboration on Some of the Experimental Tests

Some of the experiments shown in Fig. 56 are further elaborated here. They correspond to CLC and PLP tests of $(45^o, 45^o)$ tests at $0.5R'_{H_c}$, R'_{H_c}, and $1.5R'_{H_c}$ with the Husky rover. The energy consumption for these different scenarios are reported in Table 24.

Table 24: CLC and PLP tests of $(45^o, 45^o)$ tests at $0.5R'_{H_c}$, R'_{H_c}, and $1.5R'_{H_c}$ with the Husky rover

Scenario's Index	Path Type	R_1 (m)	R_2 (m)	Energy (J)
1	CLC	$0.5R'_{H_c}$	$0.5R'_{H_c}$	2331.36
2	PLP	0	0	2202.57
3	CLC	R'_{H_c}	R'_{H_c}	1975.263
4	PLP	0	0	2147.30
5	CLC	$1.5R'_{H_c}$	$1.5R'_{H_c}$	2055.845
6	PLP	0	0	2275.57
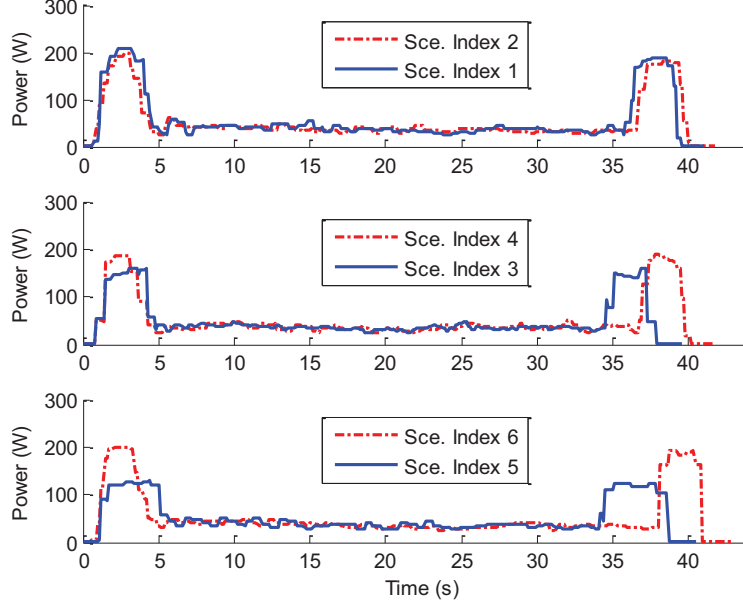
Figure 57: Power consumptions for different scenarios reported in Table 24

Based on Table 24, CLC paths of Index 3 and 5 have 8% and 11% less energy consumption compared to corresponding PLP paths of Index 4 and 6, respectively. These two results confirm an aspect of the optimal solution obtained numerically in Table 23, namely that the minimum energy consumption should happen for the path other than PLP paths. Also, the power consumptions are shown in Fig. 57.

As Fig. 57 shows, both of the peak power and the total time duration of power consumption for PLP paths of Index 4 and 6 are greater than CLC paths of Index 3 and 5, respectively. Accordingly, the energy consumption for the PLP is greater than CLC paths; Table 24 confirms this (2147.30 J > 1975.263 J and 2275.57 J > 2055.845 J).

6.3.5 Comparing the Theoretical and Experimental Results

The simulation results presented in subsection 6.3.2 predict that the minimum energy consumption should happen at the CLC paths with the following specifications:

- $R_e = R'_H$ for Husky UGV

- $R_e = R'_A$ for Argo J5

However, the experimental tests (subsection 6.3.3 and 6.3.4) indicate that minimum energy consumption occurs with CLC tests at turning radii in the following ranges:

- $R_e \in (1.5R'_H, 2R'_H)$ for Husky UGV

- $R_e \in (1.5R'_A, 2R'_A)$ for Argo J5

The difference between theoretical and experimental work is possibly due to (20) (the existing power model) being designed for skid-steer rovers on hard flat ground. It does not consider the bulldozing effect of skid-steer rover wheels on loose sands or any other

111

potentially complex wheel-soil interactions (e.g. slip sinkage). Therefore, (20) can not model the power around R' on loose sands correctly. Hence, our future work is to revise the existing power model by considering the accumulated sand from bulldozing the ground with the rover's wheels.

6.3.6 Conclusions of the Subsection

Energy-efficient path planning for skid-steer rovers is investigated in this research. As the power consumption of a skid-steer rover is highly dependent on the path's turning radius, it is considered explicitly in our calculation of consumed energy. Based on some simplifying assumptions, new path models are proposed. The assumptions are the rover moves forward on flat ground with constant sum of absolute values of right and left velocity. Numerical simulations are performed to find the optimal path from among a predefined class of paths: a combination of circular arcs and line segments (CLC paths). Experiments are conducted to compare against the theoretical predictions. From the evaluations and investigations reported here, the following findings are concluded:

- Numerically optimizing CLC paths for energy-efficiency shows that, for the existing power model and all cases examined, $R = R'$ gives the minimum energy consumption.

- Results obtained from experiments show that turning radii slightly bigger than R'_A and R'_B (up to twice these values) give minimum energy consumption for Argo J5 and Husky UGV, respectively.

- Experimental results indicate that CLC paths are more efficient than PLP in many scenarios, and a CLC path with lower energy than its corresponding PLP path could always be found for the start/end pose scenarios studied.

- The discrepancy between theoretical work and experiments is likely due to power model deficiencies on loose sandy soil.

- A new power model is required for skid-steer rovers on sand.

Accordingly, future work is defined as follows:

- Revising the existing power model for skid-steer rovers by considering the effects of accumulated sand and sinkage on the power consumption.

6.4 Sensitivity Analysis for the Power Model's Coefficients

In the following, the sensitivity analysis for the Husky UGV, with the specifications in Table 16, for the energy efficiency is provided. The considered scenario is a R'-CLC maneuver going from $(0, 0, \frac{\pi}{4})$ to $(10, 0, \frac{\pi}{4})$. The utilized energy function is stated in Eq. (222). The related parameters which are μ and G are varied with the ranges of $[0, 1]$ and $[0, 100]$, respectively. The ranges for the parameters are considered based on the experiments performed with Husky UGV on hard ground and loose soil. Hence, using the

energy equation while the parameters are changing in the mentioned ranges, the following figure is obtained.
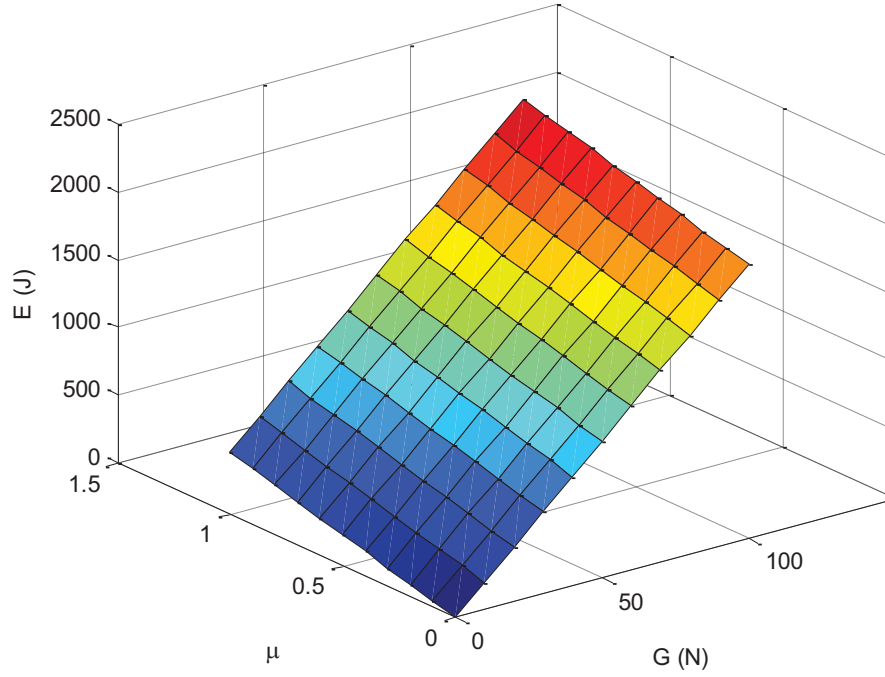
Figure 58: Sensitivity analysis for the energy consumption of a R'-CLC path

Since the power model (Eq. (20)) has a linear relation to both the parameters (μ and G), the expectation is the linear relation between the energy (integral of power) and the parameters. As it can be seen from Fig. 58, the figure is a plane.

Although we have not done sensitivity analysis for other path types, the fact that the power model (Eq. (20)) is linear with respect to μ and G suggests that the sensitivity analyses for the other path types are also likely to result in planes. So, it would be possible to use those planes in an overall sensitivity analysis of the optimal map to see how the optimal map changes with small changes to theese parameters. The mentioned analysis is a suggestion for future work.

7 Optimal Traction Forces for Four-Wheel Rovers on Rough Terrain
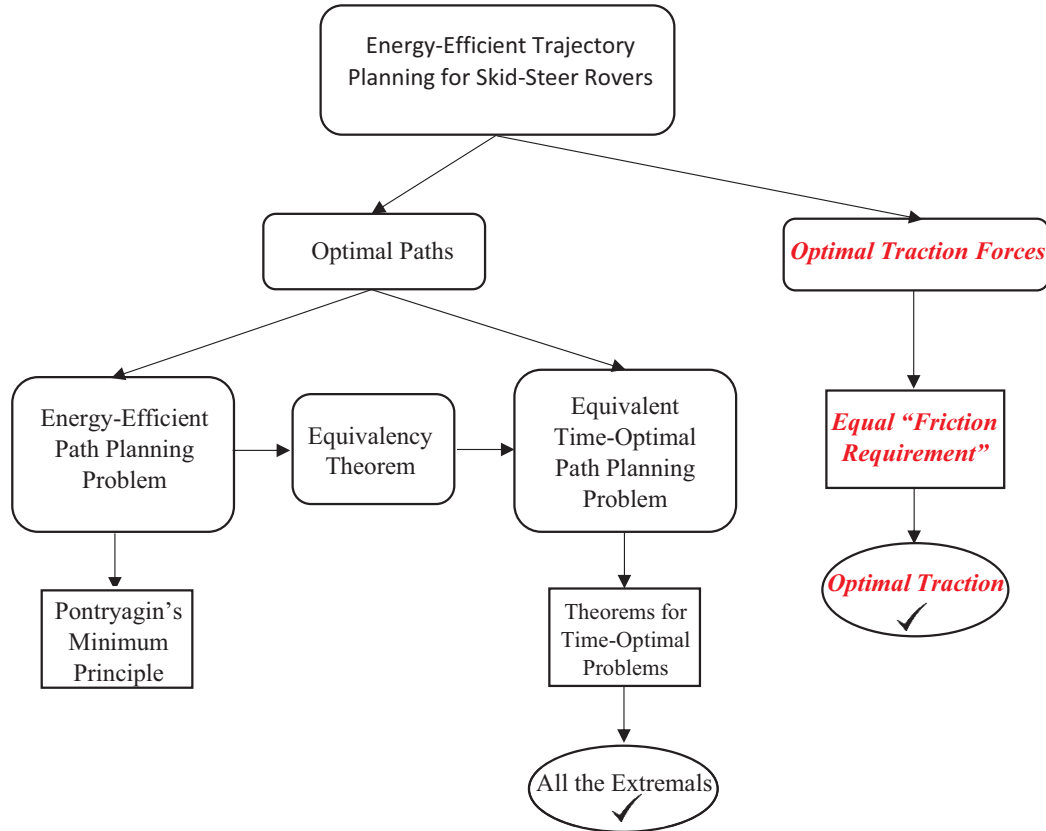
Figure 59: The tasks performed in this chapter are highlighted.

This work addresses the minimization of the risk of wheel slippage for a popular class of rovers. In the absence of any constraints on the system (e.g. force/torque balance, maximum motor torques), the optimal traction solution is known to be that with equal "friction requirements" (ratios of tractive to normal force) for all wheels. Nevertheless, the current state-of-the-art is to routinely perform computationally expensive constrained optimization, because of the presumed importance of the constraints in a real system. The contribution of this work is a thorough investigation of the configuration space for 4-wheel rovers, driving straight over rough terrain, in search of configurations where the unconstrained optimal answer does or does not satisfy the constraints, and thus, is or is not valid. Equal "friction requirements" are added to the 4-wheel rover's system of quasi-static equations and a valid solution is sought to this augmented system of equations. It is found that the equal "friction requirements" solution is almost always valid, except for the case where two of the wheels

114

are wedged against opposing vertical faces, a highly unusual and unlikely scenario. Therefore, we can conclude that computationally expensive constrained optimization is not required to achieve traction control for 4-wheel rovers.

7.1 Introduction

It is highly desirable that wheeled rovers and vehicles sustain forward motion without losing traction throughout their operations on rough terrain that each wheel may be encountering at different and continuously changing heights and local slope angles. Such motion occurs in many fields including agriculture, construction, mining, forestry, search and rescue, as well as planetary exploration. In many such cases, detailed terrain knowledge is generally unknown beforehand.

In some related work, slip is controlled by adjusting the rover's commanded wheel velocities. In [98], a desired (low) slip value is commanded and feedback from measured wheel rotation and overall rover forward motion is used to adjust the inputs to the wheel motors, while also limiting motor inputs based on a maximum torque that the soil is estimated to be able to support in shear. In [99], local terrain geometry is taken into account to adjust each wheel's speed individually to achieve more uniform slip between the wheels and thus reduce it overall.

Another fundamental approach is to control wheel torque directly, in which case it is possible to minimize the maximum ratio of the tangential to the normal force ("*friction requirement*" [100] [101]) experienced by any of the wheels [102]. This idea results in obtaining optimal traction for rough-terrain rovers to avoid wheel slippage. Assuming homogeneous or generally unknown (and thus homogeneous by best guess) solid terrain materials, this minimizes the chances of any of the wheel-terrain contacts exceeding the friction coefficient and thus losing traction. It is important to note that although defined in terms of frictional contacts, the concept has been extended and shown to be relevant to soils as well [103], making the approach relevant in sum to a very wide range of the applications mentioned above. In addition, this approach can be used to obtain the optimal traction forces not only for wheeled rovers, but also for legged robots and hybrid wheel-leg rovers [104].

It is generally accepted that the solution to the minimization of maximum "friction requirement" is to enact forces such that the "friction requirement" is the same for all wheels [102] [105]. If a tangential force is reduced on any of the wheels, at least one of the other wheels would need to increase its tangential force to maintain the quasi-static force/moment balance. This solution is presented as analogous to an optimal frictional grasping problem [102], for which equal ratios of tangential to normal forces (and thus "friction requirements") for all contact points is the optimal solution [106]. Krebs et al. [107] apply the idea (used in [106]) on CRAB and present the preliminary results. They show that the slippage is reduced at least 23% compared to using other methods such as Wheel Velocity Synchronization. In [102] (specifically, in the explanations for Eq. (3) of that paper) it is explicitly mentioned that the equations obtained from equal "friction requirement" can be added to the existing forces and moments equations of the rover to obtain the optimal traction forces of Gofor (a legged rover).

An important caveat, however, is that this set of forces can only be a true solution

to the rover traction optimization problem if it satisfies all the constraints, such as the force/moment balance for a particular rover. It has been shown that this cannot in general be taken for granted [105]. Lamon et al. [105] analyzed their novel 6-wheel "Shrimp" rover, and found that setting the torques to achieve equal "friction requirement" produces a valid solution only approximately 78% of the time (Figure 7 in [105], under the validation block for the Fixed Point Method). They use Fixed Point method to solve an unconstrained optimization problem to find the optimal tractions. Then, they check the validity of the obtained values (e.g. whether traction forces can be produced by the motor). No further analysis was undertaken to identify general distinctions between the configurations for which equal friction requirements did or did not produce valid optimal traction solutions. For the cases that equal friction requirements do no end up to valid solutions, they use Gradient Method to solve the constrained optimization problem which is more computationally expensive than solving the unconstrained problem. Iagnemma and Dubowsky [103] routinely perform constrained optimization, without ever explicitly checking the equal "friction requirements" solution.

This work investigates optimal traction forces for a 4-wheel rover. Specifically, the situation studied is where the rover is attempting to drive forward on rough terrain with all its wheels aligned pointing forward. Further, it is assumed that the rover is operating at low enough speeds that quasi-static assumptions hold. The work focuses on rovers that independently control wheel torque (i.e. motor torque) for each of their four wheels, and that maintain contact between all the wheels and a rough terrain by means of a passive rigid suspension. The latter is commonly achieved with a differencing bar/beam. An example of a rover that meets these criteria is Scarab [108].

One important class of rover that falls within the scope of our work is a skid-steer rover with four wheels (like Scarab, the example cited above). Such a rover, does not steer its individual wheels, but instead drives the left and right-side wheels at different speeds to turn like a tank. It always has all its wheels aligned pointing forward; so, anytime it is driving straight the situation studied here will apply. Skid-steer rovers are a very popular configuration due to their mechanical simplicity, from the Clearpath Husky to the Soviet Union's 8-wheel Lunokhod rovers and a series of rovers recently developed for the Canadian Space Agency (CSA) such as Juno [109], LRPDP, SPRP [110], and Artemis [111].

In this paper, we analyze a 4-wheel rover to determine in which configurations does setting the torques to achieve equal "friction requirement" produce a valid solution that satisfies all constraints. The key contribution of this work is the finding that for a very common and important class of rovers, 4-wheel rovers driving forward on rough terrains (which includes the very popular skid-steer rover configuration), the equal "friction requirement" always produces the valid solution except for one very rare and specifically identified exception. Thus, we show there is no need for constrained optimizations in search of sub-optimal solutions for this class of 4-wheel rovers. Instead, it is sufficient to solve a set of equations.

Contributions of our work compared to the three most related papers can be summarized as follows: [102] and [105] work on 6-wheel (Shrimp) and legged (Gofor) rovers, respectively, while the focus of our work is on 4-wheel rovers. In addition, the idea of using equal friction requirement to obtain optimal traction forces is presented/used in both [102] and [105], but, no one investigates the situations in which the idea does or

does not give valid answers. Meanwhile, [103] discusses the optimal traction problem more generally for any rover, but never explicitly addresses the equal friction requirements solution. We show, by performing a numerical simulation for a practical type of 4-wheel rovers, that almost always equal friction requirement can be used to obtain optimal traction forces. Our finding results in avoiding extra optimization processes that are computationally expensive.

This article is organized as follows: firstly, the related work and the motivation that it gave us to start our research are explained. Then, the problem is formalized in "problem statement" section. Moreover, "methodology" section presents theoretical part for investigations of the configuration spaces for single-wheel, 2-wheel, and the full 4-wheel rovers of interest. Furthermore, in the "numerical approach and results" section an example of practical 2-wheel and 4-wheel are analyzed numerically to find the optimal tractions. Moreover, our suggested method is compared with other methods in "system uncertainty and performance" section. Finally, the contributions and importance of our work are summarized in the "conclusion" section.

7.2   Related Work

The most related work to our research is further explained in this section.
Optimization Problem: the optimization problem to avoid wheel slippage is as follows [105]:

$$\underset{T_i,N_i}{\text{minimize}} \quad \max\{\mu_i^f\}, \ i = 1,...,n_w$$
$$\text{subject to} \quad \Sigma\boldsymbol{F} = 0 \tag{230}$$
$$\Sigma\boldsymbol{M} = 0$$
$$N_i \geq 0$$

where μ_i^f ($\frac{T_i}{N_i}, i = 1,...,n_w$) is the *"friction requirement"*; and, n_w is the number of wheels. Also, T_i and N_i are the traction and normal force of each wheel. Moreover, $\boldsymbol{F}$ and $\boldsymbol{M}$ are the forces and moments applied to the rover.
Related fact: the solution to the optimization problem in the absence of any of the constraints is [102] [105]:

$$\frac{T_1^*}{N_1^*} = ... = \frac{T_{n_w}^*}{N_{n_w}^*} \tag{231}$$

Idea: Lamon et al. [105] have used (231) and the constraints in (230) to find candidate optimal traction and normal forces for a 3-wheel planar rover. Accordingly, they solve the following set of equations.

$$\begin{cases} \Sigma\boldsymbol{F} = 0 \\ \Sigma\boldsymbol{M} = 0 \\ \frac{T_1}{N_1} = \frac{T_2}{N_2} = \frac{T_3}{N_3} \ (\mu_1^f = \mu_2^f = \mu_3^f) \end{cases} \tag{232}$$

Motivation for Our Work: Lamon et al. [105] find that the optimal solutions of (232) are valid in 78% of the cases (Figure 7 in [105], under the validation block for the Fixed Point Method). However, they have not shown in which conditions the valid answers cannot be

found. Hence, for the remaining 22% of cases, they have solved the optimization problem in (230) using Gradient Method (the Gradient Method block at Figure 7 in [105]). The distinction between these cases is important, especially in on-line operation, as it determines how much extra computation is required for solving constrained optimizations (i.e. problem (230)). An example is presented in 7.6.2 to show the superiority of solving a set of equations instead of an optimization problem for four-wheel rovers.

7.3   Problem Statement

Problem: To investigate whether there is any predictable set of scenarios that lead to the cases where an equal "friction requirement" optimal solution, for avoiding wheel slippage, is invalid. In other words, we identify in which conditions the following system of nonlinear equations can be solved to find T_i and N_i:

$$\begin{cases} \Sigma \boldsymbol{F} = 0 \\ \Sigma \boldsymbol{M} = 0 \\ \frac{T_1}{N_1} = ... = \frac{T_{n_w}}{N_{n_w}} \end{cases} \tag{233}$$

Assumptions:

- The rover operates at low enough speeds that quasi-static assumptions (i.e. the force and moment equilibrium listed in (233)) hold.

- The rover drives straight forward

- The rover moves on rough terrain

In particular, we consider these equations for 4-wheel (and first 2-wheel) rovers, with configurations typical of skid-steer rovers for example.

In (233), for both 2-wheel vehicles (section 7.4.2) and 4-wheel rovers (section 7.4.3) the equations of motion ($\Sigma \boldsymbol{F} = 0, \Sigma \boldsymbol{M} = 0$) contain more unknowns than equations. The additional degree(s) of freedom enable the optimization, with the candidate solution to this optimization included via the extra equations ($T_1/N_1 = ... = T_{n_w}/N_{n_w}$).

7.4   Methodology

This section investigates rover configurations in which the candidate optimal solution is or is not valid. The analyses progress from single-wheel to two-wheel and finally four-wheel vehicles. Our methodology is to explicitly add equations representing an optimal solution to a rover's system of equations (as it is shown in (233)). Analytical solutions are discussed in this section and the numerical results are presented in section 7.5. Also, practical considerations are discussed in section 7.7 regarding the application of these

results to real rovers.

7.4.1 Optimal Traction Force for a Single-Wheel Vehicle

A wheel (Fig. 60) is balanced if the following equation for normal (N) and traction force (T) is held [105]:

$$T \leq \mu_0 N$$
$$T = \frac{M}{r} \tag{234}$$

where μ_0, M, and r are the static friction coefficient, moment, and wheel radius, respectively.
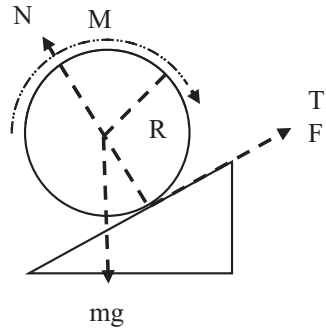
Figure 60: A wheel on a slope (m and g are the mass and gravitational acceleration, respectively)

When μ_0 is known, the relation between the traction and normal force can be obtained from the following relation [105]:

$$\frac{T}{N} \leq \mu_0 \tag{235}$$

However, since it is impossible to know μ_0 precisely (wheel interaction with an unknown terrain determines it), another approach should be taken. Assuming that the wheel does not slip makes it possible to calculate the forces T and N as a function of the moment. Therefore, to avoid the wheel slippage, T/N can be minimized. Considering the previous assumption, let's define [105]:

$$\frac{T_i}{N_i} = \mu_i, \ i = 1,...,n_w \tag{236}$$

As it can be seen, μ_i is similar to a friction coefficient. In minimizing the ratio, i.e. minimizing μ_i, we optimize our chances that this coefficient is smaller than the real static friction coefficient (μ_0). If this happens, there is no slip. Therefore, even without knowing the μ_0, the ratio of T/N should be minimized.

It should be mentioned again that (236) is valid for rigid frictional terrain [103]. The same equation can also be used for soils with low or no cohesion. For rigid wheels traveling over non-rigid terrain, the following relation can be written [103].

$$T_i \le (cA_i + N_i \tan\phi) \tag{237}$$

where c is the terrain cohesion, ϕ is the terrain internal friction angle, and A is the wheel-terrain contact area. The parameters c and ϕ could be estimated on-line [103]. When the terrain is soil with low or no cohesion, c is negligible (or zero). Accordingly, (237) can be written in the following format:

$$T_i \le N_i \tan\phi \tag{238}$$

Therefore, for soils with low or no cohesion, μ_i is $\tan\phi$, and the same minimization of T/N applies as for rigid terrains.

7.4.2 Optimal Traction Forces for a 2-Wheel Rover

In the following, firstly, the conditions are discussed in which the optimal answers, calculated by using (233) for a 2-wheel rover, are not feasible. Then, a simulation example is presented to demonstrate the superiority of using equal "friction requirement" to equal torques in obtaining the optimal forces.

7.4.2.1 Conditions to Avoid Slippage for the 2-Wheel Rover the schematic figure of the 2-wheel case is shown in Fig. 61. The purpose is to solve the following set of equations for T_1, T_2, N_1, and N_2.

$$\begin{cases} \Sigma \mathbf{F} = 0 \\ \Sigma \mathbf{M} = 0 \\ T_1 N_2 - T_2 N_1 = 0 \end{cases} \tag{239}$$

where $\Sigma \mathbf{F} (\Sigma F_x, \Sigma F_y)$ as well as $\Sigma \mathbf{M} (\Sigma M_k)$ are as follows:

$$\Sigma F_x = T_1 cos\theta_1 - N_1 sin\theta_1 + T_2 cos\theta_2 - N_2 sin\theta_2 = 0 \tag{240}$$

$$\Sigma F_y = T_1 sin\theta_1 + N_1 cos\theta_1 + T_2 sin\theta_2 + N_2 cos\theta_2 \\ - m_1 g - m_2 g = 0 \tag{241}$$

$$\Sigma M_k = m_1 g sin\theta_1 r_1 - m_2 g \Delta x_{kc_2} + N_2 sin\theta_2 \Delta y_{ks} \\ + N_2 cos\theta_2 \Delta x_{ks} + T_2 sin\theta_2 \Delta x_{ks} - T_2 cos\theta_2 \Delta y_{ks} = 0 \tag{242}$$

$$\Delta y_{ks} = r_1 cos\theta_1 + l sin\alpha - r_2 cos\theta_2 \tag{243}$$

$$\Delta x_{ks} = r_2 sin\theta_2 + l cos\alpha - r_1 sin\theta_1 \tag{244}$$

$$\Delta x_{kc_2} = l cos\alpha - r_1 sin\theta_1 \tag{245}$$

where T_i, N_i (i=1,2), F_x, F_y, and M_k are the traction force, normal force, force in the x direction, force in the y direction, and moment around point k, respectively. Also, m$_i$, θ_i, and c$_i$ ($i = 1, 2$) are mass, angle of slope, and center of a wheel, respectively. Moreover, l and α are the length of the rod and its angle with the x axis. In addition, s and k are the contact points of each wheel with the slopes. Furthermore, r_1 and r_2 are radius of the first and second wheels, respectively.
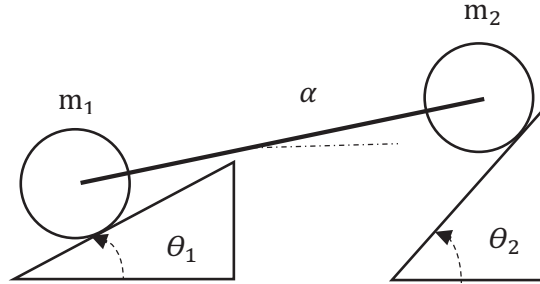
Figure 61: Two-wheel rover on slopes

Analytical Approach: analytical solutions were also sought to the optimal system of equations (shown in (239)), to see if additional insight could be gained into the regions with no solution. Singularities of the resulting equations were analyzed in light of their potential physical relevance. However, the analytical methods produced some conditions for which solutions were indeterminate even though numerical solutions could be found (see appendix D). In other words, singularities were found that did not necessarily always correspond to physical conditions lacking a solution but rather just limitations of the analytical method in finding those solutions. It was judged that such results detracted from, rather than enhanced, the clarity of the numerical results. Furthermore, it was found that the analysis could not be extended to the physically relevant 4-wheel rover anyway, as explained in the next section. Finally, the analytical results themselves involve dozens of pages of equations. For all these reasons, the details of the analyses are omitted for brevity.

7.4.3 Optimal Traction and Normal Forces for the 4-Wheel Rover

In this subsection, a case for a 4-wheel rover is considered. Fig. 62 shows the 4-wheel rover on rough terrain. As it can be seen, each wheel contacts the terrain at a different height and at a different contact angle.

7.4.3.1 Assumptions   the assumptions which are considered for the 4-wheel rover are as follows:

- Operating at low enough speeds that quasi-static assumptions hold.

- Driving forward

- Moving on rough terrain

- The rover's roll angle (ϕ) is small enough to be neglected

- The cross-bar connecting the two sides of the rover is assumed horizontal
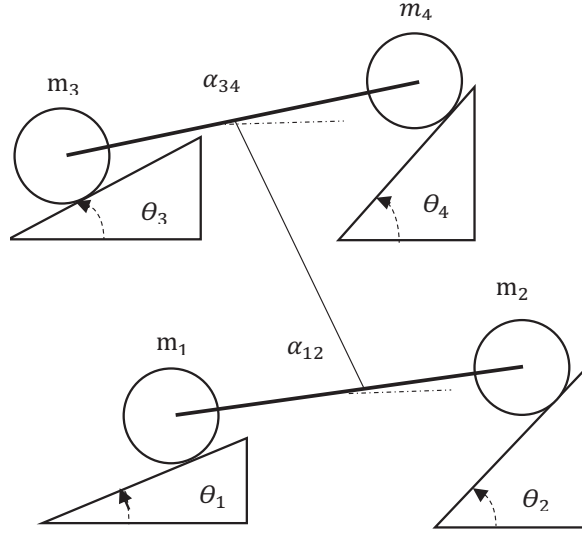
Figure 62: The four-wheel rover on rough terrain

7.4.3.2 Equations to Obtain Optimal Forces   in the following, equations of motion and equal "friction requirement" for the 4-wheel rover are presented.

$$\Sigma \boldsymbol{F} = 0 \tag{246}$$

$$\Sigma \boldsymbol{M} = 0 \tag{247}$$

$$T_1 N_2 - T_2 N_1 = 0 \tag{248}$$

$$T_2 N_3 - T_3 N_2 = 0 \tag{249}$$

$$T_3 N_4 - T_4 N_3 = 0 \tag{250}$$

The equations for $\Sigma \boldsymbol{F}$ and $\Sigma \boldsymbol{M}$ are obtained according to the following calculations.

$$\Sigma \boldsymbol{F} = \sum_{i=1}^{4} \vec{\boldsymbol{F}}_i^{I} \tag{251}$$

$$\Sigma \boldsymbol{M} = \sum_{i=1}^{4} \vec{\boldsymbol{M}}_i^{I} \tag{252}$$

122

where $\vec{F}_i^I$ and $\vec{M}_i^I$ are the forces and moments applied to each wheel in the inertial frame, respectively. They can be obtained from the following equations:

$$\vec{F}_i^I = R_{w_i}\vec{F}_{T_iN_i}^{B_i} + \vec{W}_i^I, i = 1,...,4 \tag{253}$$

$$\vec{M}_i^I = \vec{r}_{T_iN_i}^I \times \vec{F}_{T_iN_i}^I + \vec{r}_{W_i}^I \times \vec{W}_i^I, i = 1,...,4 \tag{254}$$

where $\vec{F}_{T_iN_i}^{B_i}$ and $\vec{F}_{T_iN_i}^I$ are the applied traction and normal force to each wheel in its body coordinate system and inertial frame, respectively. Also, R_{w_i} is the transfer matrix for each wheel that transfers forces from the body to the inertial coordinate system. Moreover, $\vec{W}_i^I$ is the vector of weight applied to each wheel, while, $\vec{r}_{T_iN_i}^I$ is the positions of contact point of each wheal to the ground, in the inertial frame. Also, $\vec{r}_{W_i}^I$ is the position of each wheel's center in the inertial frame.

$$\Delta\alpha = \alpha_{34} - \alpha_{12} \tag{255}$$

$$\alpha_{13} = -sin^{-1}(L\frac{sin(\Delta\alpha)}{2l_{13}}) \tag{256}$$

$$\vec{F}_{T_iN_i}^{B_i} = \begin{bmatrix} T_i \\ 0 \\ -N_i \end{bmatrix}, i = 1,...,4 \tag{257}$$

$$\vec{W}_i^I = \begin{bmatrix} 0 \\ 0 \\ m_ig \end{bmatrix}, i = 1,...,4 \tag{258}$$

$$R_{w_i} = \begin{bmatrix} cos(\theta_i) & 0 & -sin(\theta_i) \\ 0 & 1 & 0 \\ sin(\theta_i) & 0 & cos(\theta_i) \end{bmatrix} \tag{259}$$

$$R_{R_{ij}} = \begin{bmatrix} cos(\alpha_{ij}) & 0 & -sin(\alpha_{ij}) \\ 0 & 1 & 0 \\ sin(\alpha_{ij}) & 0 & cos(\alpha_{ij}) \end{bmatrix}, \\ (i,j) \in \{(1,2),(3,4)\} \tag{260}$$

$$\vec{r}_{T_1N_1}^I = \begin{bmatrix} x_1 \\ y_1 \\ z_1 \end{bmatrix} \tag{261}$$

$$\vec{r}_{W_1}^I = \vec{r}_{T_1N_1}^I + R_{w_1}\begin{bmatrix} 0 \\ 0 \\ -r_1 \end{bmatrix} \tag{262}$$

$$\vec{r}_{T_2N_2}^I = \vec{r}_{W_1}^I + R_{R_{12}}\begin{bmatrix} l_{12} \\ 0 \\ 0 \end{bmatrix} + R_{w_2}\begin{bmatrix} 0 \\ 0 \\ r_2 \end{bmatrix} \tag{263}$$

123

$$\vec{r}^I_{W_2} = \vec{r}^I_{W_1} + R_{R_{12}} \begin{bmatrix} l_{12} \\ 0 \\ 0 \end{bmatrix} \tag{264}$$

$$\vec{r}^I_{T_3 N_3} = \vec{r}^I_{W_1} + \begin{bmatrix} 0 \\ l_{13} cos(\alpha_{13}) \\ -l_{13} sin(\alpha_{13}) \end{bmatrix} + R_{w_3} \begin{bmatrix} 0 \\ 0 \\ r_3 \end{bmatrix} \tag{265}$$

$$\vec{r}^I_{W_3} = \vec{r}^I_{W_1} + \begin{bmatrix} 0 \\ l_{13} cos(\alpha_{13}) \\ -l_{13} sin(\alpha_{13}) \end{bmatrix} \tag{266}$$

$$\vec{r}^I_{T_4 N_4} = \vec{r}^I_{W_3} + R_{R_{34}} \begin{bmatrix} l_{34} \\ 0 \\ 0 \end{bmatrix} + R_{w_4} \begin{bmatrix} 0 \\ 0 \\ r_4 \end{bmatrix} \tag{267}$$

$$\vec{r}^I_{W_4} = \vec{r}^I_{W_3} + R_{R_{34}} \begin{bmatrix} l_{34} \\ 0 \\ 0 \end{bmatrix} \tag{268}$$

where m_i (i=1,...,4), L, and l_{13} are mass of the wheels, and lengths of the rods, respectively. Also, α_{12}, α_{13}, and α_{34} are the rover configuration angles. It should be noted that for simplicity the roll and yaw angles for each wheel are considered equal to zero.

7.4.3.3 Analytical Approach

The first approach is to solve (246) to (250) analytically for T_i and N_i ($i = 1,...,4$). However, in appendix E it is shown that according to Abel's impossibility theorem [112] there is not any algebraic solution in radicals for the set of equations. Accordingly, numerical methods are utilized to solve the set of equations.

7.5   Numerical Simulations and Results

In this section, optimal traction forces to avoid slippage for a practical two-wheel and four-wheel rover are obtained.

7.5.1   Numerical Simulation for a Two-Wheel Rover

In this section, firstly a simulation example is presented that illustrates the advantages of enforcing equal "friction requirements," as presented in "Introduction" and "Problem statement" sections. Then, the results of numerical analysis for obtaining the optimal traction forces are reported.

7.5.1.1   Simulation example

This subsection presents a simulation example that illustrates the advantage of setting torques so as to achieve equal "friction requirement," compared to setting equal torques.

The example presents a planar 2D rover like described above. The masses at the wheels are $m_1 = m_2 = 1 \ kg$. The wheels are both of radius $r = 0.05 \ m$, and the wheel centers are offset by a rigid wheelbase of $l = 0.15 \ m$. Gravitational acceleration of $1.63 \ m/s^2$ is simulated to represent a rover on the Moon.

The rover is constrained to remain in contact with the terrain. Deformation of the terrain is neglected, such that the wheel center is always located a distance r from the terrain, perpendicular to the local slope at the contact point. The wheel center locations are denoted (x_i, y_i) for $i = 1, 2$. As the wheel travels over reasonably benign terrain, the location of the wheel center traces out a path that can be described by a function $y_i = f(x_i)$ ($i = 1, 2$). The fact that the wheels have equal radii implies that the same function holds for both wheels. The following wheel-center terrain-tracing function is selected for this example:

$$y_i = x_i^2 - x_i^3 \tag{269}$$

Control is implemented to maintain a desired body velocity of 0.1 m/s as the rover traverses the terrain described by (269). The initial value of the problem is set such that $x_1(0) = -0.2$. The simulations are run for 10 seconds, within which time the rover moves forward approximately 1 (m). This terrain traversal is shown in Fig. 63.
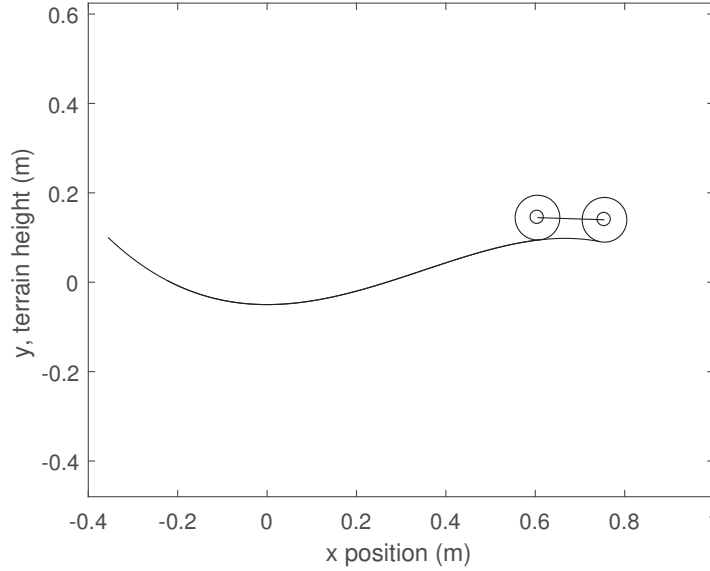
Figure 63: Rover simulation showing terrain traversed in 10 second run

With an equal friction requirement enforced using $T_1 N_2 - T_2 N_1 = 0$, the resulting friction requirement for this 10-second simulation example, for both wheels, is shown in Fig. 64.
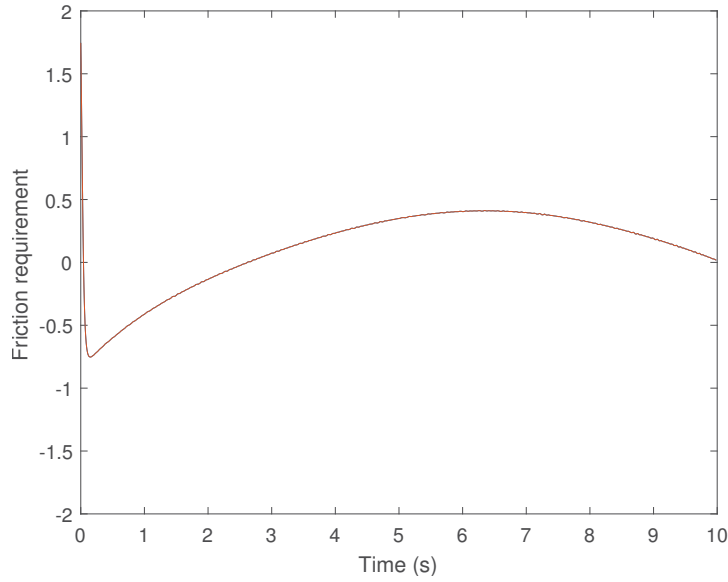
Figure 64: Friction requirements for both wheels throughout the simulation example, when equal friction requirements are enforced.

For comparison, another option for setting torque values that might be considered due to its simplicity is equal torques:

$$T_1 - T_2 = 0 \tag{270}$$

However, as can be seen in Fig. 65, this results in undesirable performance. With equal torques, the friction requirements for the two wheels are not required to stay equal and they in fact do not. From about 3 seconds on, the front wheel has a higher friction requirement meaning it is more likely to slip that the rear wheel. More importantly, comparing to the results in Fig. 64, we see that with equal torques the front wheel is more likely to slip in absolute terms compared to the equal friction requirement case. The friction requirement for the front wheel peaks at 0.57 for the equal torques case, compared to 0.41 for the equal friction requirement case.
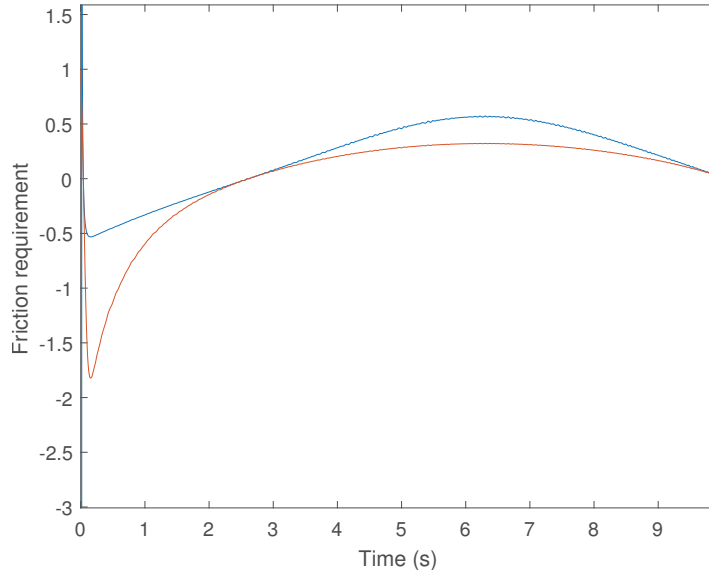
Figure 65: Friction requirements (blue for front wheel and red for rear wheel) when torques are distributed evenly. The front wheel has an increased friction requirement, both in relative and absolute terms.

Table 25: The specifications for a two-wheel rover

Parameter	Value	Unit
m_1	20	kg
m_2	20	kg
r_1	0.5	m
r_2	0.5	m
l	2	m
g	9.81	$\dfrac{m}{s^2}$

7.5.1.2 The Angles for Feasible Optimal Traction Forces (Two-Wheel Rover) The two-wheel rover specifications are reported in Table 25.

Comprehensive configuration space analysis: The range of configuration angles considered for the numerical solution, as well as the constraints checked to determine if a valid solution was obtained are presented in the following.

- Configuration space:

$$\left\{ (\theta_1, \theta_2, \alpha) \,\middle|\, \theta_i (i = 1, 2) \in \left[\frac{-\pi}{2}, \frac{\pi}{2}\right], \alpha \in \left[\frac{-\pi}{3}, \frac{\pi}{3}\right] \right\}$$

127

- Constraints:

$$\{-10\max\{m_1,m_2\}g \le T_i \le 10\max\{m_1,m_2\}g, \ i = 1,2\} \text{ and } \{0 \le N_i \le \max\{m_1,m_2\}g\}$$

In addition, it should be checked that the sign of θ_i and T_i are the same. In better words, if $\theta_i > 0$, then $T_i > 0$ and if $\theta_i < 0$, then $T_i < 0$. All these constraints are imposed to ensure the solver finds physically realistic solutions.

Numerical Analysis Results: subject to the aforementioned constraints, the system of nonlinear equations (239) is solved. Fig. 66 shows values of θ_1 and θ_2 for which a valid solution for T_i or N_i $(i = 1,2)$ is not found. Note that results for all α are overlaid in a single plot.
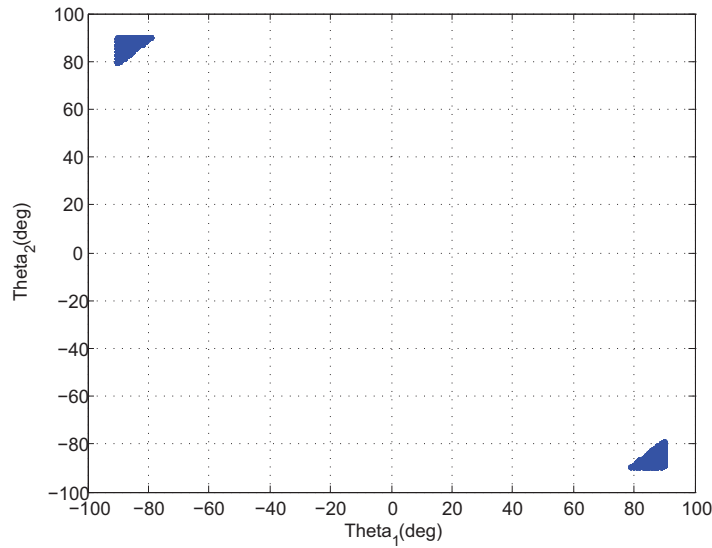
Figure 66: The values of θ_1 and θ_2, for which the numerical method solution is not feasible (results for all α overlaid) for the two-wheel rover

As can be seen from Fig. 66, the only conditions under which the optimal system of equations has no valid solution are when one of the θ_i $(i = 1,2)$ is near +80 to +90 degrees and the other is near -80 to -90 degrees.

7.5.2 Numerical Simulation for a Four-Wheel Rover

The four-wheel rover specifications are reported in Table 26.

The configuration space as well as the constraints for the problem are as follows.

- Configuration space:

$$\left\{ (\theta,\alpha) \ \middle| \ \theta_i \ (i = 1,...,4) \in [\frac{-\pi}{2}, \frac{\pi}{2}], \{\alpha_{12},\alpha_{34}\} \in [\frac{-\pi}{3}, \frac{\pi}{3}] \right\}$$

128

Table 26: The specifications for the rover

Parameter	Value	Unit
m_1	15	kg
m_2	15	kg
m_3	15	kg
m_4	15	kg
r_1	0.3	m
r_2	0.3	m
r_3	0.3	m
r_4	0.3	m
L	1.2	m
l_{13}	1.1	m
g	9.81	$\dfrac{m}{s^2}$

- Constraints:

$\{-10m_1 g \leq T_i \leq 10m_1 g,\ i = 1..4\}$ and $\{0 \leq N_i \leq m_1 g\}$

In addition, it should be checked that the sign of θ_i and T_i are the same. In better words, if $\theta_i > 0$, then $T_i > 0$ and if $\theta_i < 0$, then $T_i < 0$.

Equations (246) to (250) are solved for T_i and N_i ($i = 1,...,4$), in the mentioned configuration space for $\{\theta,\alpha\}$. MATLAB *fsolve* (trust-region-dogleg algorithm) with the function termination tolerance value of 10^{-6} is used. The total number of conditions considered for $(\theta_1,\theta_2,\theta_3,\theta_4,\alpha_{12},\alpha_{34})$ are 22,024,249 (Table 27). The number of answers for T_i and N_i that do not meet the above-mentioned constraints are 16,445 (Table 27).

Table 27: The results of the numerical solving of (246) to (250) for the mentioned configurations space

Different $(\theta_1,\theta_2,\theta_3,\theta_4,\alpha_{12},\alpha_{34})$ in the configurations space	22,024,249
Invalid T_i and N_i (i=1..4)	16,445
Percentage of cases valid	99.93%

According to Table 27, the calculations failed to converge to a valid solution in just 16,445 of the 22,024,249 conditions (0.07% of cases). It is vital to mention that in each one of these "off-condition" cases at least one $\theta_i = \dfrac{\pi}{2}$, ($i = 1,...,4$) and one $\theta_j = \dfrac{-\pi}{2}$ ($j = 1,...,4$),

simultaneously. In other words, the wheel torque optimization for the 4-wheel rover is valid for all cases except when the mentioned conditions happen. This corresponds to two of the wheels being wedged against opposing vertical faces. Although not entirely impossible, it is important to note that this is a highly unusual and unlikely scenario in practice. Therefore, the conditions for which the optimal system of equations has no solution for the 4-wheel rover are directly comparable to those which have no solution in the 2-wheel case (Fig. 66).

It should be noted that the approach to solve for optimal torques described in this paper involves numerically solving a system of non-linear equations. It is important to consider how to set the initialization for such a solver. In on-line applications (on a rover), the result from the previous timestep (for the previous state) is available and this prior solution is used to initialize the solver at the current timestep. At the very first timestep, random re-initializations can be used if required until convergence to a solution is achieved. As will be shown in Section 7.6.1, the solution varies gradually as a function of the inputs, so for smoothly varying terrain the solution from the prior timestep is a good estimate to start the solver for the current timestep. In some cases of a sudden change in input states (e.g. driving into or off of a step obstacle), random re-initializations may perhaps be again required.

7.6 On-line Application, Uncertainty and Performance

Further investigations are presented to show the validity of proposed approach for obtaining the optimal traction forces. Firstly, sensitivity of the optimal outputs to variations in the inputs is investigated. Then, the advantage of considering equal friction requirements instead of solving constrained optimization for four-wheel rovers is presented.

7.6.1 System Uncertainty for the Two-Wheel Rover

Figure 67 provides an example for sensitivity analysis of the optimal outputs to variations in the inputs. Specifically, it shows T_1 as a function of the 2-wheel rover (Fig. 61) inputs with the specifications presented in Table 25. As it can be seen, only at extreme angles for θ_1 and θ_2 is the gradient of T_1 considerable. Over the rest of the range of inputs, the optimal traction force changes gradually as the inputs are varied. Therefore, it can be concluded that the uncertainties which always exist in the sensor measurements for θ_1 and θ_2 will not cause sudden or inappropriate fluctuations in optimal torque output.

7.6.2 Comparison of our Proposed Approach and other Methods

Definition 1: **C**onstrained **O**ptimization problem for **F**our-wheel rover (COF): Solving the optimization problem defined in (230) (with the equality constraints are presented in (251) and (252)) for conditions reported in Table 28.

Definition 2: **N**on-linear **E**quations problem with equal **F**riction requirements for **F**our-wheel rover (NEFF): Solving (246) through (250) for conditions reported in Table 28.

It should be noted that we use NEFF in this paper.
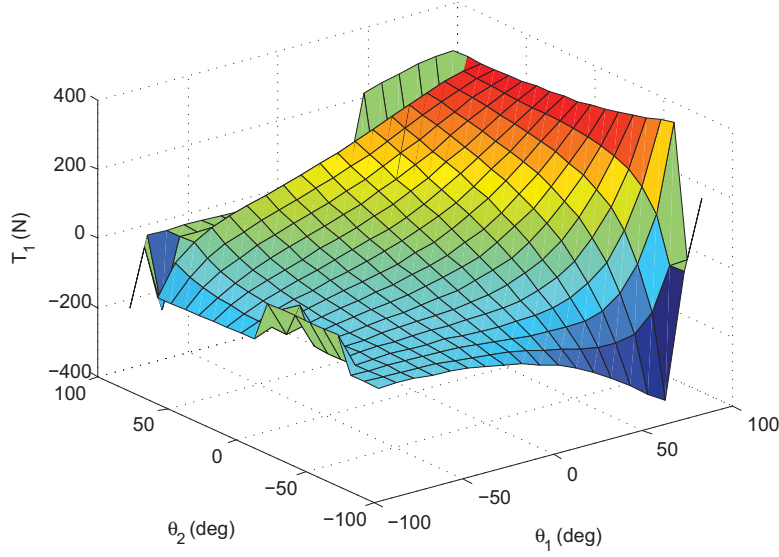
Figure 67: Optimal T_1 versus θ_1 and θ_2 for $\alpha=0$

Table 28: Conditions for comparison of COF and NEFF performances

Parameter	θ_1	θ_2	θ_3	θ_4	α_{12}	α_{34}
Value	[-10º,0]	[-10º,0]	[-10º,0]	[-10º,0]	0	0

The runtimes of COF and NEFF are compared on a PC with 2.60 GHz processor and 16 GB RAM. For numerically solving both COF and NEFF, MATLAB functions are used (*fmincon* for COF and *fsolve* for NEFF). The computations are run in the following phases:

- At the first configuration to be solved, computations are performed with random initial conditions and random restarts (with the same random conditions fed to both COF and NEFF).

- COF and NEFF are solved at steps of 2º over the ranges of inputs shown in Table 28. Both COF and NEFF solvers are initialized with the solution from the previous (i.e. neighboring) configuration, as discussed at the start of this Section.

The average time for both COF and NEFF computations are shown in Table 29. The average NEFF computation time is 0.093 sec while running in MATLAB. For on-line implementation, run times can be further reduced by using other programming languages such as C++, though this is already a reasonable computation period.

Furthermore, NEFF is around an order of magnitude faster than COF. This result is interesting because it again confirms the importance of our contribution, which is show-

ing that optimal traction forces can be obtained almost always using NEFF for four-wheel rovers.

Again it should be noted that compared to Lamon et al. [105], we have shown that the constrained optimization step is not required for four-wheel rovers.

Table 29: Performance Comparison of COF and NEFF for the Conditions presented in Table 28

Algorithm	Time
COF	1.2316 sec
NEFF	0.0928 sec

7.7 Practical Considerations for Calculating Optimal Torques

In addition to the practical contribution of identifying a less computationally expensive method of solving for optimal traction forces, other practical implementation considerations are summarized here for convenience. In previous sections, it was simply assumed that rover configuration angles, e.g. α and wheel-terrain contact angles, θ_i, could be estimated. At this point we can discuss various ways in which such an estimation could be done in practice.

Internal rover configuration angles can be determined based on suspension angle sensors (e.g. potentiometers). These can then be converted to absolute angles, relative to the horizontal plane, with reference to an inclinometer. Such a suite of sensors is routinely installed on rovers.

Estimation techniques for wheel-terrain contact angles can be divided into two main approaches: making measurements at the wheels themselves, or doing calculations based on measurements from other locations on the rover.

Iagnemma et al. [103] present a way to calculate an estimate for contact angles without having any measurements at the wheels themselves. Instead, their approach requires full rover egomotion data and configuration information. The egomotion data (presumably from a vision algorithm or something equivalent) would give the 6 degree of freedom velocity at the rover center of gravity. Through a kinematics calculation involving joint configurations and rates, these velocities could be translated to each of the 6 wheel centers. Longitudinal contact angles can then be calculated as

$$\theta_i = \arctan\left(\frac{v_y}{v_x}\right)$$

where v_x and v_y are the x and y velocities of the center of wheel i (relative to the ground frame).

Contact angles may alternately be deduced from deformation or strain at the wheel itself [113]. developed a tactile wheel for the Octopus rover, which is equipped with deformable tires and with infrared sensors attached to the wheel hub. When the wheel contacts the ground or an obstacle, the tire deforms, shortening the emitter-to-receiver path of the infrared beam for one or more of the 16 sensors. Significantly shortened paths suggest contact points, which can then be used to either estimate a single contact angle or to calculate an average contact angle. With a rigid wheel, analogous measurements could be made with strain gauges mounted along the inner circumference of the wheel.

It has been noted that the wheel torque optimization for 4-wheeled rovers is valid for all cases except when at least one $\theta_i = \frac{\pi}{2}$, (i = 1,...,4) and one $\theta_j = \frac{-\pi}{2}$ (j = 1,...,4), simultaneously. This corresponds to two of the wheels being wedged against opposing vertical faces. Although not entirely impossible, it is important to note that this is a highly unusual and unlikely scenario in practice.

7.8 Conclusion of the Chapter

When a rover's system of quasi-static equations of motion are underdetermined, augmenting this system with equations enforcing equal "friction requirement" represents optimal traction to minimize the risk of slippage. We have shown (for practical 2-wheel and 4-wheel rovers) that explicitly adding these equations to create a fully determined system of nonlinear equations is a valid method for seeking an optimal traction solution; if there is a valid solution to the system of equations, it is optimal. This significantly simplifies the problem of optimizing wheel torques for traction in this important class of rover problem.

For both a simplified 2D 2-wheel rover example, as well as a 3 dimensional 4-wheel rover model, the augmented system of equations lacks a valid solution only when one wheel encounters the terrain at an angle near 90 degrees and another is near -90 degrees, a highly unusual and unlikely scenario. Accordingly, compared to previous papers, we show that another optimization step is not required to find all of the valid answers; hence, the computational intensity of the problem is reduced.

The future work includes investigating potential effects of the rover roll angle on the equations and their solution space. Also, experimental work would be a productive direction for future work.

8   Conclusions and Future Work

In this chapter, firstly the contributions and results of this thesis are discussed and summarized in subsection 8.1. Then, the proposed/planned future work is reported in subsection 8.2.

8.1   Conclusions

Skid-steer rovers consume a lot more power in point turns compared to straight-line motion. As energy is the integral of power over time, the turning radius should be considered explicitly for this type of rover. Moreover, the thorough review of the published literature reveals that there is a lack of analytical energy-optimal path planning approaches for skid-steer rovers. Hence, the focus of this thesis is to address the problem while the rover moves on obstacle-free hard ground. From the evaluations and investigations on the problem, the following findings are concluded:

- **Equivalency Theorem**: The theorem which is a *key contribution* of this thesis indicates that, for a popular power model for skid-steer rovers on hard ground, all minimum-energy solutions follow the same path irrespective of velocity constraints that may or may not be imposed. This non-intuitive result stems from the fact that for the relevant power model, the total energy is fully parametrized by the geometry of the path alone. It is noted that the velocity constraint should not limit the range of the turning radius. According to our research, the constraint can be "constant v_c", "constant-power velocity constraint", and "bounded velocity". Our approach to solve the energy-efficient path planning problem is considering "constant-power velocity constraint", and thus converting the problem to an equivalent time-optimal problem. Hence, the *equivalency theorem* avoids the regeneration/revising/adjusting of theory for being applied to our energy-efficient problem. Instead, the *equivalent time-optimal* problem can be solved using the existing theory and process from the literature (references [50] and [62])–built upon the basis of Pontryagin's minimum principle to find the extremals for time-optimal path planning for a rigid body.

- **Extremal Paths**: Using the existing theory and proving some other theorems specified for skid-steer rovers, the answer to the equivalent time-optimal path planning problem is found. Hence, all the possible *extremal paths* for the energy-efficient path planning problem are obtained, which is another *key contribution* in this thesis. As there is a finite number of extremals, they can be enumerated to find the *minimum*. Moreover, a scenario, going from a starting point in 2D x-y space with the orientation of $\pi/4$ to the origin with orientation of 0, is provided to show the method that the extremal paths should be utilized to obtain the optimal path. The results indicate that there are 3 types of path that covers the most area of the optimal map: CLC, CCLC, and CLCC. We would expect similar results for other scenarios besides the mentioned example.

- **R'**: Another *key contribution* is introducing and investigating the importance of R', a particular turning radius equal to half of a skid-steer rover's slip track. In other

words, R' is the turning radius at which the inner wheels of a skid-steer rover are not commanded to turn. The analysis identifies that all the turns for the *non-whirls* (vast majority of the obtained *extremals paths*) have the turning radius of R'. Analysis, using KKT as well as experiments with a Husky UGV rover further demonstrate the importance of R'. When considered with respect to a popular power model for skid-steer rovers, R' corresponds to an important transition for energy consumption of a circular arc maneuver: below R' energy consumption is not a function of turning radius while above R' it is. Moreover, the results obtained from the experiments on hard ground confirm that turning radius of R' gives best results for the energy consumption of CLC paths.

- **Constant-v_c Constraint**: In this thesis we propose a practical velocity constraint for skid-steer rovers. Since the typical constant forward velocity constraint is not applicable for skid-steer rovers, as turning radius approaches zero the angular velocity becomes infinity, a new practical constraint is suggested. The proposed constraint is constant sum of absolute values of right and left velocity. The proposed constraint gives this ability to a skid-steer rover to keep constant angular velocity below R' and constant forward velocity above R'. It is worth mentioning that below R' the right and left velocity have different signs. However, they are the same above R'.

Furthermore, we investigate the **importance of "friction requirement"**. By numerical analysis it is shown that for a practical type of 4-wheel rovers, almost always *equal "friction requirement"* can be used to obtain optimal traction forces. It is worth mentioning that skid-steer rovers are a class of 4-wheel rovers. The detailed conclusion about the problem is provided in subsection 7.8.

Finally, based on the performed research, there have been several publications and presentations that are listed in subsection 1.4.

8.2 Future Work

Since the power model (Eq. (20)) is designed for hard ground, all the theoretical analysis in this thesis are performed by the assumption of moving on hard found. However, for applications such as space robotics the rover should be able to follow the optimal trajectory on loose soil. Accordingly,

- The power model (Eq. (20)) should be revised for loose soil. We performed several experimental tests[36] using Husky UGV and Argo J5 on CSA Mars yard. Moreover, some research are performed to identify the power model for loose soil around R' in [114]. However, it still requires more investigation to obtain a proper power model on loose soil. Specially, the power model should be precisely designed for the power consumption of turning radii around R'.

- After obtaining the power model on loose soil, the energy efficient path planning problem should be solved for this type of terrains. Since only the power model will

---

[36]The results are presented in subsection 6.3.

be changed, our suggested way is to follow the steps that we performed in this thesis probably with some modifications to make the analysis appropriate for loose soil.

- As mentioned in the literature review, there are several papers on simultaneous minimization of time and energy. In other words, the hybrid cost (weighted sum of energy and time) is minimized. As both energy and time can be considered in optimal trajectory planning, an interesting direction of future work is optimal path planning by minimizing the hybrid cost for skid-steer rovers. Based on this thesis, the energy cost should be converted to an equivalent time cost with a new control control space, and then the optimization should consist of some weighted combination of solutions to the equivalent time problem (energy term) and direct time optimization problem (time term), each with its own related control space. Careful investigation is required to figure out whether the process can be applied to the hybrid problem. One potential issue that arises is as follows: If the two problems generate different optimal maps, how does one reconcile the selection of a path, given that there is no obvious weighted combination of CLC and LCCLC paths, for example?

Moreover, based on the work performed in this thesis, there are several current/planned works that are reported in the following:

- It is known that PLP[37] paths are feasible between every starting and end pose. In experimental tests the simpler paths are more convenient to be implemented (i.e. PLP is easier than CCLCC). Accordingly, comparing the magnitude of energy savings of the optimal paths (see Fig. 41) to their correspondent PLPs provides more information about choosing the proper path for a real experimental test.

- As explained before, the performed work in this thesis is LPM which provides the motion primitives for the global paths[38]. Hence, the next step is to implement the optimal paths obtained in this thesis in a global path and evaluate the results.

- Another planned work is experimentally testing the designed global path as well as each of the dominant optimal paths in the optimal map (see Fig. 41) to compare the theoretical and experimental results. It should be mentioned that several experimental tests on both hard ground and loose soil are performed for CLC paths (reported in chapter 6). However, more complicated paths such CLCC and CCLC will be tested.

---

[37]Recall, PLP stands for Point turn-Line-Point turn.
[38]Global paths are designed for the scenarios that obstacles are considered.

References

[1] S. Kassel, "Lunokhod-1 soviet lunar surface vehicle," Rand Corp Santa Monica, Tech. Rep., 1971.

[2] E. Reid, P. Iles, J. Muise, N. Cristello, B. Jones, M. Faragalli, P. Visscher, D. Boucher, V. Simard-Bilodeau, D. Apostolopoulos *et al.*, "The artemis jr. rover: Mobility platform for lunar isru mission simulation," *Advances in Space Research*, vol. 55, no. 10, pp. 2472–2483, 2015.

[3] M. Farhat, T. Lamarche, E. Dupuis, A. Salerno, and S. Lake, "Developing pud–lunar rover test platform," *ASTRA*, 2011.

[4] J. Pace, M. Harper, C. Ordonez, N. Gupta, A. Sharma, and E. G. Collins Jr, "Experimental verification of distance and energy optimal motion planning on a skid-steered platform," in *Unmanned Systems Technology XIX*, vol. 10195.   International Society for Optics and Photonics, 2017, p. 1019506.

[5] C. Ordonez, N. Gupta, B. Reese, N. Seegmiller, A. Kelly, and E. G. Collins Jr, "Learning of skid-steered kinematic and dynamic models for motion planning," *Robotics and Autonomous Systems*, vol. 95, pp. 207–221, 2017.

[6] B. Shamah, "Experimental comparison of skid steering vs. explicit steering for wheeled mobile robot," Master's thesis, Carnegie Mellon University, 1999.

[7] S. M. LaValle, *Planning algorithms*.   Cambridge university press, 2006.

[8] J. H. Reif, "Complexity of the mover's problem and generalizations," in *20th Annual Symposium on Foundations of Computer Science (sfcs 1979)*.   IEEE, 1979, pp. 421–427.

[9] M. T. Heath, *Scientific computing: an introductory survey*.   SIAM, 2018, vol. 80.

[10] J. Canny and J. Reif, "New lower bound techniques for robot motion planning problems," in *28th Annual Symposium on Foundations of Computer Science (sfcs 1987)*.   IEEE, 1987, pp. 49–60.

[11] C. Ó'dúnlaing, "Motion planning with inertial constraints," *Algorithmica*, vol. 2, no. 1-4, pp. 431–475, 1987.

[12] J. Canny, A. Rege, and J. Reif, "An exact algorithm for kinodynamic planning in the plane," *Discrete & Computational Geometry*, vol. 6, no. 3, pp. 461–484, 1991.

[13] R. Raja, A. Dutta, and K. Venkatesh, "New potential field method for rough terrain path planning using genetic algorithm for a 6-wheel rover," *Robotics and Autonomous Systems*, vol. 72, pp. 295–306, 2015.

[14] G. Kewlani, G. Ishigami, and K. Iagnemma, "Stochastic mobility-based path planning in uncertain environments," in *2009 IEEE/RSJ International Conference on Intelligent Robots and Systems*. IEEE, 2009, pp. 1183–1189.

[15] S. M. LaValle, "Rapidly-exploring random trees: A new tool for path planning," 1998.

[16] S. M. LaValle and J. J. Kuffner Jr, "Randomized kinodynamic planning," *The international journal of robotics research*, vol. 20, no. 5, pp. 378–400, 2001.

[17] S. Karaman and E. Frazzoli, "Incremental sampling-based algorithms for optimal motion planning," *Robotics Science and Systems VI*, vol. 104, no. 2, 2010.

[18] L. Palmieri, S. Koenig, and K. O. Arras, "Rrt-based nonholonomic motion planning using any-angle path biasing," in *2016 IEEE International Conference on Robotics and Automation (ICRA)*. IEEE, 2016, pp. 2775–2781.

[19] A. Stentz, "Optimal and efficient path planning for partially known environments," in *Intelligent Unmanned Ground Vehicles*. Springer, 1997, pp. 203–220.

[20] S. Dogru and L. Marques, "Energy efficient coverage path planning for autonomous mobile robots on 3d terrain," in *2015 IEEE International Conference on Autonomous Robot Systems and Competitions*. IEEE, 2015, pp. 118–123.

[21] E. Bonabeau, M. Dorigo, D. d. R. D. F. Marco, G. Theraulaz, G. Théraulaz *et al.*, *Swarm intelligence: from natural to artificial systems*. Oxford university press, 1999, no. 1.

[22] M. Dorigo, M. Birattari, and T. Stutzle, "Ant colony optimization," *IEEE computational intelligence magazine*, vol. 1, no. 4, pp. 28–39, 2006.

[23] J. Kennedy and R. Eberhart, "Particle swarm optimization," in *Proceedings of ICNN'95-International Conference on Neural Networks*, vol. 4. IEEE, 1995, pp. 1942–1948.

[24] P. Wang, X. Li, C. Song, and S. Zhai, "Research on dynamic path planning of wheeled robot based on deep reinforcement learning on the slope ground," *Journal of Robotics*, vol. 2020, 2020.

[25] L. Butyrev, T. Edelhäußer, and C. Mutschler, "Deep reinforcement learning for motion planning of mobile robots," *arXiv preprint arXiv:1912.09260*, 2019.

[26] S. Luo, Q. Sun, J. Tao, W. Liang, and Z. Chen, "Trajectory planning and gathering for multiple parafoil systems based on pseudo-spectral method," in *2016 35th Chinese Control Conference (CCC)*. IEEE, 2016, pp. 2553–2558.

[27] Y. Zhu, K. Zhao, H. Li, Y. Liu, Q. Guo, and Z. Liang, "Trajectory planning algorithm using gauss pseudo-spectral method based on vehicle-infrastructure cooperative system," *International Journal of Automotive Technology*, vol. 21, no. 4, pp. 889–901, 2020.

[28] D. Mellinger and V. Kumar, "Minimum snap trajectory generation and control for quadrotors," in *2011 IEEE international conference on robotics and automation.* IEEE, 2011, pp. 2520–2525.

[29] M. M. de Almeida, R. Moghe, and M. Akella, "Real-time minimum snap trajectory generation for quadcopters: Algorithm speed-up through machine learning," in *2019 International Conference on Robotics and Automation (ICRA).* IEEE, 2019, pp. 683–689.

[30] A. Alzaydi, M. Sahaluddin, M. Islam, and S. Al-Helou, "Robotic manipulator task sequencing and minimum snap trajectory generation," *Arabian Journal for Science and Engineering*, pp. 1–22, 2020.

[31] M. Yamamoto, M. Iwamura, and A. Mohri, "Time-optimal motion planning of skid-steer mobile robots in the presence of obstacles," in *Proceedings. 1998 IEEE/RSJ International Conference on Intelligent Robots and Systems. Innovations in Theory, Practice and Applications (Cat. No. 98CH36190)*, vol. 1. IEEE, 1998, pp. 32–37.

[32] D. D. Dunlap, C. V. Caldwell, E. G. Collins, O. Chuy *et al.*, "Motion planning for mobile robots via sampling-based model predictive optimization," *Recent advances in mobile robotics*, vol. 1, 2011.

[33] B. M. Reese, "A graph based approach to nonlinear model predictive control with application to combustion control and flow control," Florida A and M University Tallahassee United States, Tech. Rep., 2015.

[34] N. Gupta, C. Ordonez, and E. G. Collins, "Dynamically feasible, energy efficient motion planning for skid-steered vehicles," *Autonomous Robots*, vol. 41, no. 2, pp. 453–471, 2017.

[35] J. Pentzer, K. Reichard, and S. Brennan, "Energy-based path planning for skid-steer vehicles operating in areas with mixed surface types," in *2016 American Control Conference (ACC).* IEEE, 2016, pp. 2110–2115.

[36] X. Zhong, J. Tian, H. Hu, and X. Peng, "Hybrid path planning based on safe a* algorithm and adaptive window approach for mobile robot in large-scale dynamic environment," *Journal of Intelligent & Robotic Systems*, pp. 1–13, 2020.

[37] A. Mohamed, J. Ren, A. M. Sharaf, and M. EI-Gindy, "Optimal path planning for unmanned ground vehicles using potential field method and optimal control method," *International journal of vehicle performance*, vol. 4, no. 1, pp. 1–14, 2018.

[38] M. Chaudhari, L. Vachhani, and R. Banerjee, "Towards optimal computation of energy optimal trajectory for mobile robots," *IFAC Proceedings Volumes*, vol. 47, no. 1, pp. 82–87, 2014.

[39] L. E. Dubins, "On curves of minimal length with a constraint on average curvature, and with prescribed initial and terminal positions and tangents," *American Journal of mathematics*, vol. 79, no. 3, pp. 497–516, 1957.

[40] H. H. Johnson, "An application of the maximum principle to the geometry of plane curves," *Proceedings of the American Mathematical Society*, vol. 44, no. 2, pp. 432–435, 1974.

[41] M. A. Patterson and A. V. Rao, "Gpops-ii: A matlab software for solving multiple-phase optimal control problems using hp-adaptive gaussian quadrature collocation methods and sparse nonlinear programming," *ACM Transactions on Mathematical Software (TOMS)*, vol. 41, no. 1, p. 1, 2014.

[42] J. Reeds and L. Shepp, "Optimal paths for a car that goes both forwards and backwards," *Pacific journal of mathematics*, vol. 145, no. 2, pp. 367–393, 1990.

[43] H. J. Sussmann and G. Tang, "Shortest paths for the reeds-shepp car: a worked out example of the use of geometric techniques in nonlinear optimal control," *Rutgers Center for Systems and Control Technical Report*, vol. 10, pp. 1–71, 1991.

[44] P. Soueres and J.-P. Laumond, "Shortest paths synthesis for a car-like robot," *IEEE Transactions on Automatic Control*, vol. 41, no. 5, pp. 672–688, 1996.

[45] J.-D. Boissonnat, A. Cérézo, and J. Leblond, "Shortest paths of bounded curvature in the plane," *Journal of Intelligent and Robotic Systems*, vol. 11, no. 1-2, pp. 5–20, 1994.

[46] B. Qin, Y. C. Soh, M. Xie, and D. Wang, "Optimal trajectory generation for wheeled mobile robot," in *Proc. 5th Int. Conf. Comput. Integr. Manuf*, vol. 1.   Citeseer, 2000, pp. 434–444.

[47] P. Tokekar, N. Karnad, and V. Isler, "Energy-optimal trajectory planning for car-like robots," *Autonomous Robots*, vol. 37, no. 3, pp. 279–300, 2014.

[48] D. J. Balkcom and M. T. Mason, "Extremal trajectories for bounded velocity differential drive robots," in *Proceedings 2000 ICRA. Millennium Conference. IEEE International Conference on Robotics and Automation. Symposia Proceedings (Cat. No. 00CH37065)*, vol. 3.   IEEE, 2000, pp. 2479–2484.

[49] D. J. Balkcom, "Time optimal trajectories for bounded velocity differential drive robots," in *Proceedings 2000 ICRA. Millennium Conference. IEEE International Conference on Robotics and Automation.*, vol. 3.   IEEE, 2000, pp. 2499–2504.

[50] D. J. Balkcom and M. T. Mason, "Time optimal trajectories for bounded velocity differential drive vehicles," *The International Journal of Robotics Research*, vol. 21, no. 3, pp. 199–217, 2002.

[51] D. J. Balkcom, P. A. Kavathekar, and M. T. Mason, "Time-optimal trajectories for an omni-directional vehicle," *The International Journal of Robotics Research*, vol. 25, no. 10, pp. 985–999, 2006.

[52] D. J. Balkcom and P. A. Kavathekar, "The minimum-time trajectories for an omni-directional vehicle," in *Algorithmic Foundation of Robotics VII*.   Springer, 2008, pp. 343–358.

[53] W. Wang and D. J. Balkcom, "Analytical time-optimal trajectories for an omni-directional vehicle," in *2012 IEEE International Conference on Robotics and Automation*.   IEEE, 2012, pp. 4519–4524.

[54] H. Chitsaz and S. M. f, "Minimum wheel-rotation paths for differential drive mobile robots among piecewise smooth obstacles," in *Proceedings 2007 IEEE International Conference on Robotics and Automation*.   IEEE, 2007, pp. 2718–2723.

[55] H. Chitsaz, S. M. LaValle, D. J. Balkcom, and M. T. Mason, "Minimum wheel-rotation paths for differential-drive mobile robots," *The International Journal of Robotics Research*, vol. 28, no. 1, pp. 66–80, 2009.

[56] D. Balkcom, A. Furtuna, and W. Wang, "The dubins car and other arm-like mobile robots," in *2018 IEEE International Conference on Robotics and Automation (ICRA)*.   IEEE, 2018, pp. 380–386.

[57] W. Wang and D. Balkcom, "Time-optimal motion of spatial dubins systems," Easy-Chair, Tech. Rep., 2019.

[58] W. Wang and D. J. Balkcom, "Sampling extremal trajectories for planar rigid bodies," pp. 331–347, 2013.

[59] A. A. Furtuna, D. J. Balkcom, H. Chitsaz, and P. Kavathekar, "Generalizing the dubins and reeds-shepp cars: fastest paths for bounded-velocity mobile robots," in *2008 IEEE International Conference on Robotics and Automation*.   IEEE, 2008, pp. 2533–2539.

[60] A. A. Furtuna and D. J. Balkcom, "Generalizing dubins curves: Minimum-time sequences of body-fixed rotations and translations in the plane," *The International Journal of Robotics Research*, vol. 29, no. 6, pp. 703–726, 2010.

[61] A. A. Furtuna, W. Lu, W. Wang, and D. J. Balkcom, "Minimum-time trajectories for kinematic mobile robots and other planar rigid bodies with finite control sets," in *2011 IEEE/RSJ International Conference on Intelligent Robots and Systems*.   IEEE, 2011, pp. 4321–4328.

[62] A. Furtuna, "Minimum time kinematic trajectories for self-propelled rigid bodies in the unobstructed plane," Ph.D. dissertation, Dartmouth College, United States, 2011. [Online]. Available: https://rlab.cs.dartmouth.edu/publications/FurtunaPhD.pdf

[63] A. A. Furtuna, W. Wang, Y.-H. Lyu, and D. Balkcom, "Structure and geometry of minimum-time trajectories for planar rigid bodies," in *2013 51st Annual Allerton Conference on Communication, Control, and Computing (Allerton)*.   IEEE, 2013, pp. 1584–1591.

[64] Y.-H. Lyu, A. Furtuna, W. Wang, and D. Balkcom, "The bench mover's problem: Minimum-time trajectories, with cost for switching between controls," in *2014 IEEE International Conference on Robotics and Automation (ICRA)*. IEEE, 2014, pp. 106–112.

[65] Y.-H. Lyu and D. Balkcom, "Optimal trajectories for planar rigid bodies with switching costs," in *Algorithmic Foundations of Robotics XI*. Springer, 2015, pp. 371–387.

[66] Y. Lyu and D. Balkcom, "Optimal trajectories for kinematic planar rigid bodies with switching costs," *The International Journal of Robotics Research*, vol. 35, no. 5, pp. 454–475, 2016.

[67] Y.-H. Lyu, *Implications of motion planning: optimality and k-survivability*. Dartmouth College, 2016.

[68] I. Ioslovich, S. Moshenberg, and P.-O. Gutman, "On the energy-optimal precise wafer stage positioning: equivalence with minimal time optimality," in *2015 IEEE 24th International Symposium on Industrial Electronics (ISIE)*. IEEE, 2015, pp. 95–99.

[69] I. Ioslovich, P.-O. Gutman, A. Berger, and S. Moshenberg, "On energy-optimal and time-optimal precise displacement of rigid body with friction," *Journal of Optimization Theory and Applications*, vol. 172, no. 2, pp. 466–480, 2017.

[70] P.-O. Gutman, I. Ioslovich, and S. Moshenberg, "On the optimal control of the rigid body precise movement: Is energy optimality the same as time optimality?" in *2015 Proceedings of the Conference on Control and its Applications*. SIAM, 2015, pp. 32–38.

[71] I. Ioslovich, P.-O. Gutman, R. Linker, and S. Moshenberg, "Optimal rigid body precise displacement-minimization of electrical energy," *IFAC-PapersOnLine*, vol. 50, no. 1, pp. 753–757, 2017.

[72] A. Berger, I. Ioslovich, and P.-O. Gutman, "Time optimal trajectory planning with feedforward and friction compensation," in *2015 American Control Conference (ACC)*. IEEE, 2015, pp. 4143–4148.

[73] A. Taitler, I. Ioslovich, E. Karpas, P.-O. Gutman, and J. Z. Ben-Asher, "Structural analysis of combined time and energy optimal trajectory planning with quadratic drag," in *2019 27th Mediterranean Conference on Control and Automation (MED)*. IEEE, 2019, pp. 153–158.

[74] A. Taitler, I. Ioslovich, P.-O. Gutman, and E. Karpas, "Combined time and energy optimal trajectory planning with quadratic drag for mixed discrete-continuous task planning," *Optimization*, vol. 68, no. 1, pp. 125–143, 2019.

[75] M. Costin, I. Voncilă, and I. Bivol, "A priori cost of the energy to perform movement on a predefined path," *Acta Polytechnica Hungarica*, vol. 15, no. 7, 2018.

[76] A. Raisch and O. Sawodny, "Consumption minimization for electromechanical drives by energy-optimal feedforward control," in *2019 IEEE International Conference on Systems, Man and Cybernetics (SMC)*. IEEE, 2019, pp. 1557–1562.

[77] S. Wang, Z. Wang, and Y. Hu, "Optimal control research on a manipulator's combined feedback device by the variational method genetic algorithm radial basis function method," *International Journal of Advanced Robotic Systems*, vol. 16, no. 3, p. 1729881419855824, 2019.

[78] Z. Shiller, "Time-energy optimal control of articulated systems with geometric path constraints," *Journal of Dynamic Systems, Measurement, and Control*, vol. 118, no. 1, pp. 139–143, 03 1996.

[79] D. Verscheure, B. Demeulenaere, J. Swevers, J. De Schutter, and M. Diehl, "Time-energy optimal path tracking for robots: a numerically efficient optimization approach," in *2008 10th IEEE International Workshop on Advanced Motion Control*. IEEE, 2008, pp. 727–732.

[80] C. Ji, M. Kong, and R. Li, "Time-energy optimal trajectory planning for variable stiffness actuated robot," *IEEE Access*, vol. 7, pp. 14 366–14 377, 2019.

[81] Y. Zhang and C. G. Cassandras, "Joint time and energy-optimal control of connected automated vehicles at signal-free intersections with speed-dependent safety guarantees," *arXiv preprint arXiv:1903.05692*, 2019.

[82] E. W. Nshama and N. Uchiyama, "Time and energy optimal trajectory generation in feed drive systems using kinematic corner smoothing with interrupted acceleration," in *2018 26th Mediterranean Conference on Control and Automation (MED)*. IEEE, 2018, pp. 102–107.

[83] H. Lyu, X. Song, D. Dai, J. Li, and Z. Li, "Time-optimal and energy-efficient trajectory generation for robot manipulator with kinematic constraints," in *2017 13th IEEE Conference on Automation Science and Engineering (CASE)*. IEEE, 2017, pp. 503–508.

[84] M. Faraj and O. Basir, "Optimal energy/time routing in battery-powered vehicles," in *2016 IEEE Transportation Electrification Conference and Expo (ITEC)*. IEEE, 2016, pp. 1–6.

[85] S. Dogru and L. Marques, "Power characterization of a skid-steered mobile field robot with an application to headland turn optimization," *Journal of Intelligent & Robotic Systems*, vol. 93, no. 3-4, pp. 601–615, 2019.

[86] S. Dorgu and L. Marques, "A physics-based power model for skid-steered wheeled mobile robots," *IEEE Transactions on Robotics*, vol. 34, no. 2, pp. 421–433, 2018.

[87] J. Morales, J. L. Martínez, A. Mandow, A. Pequeño-Boter, and A. García-Cerezo, "Simplified power consumption modeling and identification for wheeled skid-steer robotic vehicles on hard horizontal ground," in *2010 IEEE/RSJ International Conference on Intelligent Robots and Systems*. IEEE, 2010, pp. 4769–4774.

[88] A. Mandow, J. L. Martinez, J. Morales, J. L. Blanco, A. Garcia-Cerezo, and J. Gonzalez, "Experimental kinematics for wheeled skid-steer mobile robots," in *2007 IEEE/RSJ International Conference on Intelligent Robots and Systems*. IEEE, 2007, pp. 1222–1227.

[89] J. L. Martínez, A. Mandow, J. Morales, S. Pedraza, and A. García-Cerezo, "Approximating kinematics for tracked mobile robots," *The International Journal of Robotics Research*, vol. 24, no. 10, pp. 867–878, 2005.

[90] J. Morales, J. L. Martinez, A. Mandow, A. J. García-Cerezo, and S. Pedraza, "Power consumption modeling of skid-steer tracked mobile robots on rigid terrain," *IEEE Transactions on Robotics*, vol. 25, no. 5, pp. 1098–1108, 2009.

[91] J. Pentzer, S. Brennan, and K. Reichard, "Model-based prediction of skid-steer robot kinematics using online estimation of track instantaneous centers of rotation," *Journal of Field Robotics*, vol. 31, no. 3, pp. 455–476, 2014.

[92] L. Pontryagin, V. Boltyanskii, R. Gamkrelidze, and E. Mishchenko, *The Mathematical theory of optimal processes*. John Wiley, 1962.

[93] B. Spain, *Analytical conics*. Courier Corporation, 2007.

[94] J. W. Betz, *Engineering satellite-based navigation and timing: global navigation satellite systems, signals, and receivers*. John Wiley & Sons, 2015.

[95] J. Lenarcic, T. Bajd, and M. M. Stanišić, *Robot mechanisms*. Springer Science & Business Media, 2012, vol. 60.

[96] D. G. Luenberger and Y. Ye, "Linear and nonlinear programming, vol. 116," 2008.

[97] M. Effati and K. Skonieczny, "Circular arc-based optimal path planning for skid-steer rovers," in *2018 IEEE Canadian Conference on Electrical & Computer Engineering (CCECE)*. IEEE, 2018, pp. 1–4.

[98] K. Yoshida, H. Hamano, and T. Watanabe, "Slip-based traction control of a planetary rover," in *Experimental Robotics VIII*. Springer, 2003, pp. 644–653.

[99] O. Toupet, J. Biesiadecki, A. Rankin, A. Steffy, G. Meirion-Griffith, D. Levine, M. Schadegg, and M. Maimone, "Traction control design and integration onboard the mars science laboratory curiosity rover," in *2018 IEEE Aerospace Conference*. IEEE, 2018, pp. 1–20.

[100] T. Thüer, "Mobility evaluation of wheeled all-terrain robots: Metrics and application," Ph.D. dissertation, ETH Zurich, 2009.

[101] T. Thueer and R. Siegwart, "Mobility evaluation of wheeled all-terrain robots," *Robotics and Autonomous Systems*, vol. 58, no. 5, pp. 508–519, 2010.

[102] S. Sreenivasan and B. Wilcox, "Stability and traction control of an actively actuated micro-rover," *Journal of Robotic Systems*, vol. 11, no. 6, pp. 487–502, 1994.

[103] K. Iagnemma and S. Dubowsky, "Traction control of wheeled robotic vehicles in rough terrain with application to planetary rovers," *The international Journal of robotics research*, vol. 23, no. 10-11, pp. 1029–1040, 2004.

[104] C. Grand, F. Benamar, F. Plumet, and P. Bidaud, "Stability and traction optimization of a reconfigurable wheel-legged robot," *The International Journal of Robotics Research*, vol. 23, no. 10-11, pp. 1041–1058, 2004.

[105] P. Lamon, A. Krebs, M. Lauria, R. Siegwart, and S. Shooter, "Wheel torque control for a rough terrain rover," in *IEEE International Conference on Robotics and Automation, 2004. Proceedings. ICRA'04. 2004*, vol. 5.   IEEE, 2004, pp. 4682–4687.

[106] S. Mukherjee, "Dexterous grasp and manipulation," Ph.D. dissertation, The Ohio State University, 1992.

[107] A. Krebs, T. Thueer, E. Carrasco, R. Oung, and R. Siegwart, "Towards torque control of the crab rover," in *9th International Symposium on Artificial Intelligence, Robotics and Automation in Space (iSAIRAS'08)*.   Canadian Space Agency (CSA-ASC); German Aerospace Agengy (DLR), ESA, 2008.

[108] D. Wettergreen, S. Moreland, K. Skonieczny, D. Jonak, D. Kohanbash, and J. Teza, "Design and field experimentation of a prototype lunar prospector," *The International Journal of Robotics Research*, vol. 29, no. 12, pp. 1550–1564, 2010.

[109] P. Visscher and B. Jones, "Continued development of juno rover," in *50th AIAA Aerospace Sciences Meeting including the New Horizons Forum and Aerospace Exposition*, 2012, p. 632.

[110] P. Visscher, P. Edmundson, N. Ghafoor, and H. Jones, "Lunar rover trl-6 drivetrain development," in *Earth and Space 2016: Engineering for Extreme Environments*. American Society of Civil Engineers Reston, VA, 2016, pp. 290–300.

[111] E. Reid, P. Iles, J. Muise, N. Cristello, B. Jones, M. Faragalli, P. Visscher, D. Boucher, V. Simard-Bilodeau, D. Apostolopoulos *et al.*, "The artemis jr. rover: Mobility platform for lunar isru mission simulation," *Advances in Space Research*, vol. 55, no. 10, pp. 2472–2483, 2015.

[112] W. Cheney and D. Kincaid, "Linear algebra: Theory and applications," *The Australian Mathematical Society*, vol. 110, 2009.

[113] M. Lauria, Y. Piguet, and R. Siegwart, "Octopus: an autonomous wheeled climbing robot," in *Proceedings International Conference on Climbing and Walking Robots*, 2002, pp. 315–322.

[114] S. Fiset, "Effects of turning radius on skid-steered wheeled robot power consumption on loose soil," Master's thesis, Concordia University, 2019.

[115] D. E. Kirk, *Optimal control theory: an introduction*.   Dover Publications, 2004.

Appendix A Control Space for the "Constant Power" Constraint

Lemma 10 *It is known that the power model of a skid-steer rover is as follows:*

$$P = 2\mu \left| \frac{V_r - V_l}{B_s} \right| \sqrt{L^2 + (W - B_s)^2} + G(|V_r| + |V_l|)$$

To have constant power ($P = P_c$ where P_c is a constant), the V_r and V_l should have the symmetric control space shown in Fig. 16

Proof: if

$$k = 2\mu N \sqrt{L^2 + (W - B_s)^2} \tag{271}$$

where k a constant parameter, then the following equation for the power is written:

$$P = k \left| \frac{V_r - V_l}{B_s} \right| + G(|V_r| + |V_l|) \tag{272}$$

By assuming that the power is constant ($P = P_c$), then the following relations for the V_r and V_l can be obtained:

Case 1): $V_r \geq 0$, $V_l \geq 0$, and $V_r \geq V_l$

$$P_c = k \left(\frac{V_r - V_l}{B_s} \right) + G(V_r + V_l) \tag{273}$$

$$P_c = V_r \left(G + \frac{k}{B_s} \right) + V_l \left(G - \frac{k}{B_s} \right) \tag{274}$$

Therefore, the linear relation between the velocities is as follows:

$$V_r = \frac{1}{\left(G + \frac{k}{B_s} \right)} \left[P_c - V_l \left(G - \frac{k}{B_s} \right) \right] \tag{275}$$

Case 2): $V_r \geq 0$, $V_l \geq 0$, and $V_r \leq V_l$

$$P_c = k \left(\frac{V_l - V_r}{B_s} \right) + G(V_r + V_l) \tag{276}$$

$$V_r = \frac{1}{\left(G - \frac{k}{B_s} \right)} \left[P_c - V_l \left(G + \frac{k}{B_s} \right) \right] \tag{277}$$

Case 3): $V_r < 0$ and $V_l > 0$

$$P_c = k \left(\frac{V_l - V_r}{B_s} \right) + G(-V_r + V_l) \tag{278}$$

$$P_c = -V_r \left(G + \frac{k}{B_s} \right) + V_l \left(G + \frac{k}{B_s} \right) \tag{279}$$

Therefore, the linear relation between the velocities is as follows:

$$V_r = \frac{1}{\left(G + \frac{k}{B_s}\right)}\left[V_l\left(G + \frac{k}{B_s}\right) - P_c\right] \tag{280}$$

Case 4): $V_r > 0$ and $V_l < 0$

$$P_c = k\left(\frac{V_r - V_l}{B_s}\right) + G(V_r - V_l) \tag{281}$$

$$P_c = V_r\left(G + \frac{k}{B_s}\right) - V_l\left(G + \frac{k}{B_s}\right) \tag{282}$$

Therefore, the linear relation between the velocities is as follows:

$$V_r = \frac{1}{\left(G + \frac{k}{B_s}\right)}\left[V_l\left(G + \frac{k}{B_s}\right) + P_c\right] \tag{283}$$

Case 5): $V_r < 0$, $V_l < 0$, and $|V_r| > |V_l|$

$$P_c = k\left(\frac{V_l - V_r}{B_s}\right) - G(V_r + V_l) \tag{284}$$

$$P_c = -V_r\left(G + \frac{k}{B_s}\right) + V_l\left(\frac{k}{B_s} - G\right) \tag{285}$$

Therefore, the linear relation between the velocities is as follows:

$$V_r = \frac{1}{\left(G + \frac{k}{B_s}\right)}\left[V_l\left(\frac{k}{B_s} - G\right) - P_c\right] \tag{286}$$

Case 6): $V_r < 0$, $V_l < 0$, and $|V_r| < |V_l|$

$$P_c = k\left(\frac{V_r - V_l}{B_s}\right) - G(V_r + V_l) \tag{287}$$

$$P_c = V_r\left(\frac{k}{B_s} - G\right) - V_l\left(\frac{k}{B_s} + G\right) \tag{288}$$

Therefore, the linear relation between the velocities is as follows:

$$V_r = \frac{1}{\left(\frac{k}{B_s} - G\right)}\left[V_l\left(\frac{k}{B_s} + G\right) + P_c\right] \tag{289}$$

Based on the above-mentioned cases, the new control space shown in Fig. 16 can be obtained easily. ∎

Appendix B   Elaboration on Solving the Energy-Efficient Problem using Pontryagin's Minimum Principle

Firstly, *Pontryagin's Minimum Principle* is stated. Then, the detailed *energy-efficient* path planning problem which includes the equation of motions and the initial conditions is presented. Afterwards, the *Minimum Principle* is applied to the energy-efficient problem. Finally, the approaches to provide a complete solution to the problem are introduced and it is mentioned that using the *equivalent time-optimal* problem is the selected approach.

B.1   Pontryagin's Minimum Principle

Theorem 10 . *Pontryagin's Minimum Principle [115] :*
To minimize the performance measure

$$J(\boldsymbol{u}) = h(\boldsymbol{x}(t_f), t_f) + \int_{t_0}^{t_f} g(\boldsymbol{x}(t), \boldsymbol{u}(t), t) dt \tag{290}$$

subject to state equation constraints

$$\dot{\boldsymbol{x}}(t) = \boldsymbol{a}(\boldsymbol{x(t)}, \boldsymbol{u(t)}, t) \tag{291}$$

and state inequality constraints of the form

$$\boldsymbol{f(x(t)}, t) \geq 0 \tag{292}$$

where $\boldsymbol{x}$ is the $n \times 1$ sate vector, $\boldsymbol{u}$ is $m \times 1$ vector of control inputs, and $\boldsymbol{f}$ is an l-vector function. Also, t, t_0, and t_f are time, initial time, and final time, respectively. Let us define a new variable $\dot{x}_{n+1}$ by

$$\dot{x}_{n+1} = [f_1(\boldsymbol{x}(t), t)]^2 \mathbb{1}(-f_1) + ... + [f_l(\boldsymbol{x}(t), t)]^2 \mathbb{1}(-f_l) \tag{293}$$

where $\mathbb{1}(-f_i)$ is a unit Heaviside step function which is defined as follows:

$$\mathbb{1}(-f_i) = \begin{cases} 0 & \text{for } f_i(\boldsymbol{x(t)}, t) \geq 0 \\ 1 & \text{for } f_i(\boldsymbol{x(t)}, t) < 0 \end{cases} \tag{294}$$

for $i = 1, 2, ..., l$. Also, the variable $x_{n+1}(t)$ is given by:

$$x_{n+1}(t) = \int_{t_0}^{t_f} \dot{x}_{n+1}(t) dt + x_{n+1}(t_0) \tag{295}$$

which satisfies the two boundary conditions $x_{n+1}(t_0) = 0$ and $x_{n+1}(t_f) = 0$. By introducing the Lagrange multipliers $\lambda_1(t), ..., \lambda_n(t)$, the Hamiltonian will be as follows:

$$
\begin{aligned}
H(\boldsymbol{x}(t), \boldsymbol{u}(t), \boldsymbol{\lambda}(t), t) = & g(\boldsymbol{x}(t), \boldsymbol{u}(t), t) + \lambda_1(t) a_1(\boldsymbol{x}(t), \boldsymbol{u}(t), t) + ... + \lambda_n(t) a_n(\boldsymbol{x}(t) + \boldsymbol{u}(t), t) \\
& + \lambda_{n+1}(t) \{ [f_1(\boldsymbol{x}(t), t)]^2 \mathbb{1}(-f_1) + ... + [f_m(\boldsymbol{x}(t), t)]^2 \mathbb{1}(-f_l) \} \\
\equiv & g(\boldsymbol{x}(t), \boldsymbol{u}(t), t) + \boldsymbol{\lambda}^T(t) \boldsymbol{a}(\boldsymbol{x}(t), \boldsymbol{u}(t), t)
\end{aligned}
\tag{296}
$$

where $x_{n+1}(t)$ is given by Eq. (295) and

$$a_{n+1}(\boldsymbol{x}(t),t) = [f_1(\boldsymbol{x}(t),t)]^2 \mathbb{1}(-f_1) + \dots + [f_m(\boldsymbol{x}(t),t)]^2 \mathbb{1}(-f_l) \tag{297}$$

where $\lambda(t) \in \mathbb{R}$. The following equations for all $t \in [t_0, t_f]$ states the necessary conditions for optimality:

$$
\begin{cases}
\quad \dot{x}_1^*(t) = a_1(\boldsymbol{x}^*(t), \boldsymbol{u}^*(t), t) \\
\quad . \\
\quad . \\
\quad . \\
\quad \dot{x}_{n+1}^*(t) = a_{n+1}(\boldsymbol{x}^*(t), t) \\
\quad \dot{\lambda}_1^*(t) = -\dfrac{\partial H}{\partial x_1}(\boldsymbol{x}^*(t), \boldsymbol{u}^*(t), \boldsymbol{\lambda}^*(t), t) \\
\quad . \\
\quad . \\
\quad . \\
\quad \dot{\lambda}_{n+1}^*(t) = -\dfrac{\partial H}{\partial x_{n+1}}(\boldsymbol{x}^*(t), \boldsymbol{u}^*(t), \boldsymbol{\lambda}^*(t), t) = 0 \\
and \\
\quad H(\boldsymbol{x}^*(t), \boldsymbol{u}^*(t), \boldsymbol{\lambda}^*(t), t) \leq H(\boldsymbol{x}^*(t), \boldsymbol{u}(t), \boldsymbol{\lambda}^*(t), t) \\
\quad for\ all\ admissible\ \boldsymbol{u}(t) \\
and \\
\quad \left[\dfrac{\partial h}{\partial \boldsymbol{x}}(\boldsymbol{x}^*(t_f), t_f) - \boldsymbol{\lambda}^*(t_f)\right]^T \delta \boldsymbol{x}_f + \\
\quad \left[H(\boldsymbol{x}^*(t_f), \boldsymbol{u}^*(t_f), \boldsymbol{\lambda}^*(t_f), t_f) + \dfrac{\partial h}{\partial t}(\boldsymbol{x}^*(t_f), t_f)\right]\delta t_f = 0
\end{cases}
\tag{298}
$$

The boundary conditions $\boldsymbol{x}^*(t_0)$ are specified ($x_{n+1}^*(t_0) = 0$ and $x_{n+1}^*(t_f) = 0$).

B.2 Approach to Solve the Constant v_c Energy-Efficient Path Planning Problem

Using the equations presented in chapter 2, the detailed definition of the *energy-efficient* problem[39] which includes differential equations of motion for the skid-steer rover, initial conditions, and energy equation is as follows:

---

[39]Presented in subsection2.1

Problem:

$$\underset{V_r,\ V_l,\ t_f}{\text{minimize}} \quad E = \int_0^{t_f} P(t)dt, \text{ where } P(t) \text{ is presnted in Eq. (23)}$$

$$\text{subject to} \quad |V_r| + |V_l| = 2v_c$$

$$\dot{x} = \frac{V_r + V_l}{2}\cos\theta$$

$$\dot{y} = \frac{V_r + V_l}{2}\sin\theta \tag{299}$$

$$\dot{\theta} = \frac{V_r - V_l}{B_s}$$

$$x(0) = x_0,\ y(0) = y_0,\ \theta(0) = \theta_0$$

$$x(t_f) = x_f,\ y(t_f) = y_f,\ \theta(t_f) = \theta_f$$

Solution:

The *solution* for the control inputs (V_l and V_r) of the *minimization* problem (Eq. (299)) which is obtained by the calculations performed through Eq. (301) to Eq. (339) is:

$$(V_l^*, V_r^*) \in \{(v_c, v_c), (-v_c, -v_c), (0, 2v_c), (0, -2v_c), (2v_c, 0), (-2v_c, 0)\}$$

$$\text{Or} \tag{300}$$

$$(V_l^*, V_r^*) \text{ on the line segments of quadrant 2 or 4 of Fig. 13}$$

Equation (300) conveys that the extremal paths should be built from the following motions:

- (v_c, v_c): straight forward motion

- $(-v_c, -v_c)$: straight backward motion

- $(0, 2v_c)$: forward CCW[40] turn with R' (see Eq. (18))

- $(0, -2v_c)$: backward CW[41] turn with R' (see Eq. (18))

- $(2v_c, 0)$: forward CW turn with R' (see Eq. (18))

- $(-2v_c, 0)$: backward CCW turn with R' (see Eq. (18))

- (V_l^*, V_r^*) on the line segment of quadrant 2 or 4: pure turns with a constant angular velocity for $R \in [0, R')$

The process to obtain Eq. (300) is explained in the following:

Lets define $\mathbf{x(t)} = [x(t),\ y(t),\ \theta(t)]^T$ and $\mathbf{u(t)} = [V_l(t),\ V_r(t)]^T$. Therefore, the Hamiltonian (in Theorem 10) is as follows:

$$H_E(\mathbf{x}(t), \mathbf{u}(t), \lambda(t), t) = k\frac{|V_r - V_l|}{B_s} + 2Gv_c + \lambda_1\left(\frac{V_r + V_l}{2}\cos\theta\right)$$

$$+ \lambda_2\left(\frac{V_r + V_l}{2}\sin\theta\right) + \lambda_3\left(\frac{V_r - V_l}{B_s}\right) \tag{301}$$

---

[40] Counter Clockwise
[41] Clockwise

Using the above equation for $H_E(\mathbf{x}(t), \mathbf{u}(t), \boldsymbol{\lambda}(t), t)$ and Eq. (298):

$$\dot{x}^* = \frac{V_r^* + V_l^*}{2} \cos\theta^* \tag{302}$$

$$\dot{y}^* = \frac{V_r^* + V_l^*}{2} \sin\theta^* \tag{303}$$

$$\dot{\theta}^* = \frac{V_r^* - V_l^*}{B_s} \tag{304}$$

$$\dot{\lambda}_1^* = -\frac{\partial H_E}{\partial x} = 0 \tag{305}$$

Therefore, λ_1^* is constant:

$$\lambda_1^* = c_{\lambda_1} \tag{306}$$

where c_{λ_1} is an arbitrary constant.

$$\dot{\lambda}_2^* = -\frac{\partial H_E}{\partial y} = 0 \tag{307}$$

Therefore, λ_2^* is constant:

$$\lambda_2^* = c_{\lambda_2} \tag{308}$$

where c_{λ_2} is an arbitrary constant.

$$\dot{\lambda}_3^* = -\frac{\partial H_E}{\partial \theta} \tag{309}$$

Hence,

$$\dot{\lambda}_3^* = c_{\lambda_1} \left(\frac{V_r^* + V_l^*}{2} \sin\theta^* \right) - c_{\lambda_2} \left(\frac{V_r^* + V_l^*}{2} \cos\theta^* \right) \tag{310}$$

which means:

$$\dot{\lambda}_3^* = c_{\lambda_1} \dot{y}^* - c_{\lambda_2} \dot{x}^* \tag{311}$$

After taking integral:

$$\lambda_3^* = c_{\lambda_1} y^* - c_{\lambda_2} x^* + c_{\lambda_3} \tag{312}$$

where c_{λ_3} is an arbitrary constant.

Note: *Based on the Pontryagin's minimum principle, the adjoint function which is $\dot{\boldsymbol{\lambda}}^* = -\dfrac{\partial H}{\partial \mathbf{x}}$ in Eq. (298), cannot be identically zero. In other words, c_{λ_1}, c_{λ_2}, and c_{λ_3} are not all zero.*

Now, the following condition should be checked.

$$H_E(\mathbf{x}^*(t), \mathbf{u}^*(t), \boldsymbol{\lambda}^*(t), t) \le H_E(\mathbf{x}^*(t), \mathbf{u}(t), \boldsymbol{\lambda}^*(t), t)$$
$$\text{for all admissible } \mathbf{u}(t) \tag{313}$$

Accordingly, the following optimization problem should be solved to obtain $\mathbf{u}^*(t)$.

$$\begin{aligned} \underset{V_l, V_r}{\text{minimize}} \quad & H_E(\mathbf{x}^*(t), \mathbf{u}(t), \boldsymbol{\lambda}^*(t), t) \\ \text{subject to} \quad & |V_r| + |V_l| = 2v_c \end{aligned} \tag{314}$$

By using Eq. (301) and Eq. (312), the following relation for $H_E(\mathbf{x}^*(t), \mathbf{u}(t), \boldsymbol{\lambda}^*(t), t)$ is obtained:

$$H_E(\mathbf{x}^*(t), \mathbf{u}(t), \boldsymbol{\lambda}^*(t), t) = k\frac{|V_r - V_l|}{B_s} + 2Gv_c + c_{\lambda_1}\frac{V_r + V_l}{2}\cos\theta^*$$
$$+ c_{\lambda_2}\frac{V_r + V_l}{2}\sin\theta^* + (c_{\lambda_1}y^* - c_{\lambda_2}x^* + c_{\lambda_3})\left(\frac{V_r - V_l}{B_s}\right) \tag{315}$$

In the following, each quadrant of Fig. 13 is considered separately to solve the optimization problem presented in Eq. (314).

(I) **First Quadrant of Fig. 13:**

Since both of the velocities are greater or equal to zero, the constraint in Eq. (314) is converted to

$$V_r + V_l = 2v_c \tag{316}$$

Hence, Eq. (315) becomes:

$$H_E(\mathbf{x}^*(t), \mathbf{u}(t), \boldsymbol{\lambda}^*(t), t) = k\frac{|V_r - V_l|}{B_s} + 2Gv_c + c_{\lambda_1}v_c\cos\theta^*$$
$$+ c_{\lambda_2}v_c\sin\theta^* + (c_{\lambda_1}y^* - c_{\lambda_2}x^* + c_{\lambda_3})\left(\frac{V_r - V_l}{B_s}\right) \tag{317}$$

Because of $|V_r - V_l|$, three different cases are considered:

(a) $V_r > V_l$

Eq. (317) is simplified to:

$$H_E(\mathbf{x}^*(t), \mathbf{u}(t), \boldsymbol{\lambda}^*(t), t) = (k + c_{\lambda_1}y^* - c_{\lambda_2}x^* + c_{\lambda_3})\left(\frac{V_r - V_l}{B_s}\right)$$
$$+ 2Gv_c + c_{\lambda_1}v_c\cos\theta^* + c_{\lambda_2}v_c\sin\theta^* \tag{318}$$

Depending on the sign of $(k + c_{\lambda_1}y^* - c_{\lambda_2}x^* + c_{\lambda_3})$[42] while considering Eq. (316), the following results are concluded:

(i) if $(k + c_{\lambda_1}y^* - c_{\lambda_2}x^* + c_{\lambda_3})$ is positive, to minimize Eq. (318) the right and left velocities are almost equal (while V_r^* is slightly greater than V_l^*):

$$\boxed{(V_l^*, V_r^*) = (v_c, v_c + \epsilon_{E_1})} \tag{319}$$

where ϵ_{E_1} is a small positive infinitesimal quantity.

(ii) if $(k + c_{\lambda_1}y^* - c_{\lambda_2}x^* + c_{\lambda_3})$ is negative, to minimize Eq. (318) $V_r - V_l$ should have its maximum value which means:

$$\boxed{(V_l^*, V_r^*) = (0, 2v_c)} \tag{320}$$

---

[42]Since $k > 0$ (see Eq. (24)), $(k + c_{\lambda_1}y^* - c_{\lambda_2}x^* + c_{\lambda_3}) \neq 0$

(b) $V_r = V_l$

By using 316:

$$(V_l^*, V_r^*) = (v_c, v_c) \tag{321}$$

(c) $V_r < V_l$

Eq. (317) is simplified to:

$$H_E(\mathbf{x}^*(t),\, \mathbf{u}(t),\, \boldsymbol{\lambda}^*(t),\, t) = (k - c_{\lambda_1} y^* + c_{\lambda_2} x^* - c_{\lambda_3})\left(\frac{V_l - V_r}{B_s}\right)$$
$$+ 2Gv_c + c_{\lambda_1} v_c \cos\theta^* + c_{\lambda_2} v_c \sin\theta^* \tag{322}$$

Depending on the sign of $(k - c_{\lambda_1} y^* + c_{\lambda_2} x^* - c_{\lambda_3})$ while considering Eq. (316), the following results are concluded:

(i) if $(k - c_{\lambda_1} y^* + c_{\lambda_2} x^* - c_{\lambda_3})$ is positive, to minimize Eq. (322) the right and left velocities should be almost the same (while V_l^* is slightly greater than V_r^*):

$$(V_l^*, V_r^*) = (v_c + \epsilon_{E_2}, v_c) \tag{323}$$

where ϵ_{E_2} is a small positive infinitesimal quantity.

(ii) if $(k - c_{\lambda_1} y^* + c_{\lambda_2} x^* - c_{\lambda_3})$ is negative, to minimize Eq. (322) $V_l - V_r$ should have its maximum value which means:

$$(V_l^*, V_r^*) = (2v_c, 0) \tag{324}$$

(II) **Second Quadrant of Fig. 13:**

Because the right and left velocities are considered in the second quadrant, the constraint in Eq. (314) is converted to

$$V_r - V_l = 2v_c \tag{325}$$

Therefore, the *Hamiltonian* in Eq. (315) is simplified to:

$$H_E(\mathbf{x}^*(t),\, \mathbf{u}(t),\, \boldsymbol{\lambda}^*(t),\, t) = k\frac{2v_c}{B_s} + 2Gv_c + (c_{\lambda_1}\cos\theta^* + c_{\lambda_2}\sin\theta^*)\frac{V_r + V_l}{2}$$
$$+ (c_{\lambda_1} y^* - c_{\lambda_2} x^* + c_{\lambda_3})\left(\frac{2v_c}{B_s}\right) \tag{326}$$

(a) if $(c_{\lambda_1}\cos\theta^* + c_{\lambda_2}\sin\theta^*) > 0$, to minimize the *Hamiltonian* (Eq. (326)), $V_r + V_l$ should have its minimum value. Therefore,

$$(V_l^*, V_r^*) = (-2v_c, 0) \tag{327}$$

(b) if $(c_{\lambda_1}\cos\theta^* + c_{\lambda_2}\sin\theta^*) < 0$, to minimize the *Hamiltonian* (Eq. (326)), $V_r + V_l$ should have its maximum value. Therefore,

$$(V_l^*, V_r^*) = (0, 2v_c) \tag{328}$$

154

(c) if $(c_{\lambda_1} \cos \theta^* + c_{\lambda_2} \sin \theta^*) = 0$, then V_r and V_l are just constrained by Eq. (325). This happens for:

- $(c_{\lambda_1}, c_{\lambda_2}) = (0,0)$. Hence, V_l^* and V_r^* can take all the values on the control line segment in the second quadrant of Fig. 13.
- $\theta^* = n\pi$ where $n \in \mathbb{Z}$, for $c_{\lambda_1} = 0$ and $c_{\lambda_2} \in \mathbb{R}$. Therefore, the correspondent V_l^* and V_r^* to the θ^* should be considered; V_l^* and V_r^* are in the second quadrant.
- $\theta^* = (2n+1)\pi/2$ where $n \in \mathbb{Z}$, for $c_{\lambda_2} = 0$ and $c_{\lambda_1} \in \mathbb{R}$. Therefore, the correspondent V_l^* and V_r^* to the θ^* should be considered; V_l^* and V_r^* are in the second quadrant.

(III) **Third Quadrant of Fig. 13:**

In the *third* quadrant, the constraint in Eq. (314) is converted to

$$V_r + V_l = -2v_c \tag{329}$$

Hence, Eq. (315) becomes:

$$H_E(\mathbf{x}^*(t), \mathbf{u}(t), \boldsymbol{\lambda}^*(t), t) = k\frac{|V_r - V_l|}{B_s} + 2Gv_c - c_{\lambda_1}v_c \cos\theta^*$$
$$- c_{\lambda_2}v_c \sin\theta^* + (c_{\lambda_1}y^* - c_{\lambda_2}x^* + c_{\lambda_3})\left(\frac{V_r - V_l}{B_s}\right) \tag{330}$$

By utilizing the similar method explained for the *first quadrant of Fig. 13*, the following results are obtained:

(a) $V_r > V_l$

(i) if $(k + c_{\lambda_1}y^* - c_{\lambda_2}x^* + c_{\lambda_3})$ is positive,

$$\boxed{(V_l^*, V_r^*) = (-v_c, -v_c + \epsilon_{E_3})} \tag{331}$$

where ϵ_{E_3} is a small positive infinitesimal quantity.

(ii) if $(k + c_{\lambda_1}y^* - c_{\lambda_2}x^* + c_{\lambda_3})$ is negative,

$$\boxed{(V_l^*, V_r^*) = (-2v_c, 0)} \tag{332}$$

(b) $V_r = V_l$

$$\boxed{(V_l^*, V_r^*) = (-v_c, -v_c)} \tag{333}$$

(c) $V_r < V_l$

(i) if $(k - c_{\lambda_1}y^* + c_{\lambda_2}x^* - c_{\lambda_3})$ is positive,

$$\boxed{(V_l^*, V_r^*) = (-v_c + \epsilon_{E_4}, -v_c)} \tag{334}$$

where ϵ_{E_4} is a small positive infinitesimal quantity.

(ii) if $(k - c_{\lambda_1} y^* + c_{\lambda_2} x^* - c_{\lambda_3})$ is negative,

$$(V_l^*, V_r^*) = (0, -2v_c) \tag{335}$$

(IV) Fourth Quadrant of Fig. 13:

Because the right and left velocities are considered in the fourth quadrant, the constraint in Eq. (314) is converted to

$$V_r - V_l = -2v_c \tag{336}$$

Therefore, the *Hamiltonian* in Fig. 315 is simplified to:

$$
\begin{aligned}
H_E(\mathbf{x}^*(t), \mathbf{u}(t), \boldsymbol{\lambda}^*(t), t) = {}& k\frac{2v_c}{B_s} + 2Gv_c + (c_{\lambda_1}\cos\theta^* + c_{\lambda_2}\sin\theta^*)\frac{V_r + V_l}{2} \\
& + (c_{\lambda_1} y^* - c_{\lambda_2} x^* + c_{\lambda_3})\left(\frac{-2v_c}{B_s}\right)
\end{aligned} \tag{337}
$$

By utilizing the similar method explained for the *second quadrant of Fig. 13*, the following results are obtained:

(a) if $(c_{\lambda_1}\cos\theta^* + c_{\lambda_2}\sin\theta^*) > 0$,

$$(V_l^*, V_r^*) = (0, -2v_c) \tag{338}$$

(b) if $(c_{\lambda_1}\cos\theta^* + c_{\lambda_2}\sin\theta^*) < 0$,

$$(V_l^*, V_r^*) = (2v_c, 0) \tag{339}$$

(c) if $(c_{\lambda_1}\cos\theta^* + c_{\lambda_2}\sin\theta^*) = 0$, V_r and V_l are just constrained by Eq. (336). This happens for:

- $(c_{\lambda_1}, c_{\lambda_2})=(0,0)$. Hence, V_l^* and V_r^* can take all the values on the control line segment in the fourth quadrant of Fig. 13.
- $\theta^* = n\pi$ where $n \in \mathbb{Z}$, for $c_{\lambda_1}=0$ and $c_{\lambda_2} \in \mathbb{R}$. Therefore, the correspondent V_l^* and V_r^* to the θ^* should be considered; V_l^* and V_r^* are in the fourth quadrant.
- $\theta^* = (2n+1)\pi/2$ where $n \in \mathbb{Z}$, for $c_{\lambda_2}=0$ and $c_{\lambda_1} \in \mathbb{R}$. Therefore, the correspondent V_l^* and V_r^* to the θ^* should be considered; V_l^* and V_r^* are in the fourth quadrant.

Conclusion of the Subsection: As it is stated by Eq. (300), there are different extremal control inputs:

1. Forward or backward straight line motions.

2. CW/CCW R'-turns which can be forward or backward.

3. Infinite CW/CCW pure turns with a constant angular velocity.

Hence, to obtain the corespondent paths to the extremal control inputs the following process should be followed:

- The number of extremal CW/CCW pure turns should be limited (for case 3).

- The *switch points* between the *extremal control inputs* should be determined (for case 1,2, and 3).

- The *periodicity/length* of the *correspondent extremal paths* should be defined (for case 1,2, and 3).

B.3 Different Approaches to Solve the Energy-Efficient Path Planning Problem

As explained in subsection B.2, the *extremal control inputs* (see Eq. (300)) are obtained for the energy-efficient path planning problem. However, the main challenges are limiting the number of extremal *pure turns*, finding the *switch points* between the *extremal inputs*, and defining the *periodicity/length* of the *correspondent extremal paths*. Accordingly, to solve the energy-efficient path planning problem (Eq. (299)) two approaches can be considered:

1. *To prove several theorems specified for skid-steer rovers to obtain all the extremal paths for the energy-efficient path planning problem*: In this approach almost similar theorems and process performed by A. Furtuna [62] should be regenerated and then be revised/adjusted for our problem (Eq. (299)).

2. *To find an equivalent time-optimal for the energy-efficient problem* (Eq. (299)): Hence, the theorems that are proved by A. Furtuna [62] can be used directly for solving the *equivalent time-optimal* problem. Therefore, the answers to the energy-efficient path planning problem (Eq. (299)) will be obtained.

Before explaining which approach is chosen, it is described why in approach 1 it is not feasible to use directly A. Furtuna's theorems for our energy-efficient path planning problem. In A. Furtuna's thesis [62], Hamiltonian[43] for the time-optimal path planning problem of a rigid body is:

$$H_T = \lambda_1 \dot{x} + \lambda_2 \dot{y} + \lambda_3 \dot{\theta} \tag{340}$$

However, in my thesis, Hamiltonian for the energy-efficient path planning problem for skid-steer rovers is Eq. (301) which can be written in the following format:

$$H_E = H_T + k|\dot{\theta}| + 2G v_c \tag{341}$$

Therefore, H_E and H_T are not the same. In A. Furtuna's thesis [62] all the theorems [44] are using H_T.

---

[43]Equation 4.10 of [62]

[44]i.e. theorems proved for *whirls* in section 4.2 of A. Furtuna's thesis as well as the theorems in Chapter 5 and 6 of the thesis to prove the periodicity of *non-whirls* paths

In this thesis, the *second approach* which is utilizing *the equivalent time-optimal* problem is chosen. The reasons are mentioned in the following:

- Based on the literature review in subsection 1.2.2, using an *equivalent optimal path planning problem* to solve the original path planning problem for rovers is a new approach.

- The *equivalent time-optimal path planning problem* enabled us to use directly the published theorems by A. Furtuna [62]. Hence, we obtained the answers for our original energy-efficient path planning problem.

Hence, the extremal paths including non-whirls (Table 3) and whirls (subsection 4.1) for the equivalent time-optimal problem, and thus, for the *energy-efficient problem* are obtained.

Appendix C   Elaborating on Cases Presented in Table 8

Case 4: $\left(\mu_1 = 0, \mu_2 > 0, \mu_3 = 0, \mu_4 = 0, \mu_5 = 0, \mu_6 = 0\right)$

$$\mu_2 > 0 \Rightarrow \theta_{B_1}^{*P} = \frac{\pi}{2k} \tag{342}$$

Eq. (190) should be solved when $\mu_1 = 0$, $\pi/2k$, $\mu_3 = 0$, $\mu_4 = 0$, $\mu_5 = 0$, and $\mu_6 = 0$ and The following conditions should be checked.

$$0 < R_1 \le \frac{W}{2}, 0 < R_2 \le \frac{W}{2}, \mu_2 > 0 \tag{343}$$

Accordingly, R_1^*, R_2^*, and $\theta_{B_1}^{*P}$ will be obtained.

Case 5: $\left(\mu_1 > 0, \mu_2 = 0, \mu_3 = 0, \mu_4 = 0, \mu_5 = 0, \mu_6 = 0\right)$

$$\mu_1 > 0 \Rightarrow \theta_{B_1}^{*P} = \frac{\epsilon_1}{k} \tag{344}$$

Eq. (190) should be solved while $\theta_{B_1}^{P} = \frac{\epsilon_1}{k}$, $\mu_2 = 0$, $\mu_3 = 0$, $\mu_4 = 0$, $\mu_5 = 0$, and $\mu_6 = 0$ and the answers should be checked for

$$0 < R_1 \le \frac{W}{2}, 0 < R_2 \le \frac{W}{2}, \mu_1 > 0 \tag{345}$$

Accordingly, R_1^*, R_2^*, and $\theta_{B_1}^{*P}$ will be obtained.

Case 6: $\left(\mu_1 = 0, \mu_2 = 0, \mu_3 > 0, \mu_4 > 0, \mu_5 = 0, \mu_6 = 0\right)$

$$\mu_3 > 0, \mu_4 > 0 \Rightarrow R_1^* = \epsilon_2, R_2^* = \epsilon_3 \tag{346}$$

Eq. (190) should be solved while $R_1 = \epsilon_2$, $R_2 = \epsilon_3$, $\mu_1 = 0$, $\mu_2 = 0$, $\mu_5 = 0$, and $\mu_6 = 0$ and the following conditions should be checked.

$$0 < k\theta_{B_1} \le \frac{\pi}{2}, \mu_3 > 0, \mu_4 > 0 \tag{347}$$

Accordingly, R_1^*, R_2^*, and $\theta_{B_1}^{*P}$ will be obtained.

Case 7: $\left(\mu_1 = 0, \mu_2 > 0, \mu_3 = 0, \mu_4 > 0, \mu_5 = 0, \mu_6 = 0\right)$

$$\mu_2 > 0, \mu_4 > 0 \Rightarrow \theta_{B_1}^{*P} = \frac{\pi}{2k}, R_2^* = \epsilon_2 \tag{348}$$

Eq. (190) should be solved while $\mu_1 = 0$, $\theta_{B_1}^{P} = \frac{\pi}{2k}$, $\mu_3 = 0$, $R_2 = \epsilon_2$, $\mu_5 = 0$, and $\mu_6 = 0$ and the following conditions should be checked.

$$0 < R_1 \le \frac{W}{2}, \mu_2 > 0, \mu_4 > 0 \tag{349}$$

Accordingly, R_1^*, R_2^*, and $\theta_{B_1}^{*P}$ will be obtained.

Case 8: $\left(\mu_1 > 0, \mu_2 = 0, \mu_3 = 0, \mu_4 > 0, \mu_5 = 0, \mu_6 = 0\right)$

$$\mu_1 > 0, \mu_4 > 0 \Rightarrow \theta_{B_1}^{*^P} = \frac{\epsilon_1}{k}, R_2^* = \epsilon_3 \tag{350}$$

Eq. (190) should be solved while $\theta_{B_1}^P = \frac{\epsilon_1}{k}$, $\mu_2 = 0$, $\mu_3 = 0$, $R_2 = \epsilon_3$, $\mu_5 = 0$, and $\mu_6 = 0$ and the following conditions should be checked.

$$0 < R_1 \le \frac{W}{2}, \mu_1 > 0, \mu_4 > 0 \tag{351}$$

Accordingly, R_1^*, R_2^*, and $\theta_{B_1}^{*^P}$ will be obtained.

Case 9: $(\mu_1 > 0, \mu_2 = 0, \mu_3 > 0, \mu_4 = 0, \mu_5 = 0, \mu_6 = 0)$

$$\mu_1 > 0, \mu_3 > 0 \Rightarrow \theta_{B_1}^{*^P} = \frac{\epsilon_1}{k}, R_1^* = \epsilon_2 \tag{352}$$

Eq. (190) should be solved while $\theta_{B_1}^P = \frac{\epsilon_1}{k}$, $\mu_2 = 0$, $R_1 = \epsilon_2$, $\mu_4 = 0$, $\mu_5 = 0$, and $\mu_6 = 0$ and the answers should be checked for

$$0 < R_2 \le \frac{W}{2}, \mu_1 > 0, \mu_3 > 0 \tag{353}$$

Accordingly, R_1^*, R_2^*, and $\theta_{B_1}^{*^P}$, will be obtained.

Case 10: $(\mu_1 = 0, \mu_2 > 0, \mu_3 > 0, \mu_4 = 0, \mu_5 = 0, \mu_6 = 0)$

$$\mu_2 > 0, \mu_3 > 0 \Rightarrow \theta_{B_1}^{*^P} = \frac{\pi}{2k}, R_1^* = \epsilon_2 \tag{354}$$

Eq. (190) should be solved while $\mu_1 = 0$, $\theta_{B_1}^P = \frac{\pi}{2k}$, $R_1 = \epsilon_2$, $\mu_4 = 0$, $\mu_5 = 0$, and $\mu_6 = 0$ and the following conditions should be checked.

$$0 < R_2 \le \frac{W}{2}, \mu_2 > 0, \mu_3 > 0 \tag{355}$$

Accordingly, R_1^*, R_2^*, and $\theta_{B_1}^{*^P}$ will be obtained.

Case 11: $(\mu_1 > 0, \mu_2 = 0, \mu_3 > 0, \mu_4 > 0, \mu_5 = 0, \mu_6 = 0)$

$$\mu_1 > 0, \mu_3 > 0, \mu_4 > 0 \Rightarrow \theta_{B_1}^{*^P} = \frac{\epsilon_1}{k}, R_1^* = \epsilon_2, R_2^* = \epsilon_3 \tag{356}$$

Eq. (190) should be solved while $\mu_2 = 0$, $\theta_{B_1}^P = \frac{\epsilon_1}{k}$, $R_1 = \epsilon_2$, $R_2 = \epsilon_3$, $\mu_5 = 0$, and $\mu_6 = 0$ and the following conditions should be checked.

$$\mu_1 > 0, \mu_3 > 0, \mu_4 > 0 \tag{357}$$

Accordingly, R_1^*, R_2^*, and $\theta_{B_1}^{*^P}$ will be obtained.

Case 12: $(\mu_1 = 0, \mu_2 > 0, \mu_3 > 0, \mu_4 > 0, \mu_5 = 0, \mu_6 = 0)$

$$\mu_2 > 0, \mu_3 > 0, \mu_4 > 0 \Rightarrow \theta_{B_1}^{*^P} = \frac{\pi}{2k}, R_1^* = \epsilon_2, R_2^* = \epsilon_3 \tag{358}$$

Eq. (190) should be solved while $\mu_1 = 0$, $\theta_{B_1}^P = \frac{\pi}{2k}$, $R_1 = \epsilon_2$, $R_2 = \epsilon_3$, $\mu_5 = 0$, and $\mu_6 = 0$ and the following conditions should be checked.

$$\mu_2 > 0, \mu_3 > 0, \mu_4 > 0 \tag{359}$$

Accordingly, R_1^*, R_2^*, and $\theta_{B_1}^{*P}$ will be obtained.

Case 13: $\left(\mu_1 = 0, \mu_2 = 0, \mu_3 = 0, \mu_4 = 0, \mu_5 > 0, \mu_6 = 0\right)$

$$\mu_5 > 0 \Rightarrow R_1^* = \frac{W}{2} \tag{360}$$

Eq. (190) should be solved for $\mu_1 = 0$, $\mu_2 = 0$, $\mu_3 = 0$, $\mu_4 = 0$, $R_1 = W/2$, and $\mu_6 = 0$. Then, the answers should be checked for

$$0 < k\theta_{B_1} \le \frac{\pi}{2}, 0 < R_2 \le \frac{W}{2}, \mu_5 > 0 \tag{361}$$

Accordingly, R_1^*, R_2^*, and $\theta_{B_1}^{*P}$ will be obtained.

Case 14: $\left(\mu_1 = 0, \mu_2 = 0, \mu_3 = 0, \mu_4 > 0, \mu_5 > 0, \mu_6 = 0\right)$

$$\mu_4 > 0, \mu_5 > 0 \Rightarrow R_2^* = \epsilon_3, R_1^* = \frac{W}{2} \tag{362}$$

Eq. (190) should be solved for $\mu_1 = 0$, $\mu_2 = 0$, $\mu_3 = 0$, $R_2 = \epsilon_3$, $R_1 = \frac{W}{2}$, and $\mu_6 = 0$. Then, the answers should be checked for

$$0 < k\theta_{B_1} \le \frac{\pi}{2}, \mu_4 > 0, \mu_5 > 0, \tag{363}$$

Accordingly, R_1^*, R_2^*, and $\theta_{B_1}^{*P}$ will be obtained.

Case 15: $\left(\mu_1 = 0, \mu_2 > 0, \mu_3 = 0, \mu_4 = 0, \mu_5 > 0, \mu_6 = 0\right)$

$$\mu_2 > 0, \mu_5 > 0 \Rightarrow \theta_{B_1}^{*P} = \frac{\pi}{2k}, R_1^* = \frac{W}{2} \tag{364}$$

Eq. (190) should be solved for $\mu_1 = 0$, $\theta_{B_1}^P = \frac{\pi}{2k}$, $\mu_3 = 0$, $\mu_4 = 0$, $R_1 = \frac{W}{2}$, and $\mu_6 = 0$. Then, the answers should be checked for

$$\mu_2 > 0, \mu_5 > 0, 0 < R_2 \le \frac{W}{2} \tag{365}$$

Accordingly, R_1^*, R_2^*, and $\theta_{B_1}^{*P}$ will be obtained.

Case 16: $\left(\mu_1 > 0, \mu_2 = 0, \mu_3 = 0, \mu_4 = 0, \mu_5 > 0, \mu_6 = 0\right)$

$$\mu_1 > 0, \mu_5 > 0 \Rightarrow \theta_{B_1}^{*P} = \frac{\epsilon_1}{k}, R_1^* = \frac{W}{2} \tag{366}$$

Eq. (190) should be solved for $\theta_{B_1}^P = \frac{\epsilon_1}{k}$, $\mu_2 = 0$, $\mu_3 = 0$, $\mu_4 = 0$, $R_1 = \frac{W}{2}$, and $\mu_6 = 0$. Then, the answers should be checked for

$$\mu_1 > 0, \mu_5 > 0, 0 < R_2 \le \frac{W}{2} \tag{367}$$

Accordingly, R_1^*, R_2^*, and $\theta_{B_1}^{*P}$ will be obtained.

Case 17: $(\mu_1 = 0, \mu_2 > 0, \mu_3 = 0, \mu_4 > 0, \mu_5 > 0, \mu_6 = 0)$

$$\mu_2 > 0, \mu_4 > 0, \mu_5 > 0 \Rightarrow \theta_{B_1}^{*P} = \frac{\pi}{2k}, R_1^* = \frac{W}{2}, R_2^* = \epsilon_3 \tag{368}$$

Eq. (190) should be solved for $\mu_1 = 0$, $\theta_{B_1}^P = \frac{\pi}{2k}$, $\mu_3 = 0$, $R_1 = \frac{W}{2}$, $R_2 = \epsilon_3$, and $\mu_6 = 0$. Then, the answers should be checked for

$$\mu_2 > 0, \mu_4 > 0, \mu_5 > 0 \tag{369}$$

Accordingly, R_1^*, R_2^*, and $\theta_{B_1}^{*P}$ will be obtained.

Case 18: $(\mu_1 > 0, \mu_2 = 0, \mu_3 = 0, \mu_4 > 0, \mu_5 > 0, \mu_6 = 0)$

$$\mu_1 > 0, \mu_4 > 0, \mu_5 > 0 \Rightarrow \theta_{B_1}^{*P} = \frac{\epsilon_1}{k}, R_2^* = \epsilon_3, R_1^* = \frac{W}{2} \tag{370}$$

Eq. (190) should be solved for $\theta_{B_1}^{*P} = \frac{\epsilon_1}{k}$, $\mu_2 = 0$, $\mu_3 = 0$, $R_1 = \frac{W}{2}$, $R_2 = \epsilon_3$, and $\mu_6 = 0$. Then, the answers should be checked for

$$\mu_1 > 0, \mu_4 > 0, \mu_5 > 0 \tag{371}$$

Accordingly, R_1^*, R_2^*, and $\theta_{B_1}^{*P}$ will be obtained.

Case 19: $(\mu_1 = 0, \mu_2 = 0, \mu_3 = 0, \mu_4 = 0, \mu_5 = 0, \mu_6 > 0)$

$$\mu_6 > 0 \Rightarrow R_2^* = \frac{W}{2} \tag{372}$$

Eq. (190) should be solved for $\mu_1 = 0$, $\mu_2 = 0$, $\mu_3 = 0$, $\mu_4 = 0$, $\mu_5 = 0$, and $R_2 = \frac{W}{2}$. Then, the answers should be checked for

$$0 < k\theta_{B_1} \leq \frac{\pi}{2}, 0 < R_1 \leq \frac{W}{2}, \mu_6 > 0 \tag{373}$$

Accordingly, R_1^*, R_2^*, and $\theta_{B_1}^{*P}$ will be obtained.

Case 20: $(\mu_1 = 0, \mu_2 = 0, \mu_3 > 0, \mu_4 = 0, \mu_5 = 0, \mu_6 > 0)$

$$\mu_3 > 0, \mu_6 > 0 \Rightarrow R_1^* = \epsilon_2, R_2^* = \frac{W}{2} \tag{374}$$

Eq. (190) should be solved for $\mu_1 = 0$, $\mu_2 = 0$, $R_1^* = \epsilon_2$, $\mu_4 = 0$, $\mu_5 = 0$, and $R_2 = \frac{W}{2}$. Then, the answers should be checked for

$$0 < k\theta_{B_1} \leq \frac{\pi}{2}, \mu_3 > 0, \mu_6 > 0 \tag{375}$$

Accordingly, R_1^*, R_2^*, and $\theta_{B_1}^{*P}$ will be obtained.

Case 21: $(\mu_1 = 0, \mu_2 > 0, \mu_3 = 0, \mu_4 = 0, \mu_5 = 0, \mu_6 > 0)$

$$\mu_2 > 0, \mu_6 > 0 \Rightarrow \theta_{B_1}^{*P} = \frac{\pi}{2k}, R_2^* = \frac{W}{2} \tag{376}$$

Eq. (190) should be solved for $\mu_1 = 0$, $\theta_{B_1}^{*P} = \dfrac{\pi}{2k}$, $\mu_3 = 0$, $\mu_4 = 0$, $\mu_5 = 0$, and $R_2 = \dfrac{W}{2}$. Then, the answers should be checked for

$$\mu_2 > 0, \mu_6 > 0, 0 < R_1 \le \frac{W}{2} \tag{377}$$

Accordingly, R_1^*, R_2^*, and $\theta_{B_1}^{*P}$ will be obtained.

Case 22: $\left(\mu_1 > 0, \mu_2 = 0, \mu_3 = 0, \mu_4 = 0, \mu_5 = 0, \mu_6 > 0\right)$

$$\mu_1 > 0, \mu_6 > 0 \Rightarrow \theta_{B_1}^{*P} = \frac{\epsilon_1}{k}, R_2^* = \frac{W}{2} \tag{378}$$

Eq. (190) should be solved for $\theta_{B_1}^{*P} = \dfrac{\epsilon_1}{k}$, $\mu_2 = 0$, $\mu_3 = 0$, $\mu_4 = 0$, $\mu_5 = 0$, and $R_2 = \dfrac{W}{2}$. Then, the answers should be checked for

$$\mu_1 > 0, \mu_6 > 0, 0 < R_1 \le \frac{W}{2} \tag{379}$$

Accordingly, R_1^*, R_2^*, and $\theta_{B_1}^{*P}$ will be obtained.

Case 23: $\left(\mu_1 > 0, \mu_2 = 0, \mu_3 > 0, \mu_4 = 0, \mu_5 = 0, \mu_6 > 0\right)$

$$\mu_1 > 0, \mu_3 > 0, \mu_6 > 0 \Rightarrow \theta_{B_1}^{*P} = \frac{\epsilon_1}{k}, R_1^* = \epsilon_2, R_2^* = \frac{W}{2} \tag{380}$$

Eq. (190) should be solved for $\theta_{B_1}^{*P} = \dfrac{\epsilon_1}{k}$, $\mu_2 = 0$, $R_1^* = \epsilon_2$, $\mu_4 = 0$, $\mu_5 = 0$, and $R_2 = \dfrac{W}{2}$. Then, the answers should be checked for

$$\mu_1 > 0, \mu_3 > 0, \mu_6 > 0 \tag{381}$$

Accordingly, R_1^*, R_2^*, and $\theta_{B_1}^{*P}$ will be obtained.

Case 24: $\left(\mu_1 = 0, \mu_2 > 0, \mu_3 > 0, \mu_4 = 0, \mu_5 = 0, \mu_6 > 0\right)$

$$\mu_2 > 0, \mu_3 > 0, \mu_6 > 0 \Rightarrow \theta_{B_1}^{*P} = \frac{\pi}{2k}, R_1^* = \epsilon_2, R_2^* = \frac{W}{2} \tag{382}$$

Eq. (190) should be solved for $\mu_1 = 0$, $\theta_{B_1}^{*P} = \dfrac{\pi}{2k}$, $R_1^* = \epsilon_2$, $\mu_4 = 0$, $\mu_5 = 0$, and $R_2 = \dfrac{W}{2}$. Then, the answers should be checked for

$$\mu_2 > 0, \mu_3 > 0, \mu_6 > 0 \tag{383}$$

Accordingly, R_1^*, R_2^*, and $\theta_{B_1}^{*P}$ will be obtained.

Case 25: $\left(\mu_1 = 0, \mu_2 = 0, \mu_3 = 0, \mu_4 = 0, \mu_5 > 0, \mu_6 > 0\right)$

$$\mu_5 > 0, \mu_6 > 0 \Rightarrow R_1^* = \frac{W}{2}, R_2^* = \frac{W}{2} \tag{384}$$

Eq. (190) should be solved for $\mu_1 = 0$, $\mu_2 = 0$, $\mu_3 = 0$, $\mu_4 = 0$, $R_1 = \dfrac{W}{2}$, and $R_2 = \dfrac{W}{2}$. Then, the answers should be checked for

$$\mu_5 > 0, \mu_6 > 0, 0 < k\theta_{B_1} \le \frac{\pi}{2} \tag{385}$$

Accordingly, R_1^*, R_2^*, and $\theta_{B_1}^{*P}$ will be obtained.

Case 26: $\left(\mu_1 = 0, \mu_2 > 0, \mu_3 = 0, \mu_4 = 0, \mu_5 > 0, \mu_6 > 0\right)$

$$\mu_2 > 0, \mu_5 > 0, \mu_6 > 0 \Rightarrow \theta_{B_1}^{*P} = \frac{\pi}{2k}, R_1^* = \frac{W}{2}, R_2^* = \frac{W}{2} \tag{386}$$

Eq. (190) should be solved for $\mu_1 = 0$, $\theta_{B_1}^{*P} = \frac{\pi}{2k}$, $\mu_3 = 0$, $\mu_4 = 0$, $R_1 = \frac{W}{2}$, and $R_2 = \frac{W}{2}$. Then, the answers should be checked for

$$\mu_2 > 0, \mu_5 > 0, \mu_6 > 0 \tag{387}$$

Accordingly, R_1^*, R_2^*, and $\theta_{B_1}^{*P}$ will be obtained.

Case 27: $\left(\mu_1 > 0, \mu_2 = 0, \mu_3 = 0, \mu_4 = 0, \mu_5 > 0, \mu_6 > 0\right)$

$$\mu_1 > 0, \mu_5 > 0, \mu_6 > 0 \Rightarrow \theta_{B_1}^{*P} = \frac{\epsilon_1}{k}, R_1^* = \frac{W}{2}, R_2^* = \frac{W}{2} \tag{388}$$

Eq. (190) should be solved for $\theta_{B_1}^{*P} = \frac{\epsilon_1}{k}$, $\mu_2 = 0$, $\mu_3 = 0$, $\mu_4 = 0$, $R_1 = \frac{W}{2}$, and $R_2 = \frac{W}{2}$. Then, the answers should be checked for

$$\mu_1 > 0, \mu_5 > 0, \mu_6 > 0 \tag{389}$$

Accordingly, R_1^*, R_2^*, and $\theta_{B_1}^{*P}$ will be obtained.

Appendix D

If (240) and (241) are solved for T_1 and T_2, the following relations will be obtained.

$$T_1 = \frac{-N_2 - N_1 cos(\theta_1 - \theta_2) + gm_1 cos(\theta_2) + gm_2 cos(\theta_2)}{sin(\theta_1 - \theta_2)} \qquad (390)$$

$$T_2 = \frac{N_1 + N_2 cos(\theta_1 - \theta_2) - gm_1 cos(\theta_1) - gm_2 cos(\theta_1)}{sin(\theta_1 - \theta_2)} \qquad (391)$$

As it is clear, $\theta_1 = \theta_2$ causes singularity in the analytical method. However, as Fig. 66 shows, when θ_1 is equal to θ_2 there are in fact feasible optimal values for T_1 and T_2.

Appendix E

T_3, T_4, and N_3 are obtained as a function of N_4 by the use of Equations (246) to (249). Then, they are substituted at Equation (250). Accordingly, four sets of equations are obtained, one of them is presented below:

$$a_1 N_4^2 = a_2 N_4 + a_3 \tag{392}$$

where the coefficients are as follows:

$$a_1 = k_1 \tag{393}$$

$$a_2 = k_2 \sigma_4 \sigma_6 + k_3 \sigma_3 \sigma_7 + k_4 \tag{394}$$

$$a_3 = k_5 \sigma_4 \sigma_6 + k_6 \sigma_3 \sigma_7 + k_7 \tag{395}$$

$$\sigma_3 = \sqrt{(c_1 N_4^2 + c_2 N_4 + c_3)} + \sqrt{c_4 N_4 + \sqrt{(c_1 N_4^2 + c_2 N_4 + c_3)} + c_5}$$
$$+ c_6 N_4 \sqrt{(c_1 N_4^2 + c_2 N_4 + c_3)} + c_7 N_4^4 + c_8 N_4^3 + c_9 N_4^2 + c_{10} N_4 + c_{11} \tag{396}$$

$$\sigma_4 = \sqrt{(c_{13} N_4^2 + c_{14} N_4 + c_{15})} \tag{397}$$

$$\sigma_6 = c_{12} \sigma_3 \tag{398}$$

$$\sigma_7 = c_{13} \sigma_4 \tag{399}$$

where $k_i (i = 1,...,7)$ and $c_j (j = 1,...,15)$ are the function of one or more of the θ_1, θ_2, θ_3, θ_4, α_{12}, α_{34}. Now, if the Equation 392 is to be expanded, the following equation will be obtained.

$$K_1 N_4^2 = k_3 \sigma_3 \sigma_{70} N_4 + ... = k_3 c_7 c_{13} N_4^5 \sqrt{c_{13} N_4^2 + c_{14} N_4 + c_{15}} + ... \tag{400}$$

As it can be seen, N_4^5 appears before even squaring any of the terms to remove the square-roots. Therefore, it is highly probable that the degree of polynomial is greater than five. The same procedure can be done for the other three sets of equation to show that the degree of their polynomial is greater than five. According to Abel Ruffini's theorem (Abel's impossibility theorem), in general there is not any algebraic solution for polynomial equations of degree five or higher with arbitrary coefficients–a solution in radicals. Therefore, it is highly probable that there is no general solution for the aforementioned set of equations.